
Lehrstuhl für Experimentelle Plasmaphysik
Universität Augsburg

# Experiments and Simulations for the Dynamics of Cesium in Negative Hydrogen Ion Sources for ITER N-NBI

Dissertation zur Erlangung des Doktorgrades
an der Mathematisch-Naturwissenschaftlichen Fakultät
der Universität Augsburg

vorgelegt von
Raphael Gutser
am 31. März 2010

Vorgelegt am 31. März 2010

Tag der mündlichen Prüfung: 21. Juli 2010

Erstgutachten: Prof. Dr.-Ing. U. Fantz

Zweitgutachten: Prof. Dr. A. Wixforth

Drittgutachten: Prof. Dr. H. Zohm

# Contents

# 1. Introduction

The injection of fast neutral particles into a magnetically-confined fusion plasma depositing energy by collision processes is an important method for plasma heating and current drive. Sources for negative or positive hydrogen ions delivering an ion beam that is accelerated to a specified energy and neutralized by a gas target are basic components of neutral beam injection (NBI) systems. The torus of the fusion experiment ITER will have large dimensions and neutral beams with a particle energy of 1 MeV are required. While the neutralization efficiency for positive hydrogen-ion beams at 1 MeV tends to zero, it is still 60 % in case of negative hydrogen ions. However, negative hydrogen ions are vulnerable to destruction processes and the current densities extracted from the corresponding ion sources are typically a factor of ten lower than from positive-ion sources. High negative-ion currents can be only achieved by using a large-scale extraction area corresponding to source dimensions of 1.9 x 0.9 $m^2$. The spatial homogeneity of the extracted negative-ion current density over the large-scale extraction area and a pulse duration of one hour are essential requirements for the ITER negative-ion source.

RF-driven sources for positive hydrogen ions have been successfully developed at IPP (Max-Planck-Institut für Plasmaphysik, Garching) for the neutral beam heating systems of the fusion experiments ASDEX Upgrade and W7-AS/W7-X. In contrast to arc-sources, the use of RF-driven sources allows a basically maintenance-free operation, which reduces the need for complex remote handling at ITER. A RF-driven negative-ion source on this basis is currently under development at the IPP, and was adopted as the reference source for the ITER neutral beam injectors.

ITER-relevant operation conditions of the ion source can be achieved by using the surface production of negative ions as opposed to the volume production often used for accelerator sources in nuclear physics. Positive or neutral hydrogen plasma particles from a plasma source are converted into negative ions by picking up electrons from a surface with a low work function. Predominantly, negative ions produced on the plasma grid surface close to the ion extraction system

contribute to the extracted negative-ion current density. This is an effect of the short survival length (a few cm) of the negative hydrogen ion.
The work function of a bare metal surface is not sufficiently low to produce enough negative ions and lowering the work function by covering the plasma grid with cesium is necessary. An evaporation system, containing the alkaline metal in its elemental state, is used to inject cesium into the ion source. The cesium from this supply has to be transported to the plasma grid surfaces where an enhancement of the surface production rate is obtained.
At present, the most critical issue is obtaining homogeneous cesium conditions over the plasma grid surface that are stable for plasma pulses with a duration of one hour. The optimization of the cesium homogeneity and control are major objectives to achieve the requirements, imposed by ITER. Investigations of the cesium injection, transport, and adsorption on the plasma grid surface during the vacuum (plasma-off) and discharge phases (plasma-on) of the ion source are required to obtain an advanced understanding of the dynamics of cesium within the source.
Besides for ITER, cesium is used all over the world in negative-ion sources for neutral beam injection systems and particle accelerators. Experience and empirical techniques are often important factors to obtain a high source performance. Hence, systematic investigations of the dynamics of cesium are of great technologic importance for negative-ion sources in general.
Numerical simulations are valuable tools to predict the dynamics and spatial distribution of cesium within the negative-ion source. Data of the de- and adsorption kinetics of cesium layers on metal samples are necessary to carry out simulations of the cesium transport within the ion source. The available data in research publications are, however, not valid for the vacuum and temperature conditions within negative-ion sources. Calculations for the thermal desorption rates from the vapor pressure of elemental cesium show that these parameters are inadequate to give results that are consistent with experimental observations at the IPP negative-ion source test facilities. This disparity indicates that the basic input parameters are strongly correlated to the specific surface and pressure conditions within the negative-ion source.
Dedicated experimental studies are required to obtain input data for the transport computation, such as the surface affinity of cesium on the walls of the ion source or the flow from the evaporation oven into the source. Thus, it is important to perform systematic investigations of the surface affinity and the desorption of cesium from metal surfaces in a laboratory experiment, where ion

source relevant temperature and pressure conditions can be obtained. Additionally, the lab experiments help to improve the understanding of factors that are highly relevant to the negative-ion production, for example, the work function. The work function of a cesium-coated metal surface is a dominant parameter for the negative-ion production.

Plasma exposition is a requirement for the surface production of negative-ions. Therefore, the influence of the plasma exposition on the work function of a cesium-coated metal sample and the comparison to measurements in the vacuum are important issues to resolve. Due to the presence of a plasma, it is impossible to determine the photocurrent from a biased metal sample, since the plasma-generated currents seriously interferes with the photocurrent measurement. A possible way to overcome this issue by the use of pulsed plasma source is investigated.

Cesium injection at the ion source test facilities requires a stable and constant cesium flow for a time period of several weeks for up to ten hours per day. No monitoring of the intensity and long-term stability of the flow from the IPP cesium evaporation oven, based on cesium evaporation from a liquid reservoir, has been done up to now. However, these data are highly desirable to evaluate the performance of the existing oven and to quantify the cesium consumption of the ion source. Furthermore, the monitoring serves to determine the influx from the cesium oven into the ion source that is required for the cesium transport simulation.

Thus, an important task is the development and testing of a robust cesium detector design in order to monitor the performance and reliability of the existing evaporation oven and to find ways to optimize the existing and new cesium injection systems. The surface ionization detection principle for atomic cesium beams in a vacuum environment is a possible approach that satisfies the requirements for a long-term flow monitoring.

The liquid reservoir-based cesium injection systems, in use at IPP, are limited regarding the long-term stability and the control of the delivered cesium flow. Thus, cesium injection by commercial dispenser sources, based on cesium release by the decomposition of stable cesium compounds, needs to be evaluated and prepared for the use at the negative-ion source. These dispensers can be either implemented directly into the ion source or used as cesium sources for a new oven.

The results of the described measurements are prerequisites for realistic numerical transport investigations. However, no commercial or scientific code

is available meeting the demands of the cesium transport within negative-ion sources. Hence, it is required to start the development of a code that considers the specific requirements of the negative-ion source.
The major objectives of the computer simulation are the computation of the dynamics and the spatial resolution of the cesium flux onto the plasma grid of negative-ion sources during vacuum and discharge phases. An investigation of the influence of the source wall temperatures and the length of the plasma pulse are important aspects that need to be simulated by the model. The investigation of these effects is primarily motivated from operational experience gained at the IPP test facilities.
The enhancement of the understanding of the cesium transport during the long-pulse operation phases of the negative-ion source is an especially important objective, since it will require a stable one hour pulse.
Besides the direct injection from the cesium source, a release of cesium from the walls of the ion source during both the vacuum and the plasma phase has to be considered in the code. Hence, important aspects of the transport simulation are to identify the physical processes and to determine the associated surface areas of the ion source walls that contribute predominantly to these transport processes. The identification of the cesium-emitting areas is required to provide an optimization of the cesium management and to explain properties of the cesium flux, such as the flux homogeneity or the fraction of cesium ions within the total flux.
Based on the contributions from the cesium oven and from the cesium release by the source walls, it is possible to simulate the dynamics and profile of the cesium flux onto the plasma grid. This is necessary to evaluate both the loss of cesium through the apertures of the grid and the homogeneity of the flux profile.
An important application for a simulation of the cesium transport is, furthermore, to find new ways in order to optimize the stability and homogeneity of the cesium flux within the source. This includes the evaluation of the effect of cesium injection by the use of several evaporation sources, as planned for future ion sources at IPP.
Additionally, calculations are required in order to devise a new method of cesium injection by an array of cesium dispensers that may improve the control and homogeneity of the cesium flux onto the plasma grid. These design calculations can be used to optimize the arrangement of the prototype of the dispenser array in front of the plasma grid and to check the feasibility of this method.
The influence of the spatial distribution of the cesium conditions on the plasma

grid on the profile of the extracted negative-ion current density over the plasma grid is an important aspect. It is not possible to treat both effects separately. The transport process of the surface-generated negative ions into the extraction apertures might possibly reduce the influence of the distribution of the ion production rate, created by the cesium flux, on the current density profile. A detailed study of this process requires, therefore, a coupling of a cesium transport code with a simulation of the transport of surface-generated negative-ions within the plasma of the ion source.

**Within the scope of this thesis, the Monte Carlo based numerical transport simulation CsFlow3D was developed, which is the first computer model that is capable of simulating the flux and the accumulation of cesium on the surfaces of negative-ion sources. Basic studies that support the code development were performed at a dedicated experiment at the University of Augsburg. Input parameters of the ad- and desorption of cesium at ion source relevant conditions were taken from systematic measurements with a quartz microbalance, while the injection rate of the cesium supply was determined by surface ionization detection. This experimental setup was used for further investigations of the work function of cesium-coated samples during plasma exposure. Additionally, the surface ionization detector was used to monitor the stability of the cesium flow from different cesium sources.**

# 2. Neutral Beam Heating of Fusion Plasmas

## 2.1. Nuclear Fusion

The energy demands of the 21th century with its continuous population growth cannot be met by relying on the conventional means of energy production based on fossil fuels or nuclear fission in the long term. The resources required for these technologies can hardly be expected to last more than hundred years, and their continued use has already caused serious environmental damage through global warming and the accumulation of large amounts of radioactive waste. A possible approach to solve these problems is nuclear fusion, which means converting lighter nuclei into heavier ones. The fusion of hydrogen isotopes into stable helium offers a very high energy release per nucleon, which is of the order of a few MeV. This is six orders of magnitude higher than the typical energy release obtained from a chemical reaction, a well known fact that can explain the potential efficiency of nuclear fusion as an energy source.

### 2.1.1. Fusion Reactions

Thermonuclear fusion reactions are the basic mechanisms of the energy production in stars. The following proton-proton chain, converting hydrogen to helium, is the predominant mechanism:

$$\mathrm{p} + \mathrm{p} \rightarrow \mathrm{D} + \mathrm{e}^{+} + \nu_{\mathrm{e}} + 0.42\ \mathrm{MeV}, \tag{2.1a}$$

$$\mathrm{e}^{+} + \mathrm{e}^{-} \rightarrow 2\gamma + 1.02\ \mathrm{MeV}, \tag{2.1b}$$

$$\mathrm{D} + \mathrm{p} \rightarrow {}^{3}\mathrm{He} + \gamma + 5.49\ \mathrm{MeV}, \tag{2.1c}$$

$${}^{3}\mathrm{He} + {}^{3}\mathrm{He} \rightarrow {}^{4}\mathrm{He} + 2\,\mathrm{p} + 12.86\ \mathrm{MeV}. \tag{2.1d}$$

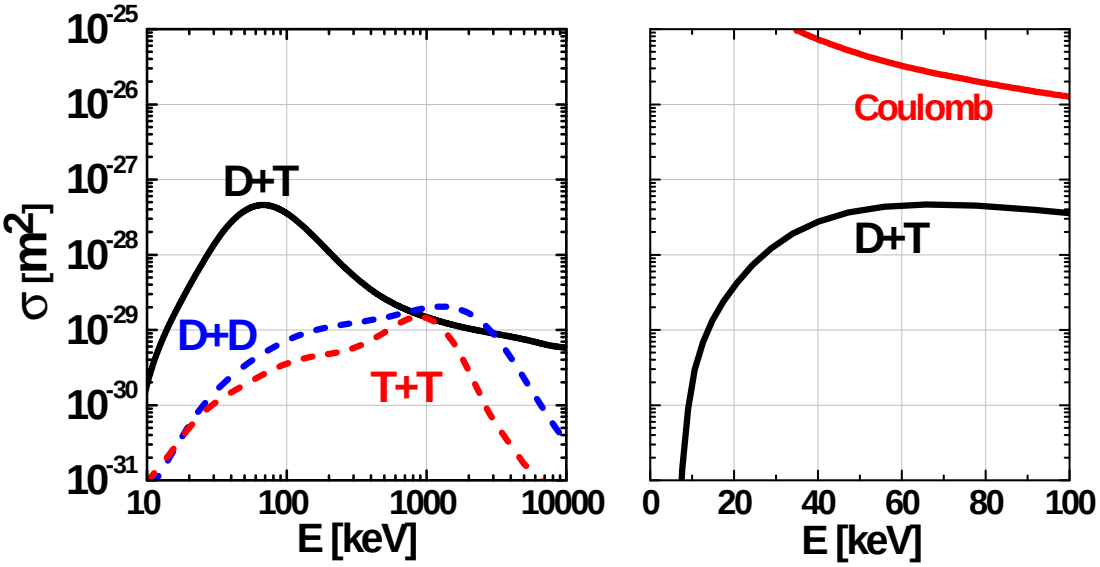


**Figure 2.1.:** Left side: cross-sections for the fusion between different hydrogen isotopes. Right side: comparison of the DT-fusion cross-section with the cross-section of elastic Coulomb scattering between the ions.

The first step involves the fusion of two hydrogen nuclei into deuterium, releasing a positron as one proton is converted into a neutron and a neutrino. This process is governed by the weak interaction, which transforms a proton into a neutron emitting a positron ($\beta^+$-decay). The weak interaction, however, results in very small reaction probabilities and the rates of fusion reactions at the densities and temperatures in stellar cores are very low. This is compensated by the huge volume of stars. As fusion reactors on earth have to be kept considerably smaller in size than a star, the use of described reaction chain 2.1a is not feasible for energy production on earth. More efficient reaction paths have to be applied in order to obtain fusion reactions at feasible reaction rates. Such nuclear reactions are determined by the strong nuclear force acting at a close distance of several fm ($10^{-15}$ m), which is in the order of the radius of the nucleus. The electrostatic interaction between the two nuclei creates a repulsive Coulomb potential and particle energies of the order of 550 keV are required to overcome this so called Coulomb-barrier. As a consequence of the tunneling-effect, which was explained in 1928 by Gamov [Gam28], fusion reactions can take place at energies far below the Coulomb barrier. An overview of fusion cross-sections for reactions between the hydrogen isotopes is shown in figure 2.1. The maximum of the D-T fusion cross-section is obtained at a lower energy in comparison to the D-D and T-T

reactions:

$$\mathrm{D} + \mathrm{T} \rightarrow {}^{4}\mathrm{He} + \mathrm{n} + 17.6\ \mathrm{MeV}. \tag{2.2}$$

Thus, a D-T mixture offers a more efficient route to power production than with pure deuterium and future fusion reactors will rely mainly on this reaction [Wes04]. While deuterium is available in sufficient amounts in seawater (0.015%), the radioactive isotope tritium (half-life: 12.3 years) is found in nature only in small amounts, where it is created by cosmic radiation in the upper atmosphere. Thus, tritium-breeding is done inside a reactor by having energetic neutrons hit a lithium blanket:

$$\mathrm{n} + {}^{6}\mathrm{Li} \rightarrow {}^{4}\mathrm{He} + \mathrm{T} + 4.8\ \mathrm{MeV}. \tag{2.3}$$

The supply of lithium is more limited than that of deuterium, but still large enough to supply the world's energy demands for more than 1000 years. A way to commence D-T-fusion reactions is to initiate collisions of accelerated reactants with a relative energy of 100 keV. Nevertheless, this approach has a negative energy balance. Figure 2.1 shows a comparison of the fusion cross-section with the cross-section of elastic Coulomb scattering. Obviously, Coulomb-collisions are the predominant process and only an insignificant number of fusion reaction processes takes place during cross-beam scattering. This is not enough to get a positive energy balance and the number of inter-particle collisions has to be increased significantly to obtain a feasible energy output.

### 2.1.2. Magnetic Confinement

The number of D-T-collisions can be increased by creating a deuterium-tritium plasma with an ion temperature of $T = 20$ keV. Strong magnetic fields are required to confine the plasma, as contact with material walls of the vacuum chamber would cool down the plasma to an unacceptable level.
Early design approaches based on a cylindrical plasma shape suffered from high energy losses at the ends of the device. To avoid these losses, it is essential to use a toroidal topology of the magnetic field lines. In simple toroidal systems, the magnetic field topology generates a $\nabla\vec{B}$-drift that goes in opposite directions for ions and electrons. The resulting electric field and the toroidal magnetic field cause an $\vec{E} \times \vec{B}$ - drift of the whole plasma, creating an unstable condition. An additional poloidal field is necessary to twist the magnetic field lines and thus to improve the magnetic confinement. This additional field can be generated by two different concepts: Stellarators and Tokamaks. Both concepts are outlined

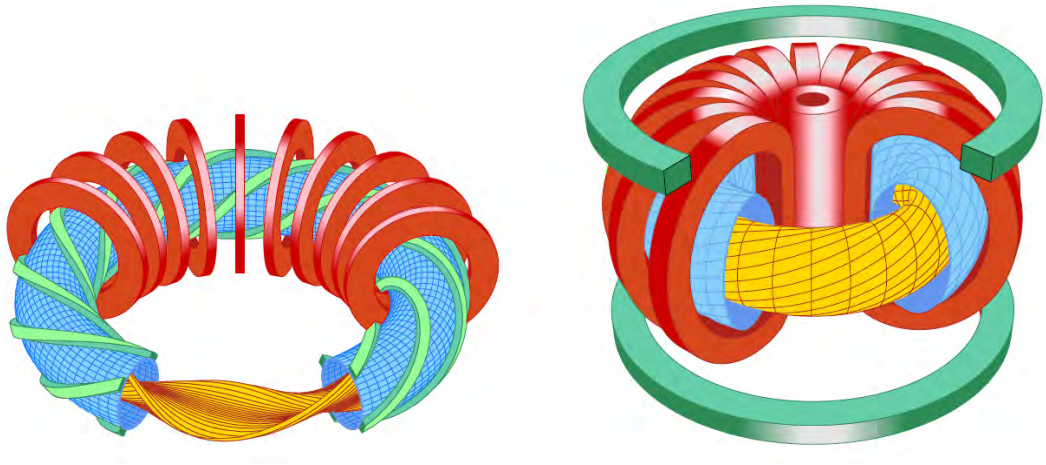

**Figure 2.2.:** Left: Schematic view of the coil design and plasma shape in a Stellarator experiment. Right: Schematic view of the coils and toroidal shape of the plasma within a Tokamak.

in figure 2.2. In the Stellarator design the helical field is generated entirely by using external field coils. The name of the second concept, Tokamak, is derived from the Russian language for toroidal chamber with magnetic confinement. In a Tokamak, a toroidal field is created by external coils arranged symmetrically to their axes, while a toroidal plasma current is used to generate a poloidal magnetic field component.

The plasma current in a Tokamak can be driven by induction with the plasma itself acting as the secondary winding of a transformer. As described in section 2.2.1, this so called Ohmic heating is not sufficient and additional, non-inductive current drive methods are required. One example is the tangential injection of high-energy neutral beams into the fusion plasma that is described in section 2.2.3. Sustaining the toroidal plasma current in Tokamaks is an energy-consuming and complex process which limits the operation time of present-day Tokamaks. This limitation can be avoided by the principle design of the Stellarator, however, at the expense of a more complex geometry.

Nevertheless, today, the Tokamak is the most advanced concept for magnetic confinement and was chosen for the ITER[1] fusion experiment, which will be the first step towards devising a commercial fusion reactor. The objective of the ITER machine is to demonstrate the feasibility of fusion by means of magnetic confinement to produce energy. A continuous supply of external heating power has to be provided in current fusion experiments in order to compensate for inevitable power losses to the walls of the vessel. The power multiplication factor

[1] ITER: from Latin **the way**, Tokamak, France

$Q$ of a fusion experiment is defined by the ratio of the generated power by the fusion reaction and the external heating power: $Q = P_{\text{Fusion}}/P_{\text{External Heating}}$. The external heating power will no longer be necessary in a fusion reactor when the $\alpha$-particle energy of 3.5 MeV from the fusion reaction can be used to replenish the power losses ($\alpha$-particle heating). A scenario of a self-sustaining plasma that is primarily heated by alpha-particle from fusion reactions generating a significant amount of neutrons, has not been achieved up to now and is the main objective of ITER [SCM+07].

### 2.1.3. Ignition Criterion

The condition that the heating of the plasma by the energy of the D-T fusion reaction is sufficient to maintain the temperature of the plasma against all losses without external power input is called ignition. It can be expressed in mathematical terms by the so called triple product:

$$n\ \tau_{\text{E}}\, T > 3 \cdot 10^{21}\ \text{sec m}^{-3}\,\text{keV}. \tag{2.4}$$

Inequality (2.4) is also known as Lawson criterion [Law67] and is determined by the plasma density $n$, energy confinement time $\tau_{\text{E}}$ and the temperature $T$ of the fusion plasma.
Significant progress has been made in the last few decades and the value of the triple product has been increased by several orders of magnitude. Modern fusion experiments reach plasma densities of $n = 10^{20}\,\text{m}^{-3}$ and plasma temperatures between 10 and 20 keV. An energy confinement time of $\tau_{\text{E}} = 1$ sec with an energy multiplication factor of $Q = 0.6$ was reached by the presently largest Tokamak JET[2] [Wes00]. To reach ignition, an enhancement of the energy confinement time to $\tau_{\text{E}} = 2$ - 3 sec will be necessary, which can be achieved by increasing the plasma size. Thus, the major radius of the ITER Tokamak vessel will be 6.2 m. This is about twice as large as the radius of JET ($R = 3$ m). A fusion power of 500 MW and a power amplification of $Q = 10$ is expected for ITER.
External heating methods will play an essential role for the success of the ITER experiment. Plasma temperatures of about 20 keV attainable to ignite a magnetically confined fusion plasma are not accessible during the start-up phase and have to be provided by external heating. Furthermore, external current drive capabilities are required to maintain and to control the plasma current, which is important for the plasma stability of the ITER Tokamak.

[2] JET: **J**oint **E**uropean **T**orus, England

Different heating and current drive methods have been successfully developed and applied to fusion experiments:

## 2.2. Plasma Heating Methods

### 2.2.1. Ohmic Heating (OH)

The toroidal plasma current driven in Tokamaks by the transformer effect generates Ohmic heating via Joule dissipation. Obviously, this method is applicable only for Tokamaks, since it would strongly modify the magnetic field structure of a Stellarator. Furthermore, Ohmic heating by itself is not sufficient to drive the plasma to reactor-relevant temperatures. The electrical conductivity of the fusion plasma increases with the plasma temperature resulting in a decrease of deposited heating power by Joule dissipation. Hence, a steady-state situation is reached at insufficient plasma temperatures of about $T = 1$ - 2 keV, so that additional heating methods are necessary in order to raise the plasma temperature to the point where the probability for the fusion reaction reaches a sufficient magnitude and the required energy balance is maintained.

### 2.2.2. Radiofrequency Heating

A common heating method is radiofrequency (RF) heating, which uses high power electromagnetic waves to transfer energy into the plasma. The magnetically confined ions and electrons of the fusion plasma move along the magnetic field lines with a characteristic gyration radius and frequency. A resonant heating process takes place if the frequency of the injected electromagnetic wave matches the frequency of gyration. This makes it possible to heat different constituents of the plasma depending on the chosen frequency and the corresponding plasma density and composition. Three frequency ranges are typically used for radiofrequency heating. Ion cyclotron resonance heating (ICRH) uses frequencies between 30 - 100 MHz to match the gyration frequency of the ions. The corresponding resonance frequency for electrons is in the range between 50 and 150 GHz. It is used for the electron cyclotron resonance heating (ECRH) method in order to deposit several MW of heating power into the plasma. Lower hybrid heating operates in the frequency range between 1 and 10 GHz, utilizing the excitation of collective plasma oscillations to interact with both ions and electrons.

### 2.2.3. Neutral Beam Injection (NBI)

An important way to deposit heating power is the injection of an energetic neutral particle beam into the fusion plasma. Neutral atoms that are not affected by the strong magnetic confinement field are able to penetrate into the plasma torus, where collisions of the neutral particles with the plasma electrons and ions cause an ionization of the neutral beam. The fast ions created in this process are confined, as well, by the magnetic field and transfer their kinetic energy to plasma ions and electrons via consecutive collisions if their energy is significantly higher than the energy of the plasma particles. In order to avoid a perturbation of the fusion process by the depletion of educts, low Z elements similar to the fusion species (H, D or T), are preferred as injected neutral particles. There are mainly three collision processes, where a conversion of fast hydrogen neutrals $H^0_{fast}$ [3] into fast hydrogen ions $H^+_{fast}$ takes place:

1. **Collisional ionization by electrons:**

$$H^0_{fast} + e^- \rightarrow H^+_{fast} + 2e^- \tag{2.5}$$

2. **Collisional ionization by plasma ions:**

$$H^0_{fast} + H^+ \rightarrow H^+_{fast} + H^+ + e^- \tag{2.6}$$

3. **Charge exchange collisions with plasma ions:**

$$H^0_{fast} + H^+ \rightarrow H^+_{fast} + H^0 \tag{2.7}$$

A neutral beam of intensity $I_0$ and velocity $v_b$ in an ideal, uniform hydrogen plasma of density $n$ is attenuated exponentially along its direction $x$ [Swe73]:

$$I(x) = I_0 \exp\left(-\frac{x}{\lambda}\right), \tag{2.8}$$

where $\lambda$ is the mean free path length for ionizing collisions, which is given by:

$$\lambda = \frac{1}{n\,\sigma_\Sigma}. \tag{2.9}$$

[3] In the following description of the physical processes, the symbol H is replaceable by D or T.

The total trapping cross-section $\sigma_\Sigma$ is calculated by forming the sum over the rate coefficients $X_\mathrm{i}$ of the three reactions (2.5), (2.6) and (2.7), divided by the beam velocity $v_\mathrm{b}$:

$$\sigma_\Sigma = \sum_\mathrm{i} X_\mathrm{i}/v_\mathrm{b}. \tag{2.10}$$

In a pure hydrogen plasma, typical values for $\sigma_\Sigma$ are $1.5\mathrm{x}10^{-15}$ cm$^2$ at 10 keV/amu, decreasing to $3\mathrm{x}10^{-16}$ cm$^2$ at 80 keV/amu [Spe89]. Applying formula (2.8) to a typical ASDEX Upgrade[4] fusion plasma with a plasma density of $5\mathrm{x}10^{19}$ m$^{-3}$, a penetration depth of 0.5 m is obtained by a 93 keV deuterium neutral beam [SCF$^+$99]. This is sufficient for the ASDEX Upgrade vessel with a minor radius of 0.5 m [SLL$^+$03]. For most of the NBI systems, a tangential injection geometry is preferred to reduce the formation of banana orbits, which are not desirable for a fusion plasma [Wes04]. The tangential injection geometry also increases the beam plasma interaction length of the fusion plasma, which is advantageous for an effective current drive. This so-called non-inductive current drive is desirable for Tokamak steady-state operations and to reach advanced regimes of superior confinement, which often depend on the current density profile.

As previously mentioned, the ITER vessel will be much larger then in present fusion experiments. The minor radius of ITER will be 2 m which is four times larger than that of ASDEX Upgrade. As a consequence, the neutral beam injection system for ITER will require a by far higher beam energy. The neutral beam energy of 1 MeV D is, in particular, required for ITER in order to provide a sufficiently high current drive efficiency. A more detailed overview of the requirements for the ITER neutral beam injection systems is given in section 2.3.3.

[4] ASDEX Upgrade: **A**xial **S**ymmetric **D**iverter **EX**periment, Tokamak fusion experiment, Germany.

## 2.3. Neutral Beam Injection Systems

### 2.3.1. Basic Components of NBI Systems

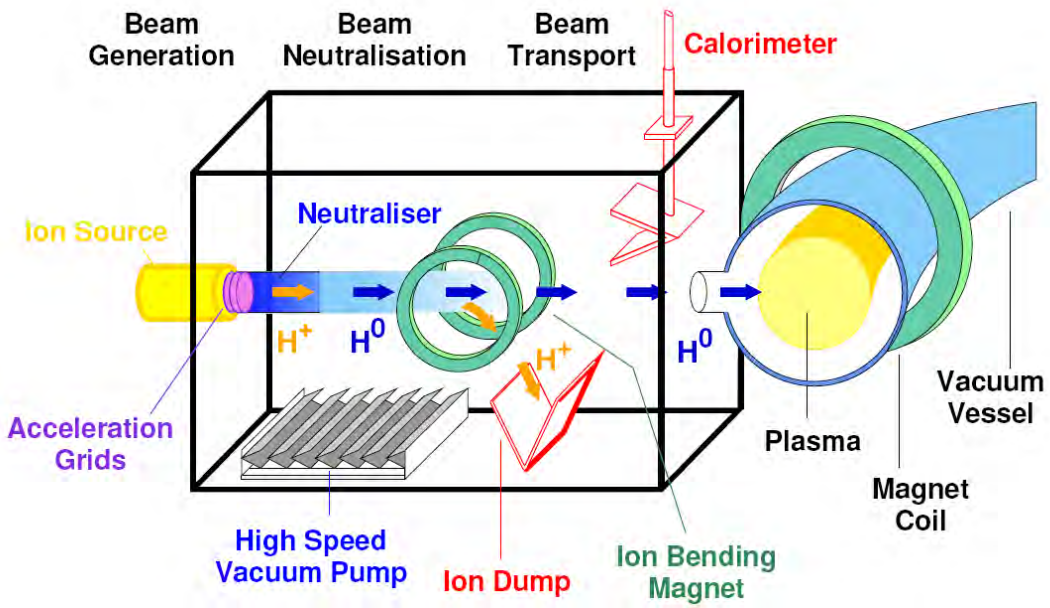


**Figure 2.3.:** Schematic view of the individual components of a neutral beam injection system for heating a magnetically-confined fusion plasma.

The schematics of a neutral beam injection system is shown in figure 2.3. Three successive steps are required for the neutral beam injection process:

1. generation of an ion beam,
2. neutralization of the ion beam,
3. transport of the neutral beam into the plasma vessel.

**Ion-Beam Generation** The generation of an ion beam is generally accomplished by extracting hydrogen ions electrostatically from a uniform hydrogen plasma source. The ions are then accelerated to energies of several tens of keV by an electrostatic lens system. A characteristic property of ion beams for neutral beam injection is the very high beam current (tens of amperes) needed to achieve the required power (several MW) and the consequently large beam cross-section (hundreds of $cm^2$). Because of its large size, the beam has to be subdivided into many

beamlets using electrodes with multiple apertures in order to avoid aberration effects on the ion optics at the edge of a large aperture. This subdivision is not required in regular ion sources for particle colliders and medical applications, where significantly lower beam cross-sections (several $cm^2$) from single-aperture systems are sufficient.

**Neutralization** A gas target is used to neutralize the accelerated ions by charge-exchange collisions with cold hydrogen molecules. The overall neutralization efficiency for positive and negative ions is limited and depends on the energy of the ion beam, as shown in figure 2.4. A high gas load is generated by the neutralizer within the NBI system. High-speed vacuum pumps are required to remove the remaining hydrogen gas behind the neutralizer in order to create the proper vacuum conditions to connect the NBI system to the plasma vessel.

**Transport** Depending on the neutralization efficiency, fast residual ions within the neutral beam may represent a significantly large fraction of the total beam power. These fast ions can create high power loads on the components of the fusion experiment. A bending magnet system is used to deflect and thermalize the ions on a suitable surface (ion dump). The remaining high energy neutral particles are then injected into the fusion device. A calorimeter can be placed into the beam for measuring the beam power and for conditioning the ion sources independently of the fusion experiment.

An important component of the neutral beam injection system is the ion source, which determines the essential beam properties such as beam homogeneity and the extracted beam current. The development of high-performance ion sources is therefore one of the most important objectives of research for NBI systems.

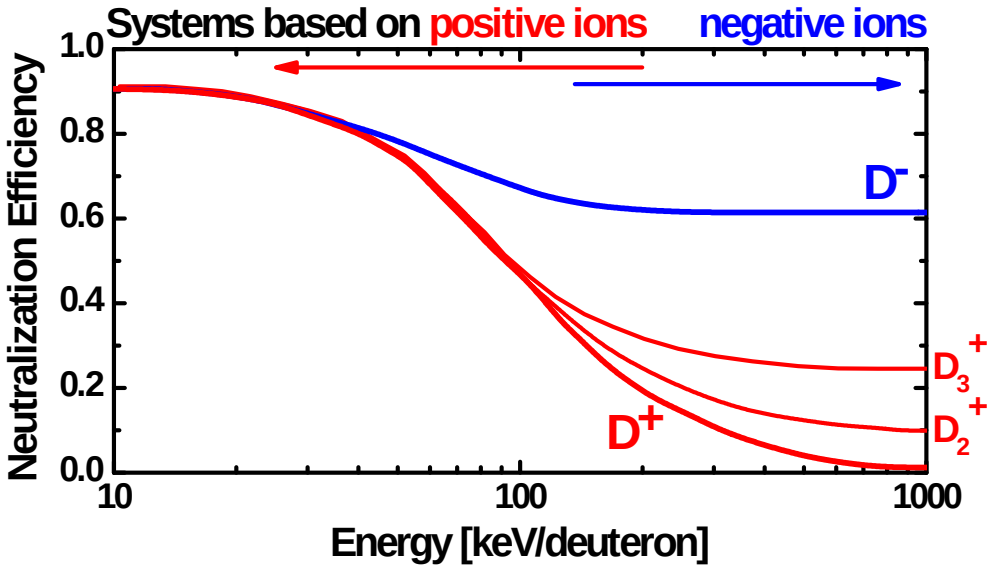


**Figure 2.4.:** Optimum neutralization efficiency for a neutral beam injection system that is based on the acceleration of positive and negative deuterium ions, in dependence of the beam energy per deuteron.

## 2.3.2. Comparison of Positive and Negative-Ion Sources

Neutral particle beams can be created by the acceleration and neutralization of positive or negative hydrogen ions. Both, negative and positive-ion based neutral beam systems are applied in today's fusion experiments depending on the specific application of the system.

### Positive-Ion based Systems

Positive-ion based neutral beam injection systems are reliable and represent well advanced heating devices in ongoing experiments, such as ASDEX Upgrade [SFH+02][SLL+03]. Unfortunately, positive-ion based systems have a serious physical limitation, which will restrict their application when a high particle energy is required. The neutralization efficiency for positive ions decreases drastically if the ion energy exceeds 100 keV/deuteron. Figure 2.4 shows the neutralization efficiency for positive and negative deuterium ions [BPS75]. The neutralization of positive-ion beams with particle energy higher than 100 keV/deuteron will be fractional, and a great amount of the extracted beam current density will be lost for the neutral beam. Additionally, positive-ion sources also produce a certain amount of molecular ions ($D_2^+$,$D_3^+$) that are also accelerated. These ions

are then converted into neutral atoms with only half and third of the required energy in the neutralizer.

### Negative-Ion based Systems

**N**egative-ion based **N**eutral **B**eam **I**njection (N-NBI) is not limited by the beam energy. Even for beam energies in the range of several hundred keV/deuteron the neutralization fraction does not drop below 60 % and the remaining 40 % of the beam are more or less equally partitioned between $D_2^+$ and $D^+$. Nevertheless, the total efficiency of a N-NBI system is limited to $\approx$ 25 %, which is described in more detail in the following section.
The physical aspects of the generation and extraction of negative ions, which are explained in more detail in section 3.1.1 and 3.1.2, are totally different from those of positive ions.
The hydrogen plasma of an ion source contains a large amount of positive ions that can easily be extracted by applying a negative extraction voltage with an electrostatic lens system. Negative ions, however, form only a small part of the total hydrogen plasma and have special production channels. While the additional electron of the negative ion has a very low binding energy of 0.75 eV, which is the reason for the high neutralization efficiency, it leads to a great vulnerability to destruction processes during the transport. An overview of the destruction processes is given in section 3.1.2. Thus, a distinction between the extracted current density $j_{\mathrm{ex}}$ of negative ions, measured directly after the ions left the source, and the accelerated current density $j_{\mathrm{acc}}$, which is measured after the ions passed the acceleration distance, is necessary. Furthermore, negative-ion sources have the problem that electrons are co-extracted together with the negative ions. High energy electron beams can create serious damage to the accelerator components. Hence, the co-extracted electrons have to be removed at low particle energies and thermalized on an appropriate electron dump.
Positive-ion sources deliver extracted current densities of 2500 (2000) A/m$^2$ $H^+(D^+)$ ions [SCF$^+$99][CBC07], while extracted current densities of up to 330(230) A/m$^2$ $H^-(D^-)$ ions are available from negative-ion sources [T$^+$98][SFF$^+$06]. Very large extraction areas are therefore used in case of negative-ion sources in order to obtain a high total ion current. Negative-ion based systems are routinely being operated at the fusion experiments LHD[5]

[5]LHD: **L**arge **H**elical **D**evice, Stellarator, Japan

**Table 2.1.:** Parameters that have to be fulfilled by the negative-ion sources for the heating and diagnostic neutral beam system for ITER.

| Parameter | Heating Beam | Diagnostic Beam |
|---|---|---|
| Acc. Current Density | $> 200$ A/m$^2$ D$^-$ | $> 300$ A/m$^2$ H$^-$ |
| Electron-to-Ion Ratio | $< 1$ | $< 0.5$ |
| Accelerated Current | $> 40$ A | $> 60$ A |
| Beam Energy | 1 MeV | 100 keV |
| Pulse Length | up to 3600 sec | 3 sec every 20 sec |
| Beam Homogeneity | $\pm 10\%$ | |
| Source Pressure | $< 0.3$ Pa | $< 0.3$ Pa |

and JT-60U[6] in Japan with beam energies in the range of 100 to 400 keV and extracted current densities of 270 and 110(80) A/m$^2$ H$^-$(D$^-$), respectively [Oha98][T$^+$00][O$^+$00][K$^+$00].

### 2.3.3. ITER Requirements

As described in section 2.2.3, the neutral beam heating system for ITER will require a neutral beam energy of at least 800 keV/amu. This challenging objective cannot be achieved by a neutral beam system based on the production and neutralization of positive ions and requires the development of neutral beam systems based on negative-ion technology.
A neutral beam energy of 1 MeV/amu D was chosen in order to satisfy the central heating and, especially, the current drive requirement for ITER [IAE02]. Thus, a neutral beam power of 33.2 MW, delivered by two tangential arranged injectors, is required [HTA08]. The beam power has to be maintained for a pulse duration of 3600 sec. An extracted negative-ion current of 40 A D$^-$ per beam line is required in order to generate an initial power of 40 MW according to a final heating power of 16.6 MW per beam line. The remaining power is lost due to neutralization losses (40%) and by transmission losses in the beam transport.
A negative-ion source with dimensions of $1.9 \times 0.9$ m$^2$ and an extraction area of 0.2 m$^2$ delivering a current density of 200 A/m$^2$ D$^-$ is necessary to provide this current. The large-scale extraction area must have a plasma homogeneity better than $\pm 10\%$ for the local current density over the area to prevent damage to the

[6] JT-60U: **J**apan **T**orus, Tokamak, Japan

system by unfocused parts of the ion beam.
Another difference to positive-ion sources are the electrons extracted together with the negative hydrogen ions. In order to avoid damage on the grid structure of the accelerator by high-energy electrons, it is necessary to remove these co-extracted electrons at a low energy immediately after their extraction. This process causes a heat load on an electron sink, which is subject to the technical limitations of the cooling. Thus, it is necessary to maintain an electron-to-ion current density ratio $j_e/j_{D^-} < 1$. Furthermore, the operational pressure of the ion source has to be limited to 0.3 Pa in order to reduce destructive losses by collisions with residual gas particles in the extraction and acceleration systems. Besides the heating neutral beam, an additional diagnostic neutral beam system based on negative ions is planned for ITER. Table 2.1 gives an overview of the ITER requirements regarding the N-NBI for both systems [IAE02].

### 2.3.4. Types of Plasma Sources

Two different concepts are in use by current neutral beam injectors: arc-sources and RF-sources. Both types are in use for the ASDEX Upgrade neutral beam injection system by positive ions [SCF+99].

**Arc-Sources** The arc-source is based on applying a dc-voltage of about 100 V between heated cathode filaments and the source walls. The electrons emitted by the filaments are accelerated into the source, where ionization of gas molecules creates a plasma. Heated tungsten filaments are used as cathodes with typical total arc-currents in the order of 1000 A, producing filament temperatures between 1700 - 2700 °C. Arc-sources are reliable and have been used since the development of the first NBI systems. Nevertheless, these sources have severe disadvantages. The tungsten evaporates continuously into the source during operation, which limits the life time of the filament and it thus requires frequent replacement. Tungsten deposition also contaminates the inner walls of the source changing its surface characteristics, which is especially relevant for negative-ion production as described in section 3.1.1.

**RF-Sources** The other type of source is the RF-source. The power is inductively coupled into the plasma from an RF-antenna. For the sources developed at IPP typical frequencies and powers of 1 MHz and 100 kW are employed, respectively.

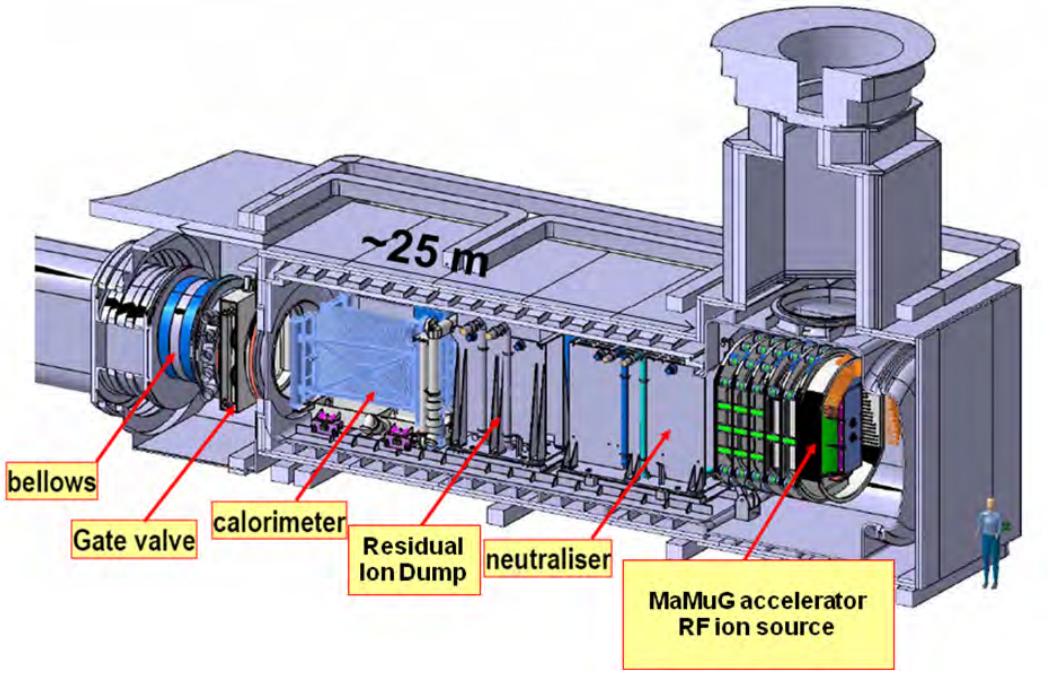


**Figure 2.5.:** Technical drawing of the planned ITER neutral beam heating injection system, showing ion source, accelerator, and neutralizer with the residual ion dump.

RF-sources have demonstrated their reliability at ASDEX Upgrade, where four 2.5 MW RF-sources for positive ions are in use. This is the only injector in the world that currently uses RF sources. There are many advantages of RF-sources. The absence of filaments in the discharge (with a limited life time) and the simplicity of the source (only three electrical connections, instead of 50 in today's arc-sources with 24 filaments) makes remote handling easier. Compared to arc-sources, RF-sources have basically maintenance-free operation, as demonstrated by the ASDEX Upgrade ion sources.
These design features are quite beneficial for ITER with its remote handling requirements. A RF-driven source for negative ions has been developed at the Max-Planck-Institut für Plasmaphysik [SFF+06], which fulfills certain aspects of the ITER requirements. Details of the negative-ion test facilities at IPP are given in section 3.2.2. As a result of this successful development, the ITER board has decided to adopt the IPP RF-driven ion source as the reference source for the ITER neutral beam injectors [HTA08].

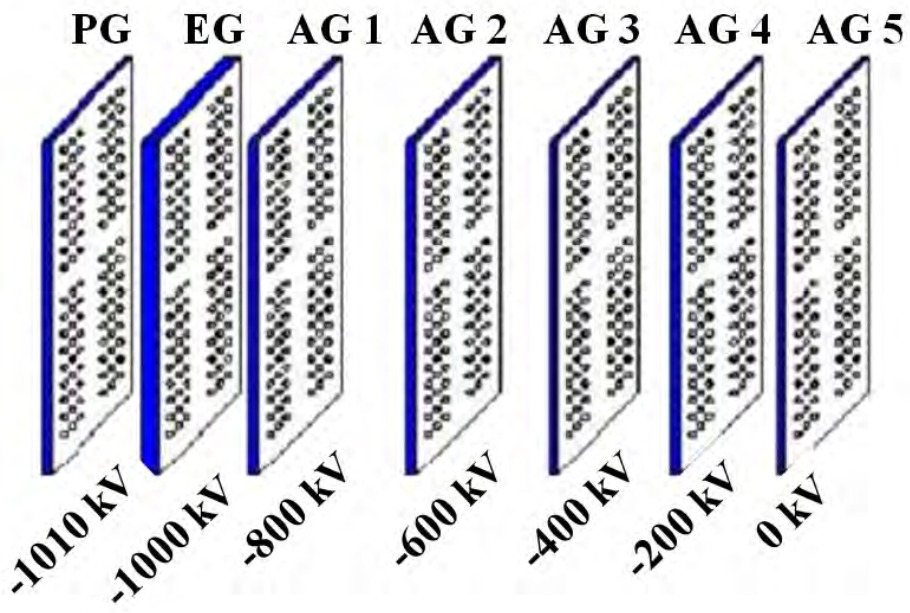


**Figure 2.6.:** Schematic drawing of the MAMuG (Multi Aperture Multiple Gap) accelerator design, consisting of 5 grids (apart from plasma and extraction grid) forming 5 accelerator stages of 200 keV each.

### 2.3.5. The ITER N-NBI System

The full-size ITER test facility will combine ion source, accelerator and neutralizer [H$^+$09]. The ITER heating neutral beam, as shown in figure 2.5, will be built by Consortio RFX (Padova, Italy) in the next few years, in close collaboration with other European associations. This is accompanied by the operation of two future neutral beam test facilities: SPIDER[7] and MITICA[8]. While SPIDER will be an ion source test facility for 100 keV negative-ion beams, MITICA will be a 1:1 prototype of an ITER injector with a full 1 MeV beam line. The design of the RF-driven ion source has been adopted from IPP Garching and the Japanese MAMuG[9] design [TIK$^+$06] is used for the acceleration system. This accelerator consists of five grids (apart from plasma and extraction grid), forming five acceleration stages of 200 keV each, as illustrated by figure 2.6. The distances between the individual grids are typically between 50 mm and 90 mm.

[7] SPIDER: **S**ource for the **P**roduction of **I**on of **D**euterium **E**xtracted from **R**F Plasma, Test Facility, Italy

[8] MITICA: **M**egavolt **ITER** **I**njector & **C**oncept **A**dvancement, Test Facility, Italy

[9] MAMuG: **M**ultiple **A**perture **Mu**ltiple **G**ap Design, Japan

# 3. Negative Hydrogen Ion Sources for ITER N-NBI

## 3.1. Negative Ion Generation and Destruction

The physical processes of formation, destruction and transport of negative hydrogen ions are described in general in the following section. Particle temperatures and densities measured at the IPP negative-ion source test facilities are used to demonstrate the relevance of specific physical processes.

### 3.1.1. Formation of Negative Hydrogen Ions

Optimizing the negative-ion production and simultaneously minimizing the electron-to-ion ratio, is essential to generate a powerful neutral beam. While positive hydrogen ions can be extracted directly from the plasma boundary, the physics of production, transport and extraction of negative ions is much more complex [Pam95]. There are two fundamental negative-ion formation processes: volume production [BND77] and surface production [BDD74]. Both formation processes are widely applied in small negative-ion sources (diameter of several cm) with a mono-aperture extraction system depending on the specific requirements. For example, the front ends of the SNS[1] [LDD+91] and LANSCE[2] [RGS+08] spallation neutron sources employ the surface production mechanism, while volume $H^-$ sources are in use at DESY[3] [Pet09] and CERN[4] [HKM+06].

[1] SNS: Spallation Neutron Source, Oak Ridge
[2] LANSCE: Los Alamos Neutron Science Center, Los Alamos
[3] DESY: Deutsches Elektronen-Synchrotron, Hamburg
[4] CERN: Conseil Europeen pour la Recherche Nucleaire, Genf

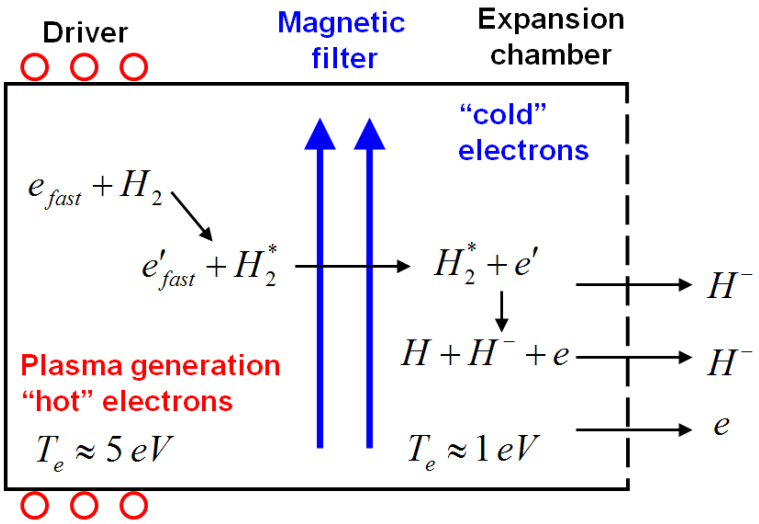


**Figure 3.1.:** Schematic drawing of a tandem source using a two-step process for the volume production of negative hydrogen ions.

### Volume Production

Negative-ion sources employing the volume production process use the dissociative attachment of slow electrons ($T_e \sim 1$ eV) to hydrogen molecules in high vibrational states [Bac06] to generate negative ions:

$$H_2(\nu'') + e_{slow} \rightarrow H^- + H, \tag{3.1}$$

where the vibrational excitation $\nu'' \geq 5$ for hydrogen and $\nu'' \geq 8$ for deuterium molecules ensures a high collision cross-section [AW78]. The most common type of volume sources are tandem ones. Figure 3.1 shows the working principle of a tandem source that is divided into two regions by a magnetic filter field. Hot electrons ($T_e = 5$ eV) generated in the driver region produce highly vibrationally excited $D_2/H_2$ molecules drifting into the second chamber, where the electron density and temperature are reduced by the magnetic filter field. This reduction in electron temperature ($T_e = 1$ eV) in the second region maximizes the dissociative attachment rate and minimizes the destruction of negative ions by collisions with fast electrons.

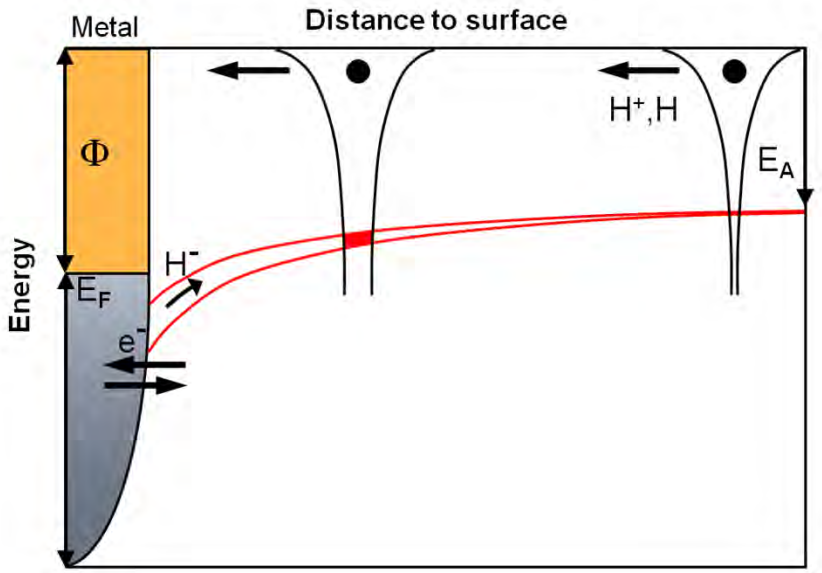


**Figure 3.2.:** Schematic figure of the surface conversion process shifting and broadening the hydrogen affinity level until electron transfer from the surface to the atom is possible.

### Surface Production

The second negative-ion generation mechanism is the surface process. This process relies on converting neutral hydrogen atoms and positive hydrogen ions from a plasma source into negative ions at a metallic converter surface with a low work function. The surface production process is based on the transfer of electrons from the surface electrode to hydrogen atoms or ions approaching the wall:

$$\mathrm{H} + \mathrm{e(surface)} \rightarrow \mathrm{H^-} \tag{3.2a}$$

$$\mathrm{H^+} + \mathrm{e(surface)} \rightarrow \mathrm{H} + \mathrm{e(surface)} \rightarrow \mathrm{H^-} \tag{3.2b}$$

Positive hydrogen ions approaching the surface are neutralized by resonant electron-transfer to an excited state with subsequent Auger de-excitation into the ground state. In the case of a preceding dissociation process, these reactions can also occur for molecules or molecular ions.
In the vicinity of the metal, the electron affinity level of the hydrogen atom is shifted and broadened as illustrated in figure 3.2. An electron tunneling process from the surface to the atom is possible, if the electron affinity level lies energetically below the Fermi level of the surface. This results in the production of a negative ion [IKS92][RWL82][AGK+85].
Hydrogen adsorbed at the surface with an affinity level that is situated between

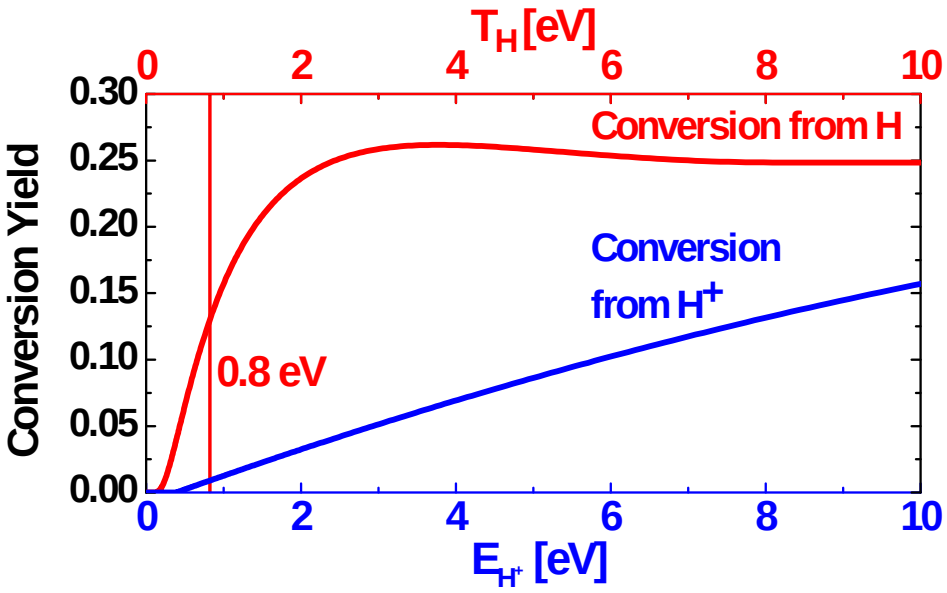


**Figure 3.3.:** Surface conversion yields for negative ions on a cesiated molybdenum surface from hydrogen atoms (red) and ions (blue).

the Fermi level and the vacuum level, has a negative effect on the negative-ion formation process. An electron that tunnels from the affinity level of the impinging hydrogen atom or ion to the affinity level of the adsorbed atom is subsequently captured into one of the many unpopulated electronic metal states above the Fermi level and cannot tunnel back to the affinity level of the hydrogen. This results in a reduction of the backscattering ion fraction, which is proportional to the density of adsorbed atoms [vAGR+86].

Experimental investigations show that increasing the temperature of the converter surface to 150 °C is beneficial to the negative-ion production process [SFF+06]. This effect is not fully understood up to now, but might be related to the removal of chemically adsorbed hydrogen from the converter surface, as described in more detail in section 4.1.4,.

The surface process depends strongly on the work function of the converter electrode. An increase of the negative-ion current by a factor of 500 by lowering the work function of a molybdenum converter surface by 2.9 eV with respect to the work function of the bare metal using a cesium coating has been reported by Lee and Seidl [LS92]. A strong increase of the performance of a negative-ion source by adding small amounts of cesium during operation has also been observed [OHI89]. Thus, a clean and homogeneous cesium layer is highly desirable on the converter surface for a high negative-ion production. Figure 3.3 shows the optimum surface

conversion yields for hydrogen atoms [LS92] and ions [IKS92] on a cesium-coated molybdenum sample for a work function that is lower than 1.6 eV. At the IPP RF-driven ion source, a neutral hydrogen temperature of $T_{\mathrm{H}} = 0.8$ eV and hydrogen ion energies $E_{\mathrm{H}^+}$ of several eV are obtained. Furthermore, the atomic hydrogen density $n_{\mathrm{H}}$ is two orders of magnitude higher than the positive ion density $n_{\mathrm{H}^+}$ at comparable particle temperatures [FFF$^+$06]. As a consequence, negative ions are predominantly produced by the neutral hydrogen flux.
Recent calculations by a plasma sheath simulation [WGF09] show that a potential well is generated in front of the plasma grid by the space charge of the surface-generated negative ions, limiting the negative-ion flux from the surface into the source. Positive ions can compensate this space charge and thus enhance the $\mathrm{H}^-$ outflux from the surface.

### Production Mechanism for ITER

The production mechanism for negative hydrogen ions for the ITER neutral beam injection system is determined by the requirements that are listed in section 2.3.3. An important requirement is the upper limit for the pressure. The amount of stripping losses, i.e. the neutralization of $\mathrm{H}^-$ in the accelerator system by collisions with the hydrogen background gas (specific reactions are described in section 3.1.2) depends on the source pressure. Thus the negative-ion source for ITER will have to operate at a hydrogen pressure of 0.3 Pa. A higher source pressure would cause intolerable stripping losses and the recently extracted negative-ion beam leaving the ion source would be neutralized prior to its acceleration to the desired energy. Even at the ITER-relevant source pressure of 0.3 Pa, a high amount of 20 - 30% of the total beam current [KH06] will be lost by this channel.
Additionally, ITER requires a low ratio of co-extracted electron and the extracted ion current density (electron-to-ion ratio) $j_{\mathrm{e}}/j_{\mathrm{H}^-} < 1$. Electron beams with a high energy cause critical heat loads on the water-cooled electron dump (extraction grid) of the ion source, but also on beam line components of the NBI system. The IPP test facilities (see section 3.2.2) are protected by limiting the co-extracted electron power on the extraction grid by an interlock system in order to avoid permanent damage done by the melting of the extraction grid. Large-size negative-ion sources are technically limited by the cooling efficiency of the electron heat load. This is not a major problem in a small negative-ion source using the volume process.
Both requirements cannot be met by the volume production. In order to extract

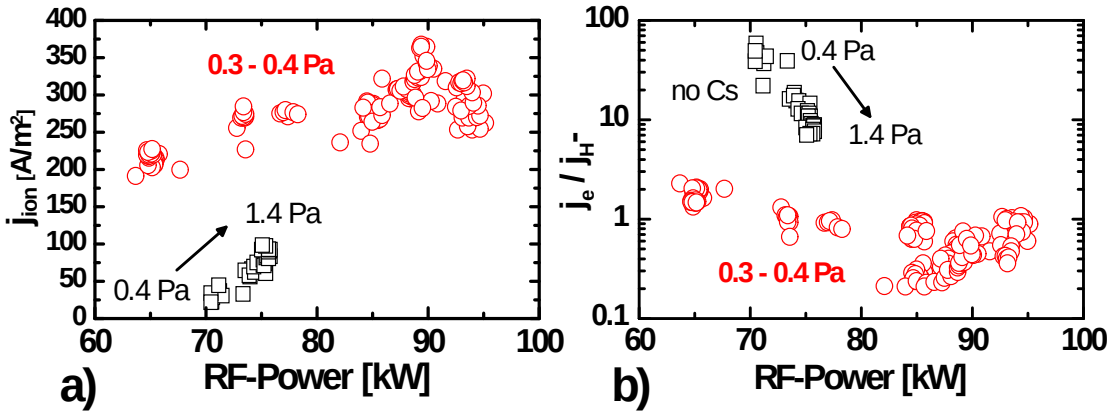


**Figure 3.4.:** Negative-ion current density a) and electron-to-ion current ratio b), extracted from a negative-ion source test facility for (pure) volume production without cesium (black squares) and surface production (with cesium, red circles) in dependence of the RF-power at different hydrogen pressures.

ITER-relevant negative-ion current densities from the dissociative attachment reaction (3.1), a high density of (excited) $H_2$ molecules and a high density of slow electrons are required in the extraction region. Hence, a high hydrogen gas density is necessary and high electron currents have to be tolerated.

Figure 3.4 shows results of measurements of negative-ion currents and electron-to-ion ratios for volume (early experiments without cesium [SFF+06]) and surface production measured at an IPP negative-ion source test facility. A negative hydrogen ion current density below 50 A/m$^2$ with an electron-to-ion high than 60 is reached at ITER-relevant source pressure conditions between 0.3 - 0.4 Pa for pure volume operation without cesium. The higher current density of 100 A/m$^2$ $H^-$ and an electron-to-ion ratio below 10 was only obtained after rising the hydrogen density by an increase of the source pressure to 1.4 Pa.

Thus, it was not possible to match the ITER requirements during volume operation. However, the enhanced source performance by the surface process due to the injection of cesium permits the extraction of ITER-relevant current densities at a source pressure of 0.3 - 0.4 Pa. The surface production does not require high densities of slow electrons. A significant reduction of the co-extracted electron current is, therefore, possible. Measurements (fig. 3.4) at the IPP test facilities show that extracted current densities of up to 350 A/m$^2$ $H^-$ with an electron-to-ion ratio below 1 can be obtained from a well-conditioned source using surface production. A variation of the source performance is observed depending on the cesium conditions within the ion source.

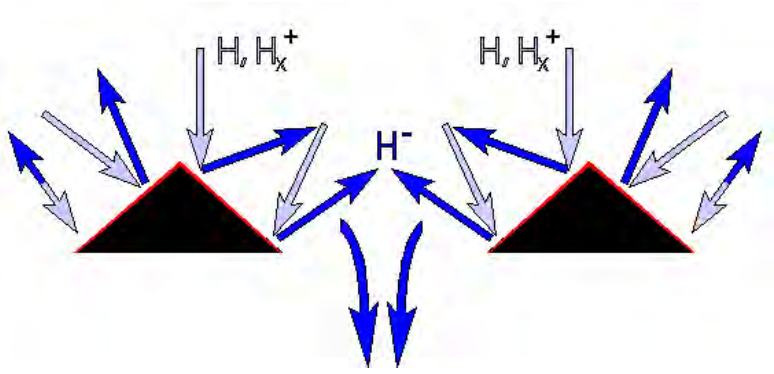


**Figure 3.5.:** Conversion of neutral and ionic hydrogen plasma particles (grey) into negative ions (blue) on a cesiated converter surface.

### 3.1.2. Negative Ion Transport and Destruction

Negative hydrogen ions can be neutralized easily after their generation by collisions with plasma and gas particles. The fragility of negative ions is a result of the low binding energy of 0.75 eV of the additional electron. While this is beneficial for the neutralization efficiency, as described in section 2.3.2, it causes undesired losses of negative ions during transport both within the ion source and in the beam.
In contrast to positive-ion sources, where the ion current can be extracted directly from the plasma interface, negative-ion sources require a transport process of the negative ions from their production surface to the extraction apertures.
Negative ions generated on the cesium covered converter surface are accelerated back into the plasma volume by the plasma sheath potential. A certain fraction of the negative ions is bent back by charge exchange collisions with plasma particles and by the Lorentz force due to magnetic fields present within the extraction region of the ion source. These ions can reach the circular extraction apertures of the plasma grid. Electric fields, formed by an extraction voltage of several kV are used to focus them into an ion beam. Figure 3.5 illustrates the transport and extraction process of surface-generated negative hydrogen ions for a single aperture. The probabilistic negative-ion transport code TrajAn[5] [GWF09] is used to visualize the described transport process. Figure 3.6 shows trajectories of surface-generated negative ions computed with TrajAn for a multi-aperture extraction system. A mean free path length of a few cm is obtained in the extraction region at the parameters of the RF-driven ion source. Because of this short survival

[5]TrajAn: Trajectory Analysis Code, R. Gutser

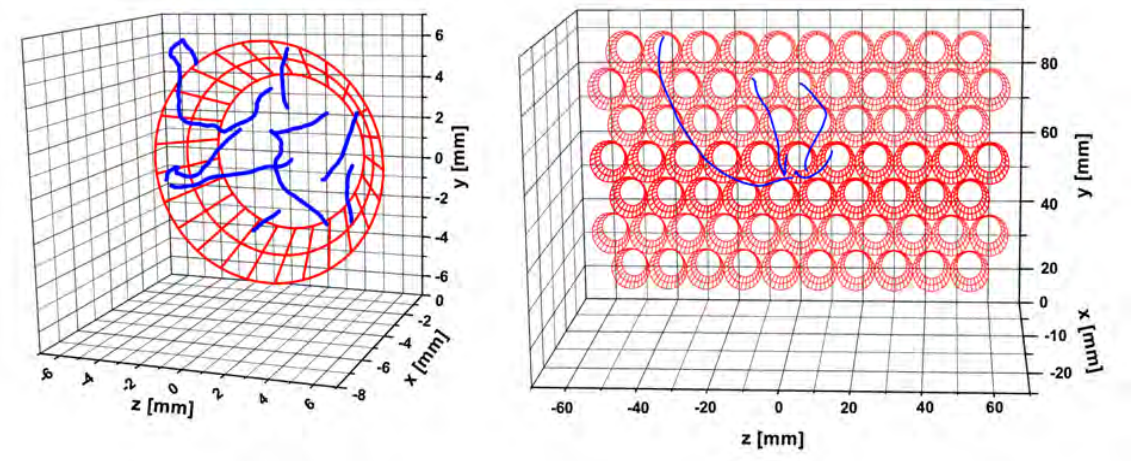


**Figure 3.6.:** Trajectories of surface generated negative hydrogen ions that reach the plasma boundary; computed with the TrajAn transport code. The negative ions are bend into the extraction apertures under the influence of magnetic fields and collisions with background particles.

length, only negative ions produced on the surface of the plasma grid contributed to the extracted current density. The computed survival probability of a negative ion during the transport into one of the extraction apertures is between 20 % and 30 %. The individual rate coefficients for the destruction of negative ions by collision processes are given in figure 3.7.

### Electron Stripping

The collision of a negative ion with an electron can strip the additional electron off [JL87]:

$$\mathrm{H}^- + \mathrm{e}^- \rightarrow \mathrm{H} + 2\,\mathrm{e}^-. \tag{3.3}$$

This process strongly depends on the energy of the colliding electron. Electron stripping is the dominating destruction process at high electron temperatures of $T_\mathrm{e} = 20$ eV. Cooling down the electrons to $T_\mathrm{e} < 2$ eV in the negative-ion source results in a reduction of the rate coefficient by two orders of magnitude. Therefore, a magnetic filter filter is used to reduce the electron temperature in the extraction region.

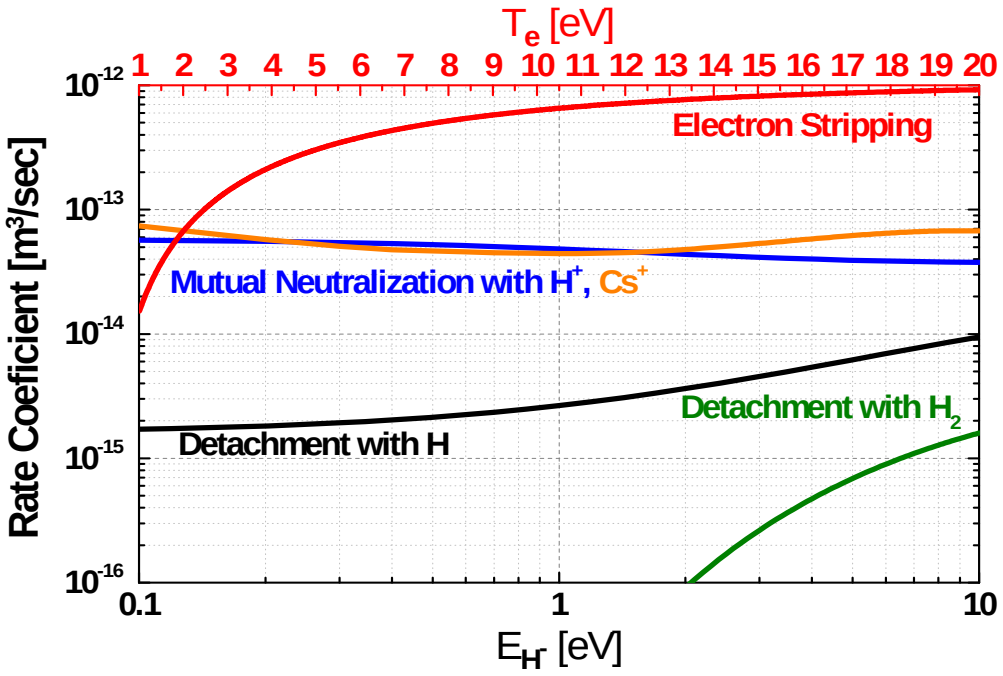


**Figure 3.7.:** Rate coefficients for negative-ion destruction reactions for different ion energies and electron temperatures for typical conditions within the extraction region of the RF-driven ion source.

### Mutual Neutralization

Mutual neutralization takes place when negative ions collide with positive $Cs^+$ [JR78] and $H_x^+$ [EdSO+95] ions of the source plasma (x = 1...3):

$$H^- + H_x^+ \rightarrow H + H_x, \tag{3.4}$$

$$H^- + Cs^+ \rightarrow H + Cs. \tag{3.5}$$

The weakly bound electron of the negative ion is transferred to the positive species, and both ions are neutralized. Mutual neutralization is the dominating destruction process at a low electron temperature of $T_e < 2$ eV, which is reached close to the production surface.

#### Associative and Collisional Detachment

Detachment reactions [JL87][Bar90] take place when negative ions collide with molecular or dissociated hydrogen:

$$H^- + H \rightarrow e^- + H_2, \tag{3.6}$$

$$\begin{aligned} H^- + H &\rightarrow e^- + 2\,H, \\ H^- + H_2 &\rightarrow e^- + H + H_2. \end{aligned} \tag{3.7}$$

While the reaction rate coefficient is two orders of magnitude lower than for mutual neutralization or electron stripping, the neutral gas density of $10^{19}$ m$^{-3}$ is two orders of magnitude higher than both, the ion and electron densities (range of $10^{17}$ m$^{-3}$) in the negative ion production region [FFF+06]. Thus, despite its low rate-coefficient, the detachment reaction is not negligible. Collisional detachment with the background gas is a significant loss process during the transport and formation of neutral beams.

## 3.2. RF-driven Ion Source for ITER N-NBI

The objective of the negative-ion source development is the optimization of the ion production via the surface effect, while minimizing destruction processes and the co-extracted electron current, in order to extract high negative-ion current densities for long pulses at ITER-relevant operation conditions.

### 3.2.1. Design of the IPP RF-driven Ion Source

The IPP RF-driven ion source is divided into three parts: driver, expansion region, and extraction region. A schematic overview of the RF-driven ion source is given in figure 3.8, while figure 3.9 shows the corresponding CAD drawing. The production and extraction of negative ions can be divided into four steps: positive and atomic hydrogen particles are generated in a RF-driven plasma source (driver). The plasma expands into the source body (expansion region), where a magnetic filter removes the hot electrons ($T_e > 2$ eV) that can effectively destroy negative ions. The positive and neutral hydrogen particles hit a converter surface, which is called plasma grid (see yellow grid in figure 3.9) with a low work

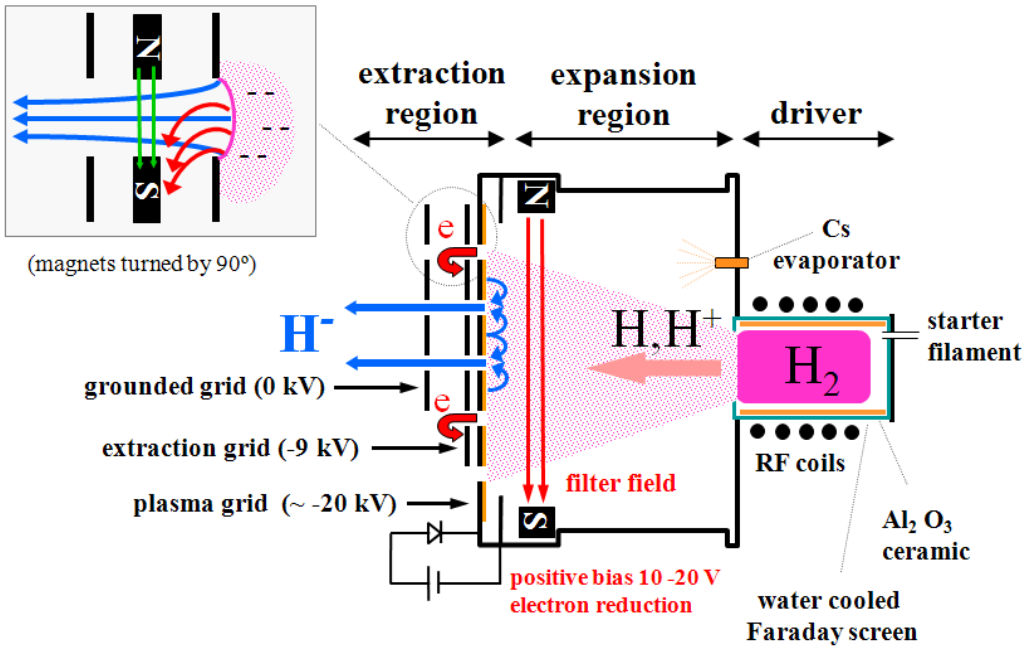


**Figure 3.8.:** Schematic drawing of the components of the IPP RF-driven ion source and the effect of the suppression magnets on the co-extracted electrons.

function and the conversion into negative ions takes place by picking up surface electrons. A positive extraction voltage in the kV-range is applied in order to extract negative ions and to forms the ion beam. Detailed descriptions of the individual parts and physical processes are given in the following subsections:

### Driver

The source plasma is generated by inductive coupling of 1 MHz RF-power to hydrogen gas inside the driver. A water-cooled coil that is wrapped around a ceramic Alumina ($Al_2O_3$) cylinder is connected to a RF generator capable of delivering up to 100 kW of power. A water-cooled and tungsten-coated Faraday screen is used inside the cylinder to protect it against thermal loads and erosion by plasma sputtering. A temporary gas puff together with an electron emitting $ThO_2$-coated tungsten starter filament at the backside of the driver ensures a reliable plasma start-up. Depending on the technical limitations of the specific test facility, plasma-pulse durations between 5 sec and 3600 sec can be obtained. A background pressure of $10^{-3}$ - $10^{-4}$ Pa is established in the vacuum phases between the plasma pulses, where a hydrogen pressure of 0.3 Pa is used.
Electron densities of $n_e \sim 10^{18}$ m$^{-3}$ and electron temperatures of $T_e > 10$ eV

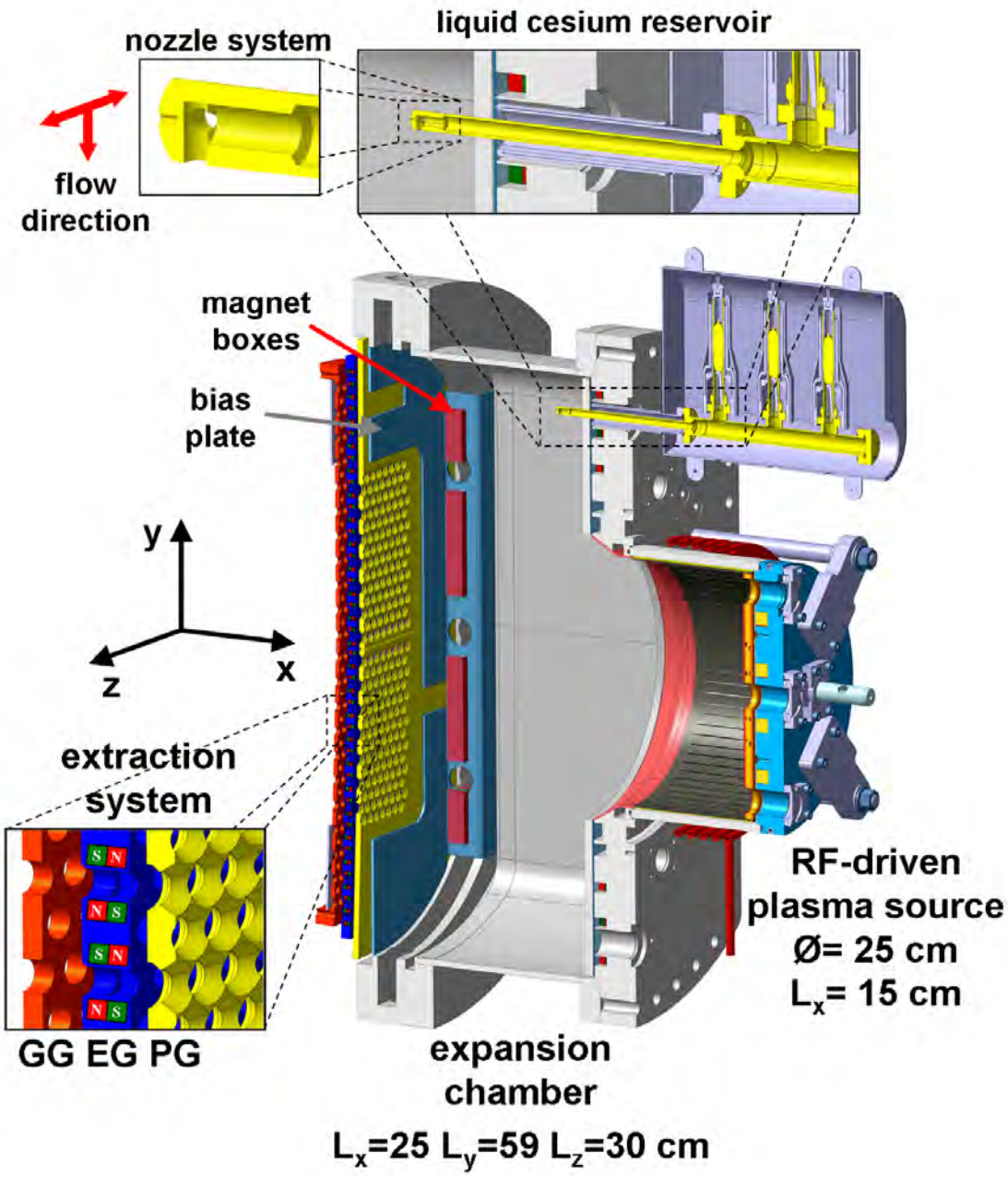


**Figure 3.9.:** Technical drawing of the individual components of the RF-driven ion source. The cesium evaporation oven (yellow) and the three grids (PG, EG and GG) of the extraction system were emphasized.

are obtained in and close to the driver [MDCK$^+$09][TBM04]. In order to avoid significant negative-ion destruction by electron stripping, the plasma parameters in the expansion region have to be changed significantly.

### Expansion Region

The expansion region contains several magnet boxes at the peripheral regions of the chamber at a distance of 2 cm (see red bars in figure 3.9) to the plasma grid. A magnetic field of a strength of 7 - 8 mT (strength at the center of the ion source) is thereby generated in order to reduce the electron temperature and density. Typical electron temperatures of $T_e < 2$ eV and electron densities of $n_e = 5\text{x}10^{17}$ m$^{-3}$ are obtained [FFF$^+$06].
Furthermore, the expansion chamber is connected to the cesium oven, evaporating the alkaline metal from a liquid reservoir into the ion source in order to generate a thin cesium layer on the plasma grid. This layer is necessary to obtain reasonable negative-ion surface production by lowering the work function of the converter surface. Cesium (see yellow ampoules in figure 3.9) is continuously injected at a constant rate of 10 mg/h from the nozzles (see yellow pipe in figure 3.9) of the oven at the backplate of the expansion chamber. The walls of the expansion chamber are coated with a copper layer in order to increase their thermal conductivity. A water cooling system is used to keep the walls at 50 °C, which is beneficial for the distribution of the evaporated cesium inside the ion source, as described in section 6.1.3.

### Extraction Region

At the required hydrogen pressure of 0.3 Pa, negative-ion production takes place predominantly by surface conversion. The surface process takes place on all cesium-covered surfaces of the negative-ion source that are sufficiently exposed to the atomic hydrogen flux. As described in section 3.1.2, negative hydrogen ions have a limited survival length of a few cm until a neutralization collision takes place. As a consequence, the surface area of the plasma grid that is in close proximity to the extraction apertures provides the dominant contribution of extracted negative ions to the ion beam. Thus, the cesium conditions of the plasma grid surface are extremely important for the extracted negative-ion current. The use of a plasma grid temperature of 150 °C was found to be beneficial for the source

performance [SFF+06], which will be explained in more detail in section 4.1.4.
A certain fraction of the surface generated negative ions is transported through the source plasma into the multi-aperture system of the plasma grid (see yellow PG apertures in figure 3.9), where they are focused into an ion beam by electric fields, formed by an extraction voltage of several kV. The penetration depth of this field is limited because of the field compensation by the space charge of the plasma particles.
Applying a bias voltage between the plasma grid and the source body is an efficient way to reduce the number of co-extracted electrons, limiting the source performance as described in section 3.1.1. The electrically isolated plasma grid is biased positively with respect to the source body. A diode is used to suppress any current back to the power supply. The effect of the bias voltage can be enhanced significantly by inserting a bias plate at a distance of 1 cm with respect to the plasma grid that is connected to the source body [SFF+06][FFK+08].

### Extraction System

A triode extraction system with three grids is used for ion-beam formation and in order to filter out the co-extracted electrons at manageable particle energies. These grids are called the following: the plasma grid (PG), the extraction grid (EG) and the grounded grid (GG). In the first step, an extraction voltage of $U_{\mathrm{ex}} = 5$ - 10 kV is applied between the plasma and the extraction grid in order to remove co-extracted electrons at reasonable energies. A second voltage of $U_{\mathrm{acc}} = 10$ - 20 kV is used at the test facilities of the IPP in order to focus the filtered negative-ion beam onto a calorimeter, which allows a measurement of the accelerated current density.
Electron removal is done by a magnetic field. This electron deflection field is generated by $Sm_2Co_{17}$ magnet rods inside the extraction grid. The field strength is high enough to deflect the electrons onto the surface of the extraction grid, while $D^-/H^-$ ions can still pass through the filter nearly unaffected because of their higher mass. Figure 3.10 shows a numerical simulation of a beam of $D^-$ ions and electrons for an extraction system with 14 mm aperture diameter computed with the KOBRA3 code [SW89]. The impact of co-extracted electrons on the extraction grid causes a heat load that must be compensated by an optimized water-cooling system. The maximum heat load that can be tolerated by the extraction grid without damage is a limiting factor for the performance of the ion source.

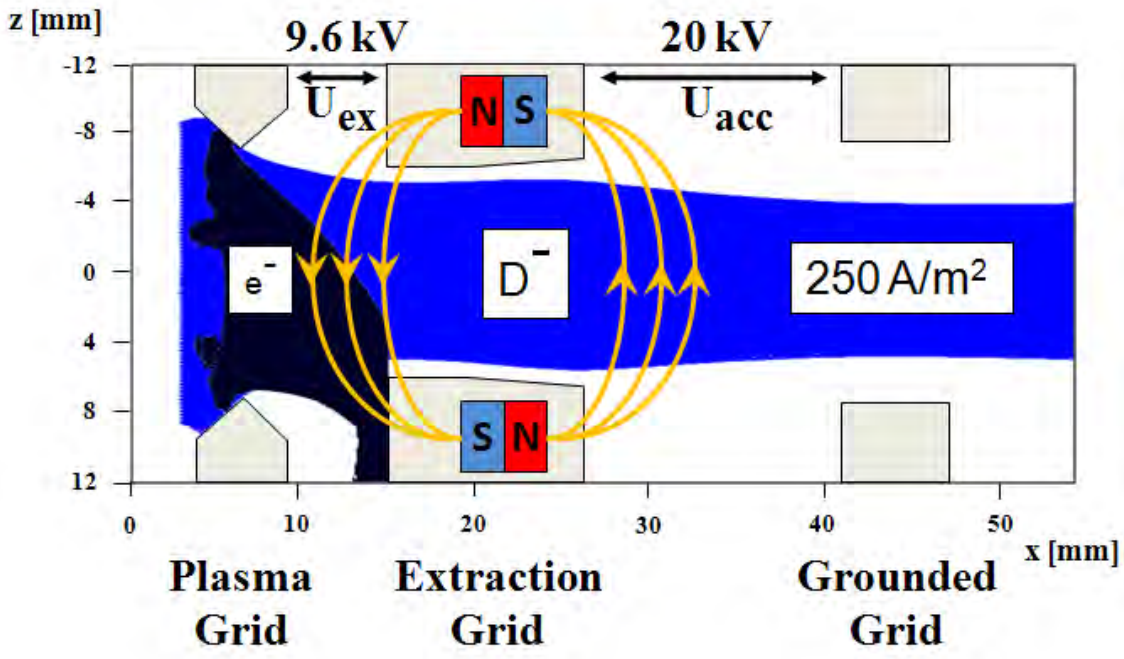


**Figure 3.10.:** Simulation of the extraction and beam formation of a negative deuterium ion beam (blue) together with the co-extracted electron beam (black) hitting the extraction grid for an extracted ion current density of 250 A/m$^2$. The suppression magnets and the associated magnetic field was rotated by 90$^o$ to show the electron deflection.

### 3.2.2. Negative-Ion Source Test Facilities at IPP

The RF-driven negative-ion source development towards ITER at IPP is done on three dedicated test facilities: BATMAN[6], MANITU[7] and RADI[8]. The future test facility ELISE[9] finished the design phase and will be operational in 2011. While the test facilities BATMAN and MANITU have moderately sized ion sources (59 x 32 cm$^2$), the test facility RADI has a source with approximately half the size (80 x 80 cm$^2$) of the future ITER source (190 x 90 cm$^2$), as shown in figure 3.11. Specifications and achieved operation parameters of the three existing test facilities and the ITER requirements are given in table 3.1. More detailed information on the test facilities are given in the following sections.

[6]BATMAN: Bavarian Test Machine for Negative Ions, IPP Garching.
[7]MANITU: Multi Ampere Negative Ion Test Unit, IPP Garching.
[8]RADI: RADial Injector, IPP Garching
[9]ELISE: Extraction from a Large Ion Source Experiment, IPP Garching.

**Table 3.1.:** Operation parameters of the existing test facilities BATMAN, MANITU and RADI in comparision with the ITER requirements

| | **BATMAN** | **MANITU** | **RADI** | **ITER** |
|---|---|---|---|---|
| Acc. Current Density [A/m$^2$] | 230 ($D^-$)<br>330 ($H^-$) | 120 ($D^-$)<br>150 ($H^-$) | | 200 ($D^-$)<br>300 ($H^-$) |
| Source Pressure [Pa] | 0.3 | 0.3 - 0.4 | 0.3 | 0.3 |
| Electron/Ion Ratio | $< 1.0$ ($D^-$)<br>$< 0.5$ ($H^-$) | $< 1.5$ ($D^-$)<br>$< 0.5$ ($H^-$) | | $< 1.0$ |
| Pulse Length [sec] | 4 | 3600 ($H^-$) | $< 10$ | 3600 |
| Dimensions [cm$^2$] | 59 x 32 | 59 x 32 | 80 x 80 | 190 x 90 |
| Extraction Area [cm$^2$] | 60 - 70 | 200 | 0 | 2000 |
| Extraction Voltage [kV] | 9 - 11 | 9 | | 9 - 10 |
| Beam Homogeneity [%] | | | | 10 |

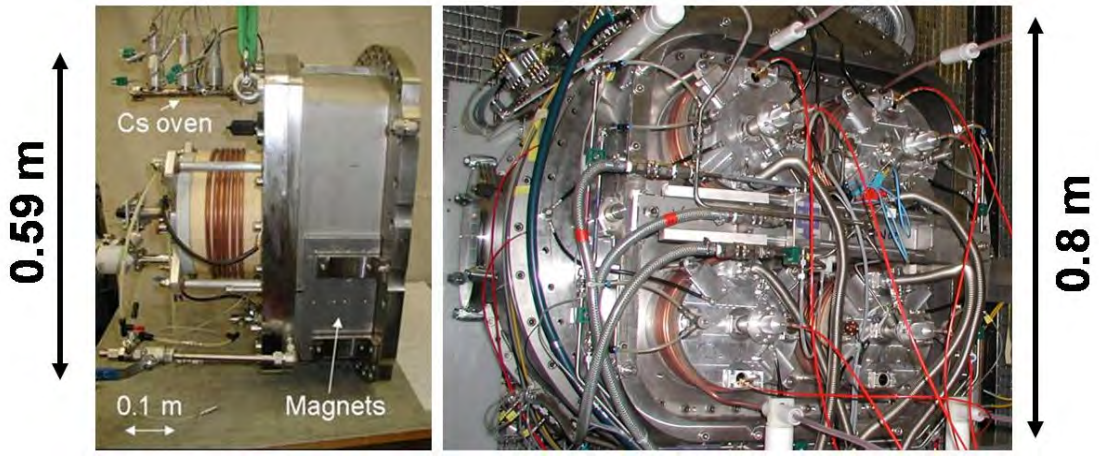


**Figure 3.11.:** Photograph of the ion source in MANITU (left hand side) with a single driver and the test facility RADI (right hand side) with four RF-driven ion sources which has approximately half the size of the ITER source.

### BATMAN

The first test facility BATMAN [SCF+99] showed the feasibility and reliability of negative-ion surface production at the required parameters on a small area (59 x 30 $cm^2$). Accelerated current densities of 330 $A/m^2$ with $H^-$ and 230 $A/m^2$ with $D^-$ [SFF+06] have been achieved with the IPP RF-driven prototype source on BATMAN at the required source pressure of 0.3 Pa and a sufficiently low electron-to-ion ratio ($<$ 1 $D^-$, 0.5 $H^-$), but with a small extraction area of 60 - 70 $cm^2$ and limited pulse length of several seconds. The test facility BATMAN is being used currently to investigate the physical aspects of negative-ion production and extraction.

### MANITU

The long-pulse test facility MANITU [KFF+08] has demonstrated its capability to provide 3600 (600) sec $H^-$ ($D^-$) extraction on a mid-size extraction area of 200 $cm^2$ using the same source as it is used in BATMAN with current densities of 150(120) $A/m^2$ $H^-$($D^-$). This stable one-hour pulse operation showed that the RF-driven ion source concept is able to meet the ITER requirement on pulse duration. Similar value than in BATMAN were obtained for shorter pulse lengths of several seconds.

### RADI

The half-size RF test facility RADI [FFH+07] is an intermediate step between the present small sources (BATMAN and MANITU) and the full-size ITER source. The RADI test facility has no ion extraction system and the plasma grid is replaced by a slotted dummy grid with a conductance comparable to the ITER grid. The objective of RADI is to demonstrate the required plasma homogeneity of a large RF-driven ion source. RADI has approximately the width and half the height of the ITER source. This allows an easy extrapolation to the full-size ITER source. A sufficiently homogeneous illumination of the total grid area can not be accomplished by a single driver; therefore, four drivers for inductive plasma generation are used in RADI, as it is shown in figure 3.11.

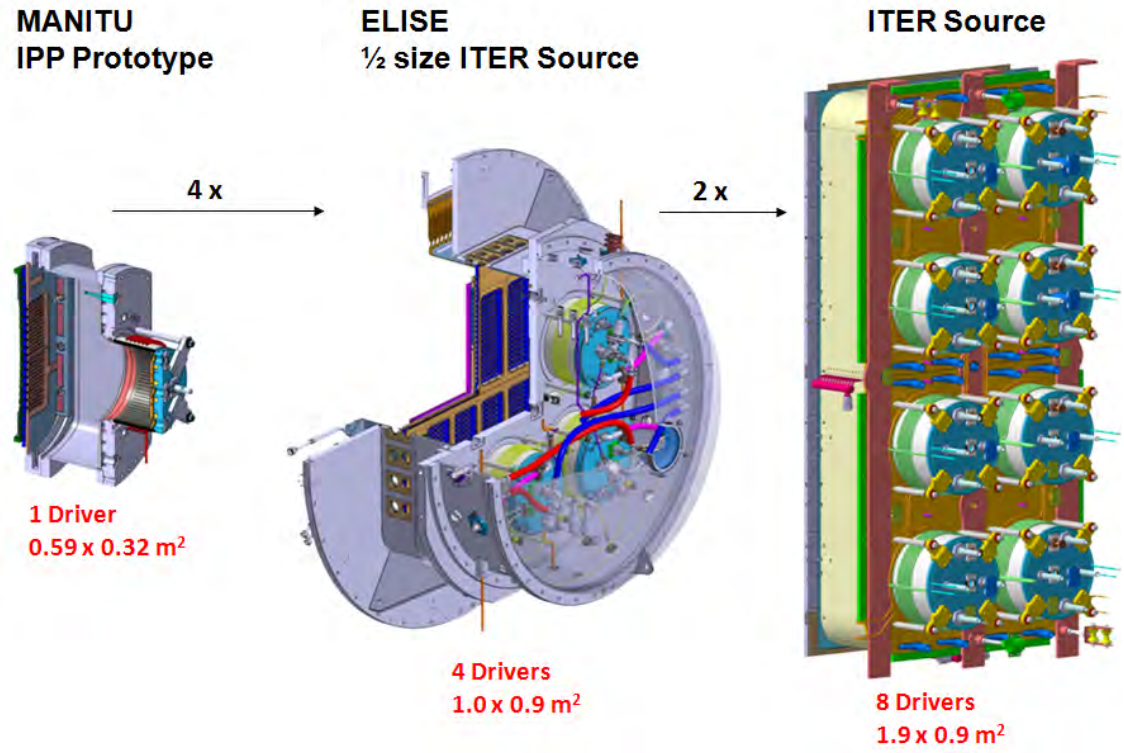


**Figure 3.12.:** Comparison of the existing IPP prototype source in MANITU and the ion source for the future ELISE test facility with the negative-ion source, planned for the ITER N-NBI.

## ELISE

The future IPP N-NBI test facility ELISE [HFF+09] will be equipped with an ion extraction system. This will allow the investigation of physical aspects of the ion production and extraction in a half-size ITER negative-ion source. Experience, acquired by the development and operation of the IPP test facilities is incorporated in the design of the future ELISE ion source test facility. ELISE will be an important step between the small IPP prototype source and the large ITER source in order to obtain early operational experience of the extraction from a large RF-source [F+08]. This scaling from the 1/8 ITER-size test facility MANITU (1 driver) to the half-size ITER source for ELISE (4 driver) and then to the full-size ITER source is illustrated by figure 3.12. ELISE will offer large experimental flexibility and wide operational margins for optimization and exploration of new concepts. The ELISE test facility will be equipped with a high voltage supply for a total voltage of 60 kV and an extraction area of 1000 $cm^2$. One of the main objectives of ELISE is to demonstrate the homogeneous ion production and extraction from a large RF-driven, cesium seeded negative-ion source.

### 3.2.3. Source Operation with Hydrogen and Deuterium

The IPP negative-ion source test facilities can be operated with hydrogen and deuterium. Both modes are required for the ITER heating and diagnostic neutral beams. However, the use of hydrogen is preferred during source conditioning and for experimental studies. Source operation with deuterium is possible only for a limited number of pulses.
The interaction of implanted deuterium in the calorimeter with the deuterium ion beam results in the associated production of neutrons by the D-D fusion reaction:

$$\mathrm{D} + \mathrm{D} \rightarrow {}^{3}\mathrm{He} + \mathrm{n} + 2.45\ \mathrm{MeV}. \tag{3.8}$$

Long-pulse deuterium operation requires, therefore, a neutron shield around both the calorimeter and the ion source, as in MANITU or a remote control system, as done in BATMAN. Despite of the radioactive exposure, the physics of deuterium discharges differs from that of hydrogen. The co-extracted electron current is higher for deuterium operation, which results in an excessively high power load on the extraction grid. This limits the allowable RF power and thus the maximum $D^-$ current density. With an increased filter field, produced by additional magnet rods near the diagnostic flange, the electron-to-ion ratio can be reduced. However, a ratio below 0.4 that is easily accessed with hydrogen pulses has not yet been achieved with deuterium [SFF+06].

### 3.2.4. Long Pulse Operation

The negative-ion source test facility MANITU is capable of running long pulses. This requires the replacement of the Ti getter pumps, used in BATMAN, by cryosorption pumps and the installation of cw[10] power supplies for the RF and high voltage system.
The reduction and stabilization of the electron current, while maintaining a sufficiently high negative-ion current, are the most critical issues for long pulses up to now. An excessively high co-extracted electron current can damage the extraction system, as described in section 3.2.1, limiting the effective pulse time. The operational experience showed that the long-pulse stability is strongly correlated to the cesium conditions on the plasma grid. These are determined by the thickness of the cesium layers and by the temperatures of the source components during the plasma and the preceding vacuum phase. Up to now it is not clear,

[10] cw: continuous wave.

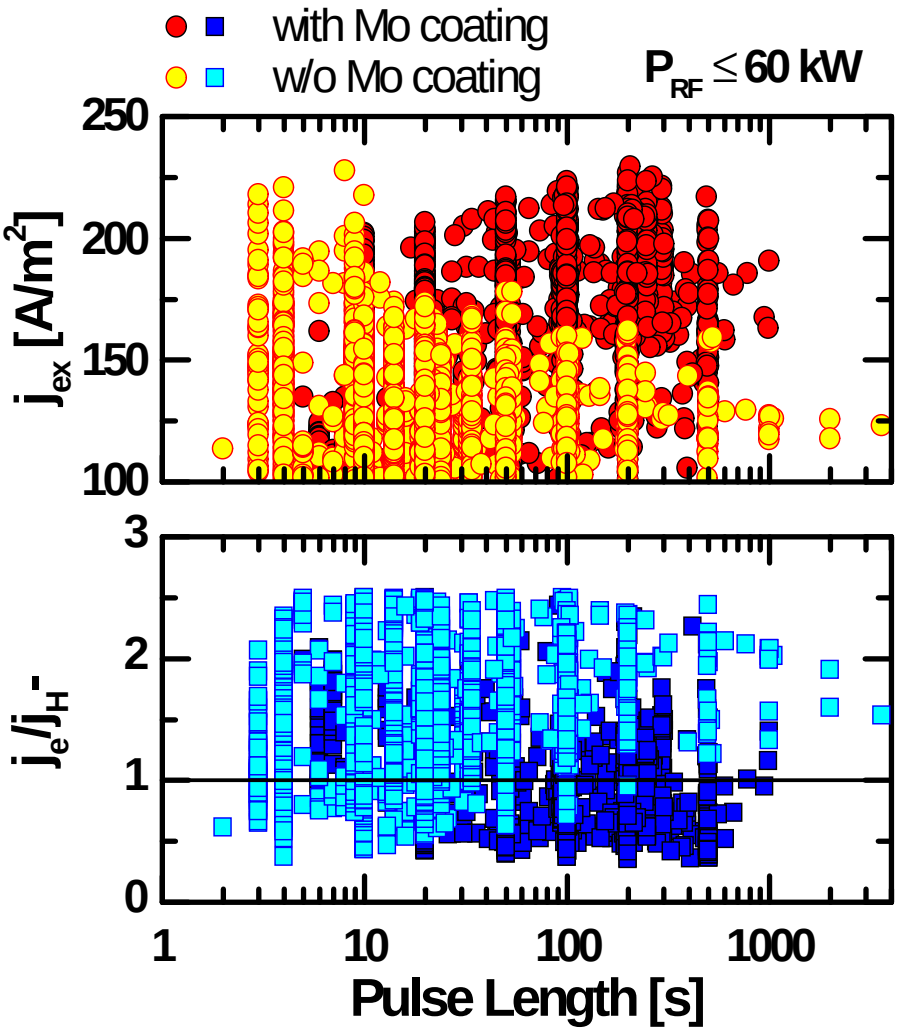


**Figure 3.13.:** MANITU long-pulse performance in hydrogen with and without (w/o) Mo coating of the source for different pulse lengths.

which parameter determines the long pulse stability.

A recent improvement in MANITU has demonstrated the importance of the chemical properties of the cesium layer for long pulse operation. The sputtering of copper was observed in MANITU deteriorating the cesium on the plasma grid surface. The coating of critical surfaces in MANITU with molybdenum resulted in a considerable increase of the source performance, as shown in figure 3.13 [KBF+09].

These promising results show the importance of the development of procedures and methods in order to obtain an advanced control of the cesium conditions.

# 4. Experimental and Theoretical Aspects for Cesium

## 4.1. Physical and Chemical Properties of Cesium

Cesium-coated metal surfaces are characterized by a very low work function. Thus, the addition of cesium into ion sources, optimized for the surface production of negative ions, makes it possible to increase drastically the conversion yield of negative ions from plasma particles. This procedure is widely used in small negative-ion sources (diameter of several cm) with mono-aperture extraction systems [LDD+91][RGS+08].

The negative-ion source for ITER will have large dimensions (190 x 90 $cm^2$) and will have to operate for pulse lengths of one hour. This will require an advanced control of the distribution and dynamics of cesium within the source in order to maintain stable cesium conditions in space and time. The properties of cesium layers and cesium vapor are important information in order to achieve these objectives.

Alkaline metals, such as cesium, are of great technological importance, for example, they are needed to produce photosensitive surfaces in photo-cathodes. The available data on cesium is related to this field of research. A convenient way to quantify the cesium coverage of a surface is to use the unit monolayer (1 ml). One monolayer of cesium corresponds to $4.5 \times 10^{14}$ cesium atoms per $cm^2$ on the metal substrates that are relevant for negative-ion sources.

As mentioned in section 3.1, cesium is injected into negative-ion sources in order to obtain a low work function. While this property is used in negative-ion sources to enhance the surface production, it explains its technologic importance in general.

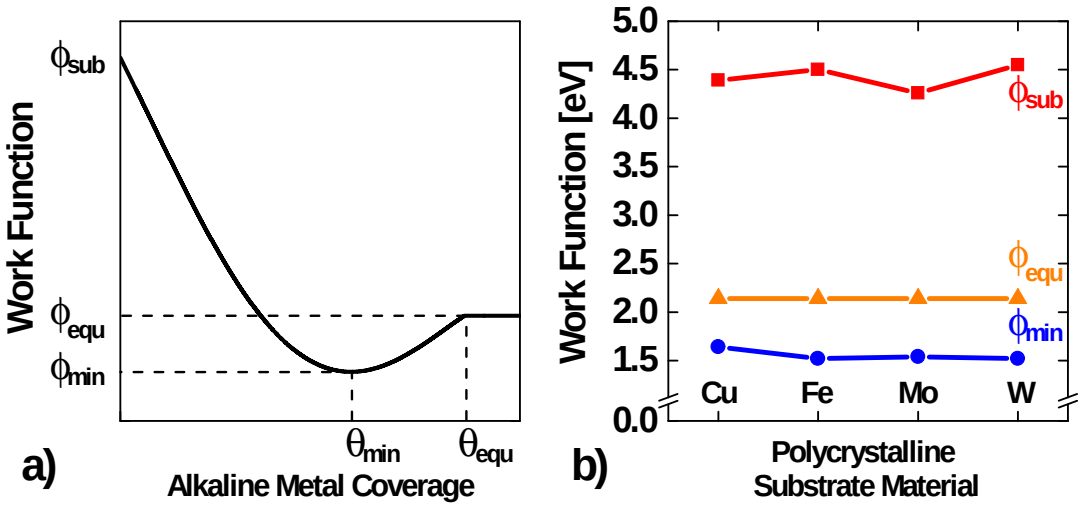


**Figure 4.1.:** a) Work function behavior of a metal substrate in dependence of the cesium coverage. b) Corresponding work function parameters for different polycrystalline substrates.

### 4.1.1. Work Function of Cesium Layers

The work function of a metal substrate $\phi_{\text{sub}}$ is found to drop with increasing alkaline metal coverage to a minimum value of $\phi_{\text{min}}$, corresponding to a coverage $\theta_{\text{min}}$. Increasing the coverage above $\theta_{\text{min}}$ results in a rise and subsequent saturation of the work function to a value of $\phi_{\text{equ}}$ at a coverage of $\theta > \theta_{\text{equ}}$, when the work function of the bulk adsorbate is reached. This physical process is illustrated in figure 4.1. The minimum work function, previously mentioned, appears at a fractional coverage between $\theta_{\text{min}} = 0.5$ - $0.7$ monolayers, depending on the substrate material and crystal orientation. The value of the minimum work function in case of a cesium layer is in the range of $\phi_{\text{min}} = 1.4$ - $1.6$ eV, which is subject to the substrate material. Figure 4.1 gives an overview of the work function parameters $\phi_{\text{sub}}$, $\phi_{\text{min}}$ and $\phi_{\text{equ}}$ for different substrate materials and coverages of cesium [Wil66a][Wil66b][SS68][LS60][Eas70][HR63]. The value of the work function for coverages above one monolayer $\phi_{\text{equ}} = 2.14$ eV [BD69] is given by the work function of cesium in the bulk.

The appearance of a work function minimum is an effect due to the formation of a chemical compound of cesium with the metal substrate creating a dipole layer. This strongly reduces the work function of the surface. A detailed overview of this phenomenon including density functional calculations is given in [WFHK83].

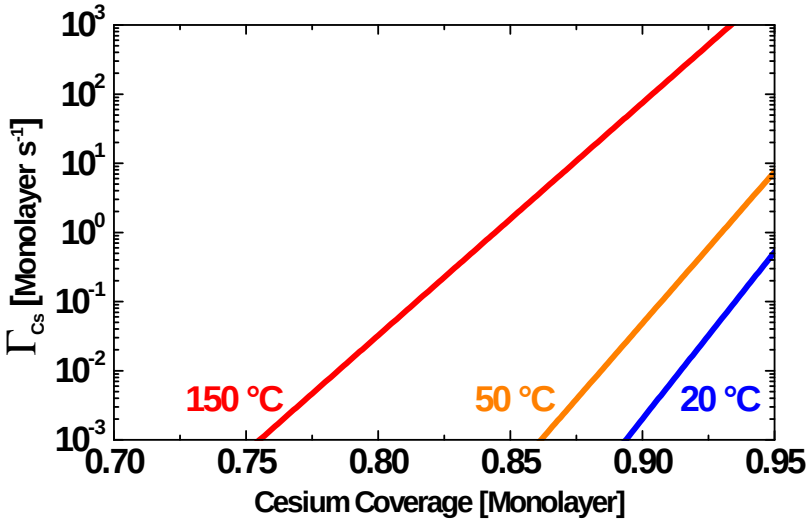


**Figure 4.2.:** Desorption flux from a cesiated tungsten substrate in dependence of the fractional monolayer coverage for relevant temperatures.

### 4.1.2. Desorption Flux from Fractional Cesium Layers

The desorption flux $\Gamma_{\mathrm{Cs}}$ of cesium from a fractional layer on a tungsten substrate at temperature $T$ depends strongly on the coverage $\theta$, given in monolayers of the metal surface:

$$\Gamma_{\mathrm{Cs}} = \Gamma_0\,\theta \exp\left(\frac{-e\ (3.37 - 2.78\,\theta)}{k_{\mathrm{b}}T}\right), \qquad 0 \leqq \theta \leqq 1, \tag{4.1}$$

where $\Gamma_0 = 7.5\mathrm{x}10^{26}$ s$^{-1}$cm$^{-2}$ is a pre-exponential factor [ATG85]. This dependence on the coverage is a consequence of the repulsive dipole interaction between the cesium atoms in the layer. This decreases the binding energy of the layer for increasing coverage. Similar dependences are found for other metal substrates. The corresponding desorption flux from tungsten for ion-source relevant temperatures is shown in figure 4.2. Hence, a very high desorption flux is expected if the sample coverage approaches a full monolayer coverage. Using a sample temperature of 50 $°C$, corresponding to the temperature of the ion source walls, results in a high desorption flux of $\Gamma_{\mathrm{Cs}} > 10$ monolayers per second for a nearly complete monolayer coverage. When completing a full monolayer, the strong dipole bond on fractional covered metal surfaces is replaced by the weak van-der-Waals interaction between cesium atoms in the bulk, which defines the vapor pressure of cesium (see section 4.1.3).

Under ideal conditions of a pure cesium layer on a metal substrate, no multilayer growth will be present at room temperature and sufficiently low densities of ce-

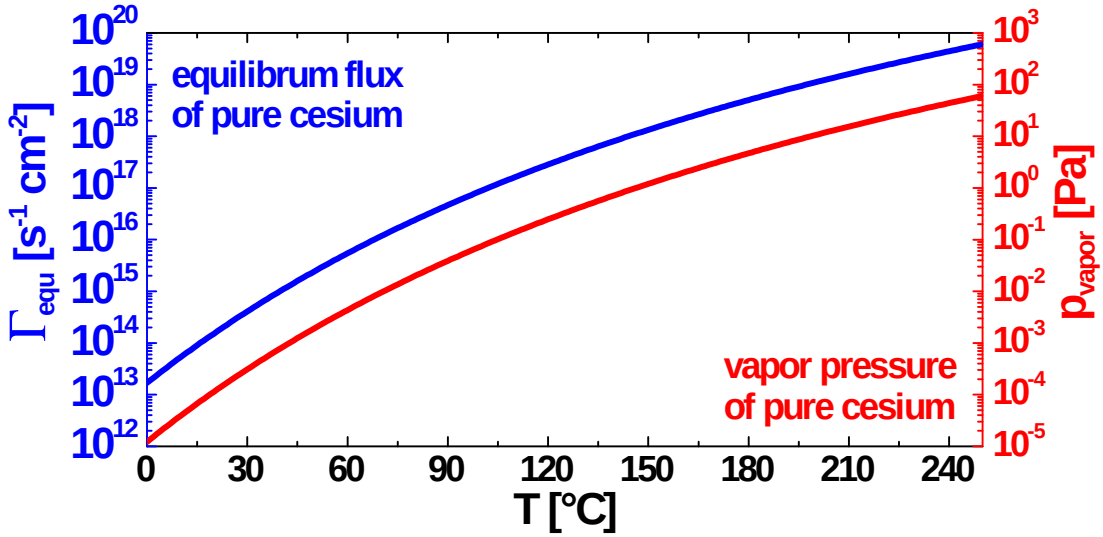


**Figure 4.3.:** Vapor pressure and corresponding balancing flux for pure cesium in the equilibrium state in dependence of the temperature of the liquid cesium.

sium vapor [Gra80]. The formation of multiple monolayers is, however, possible in the presence of high cesium densities and the corresponding high fluxes onto the surfaces. This is the case on the inner surface of a cesium source containing a reservoir of liquid cesium, which is described in section 4.2.6. The desorption flux and surface coverage is in this case determined by the vapor pressure of liquid cesium.

### 4.1.3. Vapor Pressure of Pure Cesium

Cesium is the heaviest stable alkaline metal with an atomic radius of 265 pm and a low melting temperature of 28.5 °C [Lid07]. Cesium has the lowest enthalpy of evaporation ($\Delta H_\mathrm{f}$ = 67.7 kJ/mol) and the highest vapor pressure of all stable metallic elements, except for mercury ($\Delta H_\mathrm{f}$ = 59.1 kJ/mol) [Lid07]. As a consequence, cesium can be easily injected into negative-ion sources by thermal evaporation. Figure 4.3 shows the dependence of the cesium vapor pressure $p$ on the temperature $T$ of a liquid reservoir, taken from data in [TL37]. The corresponding balancing wall-flux $\Gamma_\mathrm{equ}$ for an equilibrium situation within a closed system can be evaluated by the mean thermal velocity $\bar{v}$ and the density $n$ of cesium in the gas phase by the kinetic gas theory:

$$\Gamma_\mathrm{equ} = \frac{1}{4} n \bar{v} = \frac{p}{\sqrt{2\pi\, k_\mathrm{b} T\, m_\mathrm{Cs}}}, \tag{4.2}$$

where $m_{Cs}$ is the atomic mass of cesium. According to the data presented in figure 4.3, a desorption flux of $\Gamma_{equ} = 10^{14}$ - $10^{15}$ $s^{-1}cm^{-2}$ evolves in a system at vapor pressure equilibrium for a wall temperature ranging between $T = 20$ °C - 50 °C. The desorption balances the condensation of cesium in the gas phase according to the vapor pressure curve.
Most of the presented data were obtained for the development of photosensitive surfaces, where the negative influence of possible cesium compounds is suppressed by using an ultra-high vacuum environment and surface temperatures of several 1000 °C, avoiding the accumulation of impurity species. Cesium compounds that occur inevitably under the vacuum conditions ($10^{-3}$ - $10^{-4}$ Pa) and at the surface temperatures (20 - 50 - 150 °C) in negative-ion sources (see section 3.2) will have an important impact on the physical and chemical processes within the source.

### 4.1.4. Chemical Compounds of Cesium

The removal of the single 6s shell electron of the cesium atom results in the very stable Xe-like configuration. Thus, cesium has the highest electropositivity of all stable elements. This results in a very high chemical reactivity, forming a wide spectrum of crystalline compounds with ionic binding characteristics. Because of its high reactivity, cesium (like barium) is used as a getter material in order to absorb residual-gas particles. The flux of impurities on the inner walls of the negative-ion source can be approximated by formula (4.2) taking into account the mass of the residual gas particles. At an equilibrium wall temperature of 50 °C, one monolayer of impurities, such as $H_2O$ and $O_2$, is built up on the source walls after 3 - 4 sec for a typical background pressure of $10^{-3}$ - $10^{-4}$ Pa. Furthermore, cesium forms alloys with metals and is able to dissolve residual gas.
Cesium compounds have different physical properties than pure cesium. This has a negative impact on devices that require specific properties of elemental cesium, such as the surface wettability [PAL07]. It is reported in [Mit89] that the performance of a cesium field ion thruster will be reduced by a throttling of the cesium flow that is a consequence of the formation of cesium compounds. The non-metallic binding characteristics of cesium compounds is also unfavorable for the surface conversion process, an effect that is related to the increase of the effective work function of the layer. An overview of Cs-O-H-metal compounds that are relevant for the negative-ion source is given in the following section.

**Table 4.1.:** Overview of relevant cesium compounds that can be formed within the negative-ion source or on diagnostic systems for cesium.

| Formula | Name | Color | Properties | $T_{melt}$ [°C] | Source |
|---|---|---|---|---|---|
| Cs | cesium | silvery | alkaline metal | 28.5 | [Lid07] |
| CsH | cesium hydride | white | cub. cry. | 528 | [LB08] |
| $Cs_nO_m$ | cesium oxides | | | | [Bor86] |
| $Cs_2O$ | cesium oxide | orange | hex. cry. | 495 | [Lid07] |
| $CsO_2$ | cesium superoxide | yellow | tetr. cry. | 432 | [Lid07] |
| $Cs_2O_3$ | cesium trioxide | brown | cry | 400 | [Lid07] |
| CsOH | cesium hydroxide | white | cry hygroscopic | 342 | [LB08] |
| $CsCuO_2$ | cesium oxycuprate | black, blue shimmer | cry | 1025 | [LB08] |
| CsAu | | golden | alloy | | [LB08] |

### Overview and Melting Point of Cesium Compounds

As a result of the ionic binding, the various cesium compounds are crystalline materials with a high melting temperature. Table 4.1 gives an overview of the melting points and characteristic properties of relevant cesium compounds, such as color and crystal structure. The compound cesium oxycuprate $CsCuO_2$ can be formed by reactions of cesium with the copper surfaces of the walls of the negative-ion source, while the alloy CsAu can be formed on the quartz microbalance (see section 4.2.2) that is used for cesium detection.
All cesium compounds have melting temperatures far above the temperature range on the walls of the negative-ion source, however, thermal dissociation could be still possible for a lower temperature range.

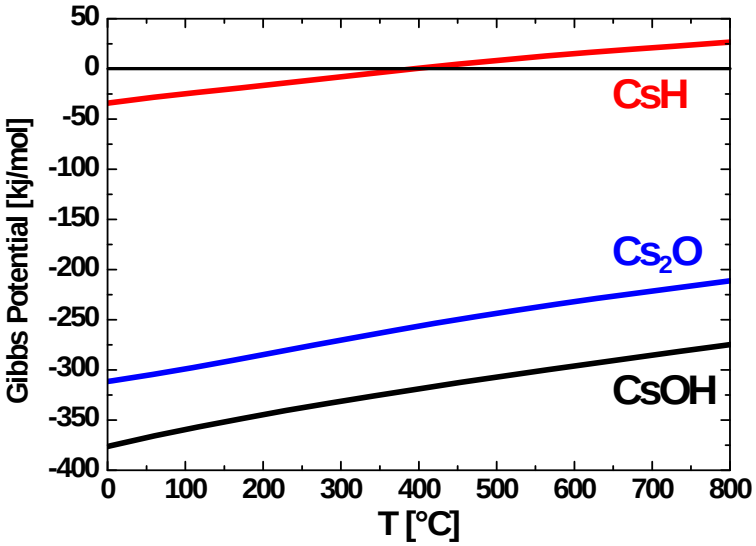


**Figure 4.4.:** Temperature dependence of the Gibbs potential for ion-source relevant cesium compounds. Cesium hydride CsH is the only substance that is instable regarding dissociation for the relevant temperature range.

### Chemical Stability of Cesium Compounds

The stability of cesium compounds against thermal dissociation can be evaluated employing the Gibbs potential. Figure 4.4 shows the Gibbs potential of the cesium compounds CsH, $Cs_2O$ and CsOH taken from [LB08]. The stability analysis shows that $Cs_2O$ and CsOH have a very high chemical stability and a thermal decomposition process is impossible within the temperature range of the ion source and the liquid reservoir. This means that the formation of the specified cesium compounds on the surfaces of the ion source and in the liquid reservoir results in a loss of the available cesium. As a consequence, the recycling of pure cesium from these compounds is not possible apart from plasma-related decomposition processes.
However, the Gibbs potential of cesium hydride CsH changes its sign within the specified temperature range, indicating the following dissociation process:

$$\mathrm{CsH} \longrightarrow \mathrm{Cs} + 1/2\,\mathrm{H_2}. \tag{4.3}$$

Figure 4.5 shows the corresponding dependence of the dissociation pressure $p_{\mathrm{diss}}$ versus the temperature of the hydride crystal [Son94] for the pressure and temperature conditions within the IPP RF-driven negative-ion source. The dissociation

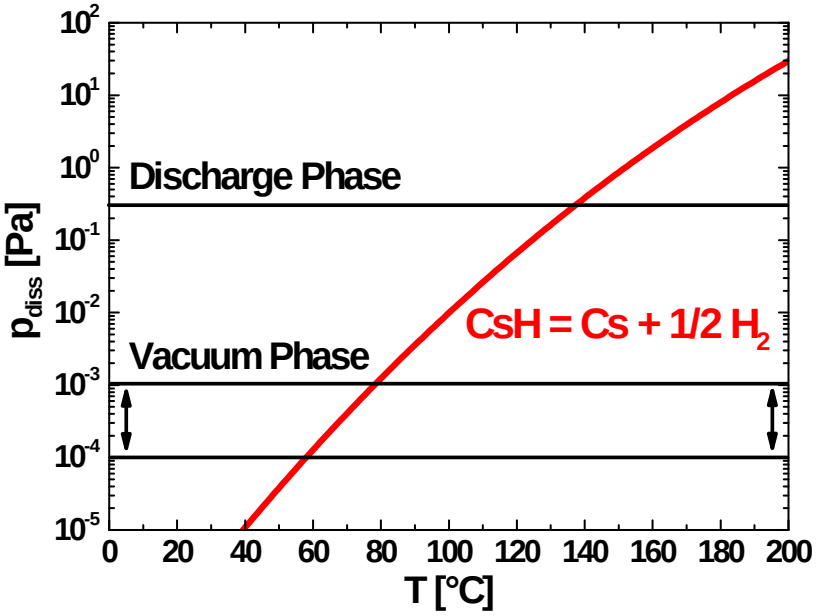


**Figure 4.5.:** Dissociation pressure of cesium hydride CsH for the hydrogen pressure conditions of the IPP RF-driven negative-ion source of $10^{-3}$ - $10^{-4}$ Pa during the plasma-off, and 0.3 Pa during the plasma-on phases.

pressure of CsH exceeds the hydrogen pressure of 0.3 Pa during the discharge only for the temperature conditions of the plasma grid of $T_{\mathrm{PG}} = 150$ °C where a dissociation process can be expected. In the plasma-off phase, the lower source pressure of $10^{-3}$ - $10^{-4}$ Pa is slightly above $p_{\mathrm{diss}}$ for the ion source wall temperature of $T_{\mathrm{Source}} = 50$ °C indicating that CsH is stable under these conditions.
As described in section 3.1.1, the production of negative ions is reduced by the influence of hydrogen, adsorbed on the plasma grid surface. The thermal dissociation of cesium hydride takes place at a temperature of 150 °C, taking into account the hydrogen background pressure of 0.3 Pa. Hence, the thermal dissociation and removal of CsH from the plasma grid is a relevant process and a corresponding increase of the negative-ion production is expected. The calculated dissociation temperature is in agreement with experimental observation, where a performance increase of the negative-ion source was observed when using a plasma grid temperature higher than 150 °C [SFF+06].

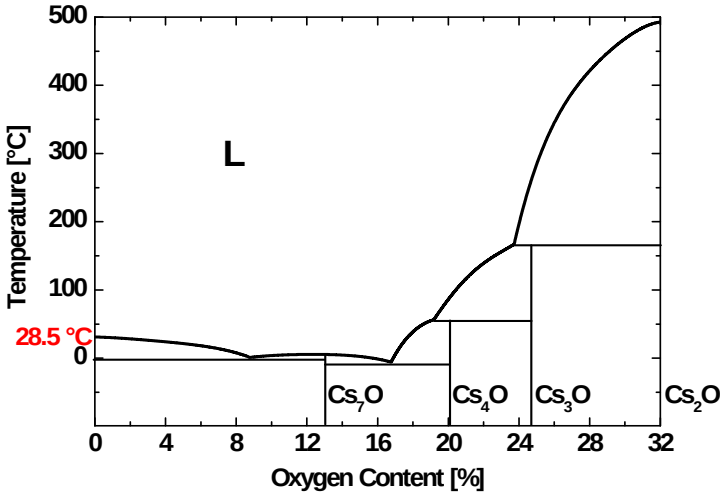


**Figure 4.6.:** Phase diagram of the Cs-O system for the relevant temperature range.

### Solubility of Impurity Species

Pure cesium is in the liquid phase for the temperature conditions at the walls of the negative-ion source and the evaporation oven (see section 3.2.1). A dissolution of impurities in the liquid cesium can take place in this case that has been investigated by Borgstedt [Bor86]: the solubility of CsH and CsOH in liquid cesium is very limited and shows no interaction with the liquid cesium phase. However, oxygen has a very high solubility in liquid cesium, as shown in figure 4.6. For a wall temperature of $T_{\mathrm{wall}} = 50$ °C, a high oxygen solubility of 18 % is expected. The phase diagram shows that the melting point of the cesium-oxygen system depends on the oxygen content. While a low oxygen content will result in a slight decrease of the melting point, cesium-oxygen compounds with higher oxygen valences, such as $Cs_2O$, which precipitate at a high oxygen content, shift the melting temperature to 495 °C. The partial pressure of cesium in the gas phase above a cesium-oxygen system drops significantly in comparison to elemental cesium. This is a result of the enthalpy of dissolution required to release pure cesium vapor.

## 4.2. Experimental Methods for Cesium Diagnostics

As described in the previous section, cesium has a very high chemical reactivity and its behavior within N-NBI systems depends strongly on the specific surface and pressure conditions. The development and application of cesium diagnostics is therefore essential for understanding the fundamental processes taking place within the negative-ion source. Diagnostics systems are also highly important for determining input parameters for cesium transport models to be used for optimization and design calculations.
Most of the data available is for pure, metallic cesium under ultra-high vacuum conditions and does not consider chemical reactions with impurities. The availability of a wide spectrum of diagnostics that are suitable for studying specific physical or chemical processes is therefore very important. It is not possible to perform all of these systematic experiments at the IPP test facilities in parallel with the source operation, where the accessibility is limited. The flexible arrangement of the experimental configuration that requires a frequent opening of the apparatus is only given in a small-scale laboratory environment. Thus, dedicated experiments at the University of Augsburg were performed.

### 4.2.1. Experimental Setup

The experimental setup to determine properties of cesium at ion source relevant conditions requires a high degree of flexibility in order to design and use several types of different cesium diagnostics. Experiments were carried out in a small-scale, inductively-coupled plasma source where vacuum and plasma conditions comparable to those close to the converter surface of the IPP RF-driven negative-ion source could be achieved. This means that a residual gas pressure of $10^{-4}$ to $10^{-3}$ Pa is reached during the plasma-off phase, while a hydrogen gas pressure in the Pa-range with an electron density of up to $10^{17}$ m$^{-3}$ and an electron temperature of $T_e = 2$ eV is obtained during the discharge [SFAP01].
The experiments were carried out in a cylindrical vacuum chamber (stainless steel) of 15 cm in diameter and 10 cm in height. The plasma is generated by inductive coupling by a planar coil with a Faraday screen on top of the cylinder, as illustrated in figure 4.7. A generator frequency of 27.12 MHz at a maximum power of 600 W can be used.
The temperature-controlled chamber walls ($T_{wall} = 20$ °C) form a sink for the cesium flow, as described in section 5.1.1. A constant wall temperature is main-

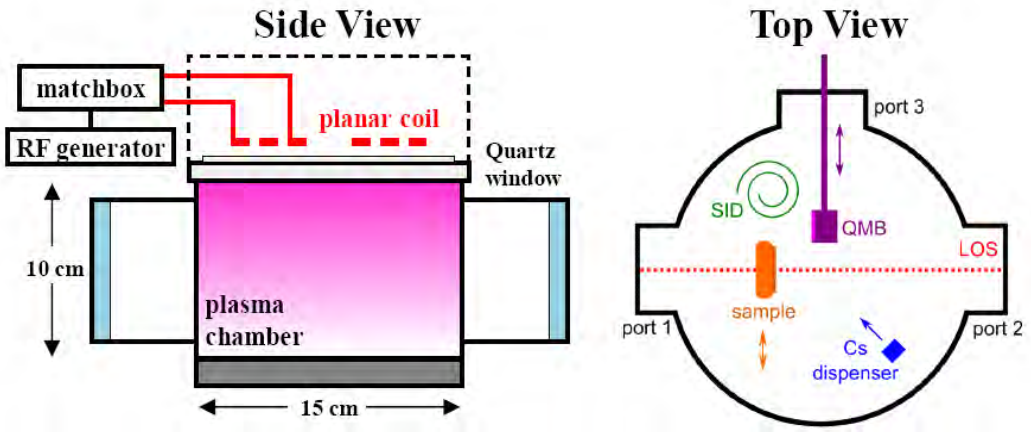


**Figure 4.7.:** Schematic side view (left) of the ICP plasma source used for basic cesium experiments. The setup of the different diagnostics, access ports and the cesium dispenser is given on the right.

tained by water cooling.
Several ports are available in order to attach cesium sources and diagnostic systems to the plasma source. The chamber is equipped with three removable quartz windows and an easily exchangeable bottom plate with additional ports. This allows a versatile arrangement of diagnostics, samples, and cesium sources as indicated in figure 4.7. The experiment setup at the University of Augsburg is called ICP experiment in this thesis.
In addition to spectroscopic methods, a surface ionization detector (SID) and a movable quartz microbalance (QMB) are available for cesium detection. A cesium dispenser, as described in section 4.2.7, and temperature stabilized metal samples can be mounted inside the system to carry out systematic experiments. Different types of cesium sources can be attached to one of the available ports.

### 4.2.2. Quartz Microbalance

The growth and desorption of cesium layers are both important aspects for understanding the dynamics of cesium inside a negative-ion source. A quartz microbalance system was used to measure the number of adsorbed cesium layers on a quartz detector plate, being covered with gold. The deposited cesium forms CsAu, ensuring the total absorption of the intercepted cesium and a negligible desorption rate from the microbalance [KF07].

A standard microbalance system uses a sensor that is based on a single quartz plate. Two quartz plates are used in order to increase the stability of the measurement. This method reduces external influences that are not related to the cesium coverage, for example temperature effects.
One quartz plate is exposed to the cesium flow, while the other one is used as a reference. The resonance frequency difference between the two quartz plates that are excited to resonant oscillations by an ac-voltage is measured. The second quartz plate is located inside the microbalance and maintains its original resonance frequency.
The frequency difference for a microbalance is given by [Sau59]:

$$\Delta f = -S_{\mathrm{f}} \frac{\Delta m}{A}. \tag{4.4}$$

The Sauerbrey constant $S_{\mathrm{f}} = 0.04844$ Hz cm$^2$/ng includes the material specific properties of the quartz plate. A frequency difference of $\Delta f = -4.995$ Hz is calculated for the area of the quartz plate of $A = 1$ cm$^2$ and a mass difference $\Delta m$ that corresponds to a single cesium monolayer on the exposed quartz plate. Therefore, the microbalance system is able to measure the amount of cesium on the detector without calibration making the microbalance perfectly suited to measure the desorption flux from a cesiated sample. However, the measurement is limited to a maximum cesium coverage on the detector plate, which causes a strong damping of the resonance frequency. This makes a further measurement impossible and a cleaning of the sensor is necessary.
Thus, the microbalance system is not suited for the monitoring of a high cesium flux over a long time period, as required for the monitoring of cesium sources that are operated over a period of several weeks. The use of a cesium diagnostic with high detector temperatures (several 100 °C) is a possible way to overcome this problem. As a consequence of temperature generated frequency instabilities, it is impossible to operate the microbalance at these high temperatures. This is possible by using surface ionization detection.

### 4.2.3. Surface Ionization Detector

A surface ionization detector that is also known as Langmuir-Taylor detector [Tay29] was designed and tested. It is a very robust device that permits a precise measurement of atomic beams in a vacuum environment.
The detection principle is based on the surface ionization process and makes use of the large ionization probability of ground state atoms from elements with a

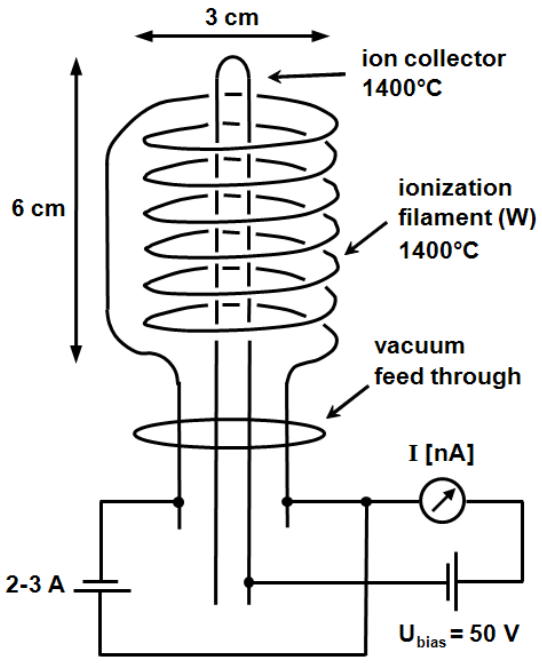


**Figure 4.8.:** Schematic illustration of a surface ionization detector (SID) consisting of the tungsten ionization filament and the biased ion collector.

low ionization potential. Therefore, this type of detector is mostly used for alkali atoms, such as cesium. In particular cesium has the lowest ionization potential ($\Phi_{\mathrm{Ion}} = 3.89$ eV) of all elements [Lid07].

A hot metal filament made from a high work function material (tungsten) is placed directly in the cesium flow. Cesium atoms, sticking on the filament for a short time, undergo a surface ionization process and leave the filament as cesium ions. A bias voltage is used to drain the cesium ions from the filament onto a collector cathode that is heated to the same temperature as the filament in order to avoid a perturbation of the measurement by ad- and desorption of cesium from the detector. The drain current within the range of several hundred nA is measured between the filament and collector. A schematic illustration of the surface ionization detector system is shown in figure 4.8.

The ionization detector allows a time-resolved detection of the number of atoms per second in the cesium beam. The detected ion current strongly depends on the surface conditions of the ionization filament. Surface ionization of a cesium atom takes place when the ionization potential $\Phi_{\mathrm{Ion}}$ of the atom is comparable to the work function $\phi$ of the tungsten filament at a surface temperature $T$. The atom is re-emitted from the surface as a positive $Cs^+$ ion with a probability $P^+$ and as a neutral atom with the probability $1 - P^+$. The probability $P^+$ is given

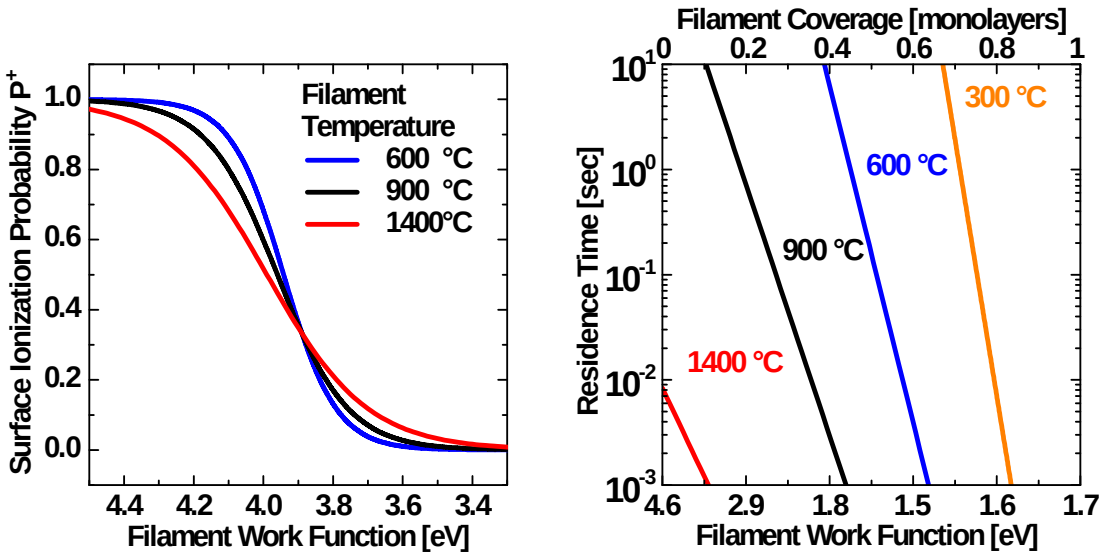


**Figure 4.9.:** Cesium ionization probability (left hand side) and mean residence time of cesium (right hand side) on the hot filament of the SID versus the work function and coverage of the filament metal for a range of relevant temperatures.

by the Saha-Langmuir law:

$$P^+ = \frac{1}{1 + \frac{g^0}{g^+} \exp(\frac{\Phi_{\mathrm{Ion}} - \phi}{k_\mathrm{b}\, T})}, \tag{4.5}$$

where $g^0$, $g^+$ are statistical weights of the ionic and atomic ground state. While the work function of a pure tungsten surface is 4.55 eV (see section 4.1), cesium is known to lower the work function of a surface significantly.

Figure 4.9 shows the dependence of the ionization probability of cesium on the filament work function for relevant filament temperatures. The work function dependence on the cesium coverage for polycrystalline tungsten was taken from [TL33]. Low filament temperatures result in a low work function of the filament itself by the formation of a permanent cesium coating according to the calculations presented in figure 4.9. Temperatures below 1000 °C create a cesium layer on the filament with a work function below 2.9 eV and a residence time within the range of seconds, which results in a negligible ionization probability. A filament temperature of 1400 °C is necessary to reduce the residence time to 0.01 sec in order to obtain a clean tungsten surface so that a high work function of the filament surface and a high ionization probability of cesium can be ensured. In doing so, a reliable and reproducible operation of the detector can be provided.

The surface ionization detector is a powerful device to measure intense cesium flows over a long time, because the absorbed cesium is evaporated by the hot

surfaces within short times. This is ideal for testing the operation of cesium sources. Nevertheless, the ionization detector is not suitable for measurements in temperature-sensitive situations, such as the measurement of the desorption flux from cesium-covered metal surfaces. Perturbation effects caused by the radiative heat flux from the hot filament on the sample surface will influence the measurement. Due to the complex nature of the ionization detector measurement by the dependence on the filament geometry, a calibration by a cesium source of a known flux is required.
The use of the ionization detector is, however, restricted to measurements in a vacuum environment, as a finite resistance is created between filament and the biased collector in a plasma environment. Thus, the ionization detector measurement is disturbed by the electron or ion currents present during the discharge.

### 4.2.4. Optical Emission Spectroscopy

Optical emission spectroscopy (OES) is a non-perturbative method that measures the spectral intensity distribution of the radiation emitted from a specific plasma volume. It can be used to determine the densities of species in a plasma. The excitation of atomic cesium from the ground state can take place when collisions with electrons occur or when photons are absorbed according to the following processes:

$$\begin{aligned} \mathrm{Cs(6s)} + \mathrm{e}^- &\longrightarrow \mathrm{Cs(6p)} + \mathrm{e}^-, \\ \mathrm{Cs(6s)} + h\nu &\longrightarrow \mathrm{Cs(6p)}. \end{aligned} \tag{4.6}$$

De-excitation from the state $i = 6\mathrm{p}$ to the ground state $k = 6\mathrm{s}$ can take place by spontaneous emission of light at $\lambda = 852.1$ nm. De-excitation by electron collisions is not important for the given case due to the relatively low electron density ($n_\mathrm{e} < 10^{18}$ m$^{-3}$). The intensity of the emitted radiation $\varepsilon_{ik}$ is given by the population density $n_\mathrm{i}$ of the state 6p and the corresponding Einstein coefficient $A_{ik}$, which is the probability for de-excitation by spontaneous emission:

$$\varepsilon_{ik} = n_i \, A_{ik}. \tag{4.7}$$

The OES gives a line-of-sight integrated signal of the emitted radiation at the specific wavelength. An optical fiber is used to transmit light to the spectrometer that, in turn, uses a diffraction grating to separate the different wavelengths of the light beam and then detects the spectrum with a CCD-chip[1].

[1] CCD: charge coupled device.

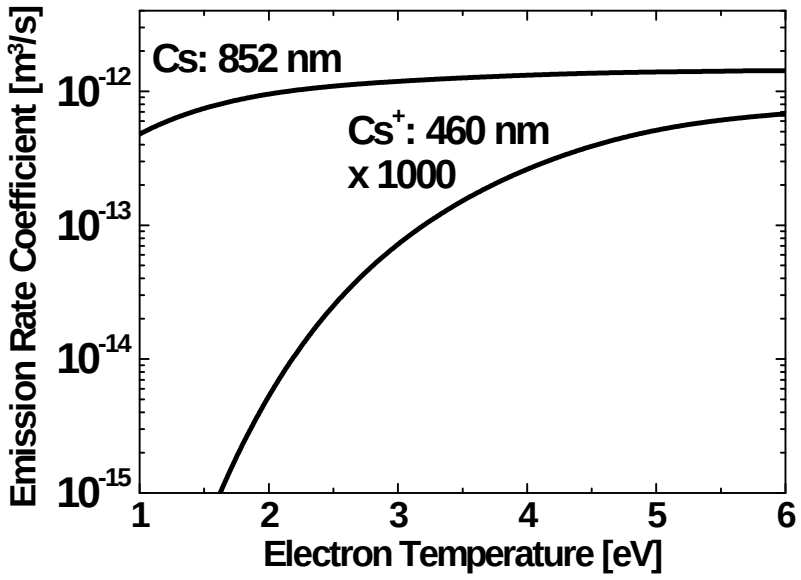


**Figure 4.10.:** Emission rate coefficients from the line of neutral cesium at 852 nm and from the line of singly-ionized cesium at 460 nm (scaled by a factor of 1000).

The population density of the excited state can then be calculated by applying equation (4.7) to the measured line intensity and using a population model (thermodynamic equilibrium, corona model, collision-radiative-model).
For example, the corona model considers only the excitation from the ground state by electron collisions, which are balanced by the spontaneous emission. This simplification is valid for very low electron densities only ($n_\mathrm{e} \lesssim 10^{17}$ m$^{-3}$) depending on the investigated particle species. The excitation by collisions with electrons gives the following intensity of emitted radiation:

$$\varepsilon_\mathrm{Cs} = \varepsilon_{ik} = n_k n_\mathrm{e} X^\mathrm{Cs}_\mathrm{eff,em}\left(T_\mathrm{e}, n_\mathrm{e}, \ldots\right), \tag{4.8}$$

where $X^\mathrm{Cs}_\mathrm{eff,em}$ is the effective emission rate coefficient for the radiative transitions by this process at the electron temperature $T_\mathrm{e}$ and density $n_\mathrm{e}$ [FFF$^+$06].
The line emission coefficient $\varepsilon_\mathrm{Cs}$ depends in the first order only on the electron density and temperature. Hence, the emission coefficient depends on the plasma parameters that may change during a discharge or between the pulses. These dependences can be eliminated by dividing the emission coefficient $\varepsilon_\mathrm{Cs}$ for the line of neutral cesium at 852 nm by the corresponding emission coefficient $\varepsilon_{\mathrm{H}_\beta}$ of the Balmer line $\mathrm{H}_\beta$. The electron densities chancel each other out while the dependence on the electron temperature is diminished significantly by dividing the two respective effective rate coefficients. Hence, the line ratio:

$$\frac{\varepsilon_{\mathrm{Cs}}}{\varepsilon_{\mathrm{H}_\beta}} = \frac{n_{\mathrm{Cs}} \not{\eta}_{\mathrm{e}} X^{\mathrm{Cs}}_{\mathrm{eff,em}}}{n_{\mathrm{H}} \not{\eta}_{\mathrm{e}} X^{\mathrm{H}_\beta}_{\mathrm{eff,em}}} \tag{4.9}$$

is used in order to evaluate an estimate of the cesium signal for the temperature evolution of the cesium density on the plasma volume. The variable $X^{\mathrm{H}_\beta}_{\mathrm{eff,em}}$ describes the corresponding effective rate coefficient for $\mathrm{H}_\beta$ and $n_{\mathrm{H}}$ the density of atomic hydrogen.
Figure 4.10 shows the emission rate coefficients from a line of neutral cesium at 852 nm and from the line of singly-ionized cesium at 460 nm, taken from [FFF+06]. According to figure 4.10, the rate coefficient for emission from cesium ions is 3 - 5 orders of magnitude lower than the one from the neutral cesium line, which depends on the electron temperature. This results directly in less radiation from the ionic line at 460 nm than for the atomic line at 852 nm for the same conditions, even if a high amount of cesium is ionized. Thus, depending on the cesium conditions within the ion source, ionic cesium is below the detection limit of the optical emission spectroscopy.

### 4.2.5. Work Function

The work function of a cesium-covered surface is an important parameter for the conversion yield in negative ion sources, as described in section 3.1.1. The work function of cesium-coated molybdenum samples, inserted in the ICP experiment, is measured utilizing the photoelectric effect. The molybdenum samples were cut from the same material that is used for the plasma grid used at the IPP test facilities. Figure 4.11 shows a schematic view of the experimental setup. A time resolved measurement of the work function is performed exposing the sample to a cesium flux, while monitoring the photocurrent generated by UV-irradiation.
Photons of a particular wavelength are produced by a high power white-light mercury vapor lamp and interference filters. A filter system for wavelengths between 239 nm and 405 nm is used to select a specified photon energy.
Electrons are released from the sample by photons with a certain energy $h\nu$, if the work function is below the photon energy:

$$h\nu = \phi + \frac{1}{2} m_{\mathrm{e}} v_{\mathrm{e}}^2, \tag{4.10}$$

where $\phi$ denotes the work function of the sample and $\frac{1}{2} m_{\mathrm{e}} v_{\mathrm{e}}^2$ the kinetic energy of the released electrons. A bias voltage is applied to the chamber and the sample

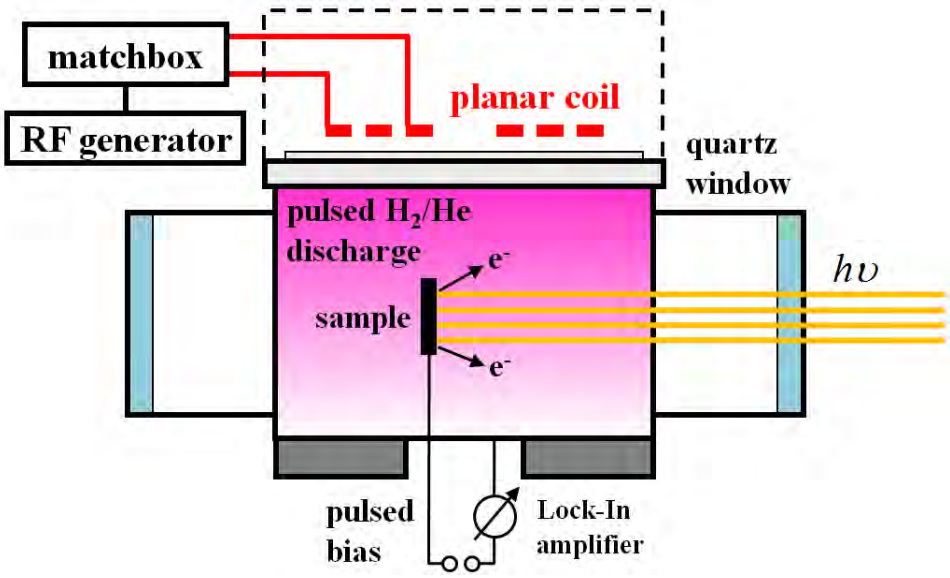


**Figure 4.11.:** Experimental setup to measure the work function of an UV-irradiated sample in a pulsed plasma environment by the photoelectric effect.

that is electrically isolated from the chamber walls in order to drain the photocurrent.

In the experiment, the intensity of the photon flux depends on the photon energy. This is caused by the transmission properties of the filters for a specific wavelength and the spectrum of the lamp. Thus, a calibration by the intensity of each filter and lamp is required. The dependence of the (calibrated) photocurrent $I$ on the photon energy $h\nu$ is analyzed by the Fowler method [Fow31]. A fitting formula with the work function $\phi$ as a fitting parameter, is applied:

$$\begin{aligned} \ln\left(\frac{I}{T^2}\right) &= C + \ln\left(\Lambda\left(\frac{h\nu-\phi}{k_b\,T}\right)\right), \\ \Lambda(x) &= \frac{\pi^2}{6} + \frac{x^2}{2} - \left[\frac{\exp(-x)}{1^1} - \frac{\exp(-2x)}{2^2} + \frac{\exp(-3x)}{3^2}\right], \end{aligned} \tag{4.11}$$

where $T$ is the temperature of the sample and $C$ is a constant. A detailed overview on the experimental setup of the work function measurement in a vacuum environment is given in [KF07].

A plasma environment is required to generate negative hydrogen ions from a low work function surface. Thus, the relevant measurements of the work function of a converter surface will have to take place during plasma operation. The resulting current on the biased sample during a discharge is several orders of magnitude higher than the photocurrent from the irradiated sample. Therefore, no work function measurement is possible during plasma exposition of the surface.

Hence, the work function setup was enhanced by operating the plasma source and the sample bias in a pulsed mode. This allows the measurement of the photocurrent from the irradiated sample in the plasma-off times with a Lock-In amplifier at quasi-continuous plasma conditions. The measurement circuit for the work function measurement setup during pulsed plasma operation is given in detail in appendix A. A pulse frequency between 16.5 Hz and 74 Hz is necessary in order to provide a sufficiently long time interval $\Delta t$ for the measurement. The admixture of helium to the hydrogen plasma is required in order to obtain an improved stability of the discharge in pulsed operation. However, helium is chemically inert and, thus, does not affect the chemical processes on the surface.
Two different types of cesium sources are used for cesium release within the scope of this work. One way to accomplish cesium release is by thermal desorption from a reservoir of pure cesium. The cesium flux from this cesium evaporation oven is regulated by adjusting the temperature of the liquid cesium. Due to the sensitivity of the evaporation rate on the temperature of the vessel that contains the cesium supply, a control of the injection rate is possible.

### 4.2.6. Cesium Evaporation Oven

Liquid cesium based systems are commonly used for cesium injection in negative-ion sources for neutral beam applications [SFF$^+$06][T$^+$00][K$^+$00][T$^+$98]. A schematic overview of the IPP cesium evaporation oven is given by figure 4.12. The oven consists of three components with individual temperature control systems: 1) the body (blue), 2) the sealed glass-ampoules containing 1000 mg of cesium (yellow) and 3) the conduction pipe (red). Component temperatures of up to 300 °C are obtained by heating elements. Temperature stability can be ensured by a system of thermocouples and feedback circuits. A new configuration with additional heating elements (red arrows in figure 4.12) at the end of the body was tested within the scope of this work.
Pure cesium is irreversibly released by breaking the glass of the ampoule from outside. Due to gravity, the liquid cesium ($T_{\mathrm{melt}} = 28.5$ °C) flows from the ampoule into the body, and cesium evaporation then starts depending on the temperature conditions of the system. The cesium vapor pressure in the body increases and a cesium flow through a set of three nozzles at the head of the conduction pipe into the expansion region of the ion source is generated.
The cesium flow through the conduction pipe is proportional to the evaporation rate of the liquid reservoir regulating the vapor pressure inside the cesium oven.

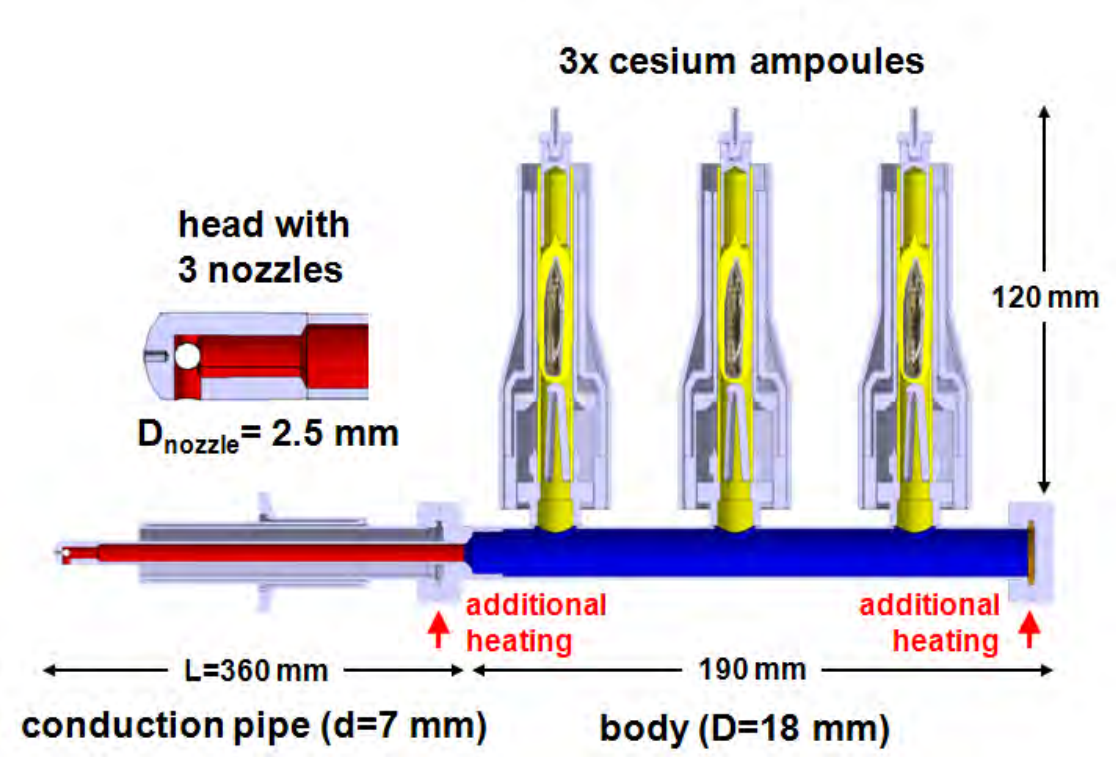


**Figure 4.12.:** Schematic drawing of the evaporation oven, developed at IPP, for cesium injection at the negative-ion source test facilities. Additional heating elements at the ends of the body were tested within the scope of the thesis. These are indicated by red arrows in the drawing.

This evaporation rate is controlled by the temperature of coldest spot within the total system, where the cesium from the ampoules condenses. The body that is directly connected to the ampoules was chosen to be the cold-spot of the system and is used for flow control. With the feedback system it is possible to set the body to a specific temperature, while the pipe and the ampoules are kept at higher temperatures ($\Delta T$ = 20 °C) to prevent cesium accumulation on these components and the associated uncontrolled evaporation. Depending on the desired cesium flow, a body temperature between 110 °C - 220 °C can be set. The response time of the cesium flow control is determined by the thermal conductivity and heat capacity of the components of the system.
The cesium evaporation oven is connected to the vacuum of the ion source without a valve system that could act as a cold-spot. Stopping the cesium flow into the ion source is done by lowering the temperatures of all components as described in section 5.3. During inactive phases of the ion source, such as overnight, all temperatures of the oven components are decreased to room temperature. How-

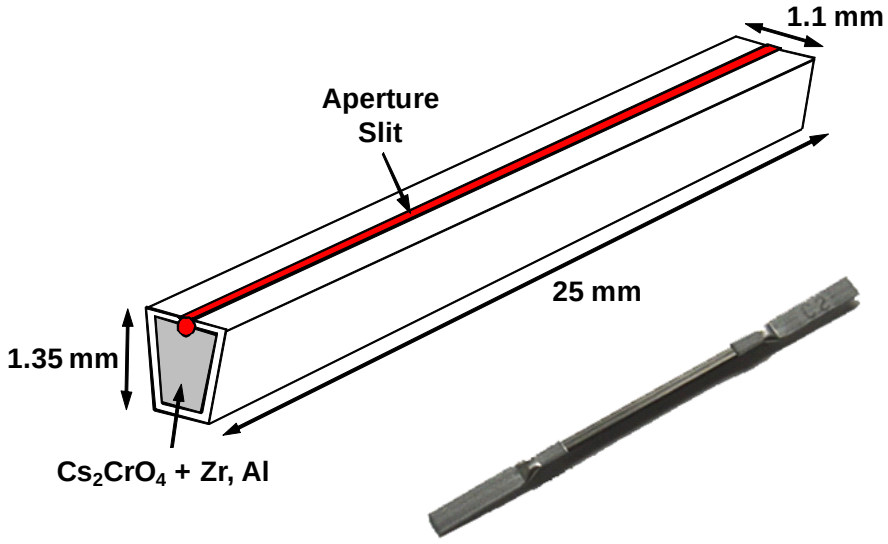


**Figure 4.13.:** Schematic picture and photograph of a SAES cesium dispenser, containing cesium chromate, equivalent to a release of 10 mg of pure cesium.

ever, the missing of a valve system has disadvantages. Besides the vulnerability of the liquid cesium to impurities from the test facilities that can enter the oven during the night, it is required to deplete the cesium in the oven before the oven can be removed from a particular vacuum system. Cesium that is exposed to atmospheric pressure becomes chemically contaminated, which is also dangerous because of the explosion hazard.

### 4.2.7. Cesium Dispenser and Dispenser Oven

A different type of cesium source is the alkaline-metal dispenser that is commercially available from SAES[2]. Dispensers were developed in order to provide a controllable release of pure cesium, as it is required for the production of photocathodes [SPA09][SCF85].
The working principle of a dispenser is based on the release of cesium from the decomposition of a stable cesium compound by a reaction with a reducing agent. Dispensers were used to perform fundamental investigation of the properties of cesium and to test diagnostic systems within the scope of this work. Figure

[2]SAES Getters S.p.A., Viale Italia 77, 20020 Lainate (Milan), Italy.

4.13 shows a photograph and a schematic view of a commercial available cesium dispenser (Cs/NF/8/25/FT 10+10) containing an equivalent to 10 mg of pure cesium.
In contrast to liquid reservoir based systems, alkaline-metal dispensers do not contain pure cesium. A SAES dispenser contains cesium chromate $Cs_2CrO_4$ and the getter material ST 101, a mixture of zirconium and aluminium. This mixture is thermodynamically stable for temperatures below 500 °C. In the absence of the getter material ST 101, the $Cs_2CrO_4$ itself is stable and will not release cesium until nearly 1000 °C [SPA09]. The production and release of pure cesium starts at elevated temperatures according to the given reaction paths:

$$\begin{aligned} 4\,Cs_2CrO_4 + 5\,Zr &\longrightarrow 8\,Cs(g) + 5\,ZrO_2 + 2\,Cr_2O_3, \\ 6\,Cs_2CrO_4 + 10\,Al &\longrightarrow 12\,Cs(g) + 5\,Al_2O_3 + 3\,Cr_2O_3. \end{aligned} \tag{4.12}$$

Heating the dispenser housing generates the required temperature to initiate reaction (4.12). Regulation of the reaction and thus the cesium evaporation rate is possible by adjusting the current through the dispenser. Currents of the order of 6 - 7 A are typically used to operate the specified dispenser. It is necessary to activate the dispenser by applying a heating current of 3 A for several minutes before cesium is released.
Reactive species like $H_2O$ and $O_2$ are harmful to the ST 101 getter material, since they can form refractory compounds with Zr and Al. A vacuum environment is therefore necessary to store the dispensers. The angular distribution of the cesium flow from the slit of the dispenser is given by an equally distributed flow within an opening angle of 120° [PBB07].
Dispenser systems are used routinely for laboratory investigation of cesium properties and have proven their reliability and stability in small (several $cm^2$) negative-ion sources with mono-aperture extraction systems. For example, cesium dispensers are successfully applied on the negative-ion source front end of the SNS spallation neutron source at Oak Ridge National Laboratory [WSMK05].
In comparison to the evaporation oven containing liquid cesium, dispensers have many advantages, like their compact design and the chemical stability of the cesium compound in contrast to liquid cesium. These advantages are explained in more detail in section 5.3.2. Nevertheless, there are also disadvantages like the limited reservoir of cesium and the sensitivity to thermal loads during plasma exposure. The corresponding heat load is capable of increasing the dispenser temperature, which interferes with the temperature control by the applied heating current. This effect can result in a quick depletion of the total cesium inventory

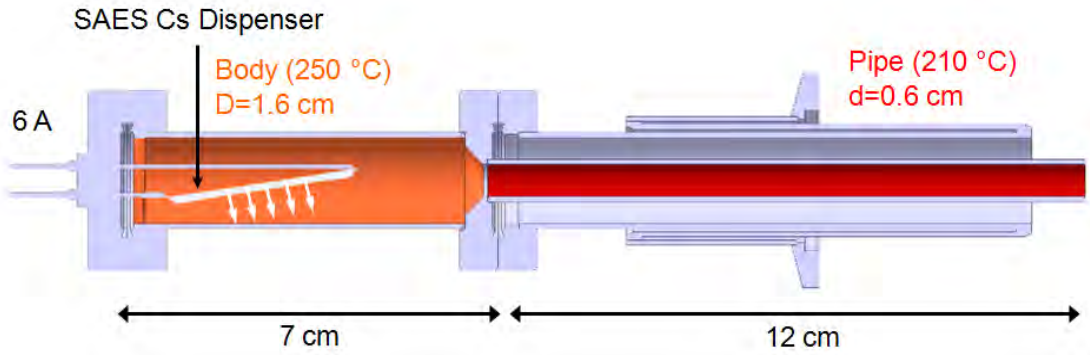


**Figure 4.14.:** Schematic drawing of a dispenser-based cesium oven. The dispenser is located in the body (orange) of the system. A heating current of 6 - 7 A is used to create the cesium release. The pipe (red) is connected to the vacuum system of the experiment.

of the dispenser.

The application of dispensers at the IPP negative-ion source test facilities is under discussion for the future either by a direct mounting in the ion source chamber (see section 6.3.2) or by the replacement of the cesium ampoules in the cesium evaporation oven, as described in the following. A prototype for a dispenser-based cesium oven (cesium dispenser oven) was designed and constructed within the scope of this work in order to find ways for advanced cesium control. The oven housing is necessary to protect the dispenser from the heat load by the plasma that, as described above, creates uncontrolled cesium release from the dispenser. This dispenser-based cesium oven is the first step towards the advanced engineering of this concept for the future use at the IPP negative-ion source test facilities. However, the dispenser oven prototype will be a small-scale cesium injection system that can be used as a stable and reliable cesium source for cesium experiments at the University of Augsburg. The use of the dispenser oven is especially interesting for experiments during discharge phases where the operation of the unprotected dispenser is disturbed by thermal load in the plasma. A flexible use of liquid reservoir based systems is limited by the high amount of cesium (1000 mg) in an ampoule, which has to be depleted before the oven can be opened safely.

Figure 4.14 shows a CAD drawing of this dispenser oven. The dispenser is located in the body of the oven that is heated to a temperature of 250 °C by heating circuits in order to avoid cesium accumulation and uncontrolled thermal desorption from the walls of the system. Cesium transport into the chamber of the associated experiment takes place through the connecting pipe that is heated to a temperature of 210 °C.

The cesium release is solely controlled by the heating current through the dispenser. Therefore, the temperatures of the oven components are kept permanently at the specified temperature during the operational period of the system. The chosen temperatures are significantly higher than in the evaporation oven in order to avoid cesium condensation and re-evaporation effects.

## 4.3. Cesium Transport Code CsFlow3D

Numerical simulations are essential tools to improve the understanding of cesium transport processes within the negative-ion sources. Model calculations can help to optimize the operation of the ion source and contribute to the development of new ion sources and associated components.
The test-particle Monte Carlo algorithm is an important method to study macroscopic transport phenomena. It relies on the computation of large ensembles of independent test particles within a specified particle background for a static electric and magnetic field. This method is applicable for systems, where the interaction between the particles of the transported species can be neglected. Hence, the method is suitable to compute the transport of minority species through a background of field particles at a high density with respect to the density of the test particles. At the parameters of negative-ion sources, this condition is valid for the transport of neutral and ionic cesium, but also for the transport of negative hydrogen ions [GWF09].
An extension to the consideration of particle-interaction, related to charge-generated forces, is done by the Particle-In-Cell (PIC) algorithm [BL91][HE88] that treats a large number of interacting, charged particles simultaneously. The electric forces, generated by the space charge of the particles itself, are projected onto a computational grid at each time step to compute the particle positions and velocities in the next time step. However, PIC algorithms have high demands on computation time and memory. This limits their application for the plasma parameters of the negative-ion source to a small computation domain (several cm). Simulating the plasma sheath that is of the order of several Debye lengths requires the consideration of the described particle interaction.
This is done by the 1D3V PIC-code BACON [WGF09] that was developed at the IPP to improve the understanding of the plasma sheath in negative-ion sources. In order to simulate the transport of neutral and atomic cesium, a computational domain of the size of the total negative-ion source is necessary. The applica-

tion of a PIC-based algorithm for this type of cesium transport problems would exceed the limits of today's computation power by far, while probabilistic particle-transport codes can be applied at more reasonable computational demands.
The test-particle Monte Carlo method has been applied successfully to simulate the impurity transport in Tokamak research [MCT+08][KPW+00]. The latter reference describes the ERO code that is used to investigate the erosion and deposition processes in the vicinity of a limiter in the boundary layer of a magnetically confined fusion plasma. Nevertheless, the ERO code is not applicable to model the cesium transport in negative-ion sources: the transport simulation of cesium has to consider a strong temporal variation of the flow conditions, which is a consequence of alternating hydrogen pressure conditions in the negative-ion source for plasma-on and off phases. This results in an alternation of transport regimes for cesium and cesium ions, which is not considered in a Tokamak transport code.
No simulation for the transport of cesium during the vacuum and discharge phases of negative-ion sources has been available in scientific literature. Therefore, the Monte Carlo based transport code CsFlow3D, considering the specific conditions within negative-ion sources, was newly developed and applied to study cesium transport processes.

## 4.3.1. Test-particle Monte Carlo Method

### Transport Equation

CsFlow3D uses the test-particle Monte Carlo algorithm and traces a significant amount ($10^4$ per cm$^2$) of independent test particles through the electric and magnetic fields of the ion source, considering collisions with a predefined background of field particles at a given density and velocity distribution. An isotropic Maxwell distribution was used for the temperature distribution of all field particles.
The species of the test particle is subject to changes during the trajectory computation due to the ionization of cesium. Thus, different force terms have to be considered for the transport computation.
In case of atomic cesium, this force is solely given by a collision term, while the simulation of ionic cesium requires the consideration of an additional Lorentz force term in order to consider the effect of electric and magnetic fields on the ion. The force $\vec{F}$ acting on a test particle with charge $q$ and mass $m$, located at position $\vec{r}$ with velocity $\vec{v}$, is given by a combination of the Lorentz force (for the

electric field $\vec{E}(\vec{r})$ and the magnetic field $\vec{B}(\vec{r})$) and the collision term $\vec{F}_{\mathrm{Col}}$:

$$\vec{F}(\vec{r},\vec{v}) = q\left(\vec{E}(\vec{r}) + \vec{v}\times\vec{B}(\vec{r})\right) + \vec{F}_{\mathrm{Col}}(\vec{r},\vec{v}). \tag{4.13}$$

The collision term is determined by the local density $n_i(\vec{r})$ and temperature $T_i(\vec{r})$ of the species of the field particles involved in the collision process:

$$\vec{F}_{\mathrm{Col}}(\vec{r},\vec{v}) = \vec{F}_{\mathrm{Col}}(n_1(\vec{r}),T_1(\vec{r})...n_N(\vec{r}),T_N(\vec{r}),\vec{v}), \tag{4.14}$$

for $N$ different species of field particles. The corresponding trajectory equation is solved by a combination of a time-step based integration method and a Monte Carlo collision algorithm. The determination of the parameter fields $\vec{E}(\vec{r})$, $\vec{B}(\vec{r})$, $n_i(\vec{r})$ and $T_i(\vec{r})$ for the test-particle computation is done by a 3D linear interpolation method. A description of the corresponding numerical methods for the time-step based integration method and for the interpolation method is available in appendix B. Contour plots of computed magnetic fields within the IPP prototype source are given in the appendix C and in [GWF09].
An overview of the probabilistic treatment of the inter-particle collision term $\vec{F}_{\mathrm{Col}}(\vec{r},\vec{v})$ is given in the following section.

### Collision Treatment

Collision processes can be characterized by the collision frequency $\omega_i$ that depends on the density $n_i(\vec{r})$ of the field particle and the distribution of the relative velocity $\Delta\vec{v}_i$ of test and field particle. The frequency for a collision with field particles with a temperature $T_i(\vec{r})$ is determined by the mean value of the product of the collision cross-section $\sigma(\Delta\vec{v}_i)$ and the relative velocity $\Delta\vec{v}_i$ for a Maxwellian velocity distribution of $\vec{v}^{\,i}_{\mathrm{Field}}$ with $\Delta v_i = \|\vec{v}^{\,i}_{\mathrm{Field}} - \vec{v}\|$, multiplied by the density of field particles $n_i(\vec{r})$:

$$\omega_i = n_i(\vec{r})\left\langle\sigma(\Delta v_i)\ \Delta v_i\right\rangle_{\mathrm{Maxwell},T_i}. \tag{4.15}$$

A distinction between short-range collisions and long-range collisions is required for the Monte Carlo calculation. The use of special methods to simulate long-range collision is necessary to consider Coulomb collisions between charged particles because of the long interaction length of the Coulomb potential. Other processes, such as elastic collisions between neutral particles, have an interaction length within the order of the diameter of the atom or molecule and can therefore be treated by short-range collisions methods, described in the following section.

**Short-Range Collisions** Short-range collisions are considered by a collision probability $P^i_{\mathrm{col}}$ that determines if a collision process takes place during the time step $\Delta t$. This probability is determined by the path-length-estimator method [Bir91]:

$$P^i_{\mathrm{col}} = 1 - e^{-\omega_i \Delta t}. \tag{4.16}$$

A normally distributed random number RND $\in (0, 1)$ is used to decide whether the specified collision process takes place during the time step $\Delta t$. The collision takes place if the condition

$$\mathrm{RND} < P^i_{\mathrm{col}}, \tag{4.17}$$

is satisfied. This comparison has to be performed for each particle at each time step.

If a collision takes place, the post-collisional velocities of the test and field particle are determined according to a Monte Carlo collision treatment [MSD93]. The relative velocity $\Delta\vec{v}$ of test and field particle is rotated according to a normal probability distribution. This rotation is specified by the scattering angles $\theta$ and $\phi$ as illustrated by figure 4.15. By this way, the vector $\Delta\vec{v}_{\mathrm{rot}} = \Delta\vec{v}(t+\Delta t) - \Delta\vec{v}(t)$ is determined that is defined as the difference of the relative velocity vectors before and after the collision. The determination of the post collision velocities $v\,(t + \Delta t)$ and $v_{\mathrm{Field}}\,(t + \Delta t)$ is given by the following equations:

$$\begin{aligned} v\,(t + \Delta t) &= v\,(t) + \frac{m_{\mathrm{Field}}}{m_{\mathrm{Field}} + m}\Delta\vec{v}_{\mathrm{rot}}, \\ v_{\mathrm{Field}}\,(t + \Delta t) &= v_{\mathrm{Field}}\,(t) - \frac{m}{m + m_{\mathrm{Field}}}\Delta\vec{v}_{\mathrm{rot}}. \end{aligned} \tag{4.18}$$

It can be shown easily that momentum and energy of the binary system is not changed by applying formula (4.18).

A different treatment is, however, necessary for Coulomb collisions that have a long interaction length.

**Long-Range Coulomb Collisions** Long-range Coulomb collisions between charged test particles and charged field particles are taken into account for every time step of the trajectory computation. A cumulative deviation by frequent small angle Coulomb scattering is considered by a Gaussian probability distribution of $\theta$ and a normal distribution of $\phi$, using the collision frequency $\omega$ for Coulomb collisions as half width of the Gaussian distribution [MSD93]:

$$\theta = \left[-2\,\omega\,\Delta t\,\ln\left(1 - \mathrm{RND}_1\right)\right]^{1/2}, \tag{4.19}$$

$$\phi = 2\pi\,\mathrm{RND}_2, \tag{4.20}$$

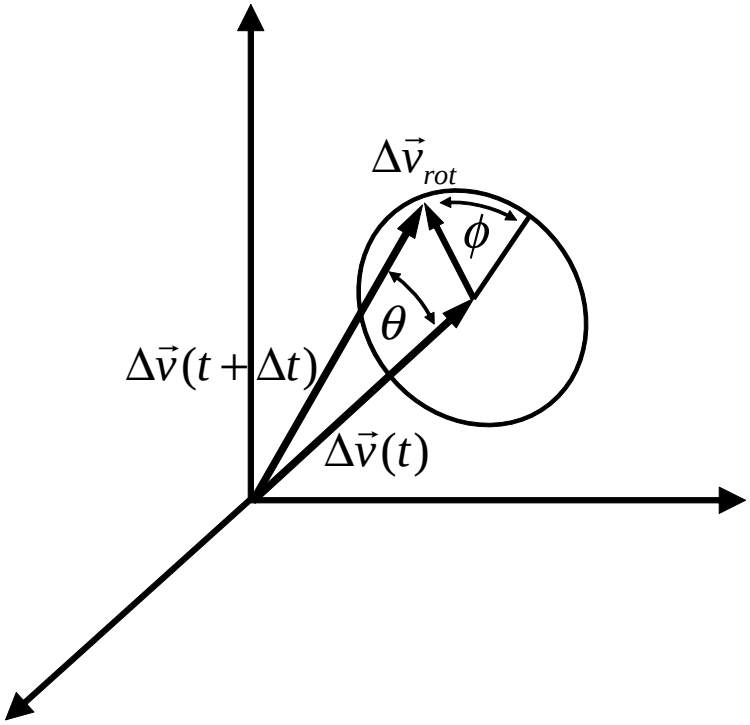


**Figure 4.15.:** *Schematic view of the rotation of the vector of the relative particle velocity $\Delta\vec{v}(t)$ according to the collision angle $\theta$ and polar angle $\phi$ to the post-collision velocity vector $\Delta\vec{v}(t+\Delta t)$.*

where $RND_1$ and $RND_2$ denote two independent random numbers with a normal distribution.

## 4.3.2. Flow Regimes

The transport of atomic and ionic cesium within the negative-ion source takes place in two different flow regimes. This is a consequence of the different hydrogen pressure conditions during the discharge and the vacuum phases between the plasma pulses.

### Vacuum or Plasma-Off Phase

A residual-gas pressure of $p \approx 10^{-3}$ - $10^{-4}$ Pa is established in the plasma-off phases. An estimation of a purely hydrogenic background density with the corresponding Cs-$H_2$ collision cross-section, described in section 4.3.3, results in

a mean-free path length $\Lambda$ of cesium within the range of several meters. Thus, a free molecular flow regime is obtained, where the atomic cesium test particles follow straight lines and the transport is determined by the geometry of the ion source.

#### Discharge or Plasma-On Phase

A hydrogen pressure of $p_{H_2} \approx 0.3$ Pa is established during the discharge, which results in a change of the flow conditions. The collision cross-section of the $Cs/Cs^+$-$H_2$ systems yields a mean free path length $\Lambda$ below 1 cm and the previously described collision processes of Cs and $Cs^+$ with $H_2$, $H^+$ and $e^-$ have to be considered.
An overview of the collision processes of atomic and ionic cesium with background gas and plasma field particles, implemented in CsFlow3D, is given in the following section.

### 4.3.3. Collision Processes

#### Collisions of Cesium with the $H_2$ Background Gas

Atomic and ionic cesium will undergo elastic collisions with the hydrogen background gas - the field-particle species with the highest density within the negative-ion source. A constant and homogeneous molecular hydrogen density of $n_{H_2} = 5\text{x}10^{19}$ $m^{-3}$ with a gas temperature of $T_{H_2} = 930$ °C during the discharge phase was used for the cesium-transport simulation [FFF+06][FW06]. The collision cross-section of cesium with the hydrogen background depends whether cesium is in a neutral or ionic state:

**Elastic Collisions of $H_2$ with Cs** Neutral cesium can undergo the following elastic collision process with $H_2$:

$$Cs + H_2 \rightarrow H_2 + Cs. \tag{4.21}$$

The collision cross-section is determined by the van-der-Waals potential $V(r) \sim r^{-6}$ between the collisions partners. Quantum mechanical scattering theory [LL58] yields an inverse velocity dependence of the cross-section:

$$\sigma(v_{cm}) = \frac{C^{VdW}}{v_{cm}^{2/5}}, \tag{4.22}$$

where $C^{\mathrm{VdW}}$ is the interaction constant for the Cs-$H_2$ system, while $v_{\mathrm{cm}}$ is the relative velocity in the center-of-mass system. A detailed overview of the interaction constant for the van-der-Waals potential and the Cs-$H_2$ system is available in [RB59].

**Elastic Collisions of $H_2$ with $Cs^+$** Cesium ions, generated by electron impact ionization from neutral cesium, can undergo the following elastic collision process with $H_2$:

$$\mathrm{Cs}^+ + \mathrm{H}_2 \rightarrow \mathrm{H}_2 + \mathrm{Cs}^+. \tag{4.23}$$

The Langevin theory describes the interaction of a cesium ion with neutral hydrogen by a polarization of the hydrogen molecule. An induced dipole moment is created by this process [LL05]. The corresponding Langevin cross-section is given by:

$$\sigma\left(v_{\mathrm{cm}}\right) = \frac{C^{\mathrm{L}}}{v_{\mathrm{cm}}}, \tag{4.24}$$

where the interaction constant $C^{\mathrm{L}}$ is related to the polarizability of the $H_2$ molecule and is available from [Lid07].

### Collisions of Cesium with the Plasma Background

An important category of processes for the cesium transport are collisions of cesium neutrals and ions with the electrons and positive hydrogen ions. The effect of the magnetic filter field and the distance between the driver and the extraction region results in a spatially varying plasma parameter profile within the negative-ion source. This creates a decrease of the ion density $n_{\mathrm{H}^+}$ and electron density $n_{\mathrm{e}}$ from the range of $10^{18}$ m$^{-3}$ at the exit of the driver of the ion source to the range of $10^{17}$ m$^{-3}$ in the expansion region was observed [FFF$^+$06][FW06]. Furthermore, the electron temperature drops from about $T_{\mathrm{e}} = 20$ eV at the driver to a temperature of $T_{\mathrm{e}} < 1$ eV near the plasma grid [Die07].
The CsFlow3D code uses the approximation of a quasi-neutral plasma with axial-symmetric maps of plasma-particle densities and temperatures. An exponential decay in x-direction and a parabolic profile in the perpendicular yz-plane (see coordinate system in figure 3.9) of the plasma density and temperature was implemented. These maps were constructed on basis of experimental data of the hydrogen ion density $n_{\mathrm{H}^+}$ and electron temperature $T_{\mathrm{e}}$, taken from probe measurements [Die07][MDCK$^+$09][TBM04]. The electron temperatures were determined

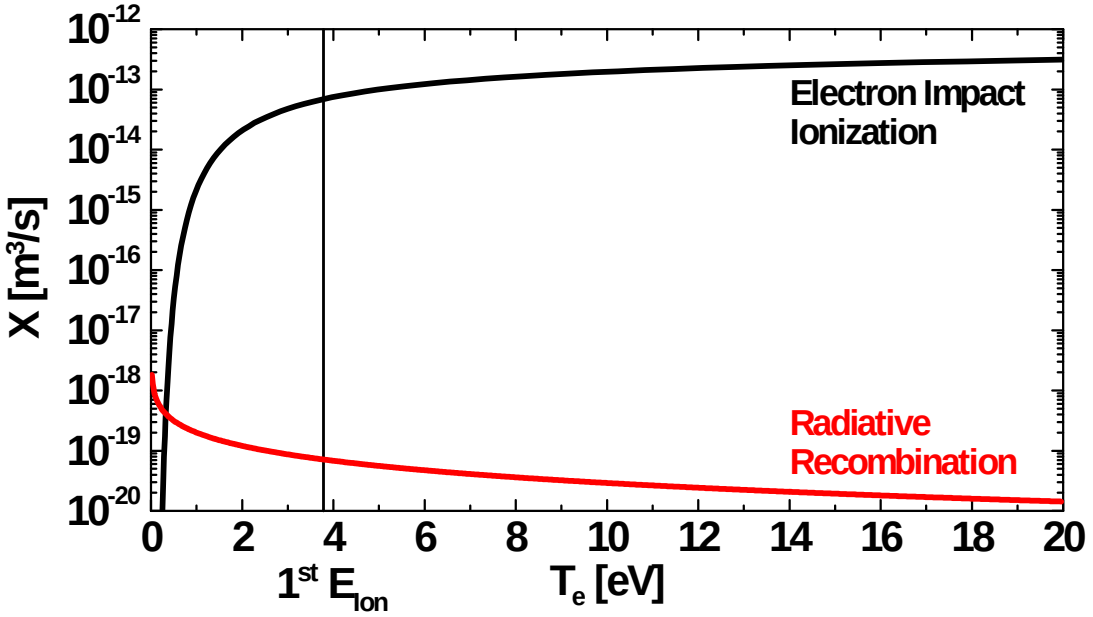


**Figure 4.16.:** Rate coefficient for electron impact ionization of neutral cesium and radiative recombination of cesium ions in dependence of the electron temperature.

by the application of the Boyd-Twiddy method [CD09]. Specific details regarding these field-particle data maps are given in appendix D.

**Ionization Collisions of Cs by $e^-$** Cesium has the lowest first ionization energy $\Phi_{\text{ion}} = 3.89$ eV of all elements [Lid07]. The ionization of neutral cesium by electron-impact collisions:

$$\text{Cs} + \text{e}^- \rightarrow \text{Cs}^+ + 2\text{e}^-, \tag{4.25}$$

is therefore expected to be a very efficient process. The rate coefficient $X_{\text{ion}} = \langle \sigma (v_{\text{e}})\ v_{\text{e}} \rangle_{\text{Maxwell}}$ for the electron-impact ionization was calculated from the experimentally determined cross-section in [ŁSK+06]. The collision frequency is then determined according to the electron density $n_{\text{e}}(\vec{r})$ and temperature $T_{\text{e}}(\vec{r})$ at the test particle position $\vec{r}$ according to formula 4.15.

Figure 4.16 shows the dependence of the electron-impact ionization rate coefficient on $T_{\text{e}}$. As a consequence of the Maxwell velocity distribution, a non-zero rate coefficient is obtained for electron temperatures below the first ionization energy. A strong decrease of $X_{\text{ion}}$ is observed for $T_{\text{e}} < \Phi_{\text{ion}}$. The inverse process of (4.25), the three-body recombination, is negligible for the electron densities within the negative-ion source.

The ionization energy of $Cs^+$ is $\Phi^+_{\text{ion}} = 23.16$ eV [Lid07] that is significantly higher than the first one. This is related to the stable Xe-like configuration of the cesium ion. As a consequence of the high second ionization energy, the formation of $Cs^{2+}$ ions is neglected for the transport calculations. This approximation is valid since cesium is predominantly released in the expansion region were the electron temperature is not high enough for an efficient second ionization. However, the implementation of the formation of $Cs^{2+}$ ions in CsFlow3D is possible if the corresponding cross-section is available.

**Radiative Recombination of $Cs^+$** Besides the already mentioned three-body recombination, cesium ions can be neutralized by the radiative recombination process:

$$Cs^+ + e^- \rightarrow Cs + h\nu. \tag{4.26}$$

The radiative recombination rate coefficient was calculated by an empirical formula [Hut02] considering the recombination to level $n$ of neutral cesium:

$$\langle \sigma_{\text{r,n}} v \rangle = 5.2 \times 10^{-20}\, Z \left(\frac{\Phi_n}{T_e}\right)^{3/2} \exp\left(\frac{\Phi_n}{T_e}\right) \text{Ei}\left(\frac{\Phi_n}{T_e}\right) \quad [\text{m}^3\,\text{s}^{-1}], \tag{4.27}$$

$$\text{Ei}(y) = \int_y^\infty \frac{\exp(-s)}{s} ds, \tag{4.28}$$

where $\Phi_n$ is the ionization energy of the $n^{\text{th}}$ level and $Z$ the ionic charge number. The total recombination rate coefficient is then determined by forming the sum of $\langle \sigma_{\text{r,n}} v \rangle$ over all levels.
Figure 4.16 shows the dependence of the rate coefficient on the electron temperature $T_e$. The rate coefficient increases especially for lower electron temperatures and values equivalent to the rate coefficient for ionization are obtained for very low electron temperatures of $T_e < 0.2$ eV. Nevertheless, the recombination coefficient is several orders of magnitude lower than the ionization coefficient for the electron temperatures within the negative-ion source, which is a consequence of the low ionization energy of cesium.

**Wall Recombination of $Cs^+$** Wall recombination is the most efficient mechanism of cesium neutralization for the parameters within the negative-ion source:

$$Cs^+ + e^-(\text{Wall}) \rightarrow Cs. \tag{4.29}$$

The process is treated rather simply in CsFlow3D. Cesium ions that hit an arbitrary wall within the ion source are converted to neutral cesium and re-emitted at a rate depending on the surface conditions.

**Elastic Coulomb Collisions of $Cs^+$ with $H_x^+$** As a consequence of the very low ionization energy of cesium and the corresponding large electron-impact ionization cross-section, a high fraction of ionic cesium is expected during the discharge phase. In this case Coulomb collisions with the positive hydrogen ions:

$$Cs^+ + H_x^+ \rightarrow H_x^+ + Cs^+, \tag{4.30}$$

will take place. The cross-section is given by the Coulomb-scattering theory:

$$\sigma\left(v_{\mathrm{cm}}\right) = \frac{C^{\mathrm{Cl}}}{v_{\mathrm{cm}}^4}, \tag{4.31}$$

where the parameter $C^{\mathrm{Cl}}$ depends on the mass of the collision partners [Hub06].

## 4.3.4. Cesium Source Terms

Several kinds of cesium source terms are considered in CsFlow3D during the vacuum phase and during the discharge. As described in section 4.2.6, elemental cesium is injected into the ion source permanently by a temperature-controlled evaporation oven. Measurements and calculations of the properties of the cesium flow from the evaporation oven that is used at the IPP test facilities are specified in section 5.3 and 6.1.1.
Additionally, other source terms, created by different physical processes during vacuum and plasma phases, contribute to the release of cesium within the negative-ion source.

### Thermal Desorption

The cesium covered surfaces of the ion source walls act as a source of cesium by thermal desorption. Experimental data of the wall desorption, depending on the temperature of the specific surface, were taken from measurements with the quartz microbalance done in parallel to the code development. An overview of this data is given in section 5.1.

### Plasma-induced Desorption

In addition to thermal desorption effects, cesium emission from the surfaces of the ion source are present during the discharge phases of the ion source:

**Physical Sputtering** Physical sputtering of cesium by positive hydrogen ions can create cesium desorption effects. The threshold energy $E_{\mathrm{th}}$ for physical sputtering is given by:

$$\begin{aligned} E_{\mathrm{th}} &= \frac{E_{\mathrm{b}}}{\gamma\,(1-\gamma)}, \\ \gamma &= \frac{4\,m_1\,m_2}{(m_1+m_2)^2}. \end{aligned} \tag{4.32}$$

The binding energy $E_{\mathrm{b}}$ of pure, metallic cesium multilayers is 0.6 eV (see section 4.1.2). While no metallic cesium is expected to accumulate on the walls of the ion source and more stable cesium compounds are formed instead, an estimated binding energy of 1 eV of the cesium multilayers was used. As a result of the ratio for the mass of the hydrogen nucleus ($m_1 = 1$ amu) in comparison to the mass of cesium ($m_2 = 133$ amu), physical sputtering is only effective for high ionic energies [ATG85]. Hence, a high sputtering threshold energy of 34 eV for protons was determined.
The TRIM code [EB85] was applied to determine the sputtering yields for physical sputtering and the energy of the backsputtered cesium particles, used in CsFlow3D. Two main contributions to the physical sputtering processes were considered in CsFlow3D: sputtering by backstreaming hydrogen ions and sputtering by hydrogen ions, created by the discharge itself.

1. Positive $H^+$ and $H_2^+$ hydrogen ions are generated by collision processes of the extracted negative-ion beam with the gas background inside the extraction system and can enter the ion source chamber through the extraction apertures after acceleration by both, the extraction and acceleration voltages. The corresponding particle energies depend on the location where the positive ions are generated inside the extraction system. Typical ion energies are of the order of several keV.
   These backstreaming ions hit the backplate of the negative-ion source and release cesium from the corresponding surfaces. The distribution of the impinging sputter projectiles was modelled according to the geometry of the extraction apertures of the MANITU plasma grid. The particle energy and

the backstreaming-ion current densities in MANITU were taken from an analysis in [Sch09].

2. Positive ions of the source plasma also contribute to the physical sputtering. The ion particle flux in the plasma sheath is given by the following equation:

$$\Gamma_i = 0.61\, n_{\text{plasma}} \sqrt{\frac{e\, T_{\text{e}}}{m_{\text{ion}}}}, \tag{4.33}$$

where $m_{\text{ion}}$ is the mass of the impinging ions [LL05]. Additionally, the influence of the magnetic field on the plasma was considered by weighing the plasma density according to the magnetic flux density on the specific surface area.
Nevertheless, the particle energies gained by acceleration in the plasma sheath are several orders of magnitude lower than the energy of the backstreaming ions, even if the ion flux is significantly higher. The corresponding particle energies were determined by the difference of the plasma potential $\Phi_{\text{Plasma}}(\vec{r})$ and the potential of the grounded chamber walls.
Results from Langmuir-probe measurements [MDCK$^+$09][Die07][CKF08] were used to construct a plasma-potential map (see appendix D). A plasma potential of 50 V in the driver and 40 V at the driver exit has been measured, falling to 20 V in the extraction region. According to these measurements, the described physical sputtering process is relevant only in the driver and at the surface areas close to the driver exit, while the energy of the hydrogen ion flux on the surface areas of the expansion region is either below the threshold energy for physical sputtering or creates only a sputtering yield that is negligible small.

**Chemical Sputtering** Observations after opening the ion source show a significant cesium desorption (see figure 6.12) from wall areas in the expansion region where physical sputtering by hydrogen ions is ineffective according to formula (4.32). This is possibly an effect of a chemical interaction of plasma particles with the deposited cesium compounds. Plasma electrons might reduce the cesium in ionic bonds on the walls of the ion source to elemental cesium that is evaporated from the surface as a consequence of its high vapor pressure.
The chemical state of cesium on the source walls is subject to further research and no analytical model or experimental data has been available in order to include the described process in CsFlow3D. A minimum erosion rate was therefore estimated by empirical observations from the ion-source test facility BATMAN,

where similar wall-desorption traces have been observed as in the long-pulse test facility MANITU. BATMAN, however, has a shorter duty cycle with a vacuum phase of several minutes, followed by a discharge with a pulse duration of several seconds. For the determination of chemical erosion in CsFlow3D, the minimum cesium erosion rate by chemical sputtering was estimated by the condition that cesium, accumulated on the specific wall areas during the 4 min of a vacuum phase, has to be removed during the 5 sec of the following discharge phase in order to reproduce the observed erosion traces.
It has to be stressed that the implemented surface-chemistry model is a very rough estimation from empirical observation. This model has to be improved, when experimental data of the chemical sputtering rates for negative-ion source relevant conditions are available.

### 4.3.5. Geometric Representation

A surface mesh of the inner chamber walls of the negative-ion source was implemented in CsFlow3D in order to simulate the transport of cesium between the individual surface-mesh elements and to compute the accumulation of cesium on a specific position on the chamber walls at a time $t$.
Several types of surface-mesh elements have to be considered for the transport calculation:

#### Emitting Elements

Cesium-emitting surface elements are used to consider the injection of atomic cesium by the evaporation oven or dispenser into the ion source chamber. The angular intensity distribution of the corresponding cesium flux depends strongly on the geometry of the nozzle system of the particular cesium source.
A separate simulation of the nozzle flow profile (see section 6.1.1) was therefore done in order to consider the specific nozzle geometry of the IPP evaporation oven.

#### Loss Elements

The negative-ion source vessel is not a closed system due to the extraction apertures in the plasma grid. While the high potential (kV) during extraction prevents

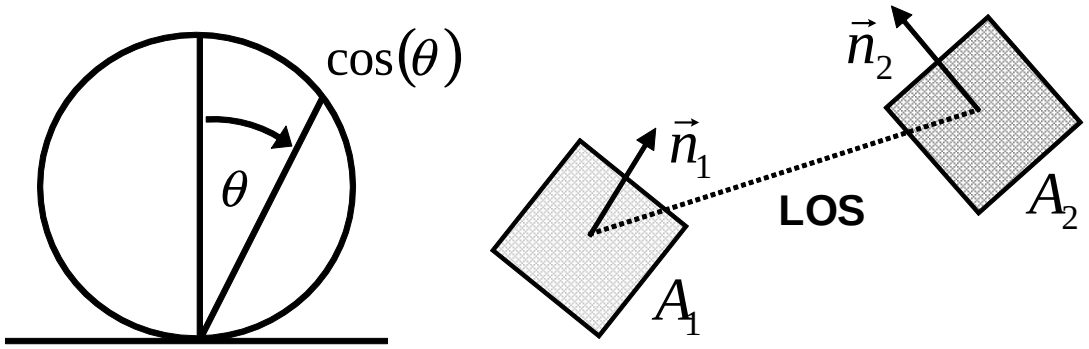


**Figure 4.17.:** Illustration of the re-distribution process of cesium from a surface element according to a cosine distribution (left hand side) of the re-emitted cesium flux. The cesium is transferred between two area elements (right hand side) with area $A_\mathrm{i}$ and a surface normal vector $\vec{n}_i$ that are connected by a line-of-sight (LOS).

the positive cesium ions from escaping through the apertures, neutral cesium is able to leave the ion source during both the vacuum and the plasma phase.
Cesium losses through the extraction apertures are in particular relevant during the vacuum phases, where cesium is in its neutral state. Circular extraction apertures were implemented according to the MANITU plasma grid as shown in figure 3.9. The strong electrical fields during extraction were modelled by a reflective boundary for ionic cesium.

### Absorbing and Emitting Elements

The surface elements of the ion source walls can absorb and emit cesium. Cesium can be accumulated on surface elements, but also re-emitted according to the physical processes described in section 4.3.4. The cesium transport between two surface-area elements $A_1$ and $A_2$ with surface-normal vectors $\vec{n}_1$ and $\vec{n}_2$ is governed by a cosine distribution of the emitted cesium flux from the chamber walls [Gre02], as illustrated by figure 4.17.
The transport process is determined by geometry related effects, such as distance and relative orientation of the two surface elements, and by the flow regime that is subject to change during source operation.

# 5. Experimental Results and Input Parameters

The overview of the properties of cesium that was given in section 4.1 shows that the high reactivity of cesium results in a strong dependence of the relevant parameters on the surface conditions and the pressure of the individual system. Hence, it is necessary to investigate the following phenomena at negative-ion source relevant pressure and temperature conditions:

- condensation and desorption kinetics from surfaces for different sample temperatures,
- time evolution of the work function of cesium layers on metal substrates,
- properties and characteristics of cesium flows from dispenser and evaporation sources.

Dedicated experiments were carried out in order to determine the described parameters. Data regarding cesium evaporation, distribution and re-distribution, obtained by these investigations are used as input parameters for CsFlow3D in order to simulate the dynamics of cesium within the negative-ion source.

## 5.1. Desorption and Condensation Kinetics

Understanding the temperature-dependent desorption and condensation kinetics of gaseous cesium on the chamber walls is essential in order to simulate the cesium transport within negative-ion sources. As it was mentioned in section 4.1.2, literature data and related analytical expressions are limited to the desorption flux in a vapor pressure equilibrium of pure cesium and to the kinetics of cesium monolayers on metals under ultra-high vacuum conditions ($10^{-7}$ Pa) and sample

temperatures of several 1000 °C. No experimental data is available for the desorption kinetics of cesium at the vacuum ($10^{-3}$ - $10^{-4}$ Pa) and temperatures ($T_{\mathrm{wall}}$ = 20/50/150 °C) conditions relevant for negative-ion sources at IPP.
Thus, dedicated desorption experiments were performed under vacuum and surface conditions that are comparable to those in the ion source (see section 4.2.1). A 3x2 $cm^2$ molybdenum sample was cut from the material that is used for the plasma grid and mounted on a temperature-controlled sample holder, using a thermocouple to measure the sample temperature. The sample was exposed to a cesium flux from a dispenser and the release of cesium from the metal surface was measured in-situ by the movable quartz microbalance (see section 4.2.2). Two experimental procedures were applied for the investigation:

1. the desorption from a cesium-coated metal sample while the sample is heated,

2. the reflection of cesium during simultaneous cesium exposition for steady-state temperature conditions.

## 5.1.1. Desorption of Cesium

### Experimental Procedure

For the experimental investigation of the desorption of cesium, a two-step procedure was applied for cesium exposure and the measurement of cesium desorption from the heated sample. This arrangement is shown in figure 5.1.
In the first step, elemental cesium from a SAES dispenser was deposited on the sample with the temperature at $T_{\mathrm{s}}$ = 20 °C, while the microbalance was located remote from the sample. According to data from the manufacturer SAES [CMP04], ultra-pure cesium vapor is released from the dispenser. After ending cesium deposition from the dispenser, the microbalance was moved to a position a few centimeters in front of the sample. In the second step, the total accumulated amount of cesium desorbing from the sample was measured while increasing the temperature of the sample linearly. A close arrangement of microbalance and heated sample ensures that the detector covers a high solid angle with respect to the sample.

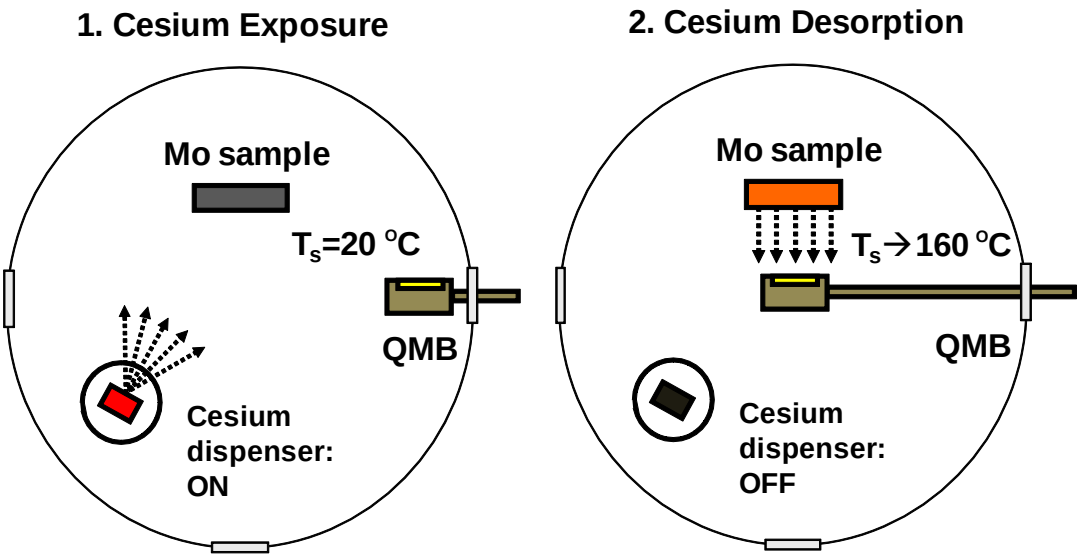


**Figure 5.1.:** Experimental setup for the investigation of the desorption and condensation kinetics of cesium layers on metal samples. In the first step, the cold sample was exposed to cesium from a dispenser. In the second step, the sample was heated and the cesium desorption was measured with the microbalance.

### Measurement Error

A non-constant, but systematic measurement error results from the radiative heat flux emitted by the heated sample onto the exposed quartz plate. This heat flux creates a thermal gradient between the two quartz plates in the microbalance. The resulting temperature asymmetry creates a frequency difference between the quartz plates. This asymmetric heating can generate a measurement error that results in an overestimation of the cesium on the microbalance depending on the temperature history of the system. The corresponding error exceeds the error by the frequency measurement of $\pm 0.3$ monolayers.

### Experimental Results

The molybdenum sample was exposed for 20 minutes to a cesium flux of $2\text{x}10^{13}$ $\text{cm}^{-2}\text{sec}^{-1}$ from the dispenser that was determined by a previous measurement with the microbalance, while maintaining a constant sample temperature of $T_\text{s} = 20$ °C. This corresponds to a total cesium exposition of approximately 50 monolayers.

The cesium-coated molybdenum sample was heated linearly to a temperature of

$T_s$ = 160 °C while the cesium deposition on the microbalance was measured. A test under similar conditions, but without previous cesium exposure was done in order to ensure that the signal on the microbalance is created by the desorption of cesium. The signal of the microbalance in dependence of the sample temperature with and without a preceding cesium exposition is given in figure 5.2. An overestimation of the detected amount of cesium by 5 monolayers was derived by the measurement without previous cesium exposure of the sample. As described before, this signal is related to the temperature difference between the quartz plates by radiative heating.

A total cesium accumulation of 33 - 40 monolayers was detected on the quartz plate after the heating procedure. The alkaline character of the substance from the microbalance sensor was identified (ex-situ) by pH indicator. This test was negative for molybdenum samples without previous cesium exposition.

A low cesium deposition that is only slightly higher than the measurement error was obtained for sample temperatures up to 50 °C. Heating the sample to a temperature of $T_s > 65$ °C results in a strong increase of the cesium accumulation on the microbalance. Forming the derivative of the time dependent cesium coverage on the microbalance shows that a maximum desorption rate of 3.5 monolayers/min from the sample is obtained at a temperature of $T_s$ = 80 °C, followed by a saturation of the accumulation at approximately 85 °C. This is a consequence of the depletion of the cesium that was deposited on the sample.

A second peak appears at a sample temperature of 120 °C, which is, presumably, created by temperature fluctuations of the quartz plates.

The experiment shows that stable multilayers of cesium can be absorbed by the metal sample at temperatures below 60 °C for negative-ion source relevant vacuum and temperature conditions. These layers get instable at higher sample temperatures and a sample temperature above 65 °C is necessary to release cesium from the sample surface. This formation of stable cesium multilayer structures on the sample is consistent with empirical observation of clearly visible cesium accumulations on the surface areas of the vacuum vessel close to the cesium dispenser. No temporal evolution of these structures or re-distribution effects were observed until their removal by cleaning the vacuum vessel after several weeks of operation. The formation of a high multilayer coverage on the sample indicates that the corresponding physical and chemical properties are independent of the sample material.

These observations cannot be explained by the desorption flux of cesium for a vapor pressure equilibrium, as calculated in section 4.1.3. Heating the sample to a

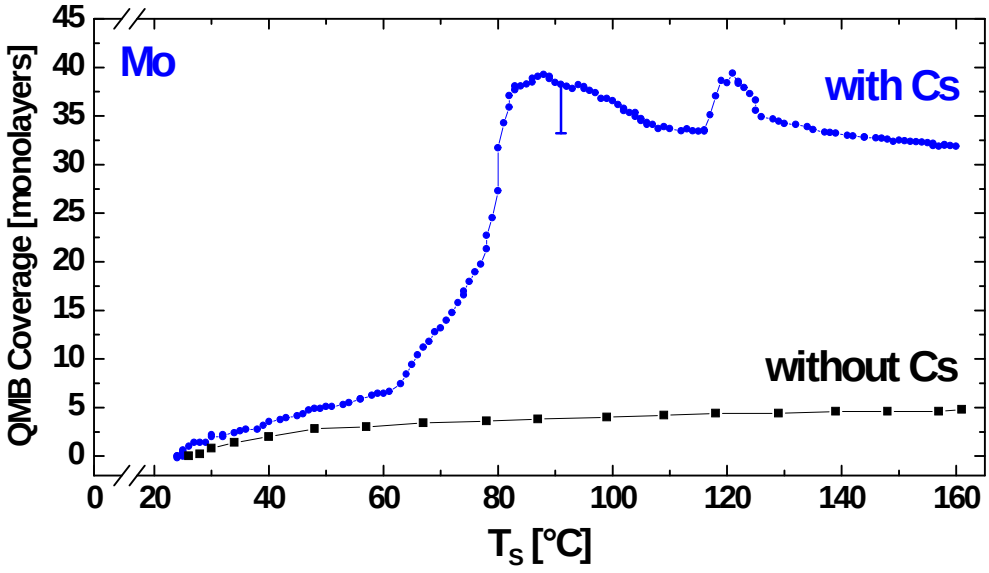


**Figure 5.2.:** Signal of the quartz microbalance close to a molybdenum sample, heated to a temperature of 160 °C, with (blue) and without (black) preceding cesium exposition from a dispenser. The negative measurement error was derived from the measurement without cesium.

temperature of 50 °C would result in an equilibrium flux of 2x$10^{15}$ $cm^{-2}$ $sec^{-1}$ from the hot sample onto the cold chamber walls ($T_{\text{walls}}$ = 20 °C). The corresponding equilibrium flux from the walls onto the sample is one order of magnitude lower and would create an effective flux of 240 monolayers/min from the hot sample onto the chamber walls, depleting the accumulated amount of cesium within several seconds.

Furthermore, the measured desorption flux at a temperature of $T_{\text{s}}$ = 85 °C is a factor of 1000 lower than expected from the equilibrium flux. The total content of injected cesium from the dispenser would be lost to the vacuum pumps after several hours even at $T_{\text{walls}}$ = 20 °C, which is in contrast to the experimental observation, where cesium traces, distributed according to the position and direction of the cesium source, are clearly visible until opening the vessel.

Thus, the accumulated cesium layers have a significant higher stability than expected from the surface affinity of pure cesium. This indicates the formation of cesium compounds. The determination of the corresponding sticking coefficients for different wall conditions is necessary to quantify the process of cesium accumulation. Sticking coefficients are essential input parameters for cesium transport simulations in the negative-ion source.

This kind of desorption measurement is not suitable to resolve this parameter as a consequence of the measurement error due to temperature variation in the

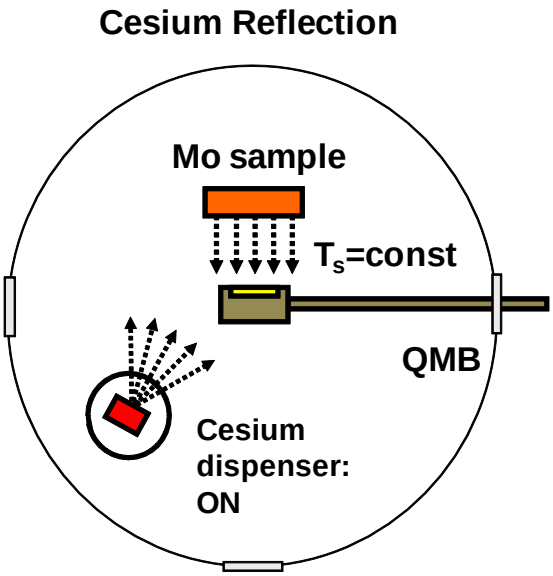


**Figure 5.3.:** Experimental setup for the investigation of the reflection of cesium from a molybdenum sample with a quartz microbalance. Exposure and measurement of cesium that is reflected from the metal sample kept at a constant temperature were done simultaneously.

microbalance, induced by heating the sample. Hence, a steady-state condition of the temperature of the microbalance was used for the measurement of the cesium reflection from the metal sample, which avoids the systematic error by the asymmetric heating process of the two quartz plates.

## 5.1.2. Reflection of Cesium

### Experimental Procedure

In case of the reflection experiment, cesium exposure of the sample and the measurement of the desorption flux from the sample were done in parallel. The experimental setup is shown in figure 5.3. Both, the cesium dispenser and the microbalance were placed in front of the sample in a triangular configuration ensuring that no cesium from the dispenser is able to hit the microbalance directly. Thus, a deposition on the microbalance is caused solely by cesium that is reflected from the sample. The systematic measurement error associated with thermal imbalances can be reduced in case of a reflection measurement at steady-state temperature conditions of the sample. In this case it is possible to wait until the thermal equilibrium of the system is reached prior to the evaporation of cesium, which is not possible when applying a temperature ramp. Hence, the

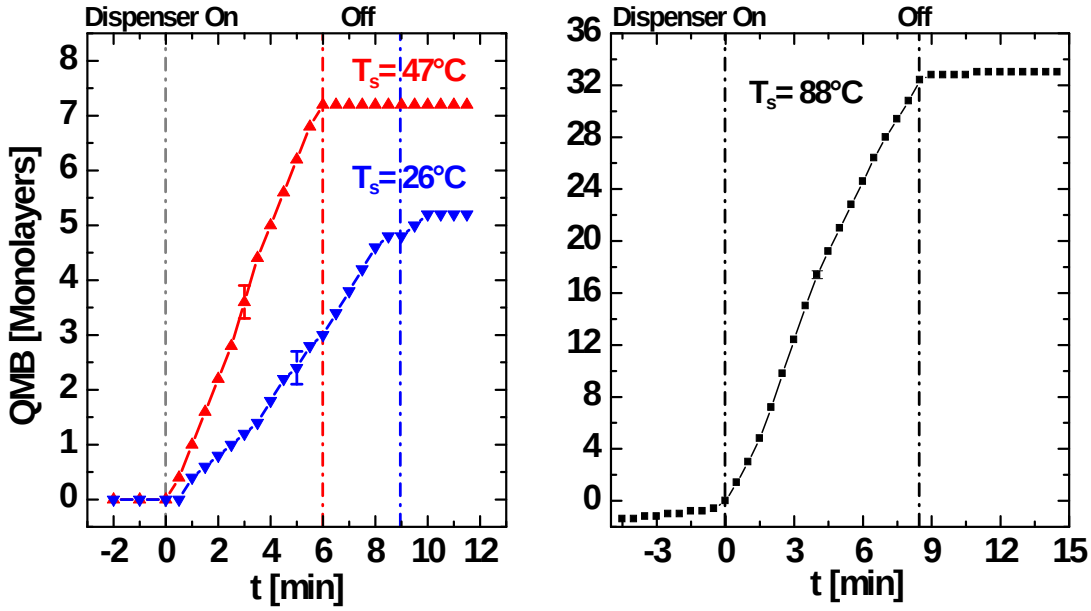


**Figure 5.4.:** Reflection of cesium from a molybdenum sample, exposed to a cesium flux from a dispenser for a sample temperature of 26 °C, 47 °C and 88 °C.

samples were kept up to 30 min at a constant temperature before cesium was released in order to establish stable initial conditions. Nevertheless, an error of ±0.3 monolayers is given by the frequency measurement itself.

### Results

The reflection measurements were done consecutively for sample temperatures of 26 °C, 47 °C and 88 °C. Figure 5.4 shows the reflected cesium from the molybdenum surface for a constant cesium flux and the three sample temperatures. The start of the cesium accumulation on the microbalance showed a good correlation with the beginning of cesium exposure after enabling the dispenser. The reflected cesium flux was determined by the derivative of the accumulation on the microbalance.

A strong temperature dependence of the reflected cesium flux was observed. Small reflection fluxes of $(3.5 \pm 0.3)\text{x}10^{12}$ $\text{cm}^{-2}\text{s}^{-1}$ (26 °C) and $(9.0 \pm 0.4)\text{x}10^{12}$ $\text{cm}^{-2}\text{s}^{-1}$ (47 °C) were detected in the lower temperature range, while a sample temperature of 88 °C results in a significant higher reflective flux of $(2.89 \pm 0.03)\text{x}10^{13}$ $\text{cm}^{-2}\text{s}^{-1}$ (3.85 monolayers/min), comparable to the previously described value of 3.5 monolayers/min, obtained by the desorption measurement.

The stop of the cesium accumulation on the microbalance is for all sample temperatures in good correlation with switching-off the cesium flux from the dispenser and no significant long-time desorption effects of the accumulated cesium took place. This is consistent with the desorption measurements where a significant release of cesium was observed at a sample temperature of above 65 °C, indicating the temperature regions of stable layer growth ($T_s$ < 65 °C) and desorption ($T_s$ > 65 °C). Thus, stable cesium multilayers are created for sample temperature conditions of $T_s$ = 26 °C and 47 °C. This indicates a chemical process, where a part of the cesium flux forms cesium compounds, while the remaining cesium is re-emitted as a result of the high vapor pressure of pure cesium.
Increasing the sample temperature to $T_s$ = 88 °C produces a high desorption of cesium. This creates a flux balance of the cesium influx from the dispenser with the desorption outflux from the sample. Thus, the absence of a desorption flux after switching off the cesium dispenser is a consequence of cesium depletion. The detected cesium outflux from the sample at $T_s$ = 88 °C is equivalent to the total influx. A determination of the sticking coefficient for cesium on the sample surface can be made by dividing the desorption flux by the total flux onto the sample. Sticking coefficients of 0.9 (26 °C) and 0.7 (47 °C) were determined by this method.

### 5.1.3. Comparison to Thermal Desorption Measurements in MANITU

The density of atomic cesium by thermal desorption from a hot metal surface can also be evaluated during long plasma pulses at MANITU. Plasma pulses with a long duration cause a thermal load on the surfaces of the ion source vessel, which is temperature stabilized to $T_{wall}$ = 50 °C by a water cooling system. The molybdenum-coated bias plate is a separate part near the plasma grid (see figure 5.5). Thus it has a less efficient cooling system and is heated up to a bias plate temperature of up to 200 °C during plasma pulses. The emission signal from atomic cesium close to the bias plate was measured with the OES during a plasma pulse of 400 sec. In order to eliminate the influence of changes in the electron density, the ratio of Cs 852 nm and the $H_\beta$ line is formed, as described in section 4.2.4. Figure 5.6 shows the dependence of the signal of the OES on the temperature of the bias plate that is measured by a thermocouple. Despite of the interference by the RF-noise, a clear trend of the cesium signal is visible.
While the OES signal shows only small deviations for a bias plate temperature

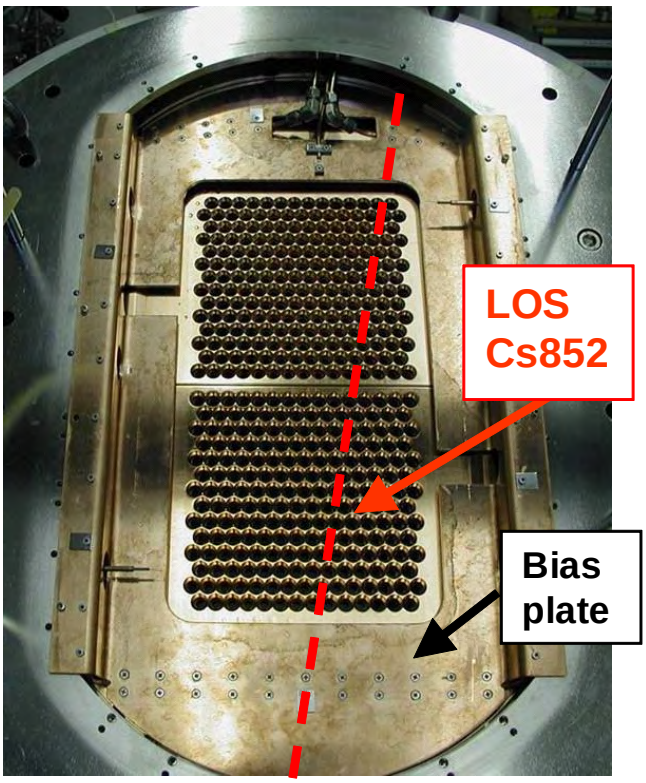


**Figure 5.5.:** Photograph of the bias plate in MANITU. The line-of-sight (LOS) of the spectroscopic measurement of the Cs852 line is printed in red.

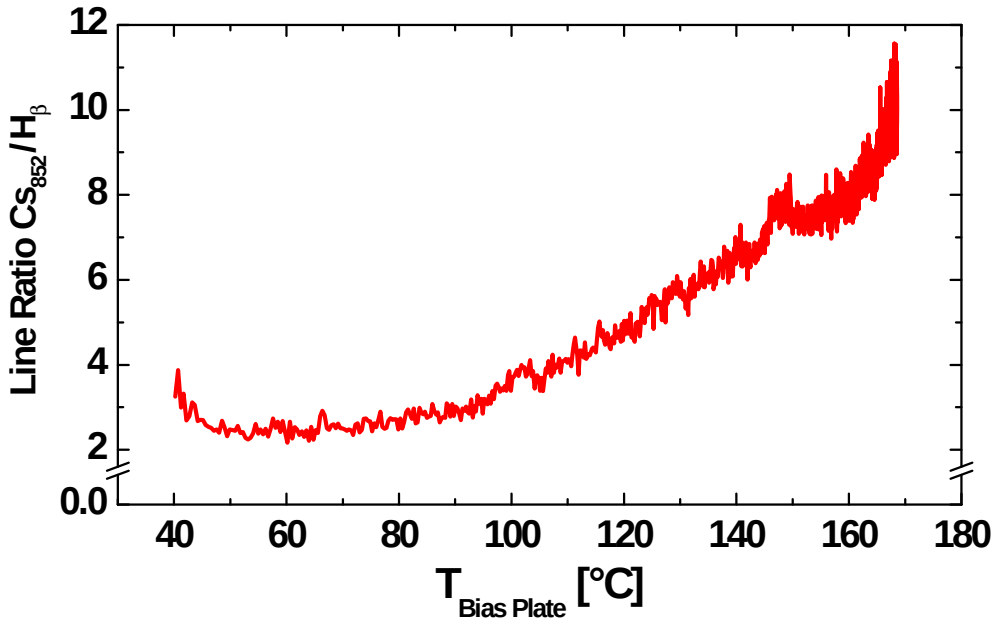


**Figure 5.6.:** Line ratio of Cs 852 nm by the $H_\beta$ line from the OES during a 500 sec plasma pulse in MANITU ($H_2$, 58 kW, 0.3 Pa) versus the temperature of the bias plate.

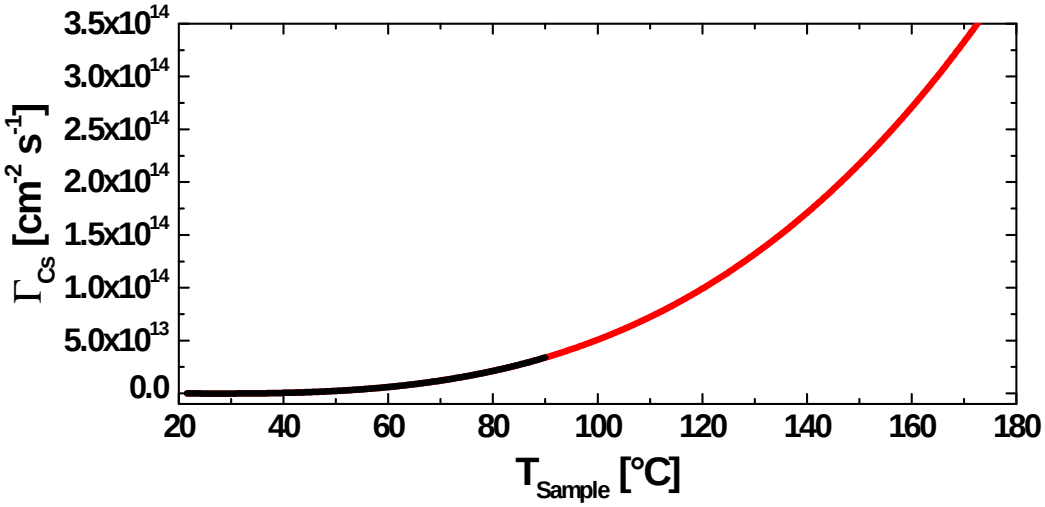


**Figure 5.7.:** Estimated temperature dependence of the desorption flux of neutral cesium, extrapolated from measurement with the microbalance. Black line: data as indicated from the measurements. Red line: extrapolated data to estimate the desorption flux at higher temperatures.

below 70 °C, a significant increase of the density can be observed at elevated bias plate temperatures above 80 °C, indicating intensive thermal desorption. However, the line-of-sight of the OES covers only a limited area of the bias plate, which might affect the measurement.

### 5.1.4. Approximation of the Thermal Desorption Rates at High Temperatures

The temperature dependence of the thermal desorption rate of cesium is a necessary input parameter for the CsFlow3D code. In order to approximate the order of magnitude of the cesium flux at high temperatures, a cubic extrapolation of the measured data that was shown in figure 5.2 and figure 5.4 was done. The cubic fit function was chosen since an exponential extrapolation creates a strong increase of the cesium flux at 120 °C that is not compatible with the desorption characteristics that were measured in MANITU.
The corresponding (rough) estimation of the temperature dependence of the thermal desorption rate is shown in figure 5.7. Nevertheless, a quadratic extrapolation would be also plausible, but does not change the order of magnitude.
This is only a first estimation and measurements at sample temperatures above

90 °C are required. However, this is not possible with the given experimental setup, since the maximum cesium flux that can be measured is limited by the amount of cesium, available from the cesium reservoir. Using a high surface temperature results in a quick depletion of the limited amount of cesium from a 10 mg dispenser. Hence, the use of 100 mg cesium dispensers, as it is described in section 5.3.2, is planned for future desorption measurements.

### 5.1.5. Formation of Cesium Compounds

All thermal desorption measurements showed a higher surface affinity compared to that expected for elemental cesium. This indicates an increase of the surface binding energy due to the formation of cesium compounds. Especially oxygen can be dissolved in liquid cesium at a large amount, as described in section 4.1.4. This is possible by the formation of cesium oxide by reactions with the residual gas. At the pressure and surface conditions within negative-ion sources, one monolayer of contaminants is built up after several seconds (see section 4.1.4). Furthermore, a direct reaction of cesium with the surface oxides of the metal substrate is possible, forming compounds of the Cs-Metal-O system. Investigations, done by Desplat et al. [DP80], show that stable cesium multilayers can be grown on a tungsten-oxide sample at room temperature, forming a 3D crystallite structure. The desorption of these layers is reported to take place at 77 °C, which is qualitatively in agreement with the described experimental observations.
Cesium can undergo a very large spectrum of chemical reactions, which have to be studied in more detail for the conditions of negative-ion sources. Further investigation of cesium compounds with a mass spectrometer, formed on metal surfaces, for the conditions within negative-ion sources are in preparation [Fri12].

## 5.2. Work Function and Surface Properties

The previous measurements showed a deviation from the de- and adsorption kinetics of pure cesium for ion-source relevant parameters, indicating that chemical processes take place.
Additional information can be derived from the work function of a surface, determining the production rate of negative ions via the surface process (see section 3.1.1).

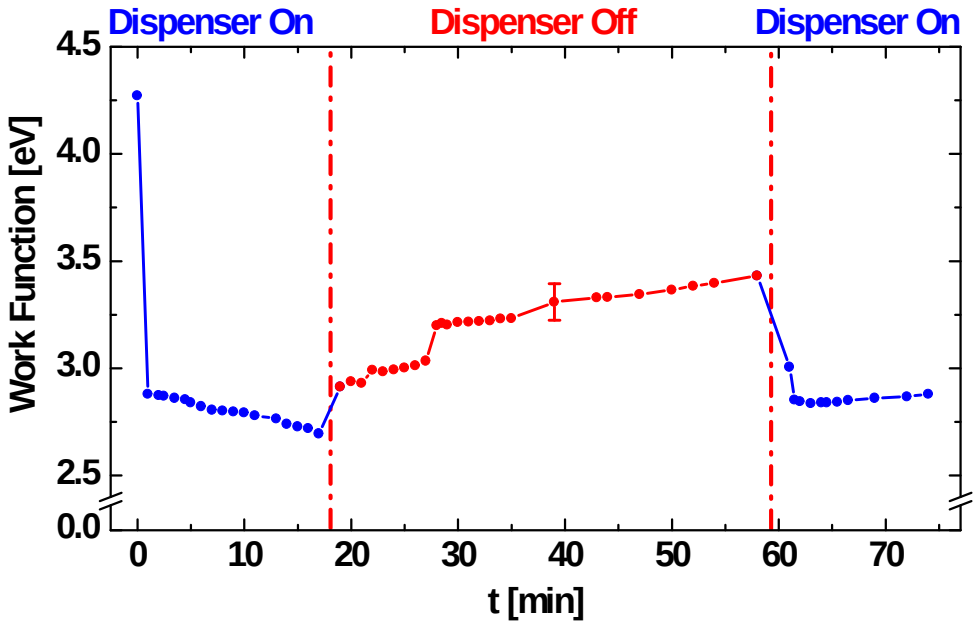


**Figure 5.8.:** Evolution of the work function of a molybdenum sample in a vacuum environment while enabling and disabling the cesium exposure from a dispenser.

### Experimental Procedure

A fresh, polished molybdenum sample at a temperature of 20 °C and a background pressure of $10^{-3}$ Pa was exposed to a cesium flux from a cesium dispenser of approximately $3x10^{13}cm^{-2}s^{-1}$ while its work function was measured in parallel utilizing the photoelectric effect (see section 4.2.5). No surface treatment was applied except of polishing. The dispenser was consecutively enabled and disabled during the experiment in order to determine the behavior of the work function under the influence of the residual gas without cesiation and the effect of a repeated cesium exposure.

### Results

Figure 5.8 shows that the cesium exposition results in the expected decrease of the work function $\phi$ of the sample. The characteristic of the curve is, however, different from the ideal behavior (see section 4.1.1). Two regions with different rates of decrease can be identified: a strong decrease of the work function of the bare metal ($\phi_{\mathrm{Mo}} = 4.27 \pm 0.08$ eV) to a value of $\phi = 2.88 \pm 0.08$ eV was detected within the first minute of evaporation, followed by a region, where only a

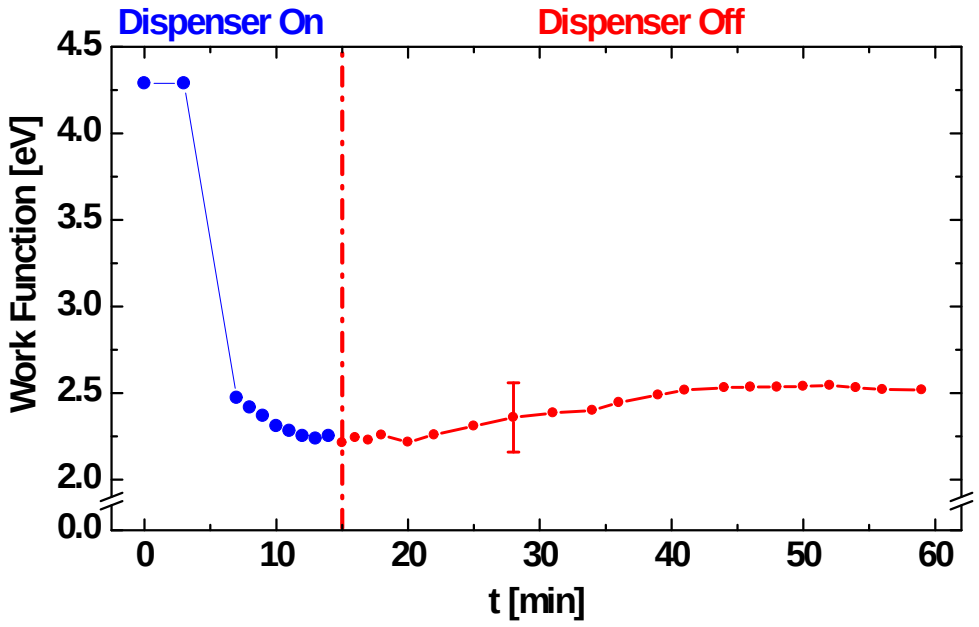


**Figure 5.9.:** Evolution of the work function of a molybdenum sample in a $H_2$/He (80% - 20%) plasma at 180 W and a pressure of 10 Pa. The cesium exposure of the sample was disabled after 15 min.

small decrease to a value of $\phi = 2.69 \pm 0.08$ eV was observed during the following 16 min. An integration of the cesium flux from the dispenser shows that a total cesium exposure to 4 monolayers was required in order to obtain a work function of 2.88 eV during the first minute, while 60 - 70 monolayers are required to lower the work function to 2.69 eV in the next 16 minutes.

After 17 min of cesium exposure, the dispenser was disabled for a time period of 40 min in order to observe the evolution of the reduced work function without any cesium influx. An increase of the work function to a value of $\phi = 3.43 \pm 0.08$ eV was detected during this phase. Re-enabling the cesium flux a second time resulted in a recovery of the work function to a value of $\phi = 2.84 \pm 0.08$ eV. The repeated reduction of the work function took again place within the first minutes of cesium exposure - a behavior that is very similar to the observation at the initial cesiation.

An exposure of the surface to a flux of hydrogen atoms and ions from a plasma source is a prerequisite for the surface production of negative ions. Thus, the work function of a molybdenum surface exposed to a cesium flux was measured during a pulsed $H_2$/He-discharge. The flux of plasma particles creates a heat load onto the sample that is only weakly connected to the temperature-controlled walls by the sample holder. A sample temperature between 150 - 200 °C, which is be-

low the gas temperature during the discharge, is obtained for this configuration [Sta05].

The results of this investigation are given in figure 5.9. These show a quite similar behavior regarding the decrease of the work function compared to the vacuum case. The obtained saturation value of $\phi_{\mathrm{Sat}} = 2.2 \pm 0.2$ eV, however, is significantly lower than the work function without the plasma. Disabling the cesium exposure results in an increase of the work function to $\phi_{\mathrm{dec}} = 2.5 \pm 0.2$ eV after a period of time of 40 min. This increase of the work function is not so strong than the increase within the vacuum environment.

The measurement of the work function in the ICP source at conditions comparable to the vacuum and plasma conditions in negative-ion sources showed a different behavior than expected from the available data for ultra-high vacuum conditions and high surface temperatures, as described in section 4.1.1. A cesium exposure to 60 - 70 monolayers was required in the ICP experiment to reach a work function of 2.69 eV which is significantly higher than the literature value of the work function of a single monolayer of pure cesium of $\phi_{\mathrm{L}} = 2.14$ eV. This value has not been obtained by any measurement for the given vacuum and temperature conditions. A reduction of the work function was, however, observed by the measurement during the pulsed discharge. This indicates a cleaning effect by the impinging plasma particle flux.

Both measurements show a degradation process of the work function without a continuous cesium deposition that is especially pronounced in the measurement in the vacuum environment. A degradation of a pure cesium metal surface was also reported in [SWF00], where a similar effect was observed under better vacuum conditions of $10^{-6}$ Pa. In this experiment, the degradation is explained by the formation of stable, chemical compounds with a high work function that contaminate the surface by increasing the effective work function. The dynamics and intensity of this degradation are determined by the specific reaction rates of the individual chemical reactions and the work function of the reaction products. A temperature dependence of this effect is expected and additional measurements are required in order to evaluate the influence of the sample temperature on the work function. A comparison of the evolution of the work function during cesium exposure in the vacuum phase for a sample temperature of 20 °C and 150 °C is in preparation.

Subsequent re-enabling of the cesium flux from the dispenser regenerates the work function by adding new layers of cesium. Therefore, a continuous and sufficiently high cesium influx onto the sample is required in order to counteract the chemi-

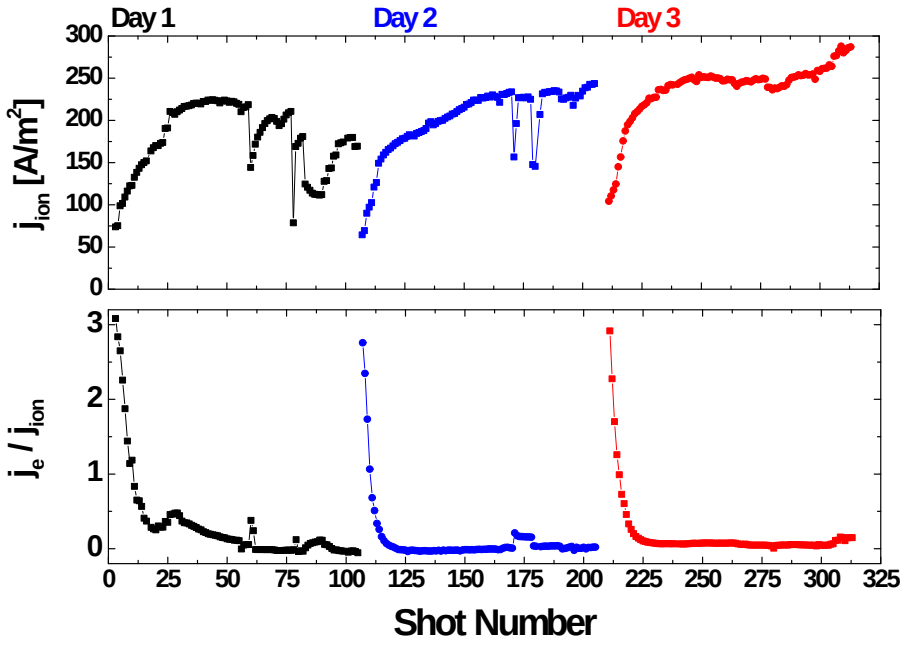


**Figure 5.10.:** Time traces of the negative-ion current and the electron-to-ion ratio in BATMAN for three consecutive days.

cal degradation and to keep the work function permanently at a low level. This condition is desired for a stable negative-ion production over long periods of time in particular during long plasma pulses.

Observations of degeneration and regeneration processes, quite similar to the ones presented in figure 5.8, were made at the N-NBI test facilities. After a long period of inactivity (10 hours) such as when the source is operated for the first time in the morning, low negative-ion and high co-extracted electron current densities are extracted. The reason for this is that the plasma grid has to be supplied with new cesium in order to balance degradation effects by reaction with the residual gas. Figure 5.10 shows the dynamics of the source performance in BATMAN for a period of three consecutive days. The source starts at a low performance and a series of conditioning pulses is necessary until the level of the previous day is obtained.

Comparative studies of BATMAN and MANITU indicate an improved conditioning time in the latter test facility, which is a consequence to the better residual gas pressure during the nights. As described in section 3.2.2 Ti getter pumps are used in BATMAN, while MANITU is equipped with more powerful cryosorption pumps.

A continuous and sufficiently high cesium flux onto the plasma grid is required to

regenerate the cesium conditions by counteracting degradation effects. The optimization of the intensity and stability of the cesium influx onto the plasma grid of a negative-ion source requires the development of reliable and stable cesium sources. Cesium injection into a negative-ion source is more complex than in the presented lab experiments. This is because only a limited number and locations of ports for the cesium source are available in negative-ion sources, while a flexible rearrangement of the components is possible in the lab experiment. Hence, the cesium flow from different cesium sources was measured in the ICP experiment with the surface ionization detector (see section 4.2.3).

## 5.3. Flow Measurement

### 5.3.1. IPP Cesium Evaporation Oven

No measurements of the intensity and long-term stability of the flow from the cesium evaporation oven in use at the IPP test facilities have been carried out up to now. A detailed description of this liquid reservoir based oven is given in section 4.2.6. However, these data are highly desirable to evaluate the performance of the oven and to control the amount of cesium that has been injected into the ion source. Up to now the extracted negative-ion current density $j_{H^-}$ was used as an indicator for the oven performance and to control the cesium injection. This method is, of course, not sufficient to provide a quantitative monitoring of the injected cesium flow.

The flow measurement is also required in order to evaluate the effect of design changes and to find the best operation parameters. The stability and reproducibility of the cesium injection rate with respect to temperature changes and the operational time were investigated in this work. Tests were made if it is advantageous to use a configuration with additional heating elements on both ends of the body of the evaporation oven, as described in section 4.2.6. Furthermore, the measurement serves to determine the influx from the cesium oven into the ion source that is required for the cesium transport simulation. This flow depends highly on the geometry and temperature conditions of the oven itself.

### Experimental Procedure

A direct flow measurement with the surface ionization detector (see section 4.2.3) was carried out to determine the cesium injection rate from the oven. The cesium flow from the nozzle system of the oven was monitored after breaking an ampoule containing 1000 mg of cesium and for operation times and temperatures similar to those that are applied for cesium injection at the IPP negative-ion sources (see section 4.2.6).
Flow monitoring was carried out over a period of 23 days until the amount of 1000 mg of cesium in a single ampoule was depleted. The oven was enabled for a typical operation period of 8 - 10 hours during the day and was kept inactive at temperatures between 20 °C and 40 °C during the nights and over the weekends. The microbalance could not be used to monitor the high cesium flow (injection rate of 10 - 100 mg/h) from the oven for a period of several days. This is a consequence of its limitation regarding the total amount of cesium on the sensor (see section 4.2.2). The ionization detector does not have this flow limitation due to the high temperatures of the tungsten filaments preventing cesium buildup. Hence, an optimized surface ionization detector design was developed for this long-term monitoring.
The evaporation oven was attached to one of the side ports of the ICP vessel (see figure 4.7) and the ionization detector filament was placed directly into the emitted cesium flow. A detection of the total cesium flow that is emitted by the oven is not possible since the solid angle of the expanding cesium flow exceeds the dimensions of the surface ionization filament. The detected ionization current was therefore integrated over the total monitoring time. The signal was normalized to the total inventory of the cesium evaporation oven of 1000 mg in order to calibrate the measurement.
A cesium flow is created by increasing the temperature of the oven components. As described in chapter 4.2.6, the temperature of the body $T_{\mathrm{Body}}$ of the evaporation oven is used for controlling the cesium injection rate and thus is defined as the coldest spot of the oven, determining the total cesium vapor pressure within the system. The temperature of the other components, such as the ampoules and the conduction pipe, is set to a temperature of 20 °C above the temperature of the body. Time traces of SID measurement of the cesium flow from the evaporation oven with additional heating elements are presented in the following section.

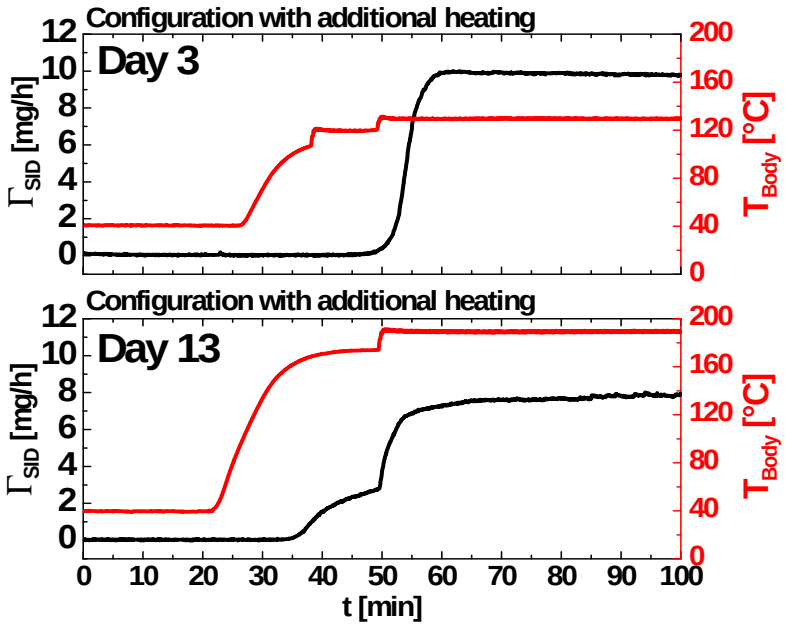


**Figure 5.11.:** Time traces of the SID signal of the cesium flow from the IPP evaporation oven (with additional heating) and the corresponding temperature of the oven body for different days of the measurement campaign.

### Results

No cesium release was detected during the inactive phases when the temperature of all components was set to 40 °C. Increasing the temperature of the oven body and the corresponding temperatures of the other components results in a significant increase of the cesium flow.

Figure 5.11 shows the time traces of the detected cesium flow $\Gamma_{\mathrm{SID}}$ and the temperature of the body $T_{\mathrm{Body}}$ for two different periods of time: two days after breaking the cesium ampoule and after two weeks with an operation time of 8 - 10 h each day.

In the early phase of the evaporation oven test, cesium release and saturation to a total injection rate of 10 mg/h was obtained at a body temperature of 130 °C. A reaction time of the cesium flow to the increase of the body temperature on the order of 10 - 20 min was detected.

However, the monitoring revealed that the temperature that is required to obtain an equivalent injection rate of 10 mg/h is subject to change during several days of operation after breaking the ampoule. A body temperature of 190 °C was necessary after two weeks of operation in order to generate a cesium flow, comparable to the one measured at the beginning of the campaign.

### Analytical Calculation of the Flow from an Evaporation Oven

An approximation of the cesium flow by an analytical calculation, considering the vapor pressure of pure cesium, was done in order to understand the dependence of the oven performance on the operation time. The results of the calculations can be used to interpret the experimental results and to determine the maximum cesium flow that is available from the evaporation oven considering ideal conditions.
The evaporation of cesium within the oven creates a vapor pressure equilibrium that depends on the temperature of the body. Because of the large amount of elemental cesium (1000 mg), released into the body by breaking the glass-ampoule, no deviation from the properties of pure cesium is expected right after the release.
As previously mentioned the body of the oven was chosen to be the coldest spot of the system and defines the total vapor pressure of the system. This vapor pressure, as given in figure 4.3, causes a gradient of the cesium pressure between the body and the vessel of the ion source. The cesium vapor pressure in the vessel is negligible, compared to the one in the evaporation oven. A cesium flow is generated by the pressure gradient that is determined by the conductance of the connecting pipe with temperature $T$. This flow is also strongly dependent on the flow regime.
The mean free path length $\Lambda$ of cesium atoms in the conduction pipe at a vapor pressure $p = p(T_{\mathrm{Body}})$ is given by [Bir94]:

$$\Lambda = \frac{1}{\sqrt{2}\sigma n} = \frac{k_b\, T}{\sqrt{2}\sigma\, p}, \tag{5.1}$$

where the cross-section $\sigma$ for collisions between cesium atoms with thermal velocity $\bar{v}(T)$ was taken from [FBS98]. The flow regime is determined by the Knudsen number Kn:

$$\mathrm{Kn} = \frac{d}{\Lambda}, \tag{5.2}$$

where $d = 7$ mm is the diameter of the conduction pipe. A Knudsen number of $\mathrm{Kn} = 0.5$ is obtained at $T_{\mathrm{body}} = 165$ °C. This puts the flow in a transition from a free molecular flow $\mathrm{Kn} \gg 1$ to a viscous flow at $\mathrm{Kn} = 0.5$ at the operation temperatures.
The following formula was used to calculate the conductance $C$ of a pipe with effective area $A$, diameter $d$ and length $L$:

$$C = \frac{\pi}{128\eta}\frac{d^4}{L}p + \frac{1}{3}\bar{v}A\,\frac{d}{L}\,\frac{1 + 1.60\frac{d}{\eta\bar{v}}\,p}{1 + 1.98\frac{d}{\eta\bar{v}}\,p}\,\left[\frac{\mathrm{m}^3}{\mathrm{sec}}\right], \tag{5.3}$$

for flows in the transition regime [Jou06]. The viscosity $\eta$ of cesium was derived from [VY88]. An approximation of the cesium flow by $\Gamma_{\mathrm{Cs}} = C(p)\,p$ is possible without accounting for the nozzle and any sticking of cesium to the walls of the system.

### Comparison with the Surface Ionization Measurements

The results of the calculation and measurement were compared to each other. Figure 5.12 shows the computed and measured cesium flow from the evaporation oven in dependence of the body temperature $T_{\mathrm{Body}}$ for configurations with and without additional heating (see red arrows in figure 4.12). According to the calculation, a cesium flow of several mg/h starts at a body temperature higher than 120 °C, while a negligible cesium flow of less than 1/200 mg/h is obtained for a body temperature lower than 40 °C.
A cesium injection rate of 10 mg/h for a body temperature of 145 °C is predicted by the calculation. This underestimates the injection rate from the SID measurement of 15 - 20 mg/h at a body temperature of 140 - 150 °C, obtained a few days after breaking the cesium ampoule. As the analytical flow calculation relies on the vapor pressure of pure, non-contaminated cesium, it can be concluded that the maximum performance of the cesium oven has been achieved at this time.
A probable explanation for the underestimation of the measured value is that the inner surface of the body has a higher temperature than it is measured by the thermocouple. This could be an effect of a heat flow from the ampoule housing and the connection pipe to the body.
The cesium flow from the oven with the additional flange heating elements was compared to the flow from the oven without this modification. Both measurements were done a few days after breaking the cesium ampoule. A maximum cesium flow of only 1 mg/h was obtained in this case even for high body temperatures $> 200$ °C. It is possible to increase the cesium flow an order of magnitude by using the additional heating at the ends of the body flange. An explanation for the beneficial effect of the additional heating elements is that both ends of the oven body form undesired "cold" spots as they are in contact with heat sinks (see figure 4.12). If the temperature of the cold spots at the ends of the body is lower than the body temperature, the total vapor pressure is limited by this temperature.
The prevention of the formation of "cold" spots at the ends of the body pipe by the additional heating has significantly improved the performance of the evapo-

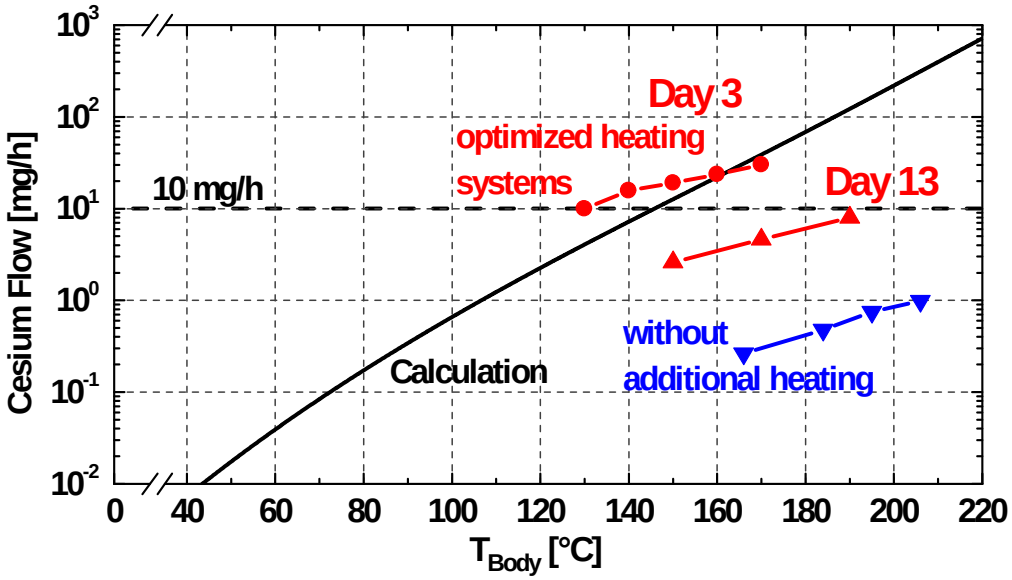


**Figure 5.12.:** Temperature dependence of the cesium flow from the evaporation oven, calculated by formula (5.3) in comparison with surface ionization detector measurements. Red: Flow from the oven with two additional heating system 3 days and 13 days after breaking the ampoule. Blue: Corresponding flow from the oven without additional heating system at the beginning of the campaign.

ration oven. However, there is still the need for improvement of the stability and reproducibility of the oven, since a time-dependent reduction of the cesium flow was detected for both configurations.
A significant decrease of the flow was detected two weeks after breaking the cesium ampoule and a body temperature of 190 °C was therefore necessary to release a comparable flow of 8 mg/h. According to the calculated values in figure 5.12, this is less than 10 % of the flow that can be expected from an oven at ideal operation conditions. A possible explanation for this effect is given in the next section.

### Kinetic Effects within the Cesium Evaporation Oven

The measured flow from the evaporation oven shows a long-term kinetic effect. It is most probably related to the evaporation dynamics and chemical reactions within the oven. A drop of elemental cesium, known for its instability to chemical reactions, is released after breaking the glass-ampoule. The cesium inside the oven permanently evaporates from the drop, where cesium is stored in a bulk with

a small surface area. At the operation temperature of the system, the cesium is re-distributed within the oven until the entire inner surface area of the body pipe is homogeneously covered with cesium layers. The resulting large surface area is disadvantageous regarding chemical reactions.
Based on the experimental results from section 5.1 and 5.2, cesium layers are vulnerable to chemical contamination under the vacuum conditions of the negative-ion source. This results in a strong decrease of the vapor pressure. Initially, very thick layers of pure cesium are formed inside the body because of the large amount of cesium that is released from the ampoule. After several days of operation, re-distribution and possible contamination processes may have significantly changed the properties of cesium inside the evaporation oven.
In order to maintain a constant cesium flux from the oven, the temperature of the components has to be increased to compensate for the decrease of the cesium vapor pressure by chemical reactions. This corresponds to experimental observations in MANITU. The temperature of the cesium oven has to be increased continuously during an operational period of the ion source (1 month per ampoule) in order to obtain an equivalent effect like at the first days after breaking the ampoule [Kra09].
As a consequence, a permanent monitoring of the cesium flow into the negative-ion source will be required in order to maintain a given injection rate. This monitoring signal from the SID can be used as a feedback system for the oven temperature in order to maintain a constant cesium injection rate. The SID was successfully applied for the long-term monitoring of the cesium flow from the evaporation oven under ion source typical conditions. This has demonstrated the long-term stability and reliability of the cesium ionization detector that was designed within the scope of this work.
Nevertheless, the use of the SID system for online monitoring at the IPP test facilities is still a big step, since there are additional requirements. For example, the long-term stability of the SID to particle bombardment by the backstreaming ions and the plasma from the driver needs to be tested.
The vulnerability of the liquid cesium within the evaporation oven to chemical contamination is inevitable for the given vacuum conditions. This effect is even more pronounced for the given configuration of the liquid reservoir-based oven, since there is no valve system. A valve could stop the contamination of the liquid cesium by impurities from the test facilities that enter the oven at the inactive phases of the ion source during the nights and weekends.
A promising approach to solve the encountered deficiencies by chemical contam-

ination in general is the use of dispensers, as described in chapter 4.2.7, in place of cesium ampoules. The cesium in dispensers is stored in chemically stable compounds that are less vulnerable to chemical contamination. It is difficult to use unprotected dispensers in a plasma environment, since the thermal load by the discharge interferes with the temperature control by the heating current. Hence, it is necessary to operate the dispenser in a dispenser oven that protects them from plasma exposure.

## 5.3.2. Cesium Dispenser Oven Prototype

A prototype of a cesium oven based on cesium release from a dispenser (see section 4.2.7), instead of the previously used thermal evaporation process, was developed and tested with the surface ionization detector. Tests of the performance and stability of this prototype oven are required in order to evaluate the dispenser oven concept for the cesium injection at the IPP test facilities. Furthermore the prototype dispenser oven is intended to be used as a flexible, small-scale cesium source for experiments at the University of Augsburg.
The main objective of this test of a prototype dispenser oven was to investigate, if it is possible to control the cesium flow entirely by the dispenser current. This includes the evaluation of re-distribution effects and the determination of the reaction time of the oven. Fundamental investigations of the performance and stability of SAES dispensers at negative-ion source relevant conditions are presented in [Wim10].
An experimental setup similar to the one for the flow measurement from the evaporation oven was used. However, because of the limited capacity of the available SAES dispensers of 10 mg, the monitoring time was limited to several hours.

### Results

Figure 5.13 shows the results of the surface ionization measurement of the atomic cesium flow from the dispenser oven, containing a 10 mg dispenser. Cesium release was measured 3 min after applying a dispenser current $I_{\mathrm{disp}}$ of 6 A and a stable cesium flow of 2 mg/h was measured for a time period of 1.5 h. A decay time of 40 min was observed after switching off the dispenser, related to the decrease of the cesium vapor pressure in the oven. After the cesium signal decreased to a low level below 0.2 mg/h, the dispenser was again heated with 6 A, resulting in an immediate recovery of the signal with a reaction time of

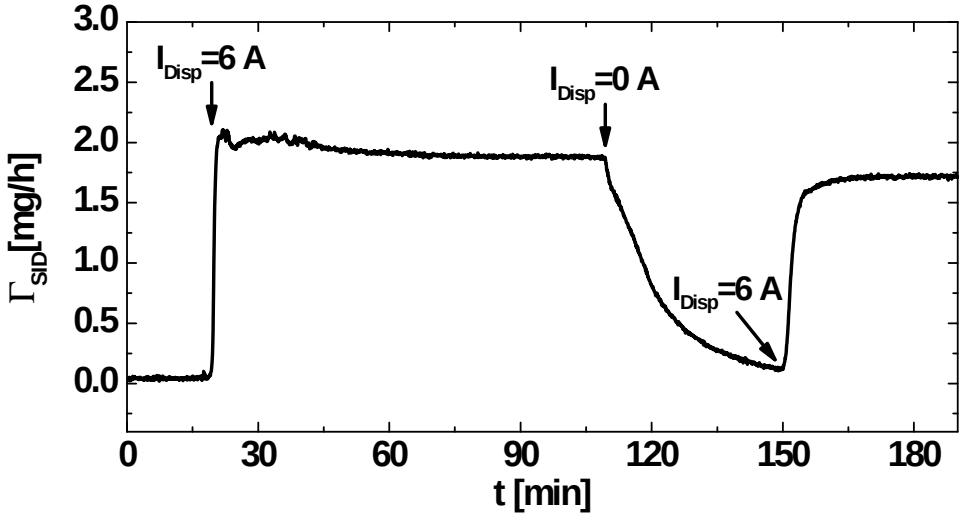


**Figure 5.13.:** Surface ionization signal of the atomic cesium beam from a prototype dispenser oven. A total cesium flow of 2 mg/h is obtained for a heating current of 6 A.

1 min. The corresponding flow is comparable to the flow at the beginning of the test. Hence, the reaction time of the dispenser oven is by a factor of 10 shorter in comparison to the liquid reservoir-based oven.
Thus, it is possible to control the cesium flow entirely by the heating current of the dispenser with a reaction time (dispenser on) of a few minutes. A stable cesium signal with no interference by uncontrolled thermal desorption effects during the test period of several hours was obtained. Further investigations with dispensers that contain several 100 mg of cesium at a monitoring time similar to the test of the evaporation oven are, however, required in order to evaluate the advantages of the dispenser oven in comparison to the liquid reservoir based system.
However, a different type of commercial cesium dispenser from ALVATEC[1] will be used for these long term studies. This type of dispenser, called ALVASOURCE, contains a cesium inventory of several 100 mg that can be released at moderate heating currents below 10 A, while dispensers from SAES with an comparable amount of cesium require heating currents of 60 A.
Besides tests with a larger reservoir, it will be required to check the operation of the dispenser-oven during plasma exposition. The SID measurement is restricted to vacuum operation only, however, it is possible to use the OES to monitor the 852 nm line of atomic cesium. A detailed overview of these test will be presented in [Fri12] and [Wim10].

[1] Alvatec Production and Sales GesmbH, Eisenstrasse 62, 9330 Althofen, Austria.

# 6. Simulation Results from CsFlow3D

The experimental results regarding the desorption of cesium layers from heated metal samples (see section 5.1) and cesium injection rates from the IPP cesium evaporation oven (see section 5.3) were used as input parameters in the CsFlow3D code, as described in section 4.3. Calculations were carried out in order to investigate the following aspects of the cesium transport within the IPP RF-driven negative-ion source:

- cesium loss through the apertures;
- distribution of the accumulated cesium on the walls of the negative-ion source;
- intensity and dynamics of the cesium flux onto the plasma grid during short and long-pulse operation;
- evaluate new ways of cesium injection for advanced control and homogeneity of the cesium flux onto the plasma grid;

The results of these investigations are important input for understanding transport processes and to enhance the performance of the ion source. New ways of cesium injection can be evaluated by comparing them with the results of CsFlow3D for the present ways of cesium injection and re-distribution.

## 6.1. Cesium Transport during the Vacuum Phase

The most intense cesium flux within the negative-ion source is obtained in close proximity to the nozzle system of the cesium evaporation oven. Knowledge of

the flow properties of the cesium flux from the nozzle system is therefore required as basic input parameter for any cesium transport simulation. The total cesium injection rate of the IPP evaporation oven (see section 4.2.6), determined by surface ionization detection, was used as input parameter for the computation of the cesium flow profile from the nozzle system.

### 6.1.1. Nozzle Flow Profile

Cesium vapor from the nozzle system of the evaporation oven expands into the vessel of the negative-ion source and forms a rarefaction flow. A schematic view of the cesium oven and the nozzle system is given in figure 3.9.
Cesium is transported into the ion source by a system of three orthogonal nozzles. A computation of the axi-symmetric cesium flux from a single nozzle of this system was done. The total flux profile was determined by coupling the flows from the individual nozzles that point in three directions. The profile from a single nozzle depends on geometric factors. An important quantity is the aperture ratio $a$ of the nozzle that is defined as:

$$a = \frac{l}{d}, \tag{6.1}$$

where $l$ is the length and $d$ the diameter of the nozzle.
For the special case of an ideal orifice, where the aperture ratio is negligible small $a << 1$, a cosine-distributed cesium flow profile is obtained [Küg09]. A non-negligible aperture ratio of $a = 1$ is obtained for the nozzle geometry of the IPP evaporation oven. Thus, a certain amount of cesium particles are adsorbed on the hot walls within the nozzle and re-distributed, causing a backscattering of cesium particles into the conduction pipe. This results in an effective narrowing of the flow profile and a reduction of the opening angle.
The cesium flux profile for the nozzle geometry of the IPP cesium evaporation oven was determined by a DSMC simulation [Bir94], considering a total cesium flux of 10 mg/h (see section 5.3) as input parameter. A projection and statistical sampling of the particle parameters from the Monte Carlo simulation on a computational grid was done in order to resolve the profile of the cesium flow.
A cesium flux at free molecular flow conditions is established within the nozzle, which is a consequence of the small dimension of the nozzle aperture with respect to the mean free path of cesium atoms (cm range) in the system.
The result of the computation of the axi-symmetric flow from a single nozzle is given in figure 6.1. In comparison to the cosine-distributed flow profile (blue)

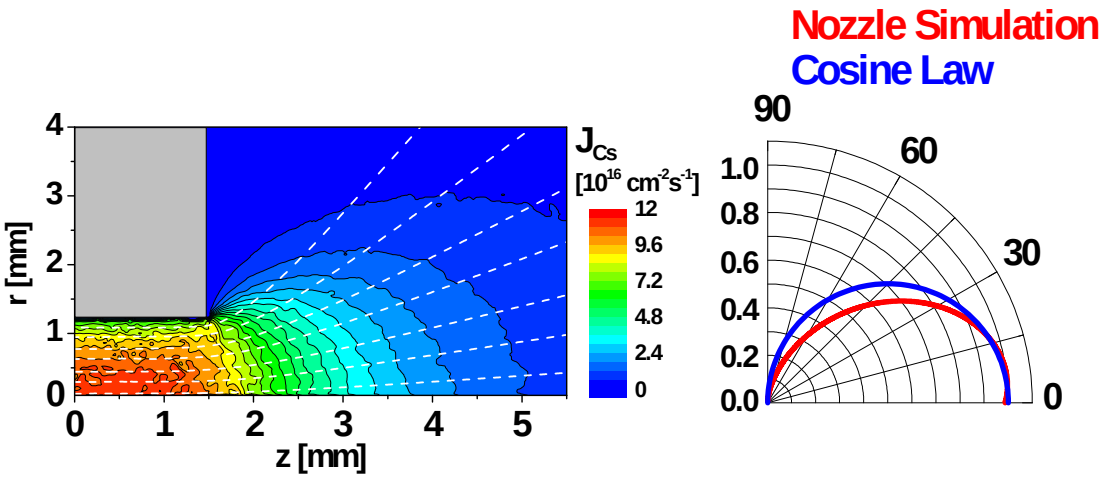


**Figure 6.1.:** Simulation results of the radial (left hand side) and angular (right hand side) flux density profile through a single nozzle of the evaporation oven, in use at the IPP. A total injection rate of 10 mg/h is considered for evaporation with three nozzles.

from an ideal orifice, the computed profile (red) is significantly narrowed. Cesium gas leaves the nozzles at a maximum flux density of $1.2\text{x}10^{17}$ $\text{cm}^{-2}\text{s}^{-1}$ that is significantly reduced in the first millimeters of the rarefaction process by the expansion into the chamber of the ion source. The computed, narrowed flow profile was used as an initial parameter for the simulation of the injection of cesium into the negative-ion source by CsFlow3D.

## 6.1.2. Cesium Distribution

### Cesium Loss

An important aspect regarding the dynamics of cesium within the negative-ion source test facilities is the loss of cesium. A multi-aperture extraction system that is transparent to flows of neutral particles is used for the beam formation process. Positively charge particles, such as cesium ions, are retained inside the ion source during extraction. However, neutral cesium is able to leave the ion source and either condenses on the electrodes of the extraction system or expands into the vacuum tank system of the test facilities. This vacuum chamber has a large volume and surface area in comparison to the negative ion-source vessel, acting as a sink for cesium.

The corresponding chamber that is planned for the ITER neutral beam injector

will even have significantly larger dimensions. Furthermore, this system will have additional electrodes for the 1 MV acceleration (see section 2.3.5). Cesium, lost through the apertures, is potentially harmful for the voltage holding capability due to covering the insulator and enhancing secondary electron emission as seen in MANITU.

A calculation of the cesium losses by using kinetic theory and the vapor pressure of elemental cesium leads to obvious discrepancies with experimental observations. The approximating of the cesium losses through the apertures based on the vapor pressure equilibrium (see figure 4.3) results in a aperture loss flux of $1.5\text{x}10^{14}$ $\text{cm}^{-2}\text{s}^{-1}$ for a wall temperature of 20 °C and $2.4\text{x}10^{15}$ $\text{cm}^{-2}\text{s}^{-1}$ for a temperature of 50 °C. Considering the transparent area of MANITU of 200 $\text{cm}^2$, cesium losses of 23 mg/h and 368 mg/h are expected, respectively. Both values exceed the typical injection rate from the evaporation oven of 10 mg/h.

The corresponding predictions are in disagreement with experimental observations of significant cesium retention within the ion source. A cesium effect on the source performance is noticeable even after several days without cesium injection. Experimental investigations of cesium desorption with a microbalance (see section 5.1) showed a higher surface affinity than expected for elemental cesium. This results in the formation of multiple layers of cesium-containing compounds at the temperature conditions of the chamber walls of the negative-ion source. Thus, the vapor pressure of elemental cesium is not adequate to predict the cesium losses through the apertures.

Therefore, the CsFlow3D code was used to determine the cesium losses for a realistic cesium surface affinity. Experimental data of the temperature dependent sticking coefficient $s$ (see section 5.1) and a standard cesium injection of 10 mg/h (see section 5.3) were considered in the calculation. According to the results from the thermal desorption experiment, only a small amount of cesium is accumulated on samples for temperatures higher than 90 °C. Hence, the amount of cesium on the hot plasma grid ($T_{\text{pg}}$ = 150 °C) is very small in comparison to the cesium accumulation on the cold ($T_{\text{walls}}$ = 26 - 47 °C) chamber walls. The sticking $s$ of cesium on the plasma grid was approximated with $s = 0$.

Figure 6.2 shows the simulated cesium losses during a vacuum phase of MANITU considering wall sticking coefficient of $s$ = 1 - $10^{-3}$. The cesium loss flux $\Gamma_{\text{loss}}$ was found to be inversely proportional to the sticking coefficient $s$ of cesium on the chamber walls.

In case of a high sticking coefficient of $s = 1.0$, the total cesium flux from the evaporation oven is absorbed from the surface areas, where the particles hit the

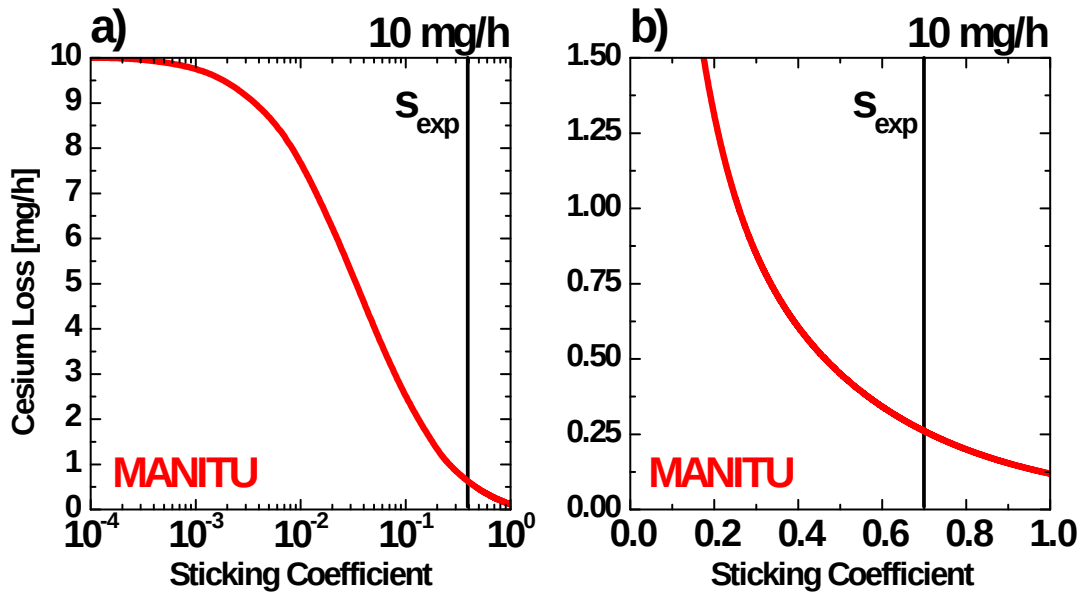


**Figure 6.2.:** a) Simulated loss flux of cesium vapor through the extraction system of MANITU during the vacuum phase in dependence of the sticking coefficient on the chamber walls, representing different temperature conditions using a logarithmic scale. b) Loss flux at a linear scale for the experimentally determined sticking coefficient.

ion source walls. The cesium distribution is in this case determined by the profile of the cesium flux from the evaporation oven. The loss flux is related to the fraction of the flow profile that forms a direct line-of-sight with the transparent areas of the plasma grid. As the nozzles of the evaporation oven are directed onto the walls of the expansion chamber, there is only a small loss flux of $\Gamma_{\text{loss}} = 0.1$ mg/h.

Decreasing the sticking coefficient to $s_{\text{exp}} = 0.7$, as it was measured by the microbalance for a wall temperature of $T_{\text{wall}} = 47$ °C, results in a loss flux of $\Gamma_{\text{loss}} = 0.25$ mg/h. This is significantly lower than the loss calculated for the vapor pressure equilibrium. It shows that the experimentally derived sticking coefficient is high enough to retain a high fraction of the injected 10 mg/h in the ion source. The numerical calculations indicate that multiple layers of cesium are absorbed by the walls of the ion source. This accumulation of large amounts of cesium is in agreement with experimental observations of the presence of large cesium reservoirs on the inner walls of BATMAN and MANITU (see for figure 6.5 and 6.12) after an operation period. These periods can last up to several months.

A further decrease of the sticking coefficient to a value of $s = 0.1$ causes an increase of the simulated cesium loss rate up to 2 mg/h. The saturation of the loss

rate to the total injection rate of 10 mg/h takes place at a sticking coefficients of $s = 10^{-3}$. In the latter case, the injected amount of cesium cannot be balanced any more by the surface absorption. The cesium loss rate is then determined by the equilibrium flow according to the vapor pressure kinetics.
The computation on the basis of the experimentally determined sticking coefficients shows significantly lower cesium losses than expected from the consideration of the vapor pressure of pure cesium, where the loss of several mg/h of cesium would take place even for low wall temperatures of $T_{\mathrm{wall}} = 26$ °C. This reduced loss rate is beneficial for the voltage holding capability of the electrodes in the accelerator system for ITER.
Hence, the absorption of cesium on the chamber walls is the dominant loss mechanism at ion source relevant vacuum and temperature conditions and only a small amount of cesium is lost through the apertures. Nevertheless, the cesium absorption in large reservoirs on the source walls close to the oven prevents cesium from reaching the plasma grid. A permanent and intensive cesium flux onto the plasma grid is, however, required to keep the work function at low levels by balancing the formation of cesium compounds.
The location and extent of the cesium reservoirs, generated during the plasma-off phases, has an effect on the cesium conditions during the discharge. Plasma-generated cesium release (see section 4.3.4) from the chamber walls creates additional cesium sources during the discharge phases. The distribution of these cesium reservoirs on the source walls that are formed during the vacuum phases is therefore an important aspect for the properties of the cesiums flow during the discharge.

### Cesium Wall Accumulation

Figure 6.3 shows the simulated cesium accumulation rate during a vacuum phase of MANITU. Wall temperatures of $T_{\mathrm{wall}} = 47$ °C ($s = 0.7$) and $T_{\mathrm{pg}} = 150$ °C ($s = 0$) were considered in CsFlow3D for the standard cesium injection rate. The simulation includes the adsorption and re-distribution from the source walls by thermal evaporation. Especially intense cesium accumulations are formed on the surfaces close to the nozzle system of the evaporation oven. Three maxima with an accumulation rate of $5\mathrm{x}10^{13}$ cm$^{-2}$ s$^{-1}$ were determined to appear on the backplate. This is an effect of the orientation of the cesium flow from the nozzles of the evaporation oven that points on the bottom- and sidewalls.
Figure 6.4 shows line plots of the accumulation rate on the side- and backplate

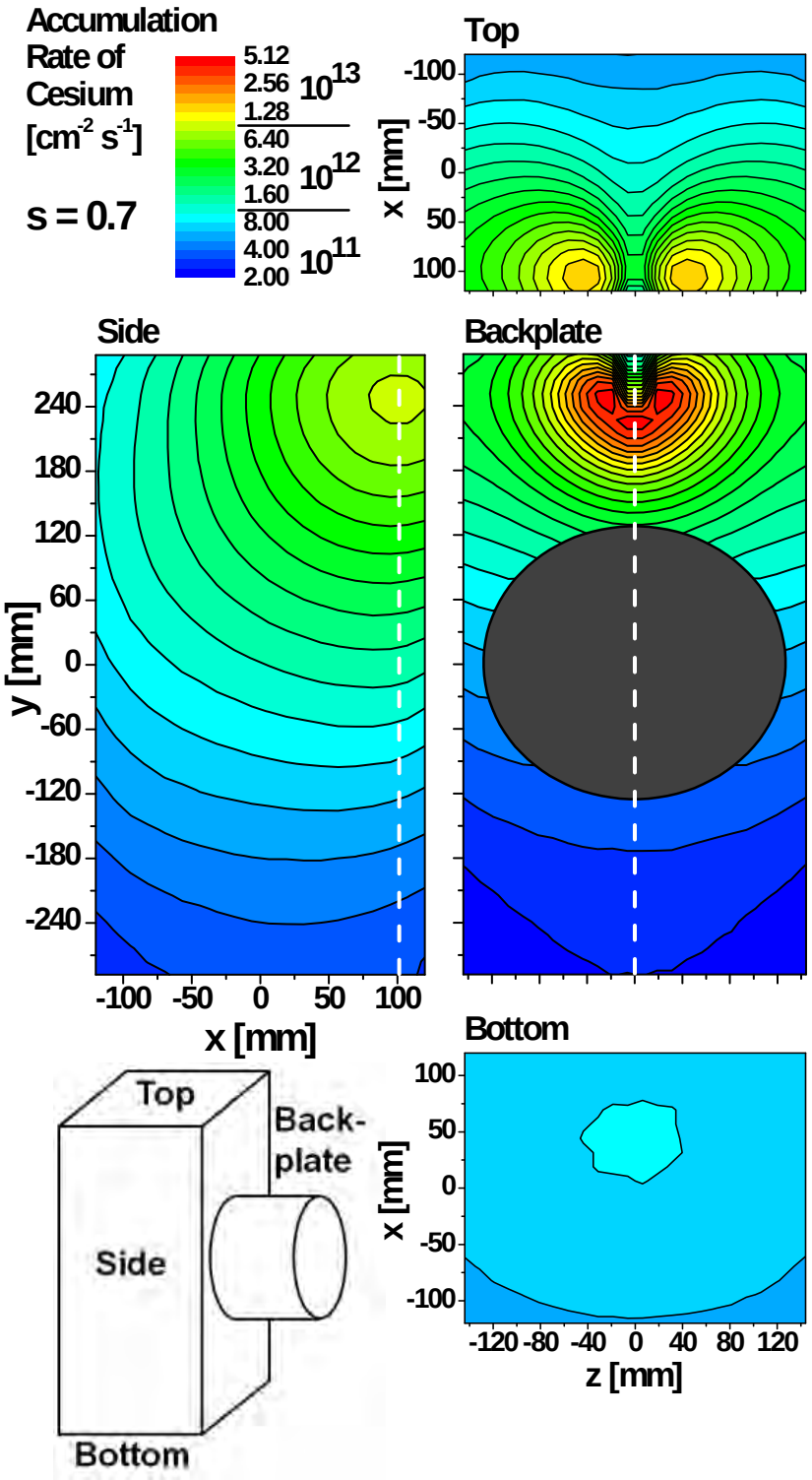


**Figure 6.3.:** Computed accumulation rate of cesium in MANITU during the vacuum phase for a sticking coefficient of $s = 0.7$, corresponding to a wall temperature of 47 $^oC$, and a total cesium influx of 10 mg/h.

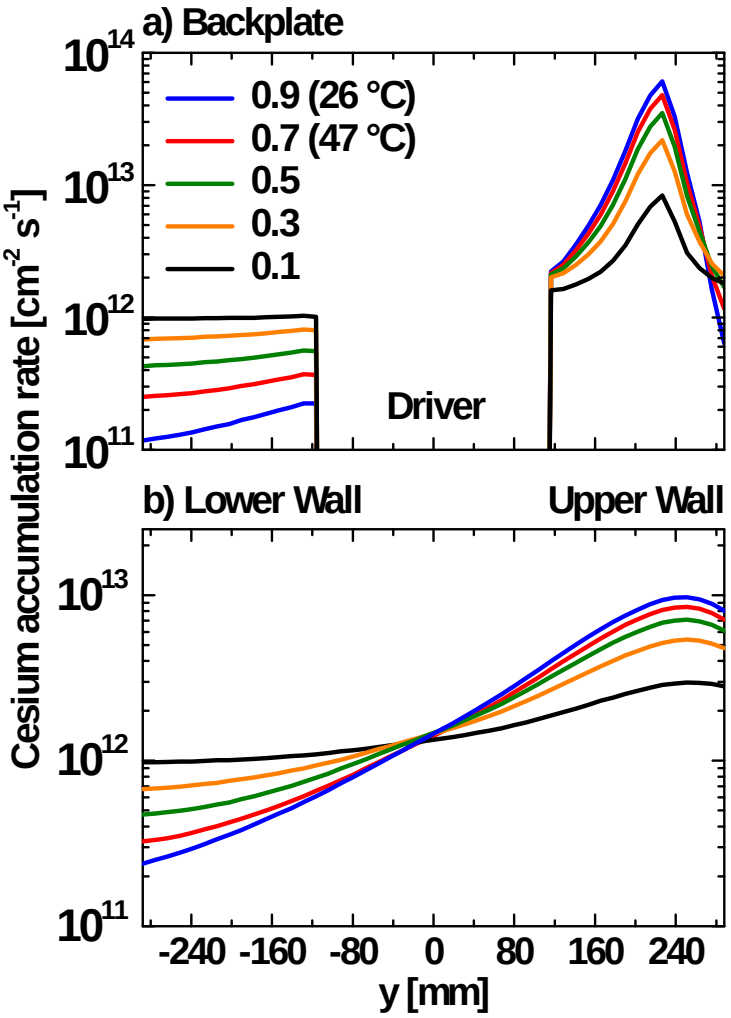


**Figure 6.4.:** Line plots of the simulated cesium accumulation rate on the backplate a) and on the upper and lower walls b) of MANITU along the white line in figure 6.3 for different wall sticking coefficients.

of the ion source along the highlighted dashed lines in figure 6.3. Peaks of the accumulation rate with respect to the center of the flow from the specific nozzle appear on the backplate and the upper wall.

As a result of the surface affinity of the cesium, the accumulation pattern is determined by both the profile of the nozzle flux and the re-distribution of cesium that is not adsorbed on the walls. In case of a wall sticking coefficient that is higher than 0.7, as determined for a wall temperature below 47 °C, the cesium distribution within the ion source is predominantly influenced by the flow profile from the nozzle system and inhomogeneous accumulation profiles are created. The effect of intensive cesium re-distribution becomes the most important factor

at sticking coefficients below 0.1 and the flow profile from the evaporation oven is negligible.
This transition can be accomplished by raising the surface temperatures or by reducing the amount of surface impurities. In case of a very low sticking coefficient, the cesium accumulation rate is more equally distributed within the source chamber. Surface areas that are at remote locations regarding the position of the cesium oven are supplied with cesium at the expense of the surface areas in the vicinity of the evaporation oven.
The results of the simulation are compared to the desorption flux of elemental cesium in the vapor pressure equilibrium in order to clarify the influence of the increased surface affinity. A desorption flux of $2\text{x}10^{15}$ cm$^{-2}$ s$^{-1}$ is expected from the vapor pressure at $T_{\text{wall}} = 47$ °C (see figure 4.3). This flux is by a factor of 40 higher than the total deposition rate of $7\text{x}10^{13}$ cm$^{-2}$ s$^{-1}$ in close proximity to the oven. In this case, the influx from the oven is compensated by thermal desorption processes and the geometry of the oven is insignificant. This results in an evenly distributed cesium flux onto all walls that is determined by the equilibrium of the cesium vapor pressure and the losses through the extraction system.

### Qualitative Comparison with Experimental Results

The presented results from CsFlow3D are qualitatively supported by the investigation of the walls of the disassembled ion source of MANITU after the evaporation of 1000 mg of cesium during a source operation period of 1 month. Two different types of clearly visible, stable cesium compound layers were identified ex-situ:

1. Black, blue-shimmering layers were observed on the copper walls.
2. White layers were observed on the molybdenum-coated backplate.

A photograph of these layers is given in figure 6.5. Several tests with a pH indicator showed the alkaline character of both substances. It was possible to identify both compounds from the table 4.1 by their color:

- The white substance was identified as hygroscopic cesium hydroxide CsOH and is formed by a reaction of Cs with $H_2O$ at atmospheric pressure after breaking the vacuum to open the ion source

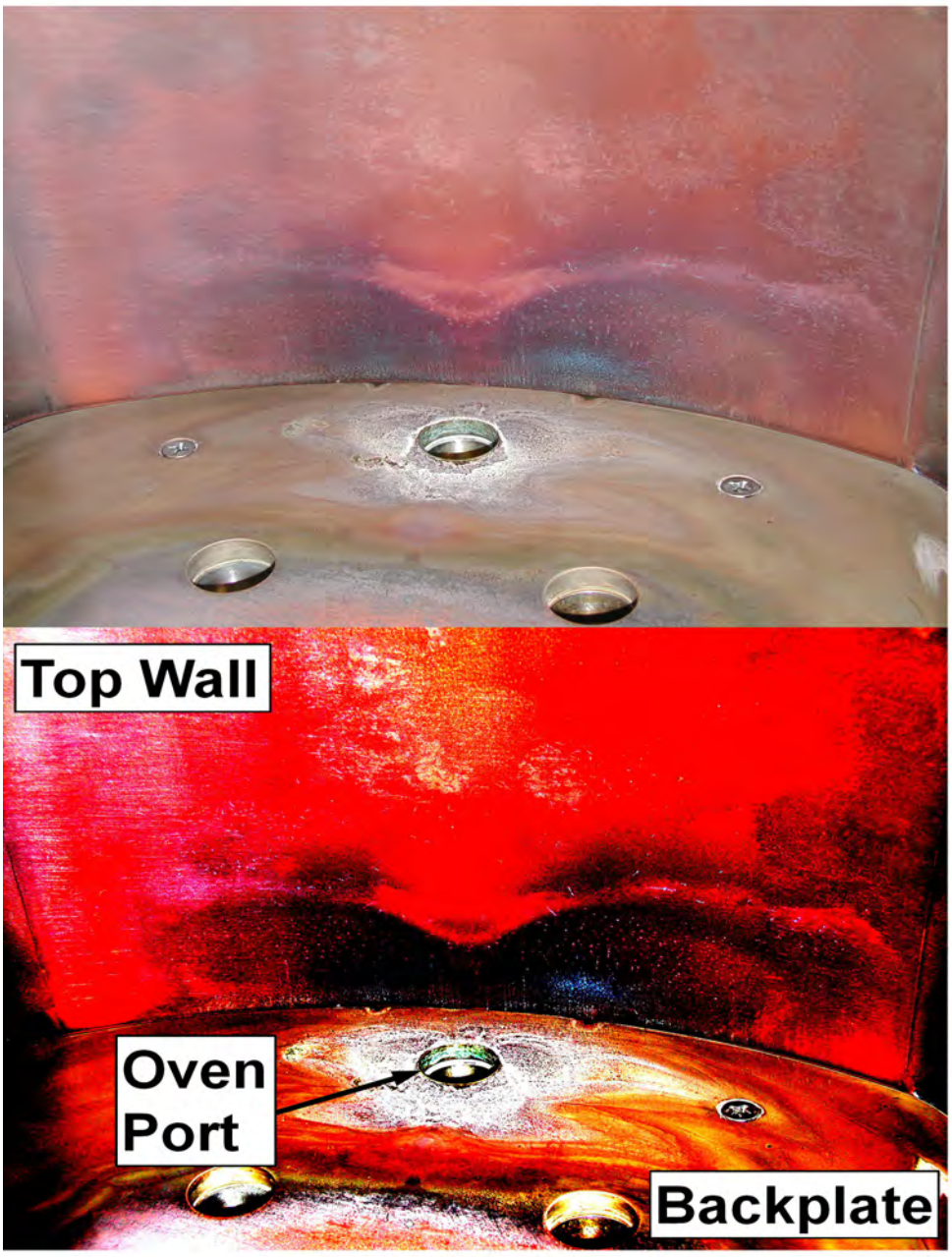


**Figure 6.5.:** Raw (upper) and high contrast (lower) photograph of the backplate (molybdenum-coated) and the upper wall (copper) of the ion source of MANITU after the evaporation of 1000 mg of cesium. The nozzle system of the evaporation oven is located at the marked port.

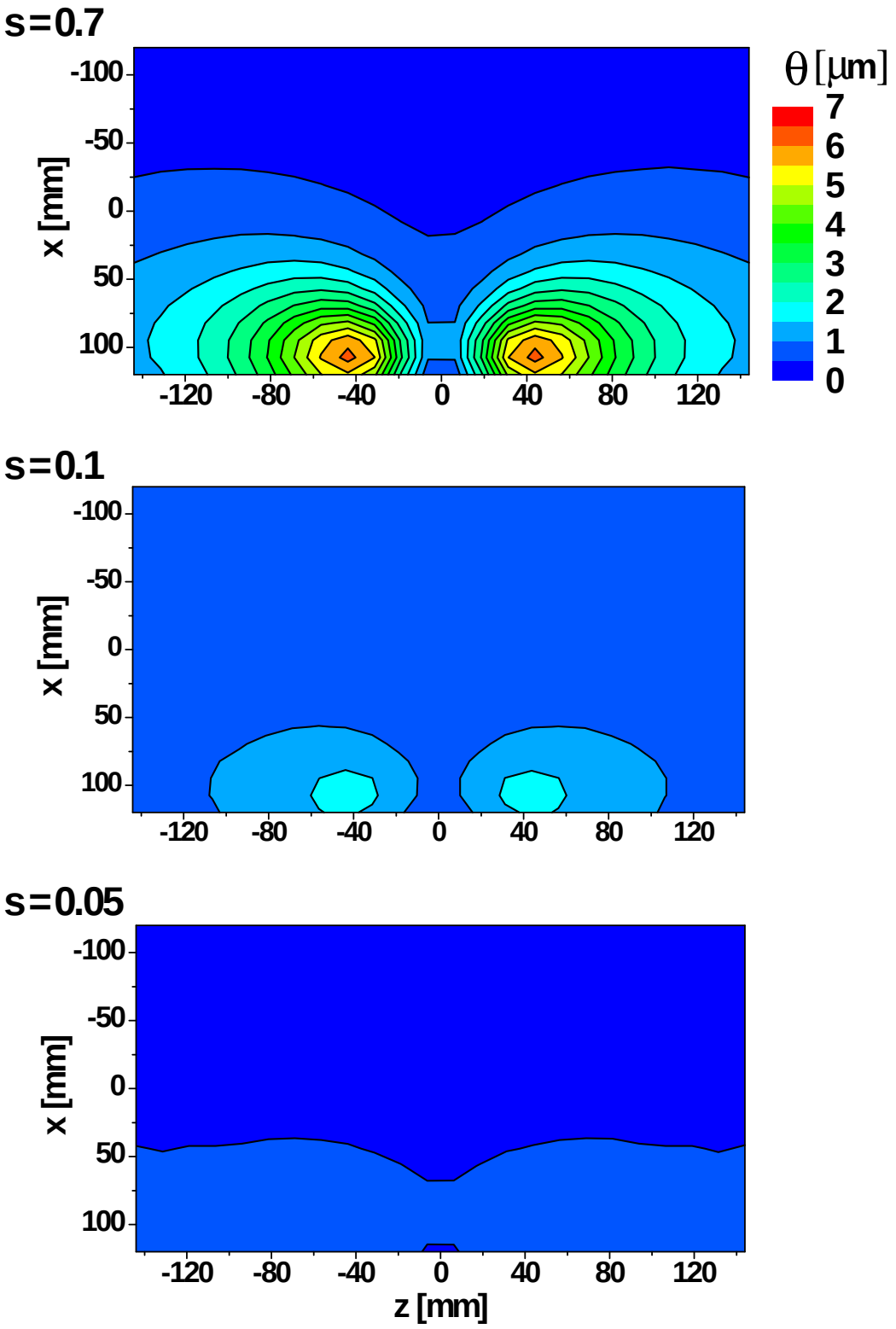


**Figure 6.6.:** Predicted thickness of the cesium layers on the upper wall of the ion source of MANITU after the evaporation of 1000 mg of cesium during the plasma-off phase at an influx of 10 mg/h for sticking coefficients of $s = 0.7$, $s = 0.1$ and $s = 0.05$.

- The black substance was identified as cesium oxycuprate $CsCuO_2$ that can be formed by a reaction of Cs with $H_2O$ and $O_2$ in combination with Cu from the walls of the ion source.

The minimum thickness of these layers can be estimated by the Lambert law [BS04]. This law states that a layer is visible if its thickness $\theta$ exceeds $\theta_{\min} \geq \frac{\lambda}{4}$, where $\lambda$ is within the range of the wavelength of visible light. This shows that the visible cesium layers must exceed a thickness of $\theta_{\min} = 200$ nm $= 400$ ml. A layer thickness of several thousand monolayers of cesium compounds is expected as a consequence of the high visibility of the layer structure. Nevertheless, this ex-situ analysis does not allow conclusions to be drawn on the chemical state of cesium before the vacuum of the source was broken.
The distance from the nozzle of the evaporation oven to the surface of the upper wall of the ion source is very short ($< 3$ cm). Therefore, the broadening of the flux profile by collisions with background particles during the plasma phase is not significant. Hence, the deposition profiles onto this specific area are very similar during the plasma and the vacuum phase of source operation.
Figure 6.6 shows the integrated cesium accumulation on the upper wall, predicted by CsFlow3D, after the evaporation of 1000 mg of cesium using the sticking coefficient of $s = 0.7$, 0.1 and 0.05. The computed profile for a sticking coefficient of $s = 0.7$ shows the formation of two lobe-shaped cesium deposition structures with a maximum layer thickness of 7 $\mu$m at the center of each lobe. These correspond to the directions of the nozzles of the evaporation oven. The structures are less pronounced for a sticking coefficient of $s = 0.1$. This results in a maximum accumulation of 1.7 $\mu$m and a more homogeneous distribution of the accumulated cesium compounds over the entire upper wall. A simulation with $s = 0.05$ shows an evenly distributed deposition with layer thickness of $\theta < 500$ nm that would be barely visible in the experiment.
The simulated deposition profile using the experimentally determined sticking coefficient for a wall temperature of 47 °C is in good qualitative agreement with the observed cesium accumulations on the upper wall of the negative-ion source. This gives additional experimental evidence regarding the increased affinity of cesium on the walls of the ion source. Large quantities of cesium are stored in stable reservoirs on the ion source walls. These are inactive during the vacuum phase for the given temperature conditions. A recycling process of cesium from specific surface areas takes place, however, during the discharge. Cesium that is not bonded to the chamber walls can contribute to the flux onto the plasma grid. This process will be discussed in the next section.

### 6.1.3. Cesium Flux onto Plasma Grid

The work function measurements during vacuum and plasma phases (see section 5.2) indicate that a permanent flux of elemental cesium onto the plasma grid is required in order to maintain a stable negative-ion production. This cesium flux onto the plasma grid was calculated for a wall temperatures of 26 °C and 47 °C and for the standard cesium injection rate. Similar to the previous simulations, the sticking of cesium on the plasma grid ($T_{\mathrm{pg}} = 150$ °C) was approximated by $s = 0$. Figure 6.7 shows the predicted cesium flux onto the plasma grid for the specified source wall temperatures.
A typical cesium flux of the order of $10^{12}$ cm$^{-2}$ s$^{-1}$ was calculated for the given sticking coefficients. This is by a factor of ten lower than the flux from the dispenser in the experiments to determine the work function of a cesium coated metal sample (see section 5.2). Thus, a less efficient regeneration of the plasma grid work function is expected during the vacuum phases of ion source operation than observed in the laboratory experiment.
The results of the calculation show in both cases an inhomogeneity regarding the cesium flux profile and the flux onto the upper area of the plasma grid is by a factor of three more intense than the one onto the lower area. This effect is caused by the position of the nozzle system with respect to the plasma grid as a consequence of the following effects:

- The profile of the direct flux of cesium from the nozzle system onto the plasma grid is more intense on the upper regions, which is as a result of the closer proximity to the nozzles of the evaporation oven. Hence, the circular flow pattern from the evaporation nozzles is especially pronounced for a high sticking coefficient of 0.9.

- The cesium flux onto the plasma grid is partly composed of cesium coming from the walls of the ion source. The intensity of the re-distributed flux is related to the number of wall interaction during the transport process. Reducing the sticking coefficient to 0.7 and below results in an enhancement of this effect.

Cesium transport from the nozzle system to remote areas, such as the lower part of the plasma grid, requires more wall interactions than it is required for the transport to areas in closer proximity to the nozzle. The increased number of wall reflections to reach distant areas results in a higher absorption of cesium on

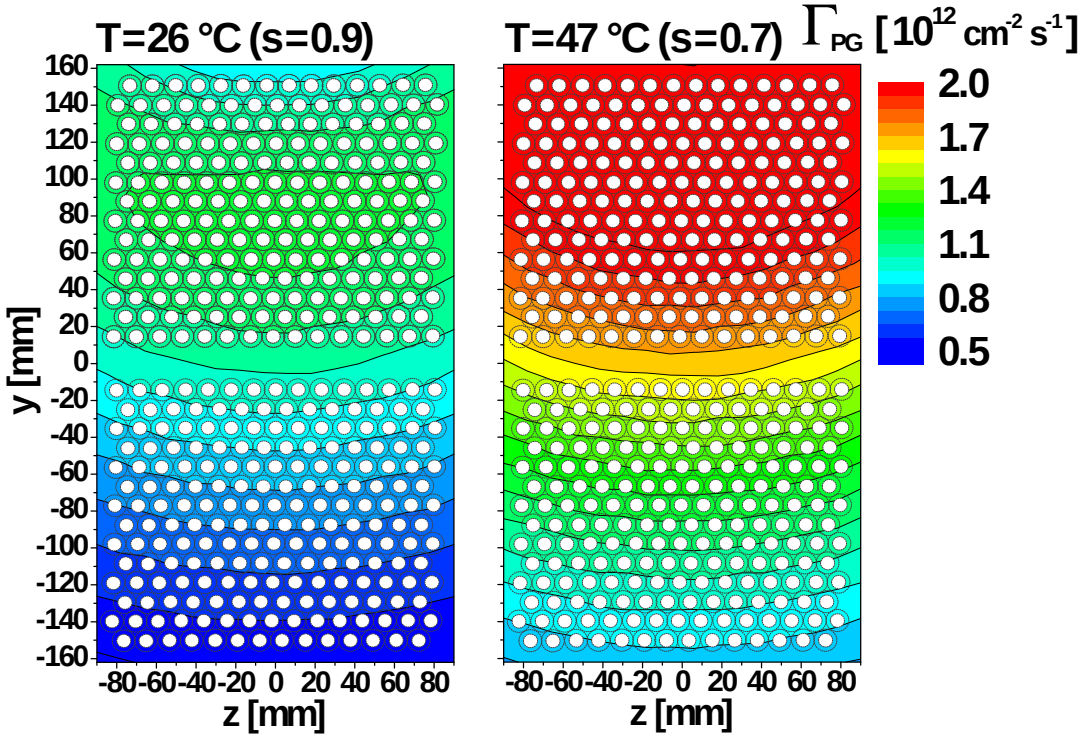


**Figure 6.7.:** Contour plots of the cesium flux on the plasma grid of MANITU during a vacuum phase, considering a wall sticking coefficient of $s = 0.9$ and $s = 0.7$ for a cesium injection rate of 10 mg/h.

wall surfaces. Thus, more cesium is lost during transport to the lower areas of the plasma grid than it is the case for the transport to the upper areas.

The cesium flux on the plasma grid can be increased by lowering the sticking coefficients of the source walls. Decreasing the sticking coefficient from $s = 0.9$ to $s = 0.7$, corresponding to an increase of the wall temperature from 26 °C to 47 °C, results in a significant increase by a factor of two of the cesium flux onto the plasma grid. The cesium flux onto the plasma grid in case of a wall temperature that is lower than 47 °C is determined by both, the flux profile of the evaporation of and re-distribution effects from the source walls.

According to the measurement of the work function dynamics, the increase of the cesium flux at a higher wall temperature is expected to be more efficient to regenerate a fresh cesium layer on the plasma grid. This is required to counteract the observed deterioration by contamination processes. A beneficial effect on the source performance is therefore expected in case of a wall temperature of 47 °C.

A limitation of the total cesium flux onto the plasma grid is created by losses through the apertures and by the absorption of cesium on the chamber walls,

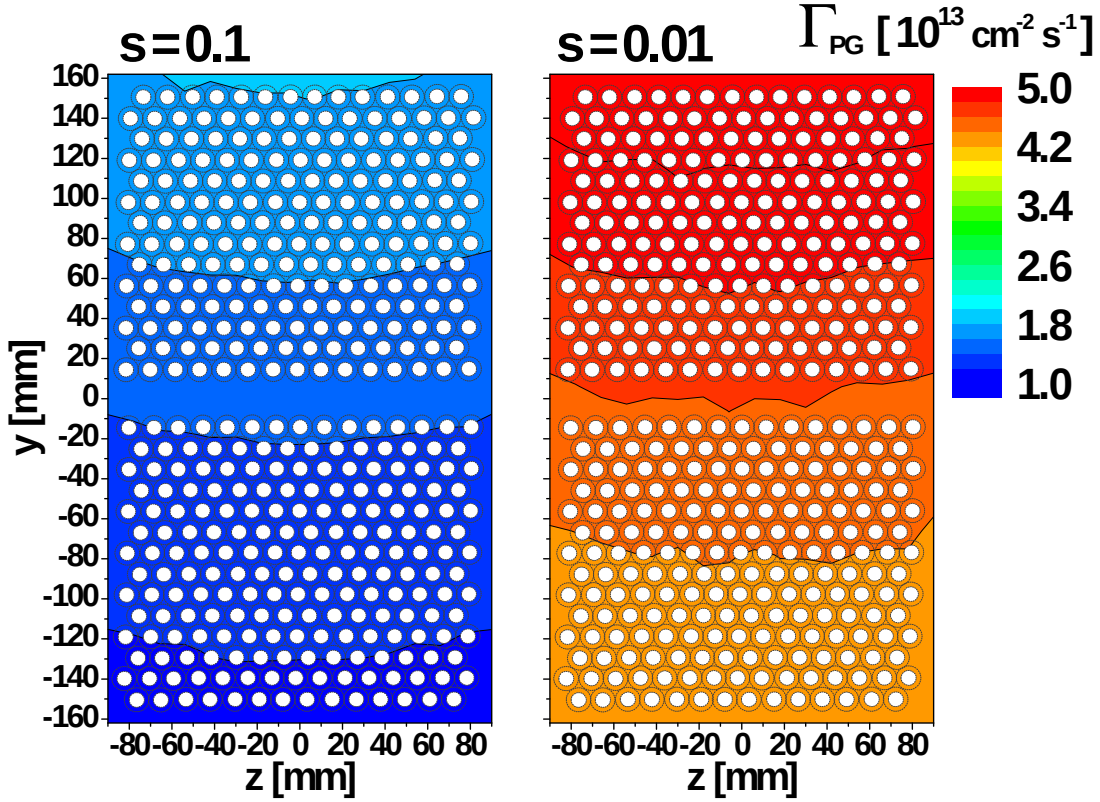


**Figure 6.8.:** Contour plot of the cesium flux on the plasma grid of MANITU during a vacuum phase for a sticking coefficient on the chamber walls of $s = 0.1$ and $s = 0.01$, considering a total injection rate of 10 mg/h.

which was the dominant factor in the previous computations. Hence, the cesium flux onto the plasma grid was investigated for the case that cesium re-distribution from the source walls dominates the flux profile of the cesium oven. A further reduction of the sticking coefficient to $s \ll 0.7$ is required to create this physical situation. This can be either related to changes of the chemical conditions of the surfaces that may take place during the operational period of the source or related to an increase of the wall temperature to $T_{\mathrm{wall}} \gg 50$ °C.

The cesium flux onto the plasma grid was therefore computed for significantly lower wall sticking coefficients of $s = 0.1$ and $s = 0.01$. An experimental determination of the corresponding wall temperature was limited by the accuracy of the microbalance. A sticking coefficient of 0.1 is approximately reached at wall temperatures higher than 70 °C, while a sticking coefficient of 0.01 requires probably a wall temperatures above 90 °C. Results of the calculations for the sticking coefficients $s = 0.1$ and $s = 0.01$ are given in figure 6.8.

Similar to the dependence of the cesium loss rate, the cesium flux onto the

plasma grid during the vacuum phase is inversely proportional to the sticking coefficient. A significantly higher total cesium flux of the order of $10^{13}$ cm$^{-2}$ s$^{-1}$ that is predominantly created by the flux contribution from the walls is predicted by the transport simulation for a low sticking coefficient of 0.1. In this case less cesium is retained on the source walls. The obtained flux is comparable to the one that was used for the experiments to reduce the work function of a cesium-coated sample. Thus, a similar time-dependence and absolute value of the work function is expected during the vacuum phases of ion source operation. Lowering the sticking coefficient has also an effect on the flux distribution. Flux inhomogeneities caused by the position of the nozzle system are compensated by frequent wall reflections. These create an evenly distributed cesium flux on the chamber walls and the cesium flux onto the plasma grid becomes independent of the source geometry or position of the oven.
A decrease of the sticking coefficient to $s = 0.01$ results in a further increase of the cesium flux onto the plasma grid by a factor of four and a significant improvement of the relative homogeneity. The dominant cesium loss term becomes the cesium outflux through the aperture system. At the standard injection rate, the available total flux onto the plasma grid is thereby limited to 6.5x10$^{13}$ cm$^{-2}$ s$^{-1}$ for negligible losses on the source walls.

### 6.1.4. Comparison to Experimental Results

The transport computation predicts a factor of two more intense cesium flux onto the plasma grid during the vacuum phase by increasing the wall temperature from 26 °C to 47 °C, considering the sticking coefficients described in section 5.1 for the surface affinity. A positive effect of increasing the wall temperature on the source performance was observed in BATMAN (see section 3.2.2).
A continuous increase of the source performance by the number of (short) plasma pulses is observed after the first day of cesium injection until a saturation takes place. Figure 6.9 shows the development of the extracted negative-ion current after breaking the cesium ampoule in the oven for a wall temperature of $T_{\mathrm{wall}} =$ 20 °C and $T_{\mathrm{wall}} = 50$ °C. Periodic fluctuations of the extracted current density are related to the development of the source performance during the individual days of operation, as explained in section 5.2.
The trend of the source performance over several days shows that the overall time for the source to be conditioned is reduced when the wall temperature is

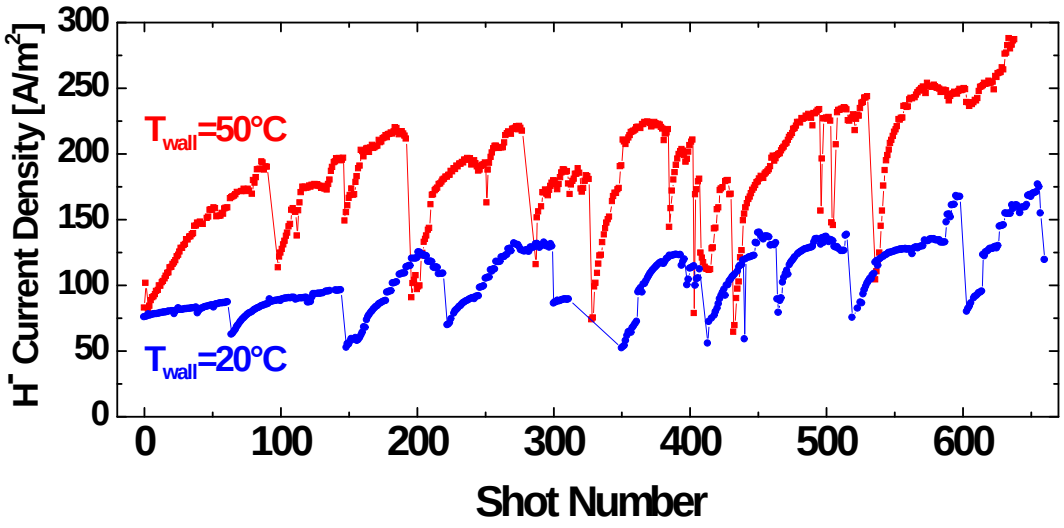


**Figure 6.9.:** Evolution of the extracted negative-ion current in BATMAN for conditioning with source wall temperature of 20 °C (blue) and an elevated temperature of 50 °C (red).

increased. A higher performance is achieved after a shorter time using a wall temperature of 50 °C for the given shots. It is, however, in some cases possible to obtain an equivalent source performance also at 20 °C, taking into account a considerably longer conditioning time, which may be not available.

The CsFlow3D code predicts a further increase of the cesium flux onto the plasma grid by using wall temperatures of $T_{\mathrm{wall}} > 70$ °C that correspond to sticking coefficients below 0.1. This might result in a further reduction of the conditioning time, but at the expense of higher cesium losses through the apertures, which may be disadvantageous for the voltage holding capabilities of the source.

The formation of thermally-stable cesium reservoirs on the source walls results in a limitation of the effective cesium flux onto the plasma grid during the vacuum phase. These reservoirs can be activated by several processes (see section 4.3.4) during the discharge phases. This results in the generation of additional cesium sources on specific surfaces that are investigated in the next section. The distribution of the cesium reservoirs, computed in the vacuum phase, is used as an initial parameter for the simulation of the cesium transport during the discharge phase.

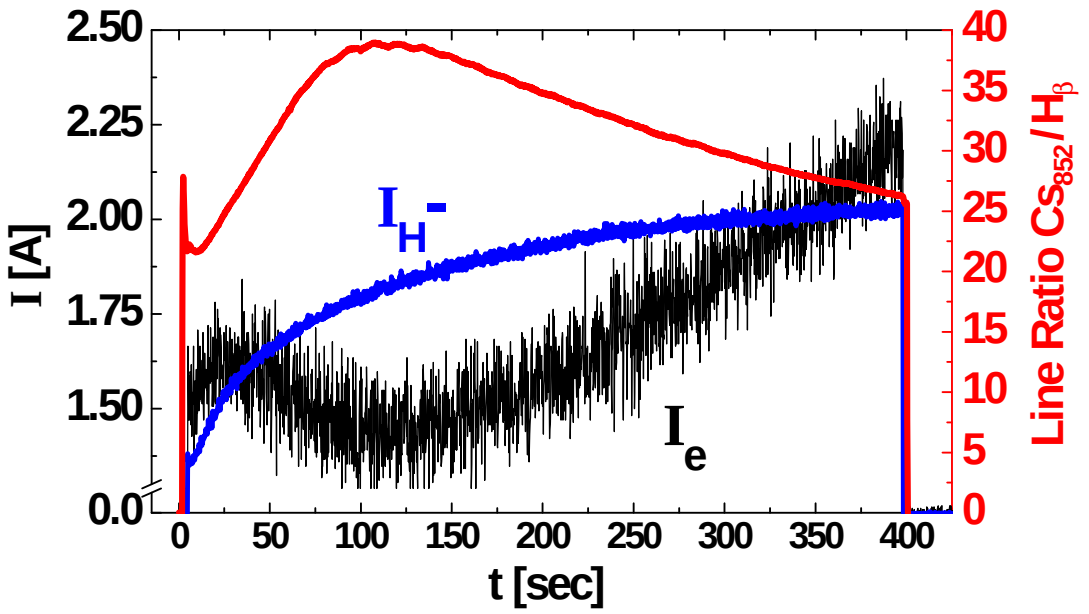


**Figure 6.10.:** Extracted electron and negative-ion current during a 400 sec plasma pulse ($H_2$, 0.4 Pa, 65 kW) in MANITU with the corresponding line ratio of the Cs 852 nm to the $H_\beta$ line from the OES.

## 6.2. Cesium Transport during the Discharge Phase

The cesium re-distribution during the discharge is different from that during the preceding vacuum phase. Besides the generation of additional cesium sources, the transport process of cesium in the plasma is significantly changed (see section 4.3.2). Collisions with background particles change the properties of the cesium flows that are emitted by the surfaces and the evaporation oven. Ionizing collisions with plasma electrons generate cesium ions that are affected by electric and magnetic field within the ion source.

Negative hydrogen ions are produced from neutral and ionic hydrogen particles that are converted on the plasma grid surface in a plasma environment. Operating the negative-ion source at ITER-relevant parameters requires a cesium flux onto the plasma grid that is homogeneous in space and stable in time. The required time-stability can be satisfied easily during short pulses of up to several seconds, but long pulses of up to one hour at a relevant source performance need a more advanced cesium control mechanism.

Figure 6.10 shows the measured electron $I_e$ and ion $I_{H^-}$ currents during a 400 sec pulse in MANITU together with the corresponding neutral cesium signal from the optical emission spectroscopy, measured in 2.5 cm distance parallel to the plasma

grid. The time trace of the extracted negative-ion current saturates after 200 sec and is then stable during the remaining pulse duration, despite of the fluctuation of the electron current and the density of atomic cesium. This behavior indicates a saturation of the work function and the corresponding negative-ion production during intensive cesium exposition of the plasma gird. A similar behavior at an equivalent time scale was observed during the work function measurement of a molybdenum sample that is exposed to a cesium flux during the discharge, as described in section 5.2.
Furthermore, this pulse demonstrates the following effect: the increase of the electron current after a pulse duration of 100 sec is correlated with the Cs852 line. As long as the cesium signal rises, the electron current is lower than the negative-ion current. As soon as the cesium signal saturates or starts to decline, the co-extracted electron current increases [KFF+09]. The effective length of the pulse is limited until the electron-generated thermal loads on the extraction grid exceed the operational limits of the extraction system (see section 3.2.1). The correlation between the co-extracted electron current and the cesium conditions is observed during the majority of pulses, but is not mandatory for every pulse. It is possibly a physical effect in the plasma volume that is generated by the altered cesium conditions on the plasma grid.
The first step to understand these effects are simulations of the cesium transport within the negative-ion source. These are required to understand the dynamics of the cesium signal and to correlate it with measurements of the extracted ion and co-extracted electron current. The cesium transport during the discharge, considering a preceding vacuum phase as initial condition, was computed with the CsFlow3D code.

### 6.2.1. Cesium Re-distribution during the Discharge

#### Cesium Erosion and Re-Distribution within the Expansion Chamber

A simulation of the cesium re-distribution within the negative-ion source was done for a plasma pulse duration of 20 sec after a vacuum phase of 240 sec, which are typical conditioning parameters in MANITU [Kra09]. The simulation was done for a constant cesium evaporation rate of 10 mg/h and a wall temperature of 47 °C ($s = 0.7$) during both, the preceding vacuum and the discharge phase. Similar to the previous computation, negligible cesium sticking was assumed on the plasma grid ($T_{\mathrm{PG}} = 150$ °C). Input parameters regarding the desorption of

cesium by the interaction with the discharge are explained in section 4.3.4. For the sake of simplicity, the simulation of the cesium dynamics during the plasma phase is always done for enabled extraction voltage, considering the effect of backstreaming ions.
Figure 6.11 shows the simulated cesium accumulation on the walls of MANITU after the discharge. Significant removal of cesium, deposited during the preceding vacuum phase (see figure 6.3), from the backplate and the side walls of the ion source is predicted by the simulation. This is an effect of cesium sputtering by plasma particles and highly energetic backstreaming ions, as described in section 4.3.4.
The cesium is transported from surface areas that are exposed to a high ion flux onto areas, where the cesium removal is less effective. Thus, erosion zones are formed close to the driver exit, where there is a high plasma density and on the backplate as a result of the backstreaming ion flux. Deposition zones are formed on the surfaces in the extraction region, where there is a lower plasma density and where there are no backstreaming ions. Figure 6.14 b) shows the computed cesium deposition on the bias plate after a 20 sec plasma pulse for a previous vacuum phase of 240 sec.
The separation of the inner surface areas of the ion source in erosion and deposition zones is a result of the variation of the plasma density across the source, which is an effect of the geometric distance to the driver and the presence of the magnetic filter field. This creates an effective route for the transport of cesium. Cesium is released from surface areas that have intense contact with the plasma (side walls) or backstreaming ions (backplate). Deposition takes then place in the extraction region where there is no activation of the reservoirs.
The simulation predicts a depletion of the cesium reservoirs at the back- and side walls of the ion source, close to the driver. Backstreaming ions contribute to the erosion at the backplate of the ion source. Their current density on the backplate is determined by the projection of the aperture pattern of the plasma grid. The surface area close to the cesium oven where the highest cesium deposition rate is predicted by the codes is, however, not included in this projection. The erosion profiles on the side walls of the source chamber are created due to the wall projection of the plasma that expands from the driver into the ion source vessel.
Nevertheless, large quantities of cesium cannot be activated by the plasma and are lost for future use. This process forms an effective sink for the cesium transport during the vacuum and discharge phases of the ion source on areas with low plasma exposition. Examples for such areas are the top wall and especially the

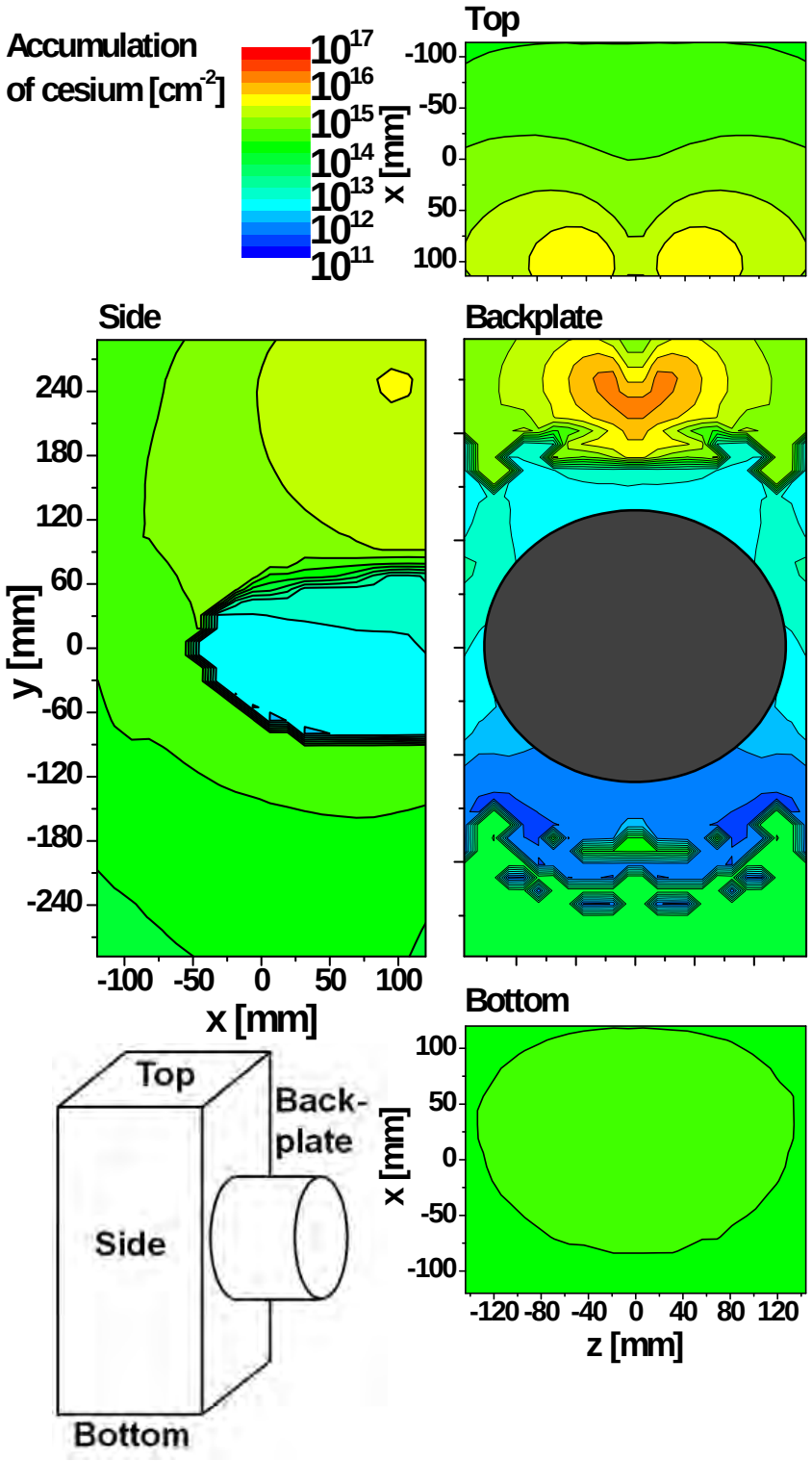


**Figure 6.11.:** Simulated cesium distribution on the walls of MANITU after a vacuum phase of 240 sec followed by a plasma phase with a pulse duration of 20 sec at a constant cesium injection rate of 10 mg/h.

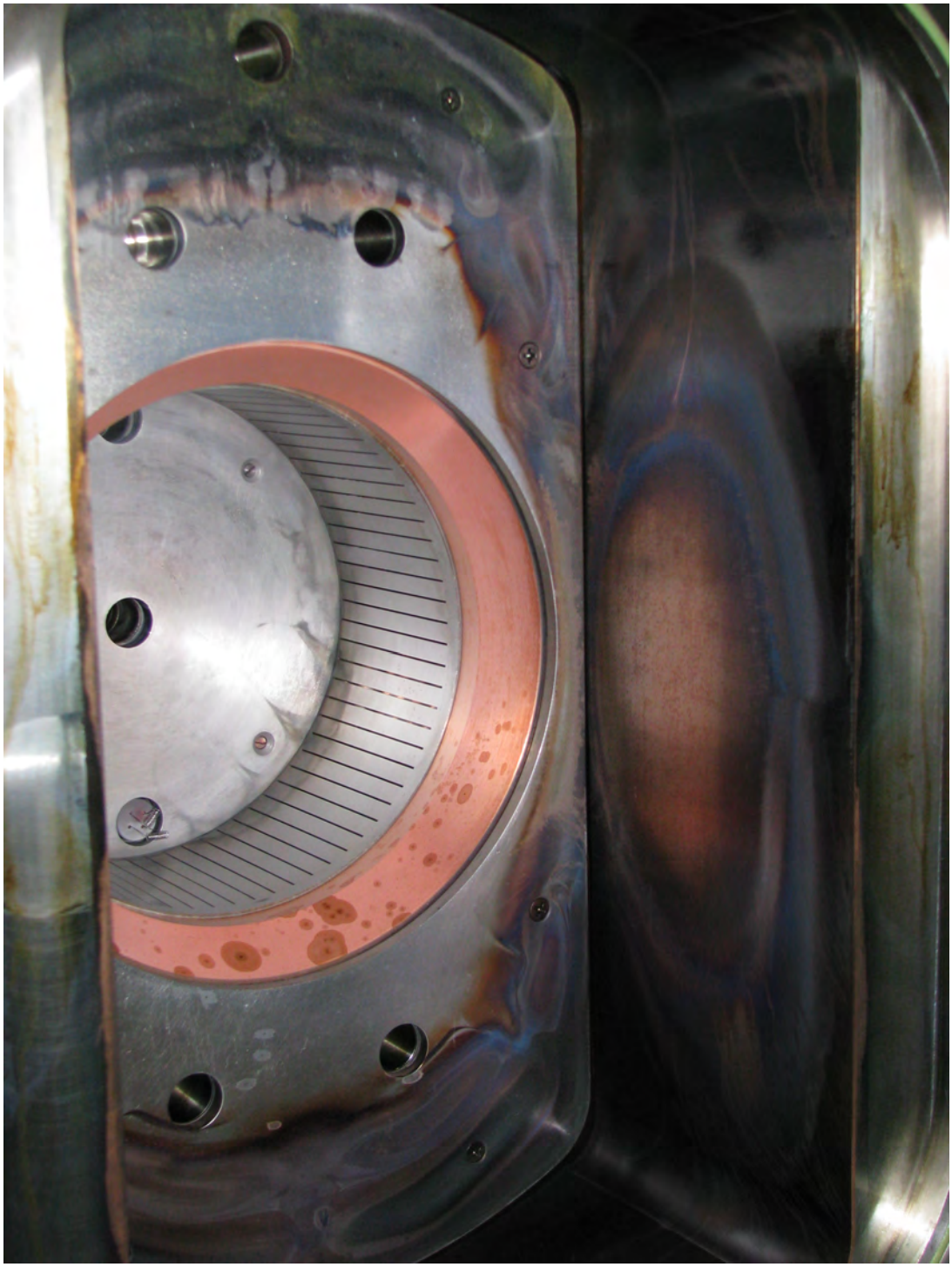

**Figure 6.12.:** Photograph of the erosion and deposition traces of cesium in MANITU after an operational period where 3 ampoules of cesium were injected. The walls of the ion source were heated to 50 °C during source operation.

area on the backplate close to the oven. These inactive reservoirs stay passive during the total operation time of the ion source until their removal by the cleaning of the disassembled source chamber. This enhances unnecessarily the cesium consumption of the ion source.

### Comparison with Experimental Results

A qualitative comparison of the simulated cesium traces with photographs of the inner walls of the chamber after opening the ion source at the end of an operation period was done. The cesium deposition in MANITU after a long operation period with a high total cesium injection of 3000 mg is shown in figure 6.12. This particular operation period was used in order to demonstrate the effects of cesium erosion during the plasma phases on the distribution within the source chamber. The circular areas at the driver exit are formed by drops of cesium hydroxide solution that flow to the bottom of the ion source.
Intensive traces of cesium erosion were detected on the backplate and the side walls of the source vessel. Furthermore, the rectangular erosion pattern on the molybdenum-coated backplate corresponds to the projection of the extraction area, which is an effect of the backstreaming ions. Thus, the simulation results are in qualitative agreement with the experimental observation. It was possible to identify the different erosion effects by comparing the observations with the results from the transport simulation.
A quantitative determination of the cesium accumulation on the lower wall of the ion source chamber was done by placing a metal sample on the bottom wall (see figure 6.11) of MANITU. The Rutherford backscattering method (RBS) that is described in [Fel86] was used to measure the amount of cesium, accumulated on the sample during ion source operation. A total amount of 1000 mg cesium was injected into the ion source for this particular experiment. The RBS measurement detected a cesium surface density of $1.3\text{x}10^{17}$ $\text{cm}^{-2}$ on the sample [Hop09]. Removing the cesium-coated sample out of MANITU required the sample, however, to be exposed to the atmosphere.
The cesium accumulation on the bottom wall was computed for a cesium injection of 10 mg/h and an integrated evaporation time of 100 h in order to validate the result from CsFlow3D by the RBS measurement. A simplified computation considering alternating vacuum and plasma phases of 240/20 sec and a wall temperature of 47 °C was done. The code predicts a total cesium accumulation of $2\text{x}10^{17}$ $\text{cm}^{-2}$ on the bottom wall. This is a good agreement considering that

the amount of cesium on the sample has probably changed under the influence of chemical reactions with water vapor during the exposure to atmospheric pressure. Thus, the assumptions made for CsFlow3D are reasonable to give a prediction of the cesium accumulation on the walls of the ion source that are not exposed to the plasma. The validation of the predicted cesium deposition on areas with intense plasma exposition is difficult because of the corresponding thermal dynamics of the sample itself.

### Cesium Deposition and Thermal Desorption from the Bias Plate

The computation of the cesium deposition on the bias plate (see figure 3.9 and photograph 5.5) that is located at a distance of $\Delta z = 1$ cm to the plasma grid is particularly important because of its close proximity to the plasma grid. Cesium release due to erosion close to the driver and from the backplate results in an effective cesium deposition onto the bias plate. In MANITU, the bias plate has no thermal connection to chamber walls of the ion source. Therefore, the bias plate has a different thermal dynamics than the walls of the ion source and its temperature stability is limited.
Figure 6.13 a) shows the measured time trace of the bias plate temperature during a long pulse in MANITU [FFK+07] for a RF-power of 58 kW. The thermal desorption flux of neutral cesium was determined by applying the dependence of the cesium desorption on the temperature, derived from the desorption experiments (see section 5.1.3). This desorption flux is shown in figure 6.13 b).
A significant desorption of the range of $10^{13}$ cm$^{-2}$ s$^{-1}$ is generated after a plasma pulse duration of 30 sec, when the bias plate exceeds a temperature of 80 °C. The equilibrium temperature of 170 °C is obtained after 240 sec. The associated flux of 3x$10^{14}$ cm$^{-2}$ s$^{-1}$ is by a factor of ten higher than the flux after 30 sec.
Hence, the short-pulse cesium dynamics is expected to be different than the long-pulse behavior, since the effect of thermal activation is more pronounced in the latter case. At first, the thermal desorption and accumulation of cesium onto the bias plate of the ion source in MANITU was simulated for short pulses. Thermal desorption processes regarding the bias plate were implemented in CsFlow3D by using the time-trace presented in figure 6.13 b).
Figure 6.14 shows the amount of cesium on the bias plate of MANITU, predicted by the code, after a vacuum phase a) and a subsequent plasma phase b). A maximum cesium deposition of 3.1x$10^{14}$ cm$^{-2}$ before and 4.3x$10^{14}$ cm$^{-2}$ after the discharge phase was computed for each pulse. Hence, the cesium reservoir on

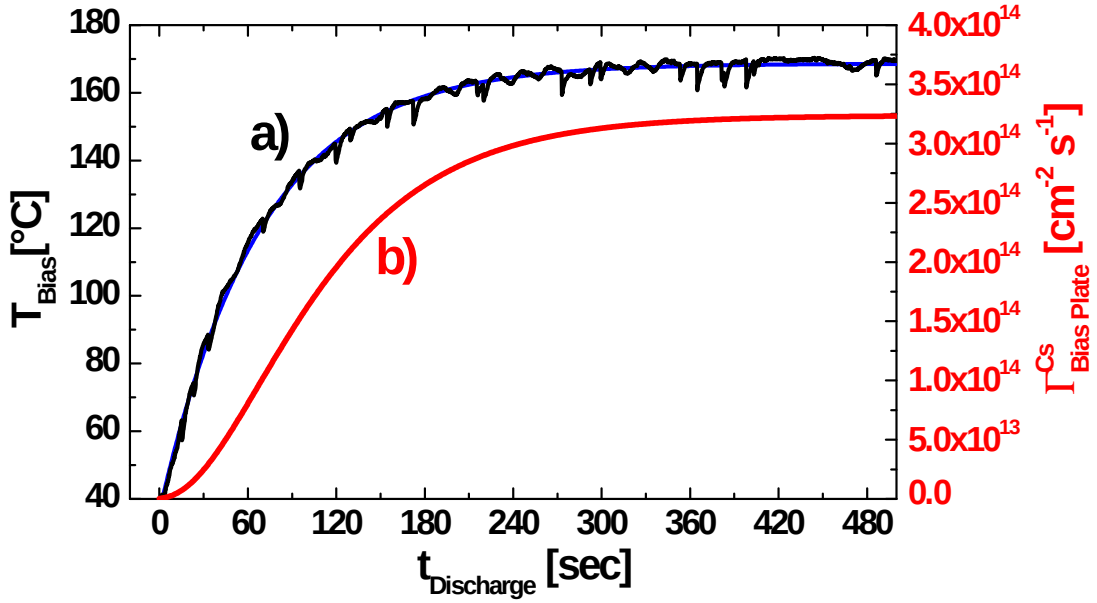


**Figure 6.13.:** a) Measured (black line) increase of the temperature of the bias plate during a 500 sec pulse in MANITU ($H_2$, 58 kW, 0.3 Pa). The blue curve represents a fit of the temperature dynamics that was derived from the measurement. b) Corresponding thermal desorption flux of neutral cesium from the bias plate.

the bias plate is increased during short pulses. The following conclusions can be drawn:

- The accumulation profile in both contour plots of figure 6.14 is asymmetric. It was shown in section 6.1.2 that the cesium accumulation during the vacuum phases is more pronounced in the upper areas of the ion source. Thus, a higher cesium accumulation is available for transport in the upper surface areas and more cesium can be deposited on the upper part of the bias plate.

- During short pulses ($<$ 20 sec), more cesium is deposited onto the bias plate than can be removed by thermal desorption. The temperature increase during short pulses is not high enough to balance the deposition processes. According to figure 6.13 b), thermal desorption from the bias plate is expected to become relevant for a long pulse duration of several hundreds of seconds when a bias plate temperature between 100 - 200 °C is reached. This effect is investigated in more detail in the following section.

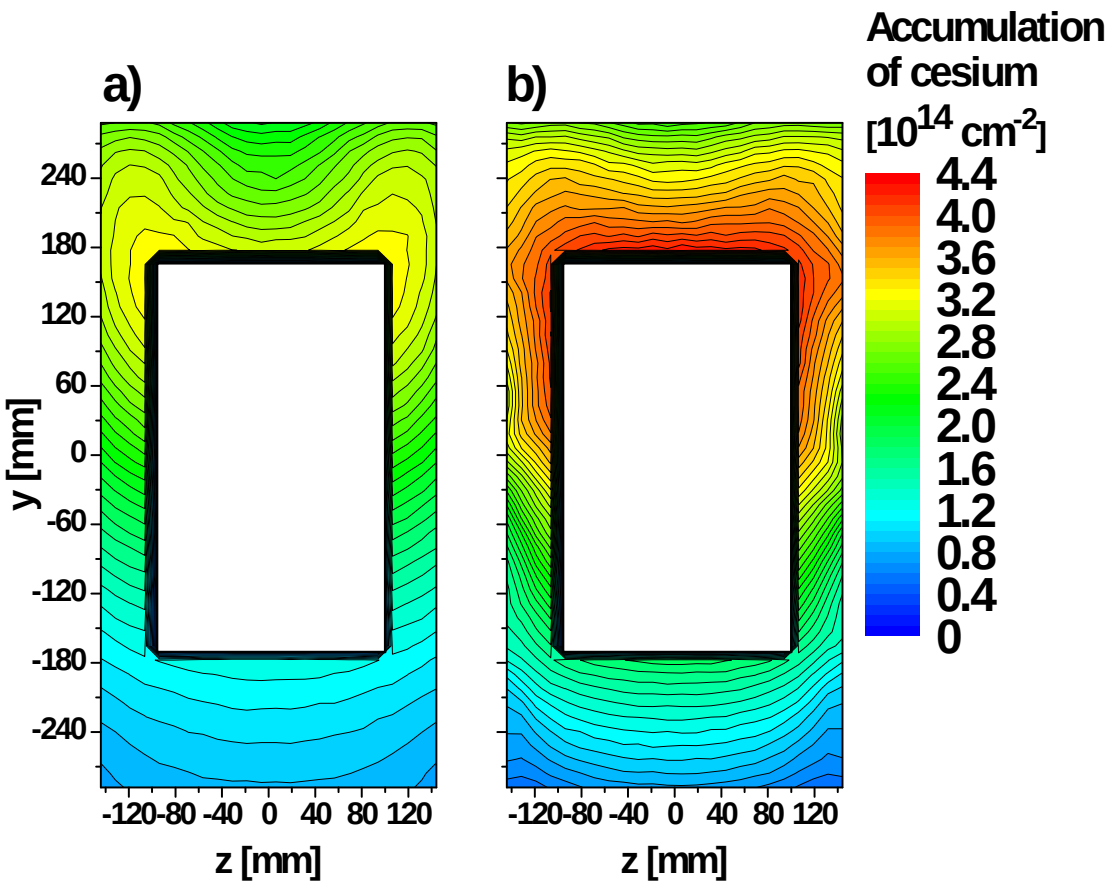


**Figure 6.14.:** Figure a): Computed cesium accumulation on the bias plate of MANITU after 4 min of cesium injection at 10 mg/h during a vacuum phase. Figure b): Computed cesium accumulation on the bias plate after 4 min cesium injection at 10 mg/h in the vacuum phase, followed by a discharge of 20 sec pulse duration.

### 6.2.2. Cesium Flux onto the Plasma Grid

The CsFlow3D code was used to simulate the cesium flux onto the plasma grid in MANITU during a 500 sec pulse after 100 short conditioning pulses with a length of 20 sec and preceding vacuum phases of 4 min. These are typical conditioning pulse times in MANITU [Kra09]. A cesium injection rate of 10 mg/h and a wall temperature of $T_{\text{wall}} = 47\ ^{\circ}\text{C}$ ($s = 0.7$) for the temperature controlled source walls was used in the simulation. Furthermore, a negligible sticking of cesium on the plasma grid was assumed, while the temperature data presented in 6.13 a) was used to consider the heating of the bias plate.

Figure 6.15 shows the simulated time traces of the cesium flux onto the plasma grid. The blue curve shows the time trace of the total cesium flux onto the

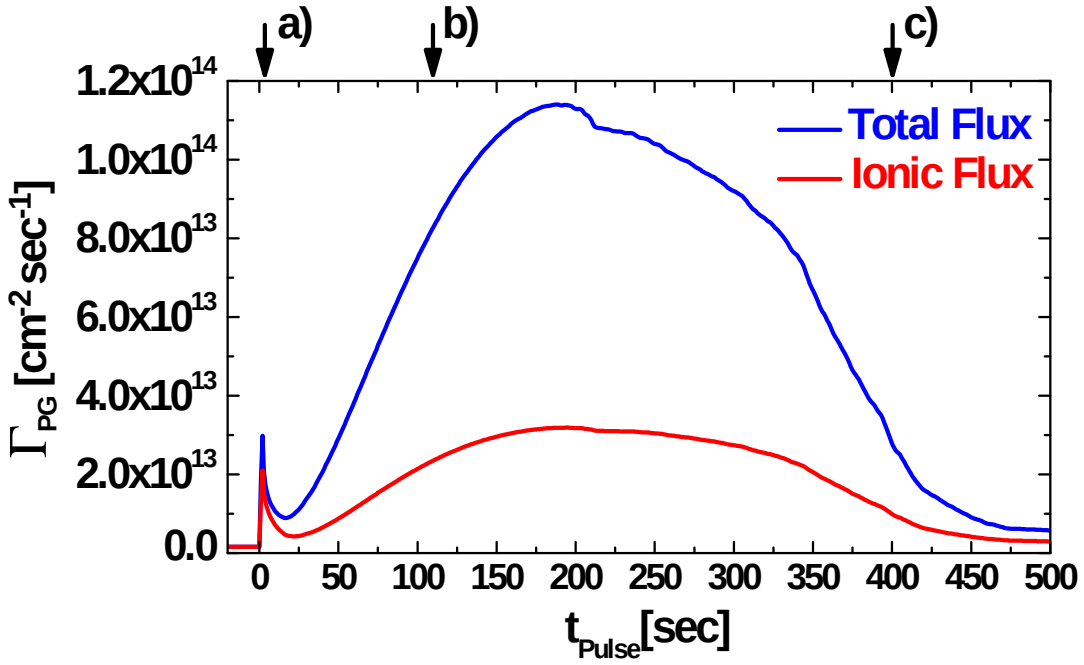


**Figure 6.15.:** Time trace of the total (blue) and ionic (red) cesium flux onto the plasma grid during a 500 sec plasma pulse in MANITU considering the increase of the bias plate temperature by the heat load from the plasma.

plasma grid, while the red curve shows the ionic contribution. An explanation of the computed time trace is given in the following sections.

### Cesium Release by Plasma-Wall Interaction

An initial peak of the simulated cesium flux onto the plasma grid within the range of 3x10$^{13}$ cm$^{-2}$ s$^{-1}$ is predicted by the simulation. This flux originates from both, the release of cesium by the interaction of the plasma and the backstreaming ions with cesium reservoirs, accumulated during the preceding vacuum phases. The contribution from the evaporation oven to the total flux is by a factor of ten lower and negligible in comparison to the cesium release from the reservoirs.
As shown in figure 6.11 and 6.12 of the previous section, the corresponding erosion zones for these processes are limited to the surface areas close to the driver exit and on the backplate of the expansion chamber. The associated high plasma density and electron temperature at these surfaces that is beneficial for cesium desorption result, however, in a short path length for ionization. At a typical electron temperature of $T_e = 8$ eV and density of $n_e = 10^{18}$ m$^{-3}$ near the driver

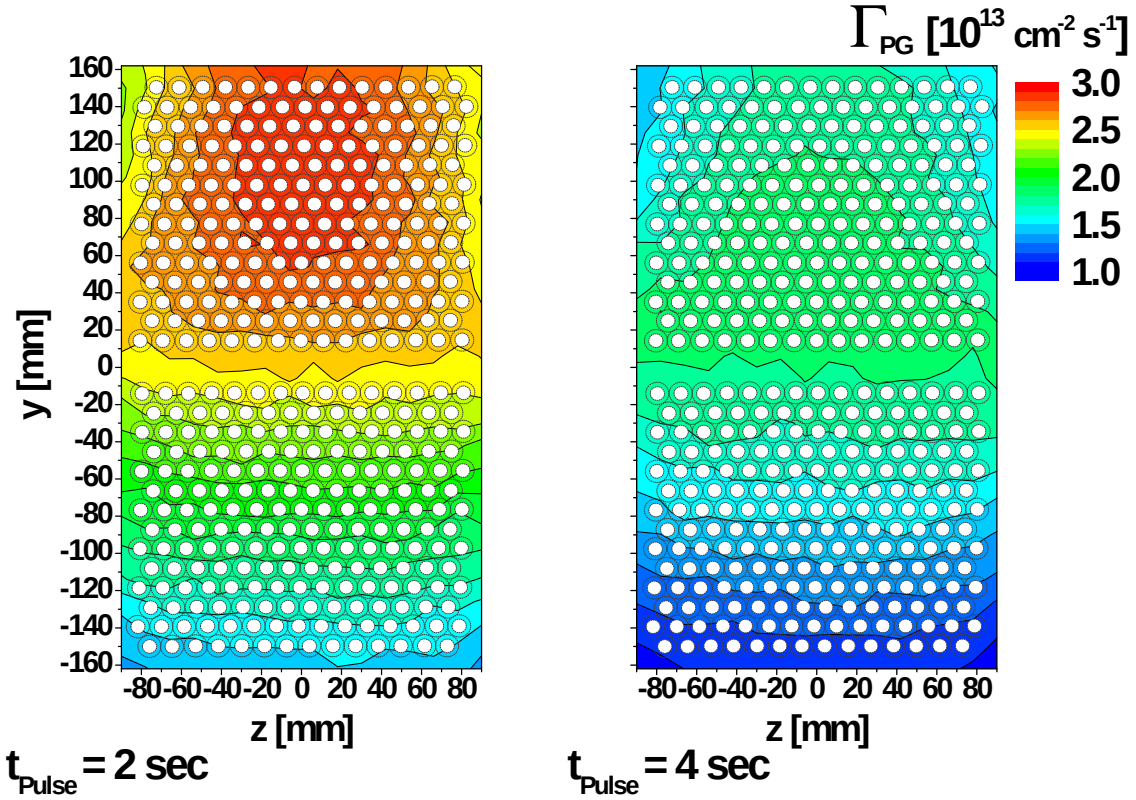


**Figure 6.16.:** Ion-dominated cesium flux onto the plasma grid at a time of 2 sec and 4 sec after the discharge was started considering a preceding vacuum phase of 4 min.

exit, the mean free path length for ionization is less than 0.5 cm. This explains the high ionic content of the initial cesium peak. The existence of a small neutral fraction in the initial peak is a consequence of wall neutralization effects on surfaces close to the plasma grid.

In contrast to the neutral cesium atoms, the cesium ions are affected by the electric potentials in the ion source. This effect is in particular relevant in the plasma sheath near the plasma grid that is positively biased against the chamber walls in order to reduce the co-extracted electron current. Depending on the potential difference between the plasma and the bias potentials, the flux of positive cesium and hydrogen ions onto the plasma grid can be modified. A reduction of the positive ion flux onto the plasma grid takes place if a bias potential higher than the plasma potential is used. In this case, only ions that have enough energy to overcome the positive sheath potential difference are capable of reaching the plasma grid. However, the interplay of the ionic cesium and proton flux onto the plasma grid with the negative-ion and co-extracted electron current is not fully understood, yet. Detailed numerical investigations are in preparation [WGF09].

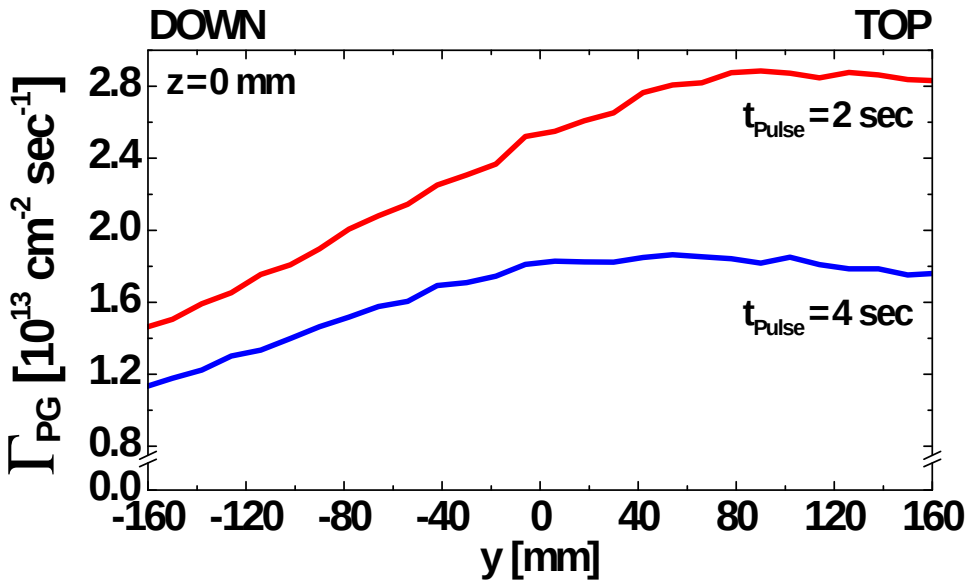


**Figure 6.17.:** Vertical line plot of the cesium flux onto the plasma grid at the beginning of the discharge for $z = 0$ mm.

Figure 6.16 shows contour plots of the ion-dominated cesium flux onto the plasma grid at $t_{\mathrm{Pulse}} = 2$ sec and $t_{\mathrm{Pulse}} = 4$ sec after the discharge was started, as marked by a) in figure 6.15. Vertical line plots of the corresponding flux are shown in figure 6.17.

A factor of ten more intense total cesium flux is generated at the beginning of the discharge than during the vacuum phase (see figure 6.7). However, the time traces indicate a quick depletion of the cesium reservoirs within the first seconds of the discharge. Similar to the cesium deposition on the bias plate during short pulses, a more intense cesium flux is created onto the upper part of the plasma grid.

The short decay time of the cesium flux onto the plasma grid might be long enough to generate proper cesium conditions for short plasma pulses of several seconds. However, the creation of stable cesium conditions during long plasma pulses of up to one hour will require more advanced ways of cesium control (see section 6.3). The described ion-dominated cesium flux is depleted within several seconds.

### Cesium Release by Thermal Desorption from the Bias Plate

A second effect is created during long pulses: the temperature increase of the bias plate activates its cesium reservoirs and creates an additional dynamics. As demonstrated by figure 6.14, short conditioning pulses result in an effective increase of the cesium inventory on the bias plate. Hence, a maximum cesium deposition of 4.4x$10^{16}$ $cm^{-2}$ (upper segment) is created on the bias plate after 100 conditioning pulses.
The thermal desorption of this reservoir generates a broad and very intense cesium flux peak after a pulse duration of 30 sec, when a bias plate temperature of 80 °C is exceeded. The thermally desorbed cesium from the bias plate is transported onto the plasma grid by collisions with the background particles and by reflection processes on the chamber walls. Figure 6.15 shows that a maximum flux density on the order of 1x$10^{14}$ $cm^{-2}$ $s^{-1}$ is predicted after a pulse time of 180 sec corresponding to the saturation of the bias plate temperature. This peak decays over the next 300 sec of the pulse.
Due to the low electron temperature $T_e = 1$ eV and density $n_e = 10^{17}$ $m^{-3}$ in the vicinity of the bias plate, the mean free path length for ionization close to the bias plate is 30 cm. As a consequence, the time trace of the ionic and atomic cesium flux onto the plasma grid, released from the bias plate, is dominated by an atomic cesium flux.
However, a small ionic fraction is generated by the following process: a fraction of cesium that is released from the bias plate reaches areas with a high electron temperature and density close to the driver, where it is instantly ionized and transported back onto the plasma grid. An axial profile of the electron temperature and density is given in section D of the appendix. Figure 6.18 shows the spatial profile of the computed flux of neutral cesium by thermal desorption from the bias plate during a plasma pulse after 110 sec and 400 sec of the pulse, as marked as b) and c) in figure 6.15. Vertical line plots of the flux onto the plasma grid at $z = 0$ mm are shown in figure 6.19. Both profiles show a higher cesium flux onto the peripheral areas of the plasma grid. This is an effect of the geometric arrangement of the bias plate around the plasma grid (see figure 5.5 and 3.9).
The intensity and profile of the predicted cesium flux onto the plasma grid changes with advancing pulse time. A profile that is symmetric in the vertical direction is predicted at the beginning of the thermal activation, as shown in figure 6.18 and 6.19 at 110 sec. The profile gets more and more asymmetric with advancing pulse length, since the cesium flux onto the lower half of the grid decreases after

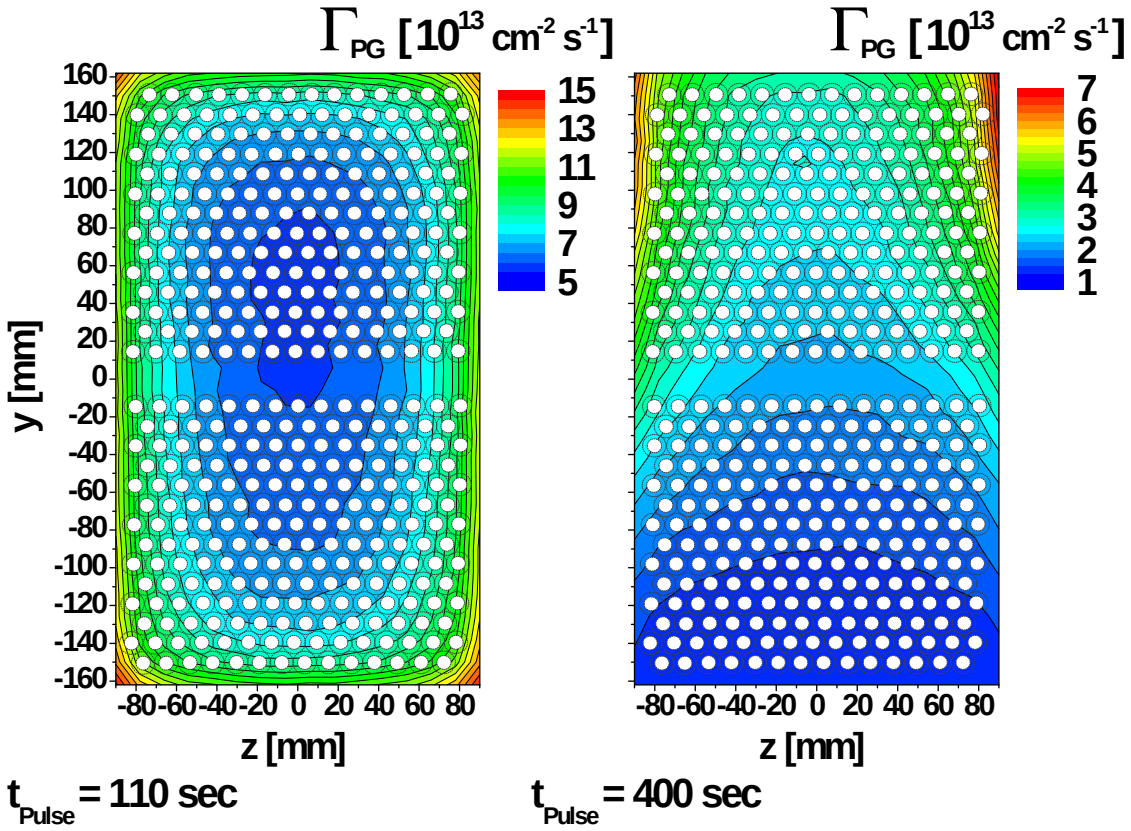


**Figure 6.18.:** Neutral-dominated cesium flux onto the plasma grid by thermal desorption from the heated bias plate after a pulse length of 110 sec and 400 sec.

200 sec. Figure 6.18 and 6.19 show asymmetric flux profiles after a pulse duration of 400 sec. This effect corresponds to the decay of the total flux in figure 6.15. The presence of a finite decay time is explained by the depletion of the non-uniform cesium deposition on the bias plate. While the cesium reservoirs on the lower surface areas of the bias plate are depleted at first and the total flux is reduced, the cesium accumulation on the upper segment remains high for a longer time.

A comparison of the prediction from CsFlow3D with the time trace of the OES signal of atomic cesium during the discharge, as shown in figure 6.10, indicates a good qualitative agreement. The peak that is observed in the OES signal during the first seconds of the plasma phase is not related to the cesium dynamics. This peak is caused by the gas puff at the beginning of the discharge that is not relevant for the transport of cesium. Therefore it is not included in the simulation of the cesium transport.

The dynamics of the increase of the OES signal during the first 200 sec of the discharge is well reproduced by the code. However, a much longer decay time

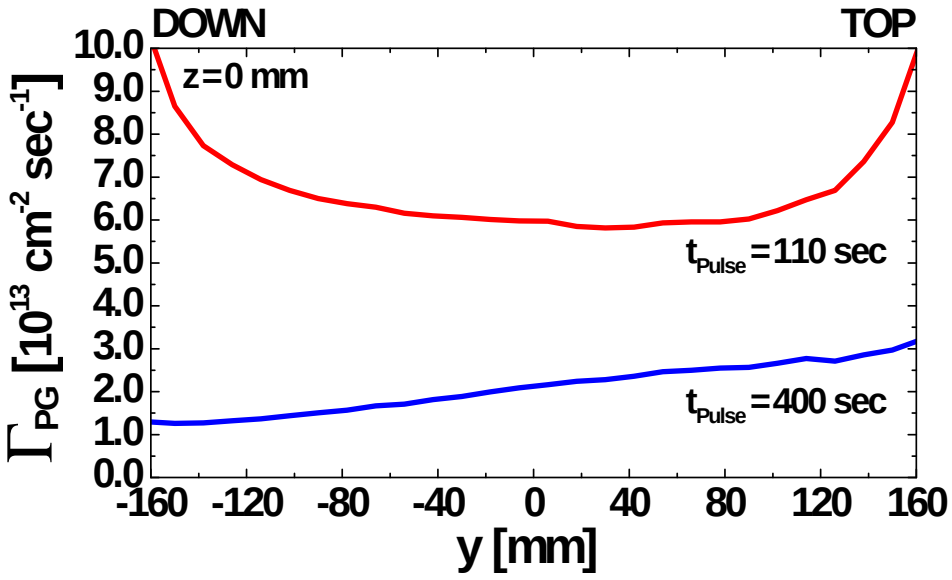


**Figure 6.19.:** Vertical line plot of the cesium flux onto the plasma grid by thermal activation of the bias plate at $z = 0$ mm.

of the OES signal was observed in the experiment. There are different possible explanations for this discrepancy. The OES gives a signal that is averaged over a line-of-sight, which covers the plasma grid and the bias plate area. Cesium desorption from the upper and lower area of the bias plate is possibly more pronounced in the OES. Furthermore, it is extremely difficult to predict the exact initial deposition of cesium on the bias plate before the pulse is started, since it is influenced by the history of cesium injection and removal during the preceding operation period.

A prediction of the cesium density $n_{\mathrm{Cs}}$ over the plasma grid is possible by using the equation of continuity $n_{\mathrm{Cs}} = \frac{j}{\langle v \rangle}$, where $\langle v \rangle$ is the mean thermal velocity and $j$ the cesium flux, taken from the transport simulation. This yields an atomic cesium density of 2x$10^{15}$ m$^{-3}$ after 110 sec that rises to a maximum of 4x$10^{15}$ m$^{-3}$ after 180 sec. A determination of the density of atomic cesium from the OES in MANITU is limited, since no Langmuir probe measurement of the electron temperature and density close to the plasma grid was available. Hence, the corresponding data were taken from probe measurements at BATMAN that has a similar source geometry, but is limited to short-pulse operation. This approximation gives a cesium density that increases from the lower to the mid range of $10^{15}$ m$^{-3}$ during the plasma pulse [Ruf10].

The following conclusions can be drawn from the results of the transport simulation:

- The thermal desorption from the bias plate is the dominant mechanism for neutral cesium to be transported onto the plasma grid during long plasma pulses. The corresponding neutral cesium flux is by a factor of four higher than the predicted maximum flux by the release of cesium by other processes, which create an ion-dominated cesium flux onto the plasma grid.
- There is a good correlation between the simulated cesium flux onto the plasma grid and the signal of the OES. Thus, the OES signal of the atomic cesium is an adequate method to predict the cesium flux onto the plasma grid.

A high and continuous flux of neutral cesium is beneficial to maintain a low work function of a cesiated surface (see section 5.2). Thus, the predicted transport of high amounts of neutral cesium from the bias plate onto the plasma grid is advantageous for the source performance.
Nevertheless, the release of cesium during the discharge takes place in an uncontrolled way. This reduces the available inventory on the surface areas within the ion source that can be activated for cesium release. The released cesium is lost to inactive areas (see section 6.2.1), forming a sink for cesium.

An important aspect of the cesium dynamics during the plasma phases is the effect of deuterium operation, since both modes are planned for the ITER neutral beam injection. The cesium transport investigations, presented within the scope of this work, are related to source operation with a hydrogen plasma. However, it is possible to draw conclusions from the previous simulations on the influence of deuterium on the cesium transport.
The higher mass of the $D_2$ molecule will have influence on the collision dynamics during the transport of Cs and $Cs^+$. Nevertheless, as a consequence of the high mass of cesium, the effect on elastic collisions is expected to play only a minor role.
According to the previously shown numerical and experimental results, the activation of cesium reservoirs on the walls and, especially on the bias plate, of the ion source determines the dynamics and homogeneity of the cesium flux onto the plasma grid. It is expected that the activation of cesium reservoirs on the walls and on the bias plate of the ion source is more intense in a deuterium discharge.
Physical sputtering by $D_2^+$ and $D^+$ ions is expected to be more effective. Con-

sidering formula (4.32), the sputtering threshold energy for $D^+$ is reduced by approximately a factor two in comparison to $H^+$. Furthermore the plasma heat load, especially on the bias plate, is expected to be different.
Measurements show a factor of 1.5 higher density of atomic deuterium $n_D$ compared to the atomic hydrogen density $n_H$ [FFF+06]. This may change the chemical processes within the source in two ways. The increased density of atomic deuterium may enhance the desorption of cesium from the surfaces by chemical sputtering. Furthermore, it may have also an influence on the chemical processes that are relevant for the negative-ion production, such as the formation and dissociation of CsD.

## 6.3. Methods and Optimizations for Advanced Cesium Control

A more effective mechanism of cesium control is required to enable an intensive cesium flux onto the plasma grid, when the source operates at a low performance, and to spare cesium when it is not required. Methods to ensure a controlled and homogeneous cesium flux onto the plasma grid were investigated with CsFlow3D. As shown in section 3.2.1, cesium injection in the chamber of the IPP prototype source is done by a cesium evaporation oven that is located at the upper region of the backplate. Cesium that is stored on the walls and the bias plate of the ion source is re-distributed by thermal evaporation and by particle bombardment.
The creation of cesium fluxes onto the plasma grid by re-distribution from the walls has disadvantages:

- Large amounts of cesium are lost to surface areas that are not immersed to the plasma. Cesium, released from these areas, can not be recycled during ion source operation and mechanical removal is required after opening the ion source.
- The geometric dependence on the position of the oven creates an inhomogeneous flux profile onto the plasma grid.
- The cesium flux during long plasma pulses in MANITU is determined by the temperature dynamics of surface areas with high cesium accumulations. This causes a strong dependence on the history of the cesium accumulation onto the specific surfaces and the corresponding temperature conditions.

Thus, it is important to find new approaches to improve the homogeneity and the control of the cesium flux onto the plasma grid. The use of a modified configurations with multiple evaporation ovens is a promising approach in order to optimize the cesium homogeneity and is planned for the use in future large-scale negative-ion sources, such as for the ELISE test facility. Technical limitations of the available space and ports at MANITU restrict, however, the use of multiple ovens for the IPP prototype source at the moment.
A numerical investigation of the use of multiple evaporation ovens at MANITU was done in order to evaluate its advantage in comparison to the use of a single oven.

### 6.3.1. Multiple Evaporation Ovens

The CsFlow3D code was used to simulate the cesium injection by two evaporation ovens each with a flux of 5 mg/h, located at the backplate of the ion source. The same parameters than for the simulation of the cesium injection from a single oven were used. Thus, a wall temperature of 47 °C ($s = 0.7$) and a time interval of 4 min between the plasma pulses was considered.
Figure 6.20 a) shows the arrangement of the two ovens at the top and bottom part of the backplate of the ion source. The upper position corresponds to the original position from the configuration with a single oven. Vertical profiles of the cesium flux ($z = 0$) onto the plasma grid of MANITU, as predicted by the simulation, are shown in figure 6.20 b). The figure shows profiles of the total cesium flux onto the plasma grid during a vacuum phase and for a time of two seconds after the beginning of the discharge. It corresponds to figure 6.16 that shows the flux for the previous configuration with a single oven.
These results show that the flux deficiency on the lower surface area of the plasma grid can be compensated by using two evaporation ovens at the specified positions. Thus, using two cesium ovens simultaneously can significantly enhance the homogeneity of the cesium flux onto the plasma grid.
Beside the flux onto the plasma grid, the cesium flux onto the inner walls of the source chamber and the bias plate during the vacuum and plasma phases becomes also more evenly distributed by the use of two ovens. This is associated with a buildup of evenly distributed cesium reservoirs that are activated during the discharge phases. As a consequence of the creation of this advantageous initial distribution, the homogeneity of the cesium flux during the plasma pulse is improved, as well.

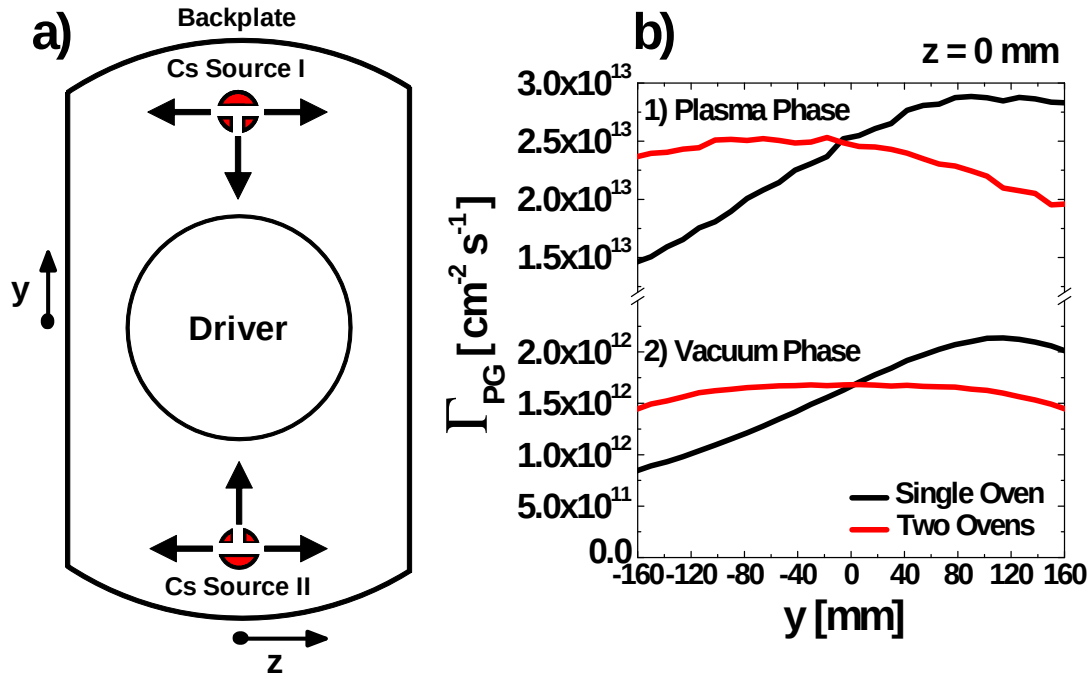


**Figure 6.20.:** a) Schematic view of the configuration with two evaporation ovens. b) Profile ($z = 0$ mm) of the ion-dominated (1) cesium flux on the plasma grid at a pulse time of 2 sec for a configuration with a single (black) and two evaporation ovens (red). Corresponding profile of the atomic (2) cesium flux onto the plasma grid during the vacuum phase of the ion source.

The application of two independent ovens requires, however, stable cesium injection rates for both ovens simultaneously. These are conditions difficult to achieve given the sensitivity of cesium on the temperature and the decay of the injection rate with advancing operation time (see section 5.3). However, this is no principle limitation and a method to overcome this issue has already been show in section 5.3: the use of surface ionization detectors with feedback loops to the temperature control systems of the ovens is a possible way to maintain equal cesium injection rates.

Using multiple cesium sources can improve the homogeneity, but does not address the problem to obtain an active control of the cesium flux onto the plasma grid. The major fraction of the cesium from the evaporation oven is absorbed on the chamber walls and the bias plate from where it is released and re-distributed during the discharge in an uncontrolled fashion.

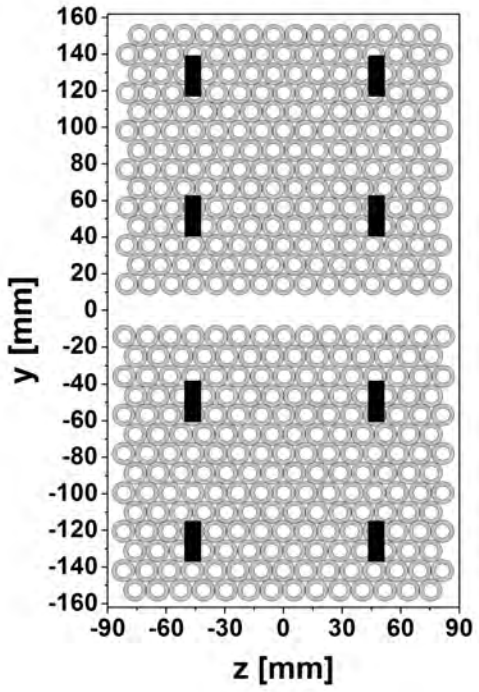


**Figure 6.21.:** Position of the individual dispensers in the array in front of the plasma grid of MANITU. The cesium flow from the dispensers is directed onto the plasma grid. In order to improve the visibility, the size of the individual dispensers was increased.

### 6.3.2. Cesium Injection close to the Plasma Grid

These inherent disadvantages of the use of the current oven system can possibly be resolved by using small cesium dispensers (see section 5.3) in close proximity to the plasma grid (several cm). This allows the control of the cesium flux onto the plasma grid directly by regulating the dispenser current. Dispensers with a capacity of up to 10,000 mg are commercially available. The properties and operation constraints of this type of cesium source are described in section 4.2.7. A thermal stabilization and protection of the dispensers from direct plasma interaction is necessary in order to avoid a depletion of the cesium inventory by an unintended temperature increase.

The cesium injection from an array of eight dispensers at a distance of several cm in front of the plasma grid was simulated with the CsFlow3D code. A total injection rate of 10 mg/h corresponding to the injection rate from the evaporation oven was considered in the calculation. The flow profile from the individual dispenser depends on the design of the corresponding nozzle that is related to the chosen geometry. Nozzles with a cosine-type flow profile that are directed

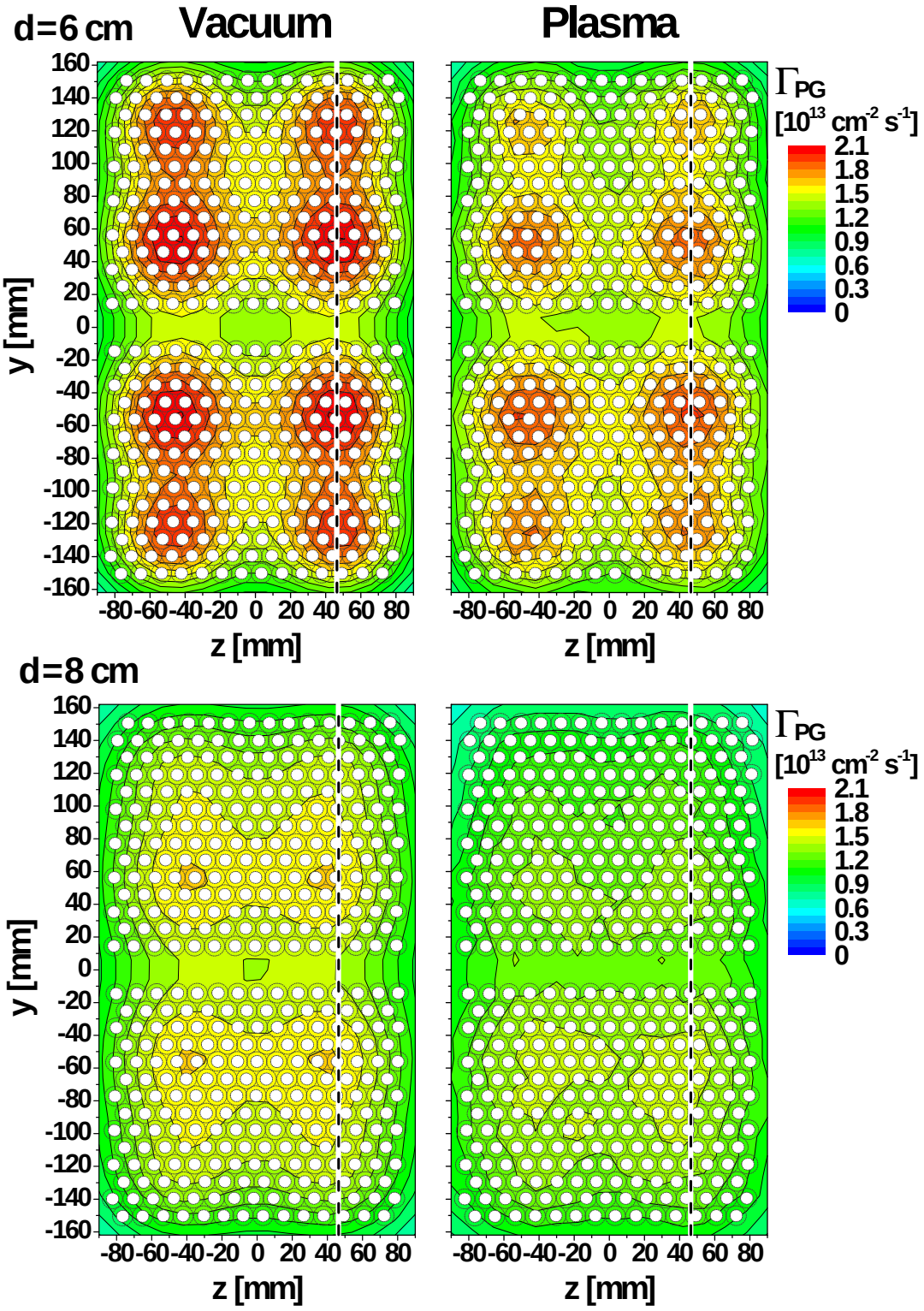


**Figure 6.22.:** Simulated cesium flux (steady-state) onto the plasma grid in MANITU during both the vacuum and the plasma phase from an array of eight dispensers at a distances of 6 cm and 8 cm to the plasma grid at a total injection of 10 mg/h. The dashed lines mark the path for the line plots shown in figure 6.23.

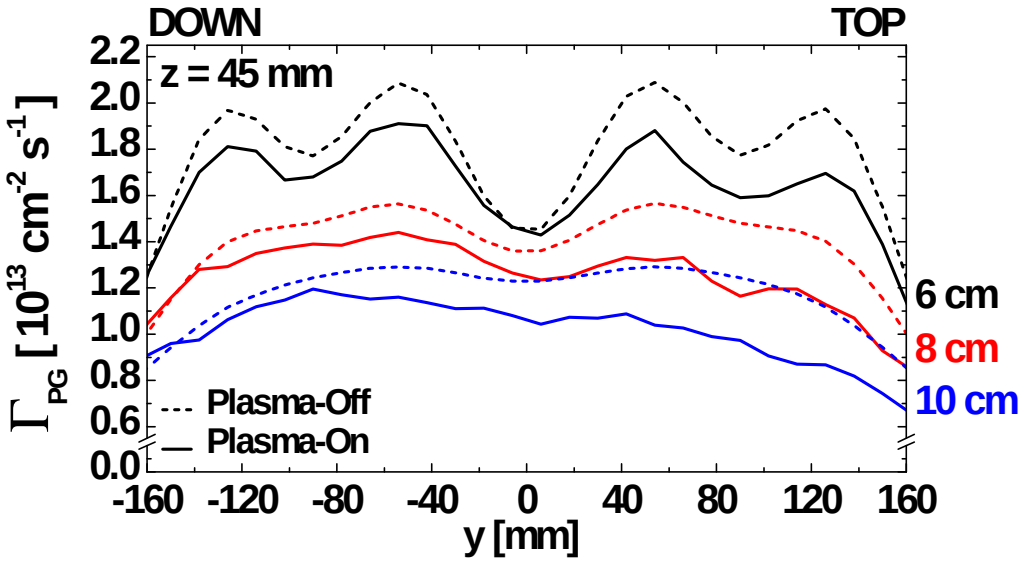


**Figure 6.23.:** Line plot along the dashed lines in 6.22 of the cesium flux distribution onto the plasma grid of MANITU from the dispenser array at a distance of 6 cm, 8 cm and 10 cm. Dashed Lines: Flux during the vacuum phase, Solid Lines: Flux during the plasma phase.

onto the plasma grid were used in the simulation, since a narrow flow profile is disadvantageous to obtain a homogeneous cesium distribution. For the sake of comparability, the remaining parameters were chosen identical to the ones that were used in the previous simulations (see section 6.2.1).

A non-cesiated source with wall temperature of $T_{\text{wall}} = 47\,^{\circ}\text{C}$ and negligible sticking on the plasma grid was used in order to show the flow characteristics of the dispenser array. The bias plate was considered to be at a stable temperature identical to the wall temperature for the dispenser studies.

Figure 6.21 shows the position of the cesium dispensers close to the plasma grid. The computed flux during a vacuum and a plasma phases at a distance of 6 cm and 8 cm from the plasma grid is shown in figure 6.22. Corresponding profile plots along the dashed lines in the contour plots are shown in figure 6.23.

The simulation predicts a total cesium flux of the range of $10^{13}$ cm$^{-2}$ s$^{-1}$ in both the vacuum and the discharge phase for a distance below 10 cm to the plasma grid. A small reduction of the total cesium flux during the discharge is obtained compared to the flux in the vacuum phase. This is an effect of the backscattering of cesium particles by collisions with the particle background during the plasma phase.

The order of magnitude of the cesium flux onto the plasma grid from the dispenser array is comparable to the cesium release at the beginning of the discharge, con-

sidering the cesium injection by the evaporation oven (see figure 6.16). A computation of the dynamics of this flux revealed, however, a short decay time during the discharge, while the dispenser array is capable of delivering a constant flux onto the plasma grid at any time. The corresponding flux from the cesium dispenser array during the vacuum phase is by a factor of ten higher (see figure 6.7) than the one by the injection with the cesium oven. This is an effect of the orientation of the array onto the plasma grid and the close distance of several cm. An analysis of the predicted homogeneity of the dispenser flux onto the plasma grid shows that the profile at a distance of 6 cm is peaked with respect to the positions of the individual dispensers. The increase of the distance to 8 cm results in an improved homogeneity. This is a consequence of the broadening of the flow profile from the individual dispensers, which results in an enhanced overlap.
The improved homogeneity takes place, however, at the expense of the total flux onto the plasma grid. Figure 6.24 shows the dependence of the total (blue curve) and ionic (red curve) cesium flux onto the plasma grid at a distance $d$ during the discharge phase. Hence, the total cesium flux onto the plasma grid is reduced by increasing the distance to the plasma grid. This effect is related to the absorption of cesium by the chamber walls, which is proportional to the distance of the dispenser array to the plasma grid. While the broad, cosine-distributed flow profile from the dispensers is beneficial to obtain a homogeneous flux profile onto the plasma grid, it is disadvantageous for the transport of cesium onto the chamber walls of the ion source.
Furthermore, an increase of the ionic fraction with the distance is predicted by the transport code. If the dispenser array is moved away from the plasma grid, a significantly higher electron temperature and density is obtained at the position of cesium release. Axial profiles of the electron temperature and density are given in section D of the appendix. A fraction of ionic cesium that is lower than 22 % is predicted by the code at a distance below 6 cm to the plasma grid. This value corresponds to axial electron temperatures in the range of 1 eV. Moving the dispenser array to a distance of 18 cm away from the plasma grid, results in an increase of the fraction of cesium ions to 87 %, which corresponds to a high electron temperature of 10 eV. Despite of the high electron temperature, a small fraction of atomic cesium reaches the plasma grid. This is an effect of the neutralization of ionic cesium on walls at low electron temperatures and the radial profile of the electron temperature.
Both, the cesium wall absorption and the ionization of atomic cesium from the dispensers, are more and more pronounced if the distance to the plasma grid is in-

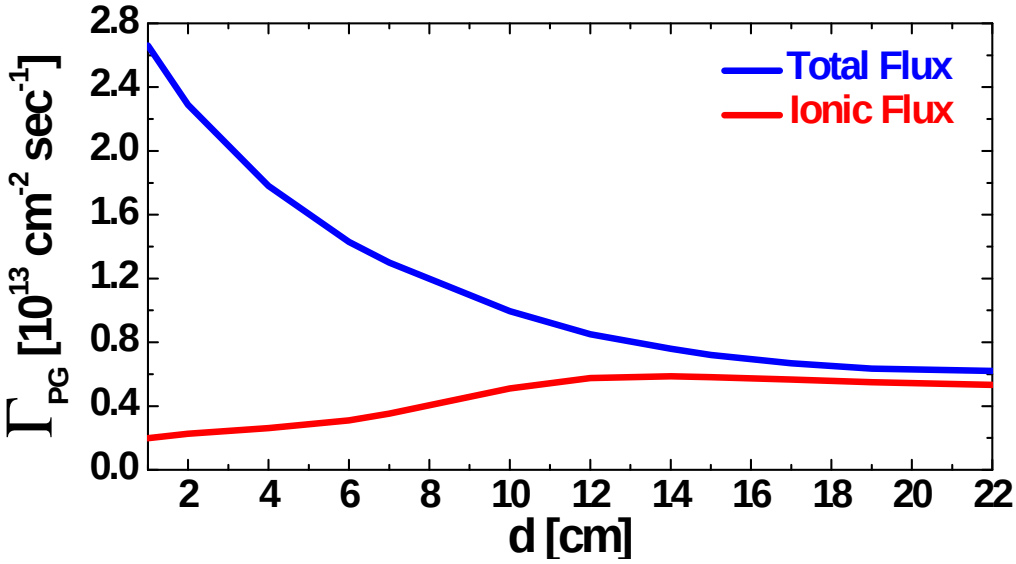


**Figure 6.24.:** Total (blue) and ionic cesium flux (red) onto the plasma grid, emitted from a dispenser array (see figure 6.21) at a distance $d$ to the plasma grid. A significant increase of the fraction of ionic cesium is caused by raising $d$.

creased. This effect results in a transition to conditions comparable to those when cesium is injected by the evaporation oven at the backplate of the ion source. The existing oven that is located at a distance of 22 cm to the plasma grid deposits the cesium predominantly on the walls of the source chamber, as described in section 6.2.2. A transition to an equivalent behavior has to be avoided in order to ensure that an effective control of the cesium flux onto the plasma grid is possible by regulating the dispenser current.

Thus, the optimization of the distance $d$ is a trade-off between the homogeneity of the cesium flux onto the plasma grid and the reduction of wall accumulations and cesium ionization. A distance of $d = 8$ cm was found to be high enough to create a homogeneous flux distribution.

This optimized dispenser configuration can be used as an instrument for independent cesium control. Even if uncontrolled cesium releases take place and the reservoirs at the walls of the source are thereby depleted, it is still possible to obtain a direct cesium control by the dispenser array.

Since the bias plate in MANITU is located close to the plasma grid, it is impossible to avoid a cesium deposition on the plate while maintaining a sufficiently homogeneous flux profile onto the plasma grid. As described in section 6.2.2, the MANITU bias plate can be thermally activated by plasma heating, which might interfere with the cesium control by the dispenser current. Hence, the use

of the dispenser array in combination with a temperature control system of the bias plate may be an option to improve the effective control. Using a bias plate temperature that is kept permanently at a high level, for example 200 °C, is a possible solution for this problem. The high temperature results in an instantaneous thermal desorption of the accumulated cesium that enhance in this case the total flux onto the plasma grid.
Nevertheless, the increased loss of cesium through the aperture system is the main disadvantage of the cesium injection close to the plasma grid. A maximum cesium loss of 1.8 mg/h (vacuum phase) is expected for the optimized dispenser arrangement at a distance of 8 cm from the plasma grid. This is by a factor of seven higher than the corresponding loss for the cesium injection by the evaporation oven (see figure 6.2). The effects of these increased cesium losses through the aperture system and the associated effect on the high voltage holding capabilities cannot be answered within the scope of this work and have to be investigated at the ion source test facilities.

## 6.4. Influence of the Cesium Conditions on the Current Density

The formation of an intense negative-ion beam is accomplished by superimposing the current contributions from the beamlets formed by the individual apertures of the extraction system (see section 3.9). Besides a sufficiently high total beam current, the neutral beam injector system for ITER has specific requirements regarding the quality of the extracted beam. A homogeneity of ±10% of the extracted beam current density over the extraction area is required in order to grant a proper beam focusing. The divergence of the negative-ion beam depends on the beam current and the acceleration voltage. A high fluctuation of the beam current density will create unfocused fractions of the 1 MeV beam that may damage the acceleration system.
Special attention is required in case of the surface production of negative ions. Geometric effects, the magnetic field and especially the cesium conditions may affect the homogeneity of the extracted current density.
An evaluation of these effects requires a computation of the transport of negative ions from the production surface into the extraction apertures. As described in section 3.1.2, the Monte Carlo based 3D transport code TrajAn [GWF09] was developed in parallel to CsFlow3D in order to investigate this process. This code

is capable of computing the local extraction probability on the plasma grid and the current density distribution over the extraction apertures. The neutralization of negative ions by collisions with plasma particles result in a significant reduction of the extracted negative-ion current density. An overview of the destruction processes that are included in TrajAn is given in section 3.1.2.
Similar to the cesium transport codes, 3D maps of the particle densities and temperature that were derived from measurements at the IPP test facilities are used in TrajAn. The 3D magnetic field topology within the ion source was determined by numerical methods (see section C of the appendix). A given distribution of the negative-ion production over the plasma grid can be used as an additional input parameter.
This permits an evaluation of the influence of the different quantities on the current-density distribution. A coupling of the simulation of the cesium conditions on the plasma grid with the production and transport of negative ions is an important objective. It allows a correlation of the extracted ion current with the homogeneity and dynamics of the cesium flux and coverage on the plasma grid.
The first step to address this objective was done by the development of a coupled simulation environment of TrajAn and CsFlow3D, which was applied to investigate the effects of inhomogeneous cesium conditions on the plasma grid. The effect of a spatial distribution of the negative-ion production rate according to the cesium conditions on the plasma grid was introduced in the transport simulation by a simplified coupling scheme: the spatial distribution of the negative-ion production flux $\Gamma_{\mathrm{H}^-}(x, y, z)$ on a specific surface area in TrajAn was weighed linearly with the cesium flux profile $\Gamma_{\mathrm{Cs}}(x, y, z)$ onto the plasma grid, computed with CsFlow3D:

$$\Gamma_{\mathrm{H}^-}(x, y, z) = \alpha\, \Gamma_{\mathrm{Cs}}(x, y, z). \tag{6.2}$$

This strong coupling of the negative-ion production with the cesium flux is strongly motivated by the observations from the work function measurements, as described in section 5.2. The results from the measurement indicate that the work function of the surface depends on the cesium flux, since it is required to counteract the influence of the surface degradation by chemical contamination. Saturation effects of the work function on the plasma grid during an intense cesium flux will, however, require a coupling that includes the creation and removal of cesium layers on the plasma grid. This is subject to further investigations.
Two different scenarios were considered to facilitate the dynamics of the cesium flux onto the plasma grid:

1. The short-pulse behavior (several sec) of the ion-source that is predominantly determined by the cesium distribution, created during the previous vacuum phase.

2. The long-pulse behavior (several 100 sec) that is strongly determined by the release of cesium from the bias plate, heated up to 200 °C during the pulse.

### 6.4.1. Homogeneous Cesium Conditions

In order to distinguish the effects of inhomogeneous cesium conditions and non-cesium related effects, such as the plasma grid geometry or the magnetic field, on the distribution of the negative-ion current density, a transport computation for the case of a high homogeneity of the cesium flux was considered. The cesium flux profile that was computed during a vacuum phase for a very low sticking coefficient of $s = 0.01$, as shown in figure 6.8, was therefore used in order to demonstrate the effects that are related to the transport process.
An important quantity for homogeneity studies in a negative-ion source is the local extraction probability on a specific surface element of the plasma grid. The plasma grid surface is partitioned into equal surface area elements for the determination of the local extraction probability. The number of extracted negative ions that were started from each of these elements is computed by the transport code. A spatially resolved local extraction probability is computed by dividing this number of extracted negative ions by the number of all negative ions, started from this element. For example, a local extraction probability of 33 % at a specific position on the plasma grid means that every third negative ion that was started at this point reaches the extraction apertures.
The profile of the local extraction probability shows the surface areas that contribute predominantly to the extracted current density. This allows an evaluation of the relevance of a specific surface element on the current density of the beam.

#### Extraction Probability Profile

The extraction probability profile was computed for the plasma grid geometry (see section 3.9) and the magnetic fields (see figure C.1) in MANITU. Negative ions, created on the plasma grid, are accelerated by the plasma sheath to a certain energy that depends on the bias voltage. A negative-ion starting energy

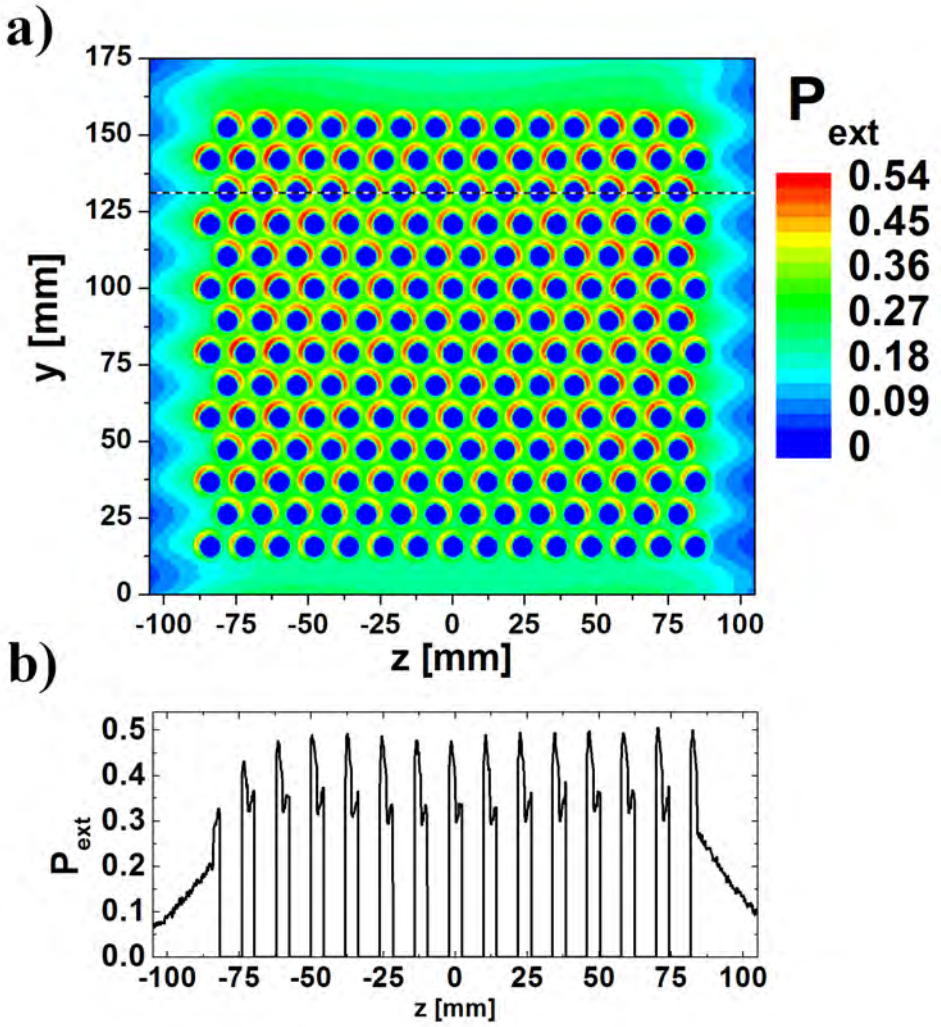


**Figure 6.25.:** a) Contour plot of the local extraction probability on the upper half of the plasma grid in MANITU, considering a negative-ion starting energy of 1 eV. b) Corresponding line plot of the extraction probability across the dashed line in figure a).

of $E_{H^-} = 1$ eV is used for the transport calculation, as described in more detail in [GWF09]. Figure 6.25 shows a contour plot of the local extraction probability for the upper half of the MANITU plasma grid.

The maximum extraction probability of 55 % is obtained at the chamfered areas (see figure 3.5) of the plasma grid surface. This means that approximately every second negative ion that is produced on the chamfered areas is extracted. The inclined starting vectors on these area segments lead to trajectories with a higher redirection probability. A large parallel component regarding the plasma grid surface of the ion velocity vector is beneficial for the bending of the ion towards

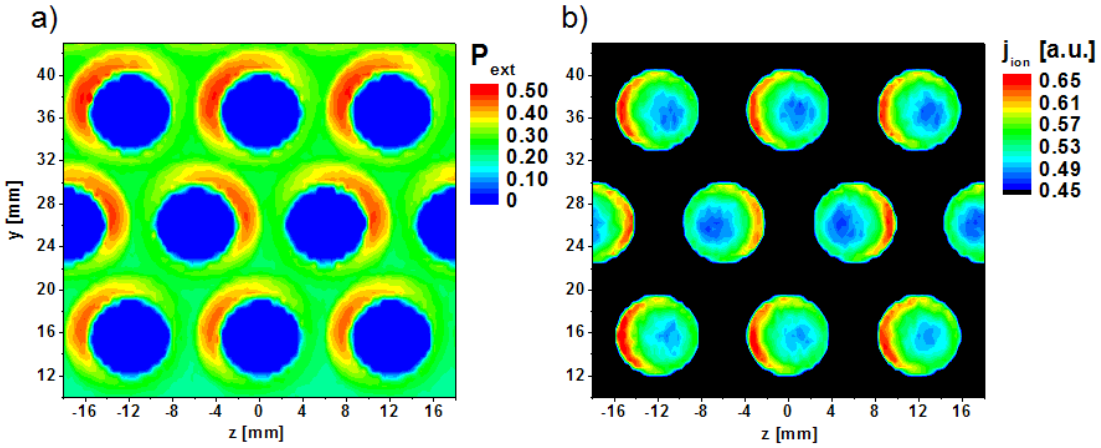


**Figure 6.26.:** a) Spatially resolved local extraction probability and b) corresponding extracted negative-ion current density for the apertures of the plasma grid in MANITU at a starting energy of 1 eV.

the plasma grid. Additionally, the trajectories with inclined starting angles are in closer proximity to the extraction fields. This increases the probability for an extraction event.

At the edges of the plasma grid, the extraction probability is drastically reduced to probabilities below 10 %. The extraction probability of negative ions that are created apart from the aperture area, is limited because of the finite mean free path length due to destruction processes.

The profile of the extraction probability is also affected by the orientation of the local magnetic field vector. This vector results from a superposition of the filter field (see figure C.1 in the appendix) in the horizontal and the electron deflection field (see figure 3.10) in the vertical direction. Each row of the extraction grid magnets has a field direction opposite to the precessing one (see figure 3.9). This creates a shift of the extraction probability that alternates in positive or negative z-direction, depending on the direction of the magnetic field of the individual magnet row pair.

Integrating the local extraction probability profile over the MANITU plasma grid area results in a total extraction probability of 27 % for the given magnet configuration (see figure C.1) and a starting energy of $E_{\mathrm{H}^-} = 1$ eV.

The negative-ion beam is formed by a superposition of the current densities from the individual beamlets, extracted by the apertures of the plasma grid.

#### Current-Density Profile

The current-density profile is determined in the simulation by dividing the number of ions extracted through an element on the transparent aperture area by the area of this element. For the case of comparison, the current-density profile was normalized with respect to the maximum current density. The total maximum of the current density $j_{\mathrm{ion}} = 1$ is obtained at the edges of the aperture array, as shown in figure 6.27 c).
Figure 6.26 shows a contour plot of the extraction probability and the corresponding extracted current density over several apertures of the plasma grid for an evenly distributed ion production. A maximum current density is obtained at the edge segments of the area of each aperture, close to the negative-ion production areas. This is a consequence of the corresponding short path length until the ions reach the extraction aperture. The maximum current density twists in the same manner as the extraction probability.
In case of an evenly distributed negative-ion production, beamlet inhomogeneities are created by effects related to the plasma grid geometry and the magnetic field topology. An effect on the divergence of the individual beamlets and thus on the extracted negative-ion beam is expected by the inhomogeneous distribution of the current-density profile.

### 6.4.2. Inhomogeneous Cesium Conditions

#### Current-Density Profile

The extraction probability that is affected by the magnetic field and geometric conditions of the plasma grid is per definition independent of the production rate. An unevenly distributed negative-ion production by an inhomogeneous cesium flux is expected to have an effect on the profiles of the extracted negative-ion current density. The transport of negative ions from the production surface into the extraction apertures, simulated by the TrajAn code, is not a linear process. Several physical effects affect this transport process:

- negative-ion scattering by elastic collisions with plasma particles in the ion source,
- ion deflection by the Lorentz force due to the magnetic field within the ion source.

Thus, the correlation between the spatial distribution of the negative-ion production and the extracted current density is not straightforward.
Cesium flux conditions that correspond to short and long plasma pulses were considered to investigate their effect on the current-density distribution. For short plasma pulses, the vacuum phases are usually by a factor of 10 longer (several 100 sec) than the consecutive discharge phase (several 10 sec). Hence, the negative-ion production during a short pulse is strongly influenced by the cesium flux distribution during the previous vacuum phase. The profile of the cesium flux during a previous vacuum phase considering a source wall temperature of 47 °C, as shown in figure 6.7 was used to simulate the short-pulse behavior. Cesium release from the bias plate was found to determine the cesium conditions during long discharges. Therefore, the profile of the atomic cesium flux onto the plasma grid after a pulse duration of 110 sec, as shown in figure 6.18, was used to compute the long-pulse characteristics.
Figure 6.27 shows the results of these calculations. The contour plots a) and b) show the current-density profile for the cesium conditions considering short and long plasma pulses. For comparison, the profile of a homogeneous cesium flux that was described in section 6.4.1 is shown in figure 6.27 c). The computed current-density profiles show that inhomogeneities of the cesium flux conditions and the corresponding unevenly distributed ion production are not compensated by broadening effects during the ion transport. Figure 6.27 d) shows horizontal and vertical line plots in order to see the differences for the short and long pulse behavior.
Comparing the current-density distribution for the homogeneous cesium flux with the one for the short pulse characteristics shows that the current density is reduced in the vertical (y) direction. While the long pulse simulation shows a symmetric profile in the vertical direction, an asymmetry was computed in the horizontal (z) direction. This enhancement of the current density at the peripheral beamlets of the plasma grid appears also for the case of a homogeneous cesium flux, but is in particular pronounced for long pulses.
This effect can be explained by the increase of the filter field closer to the permanent magnets at the edge of the plasma grid area, as shown in figure C.1 of the appendix. The strength of the magnetic field increases from 7 mT at the center to 12 mT at the peripheral apertures in the horizontal direction. Hence, the radius of ion gyration that is beneficial for the transport of the surface-generated negative ions into the aperture system is reduced at the edge. During long plasma pulses this effect is even more pronounced by the flux distribution of the cesium

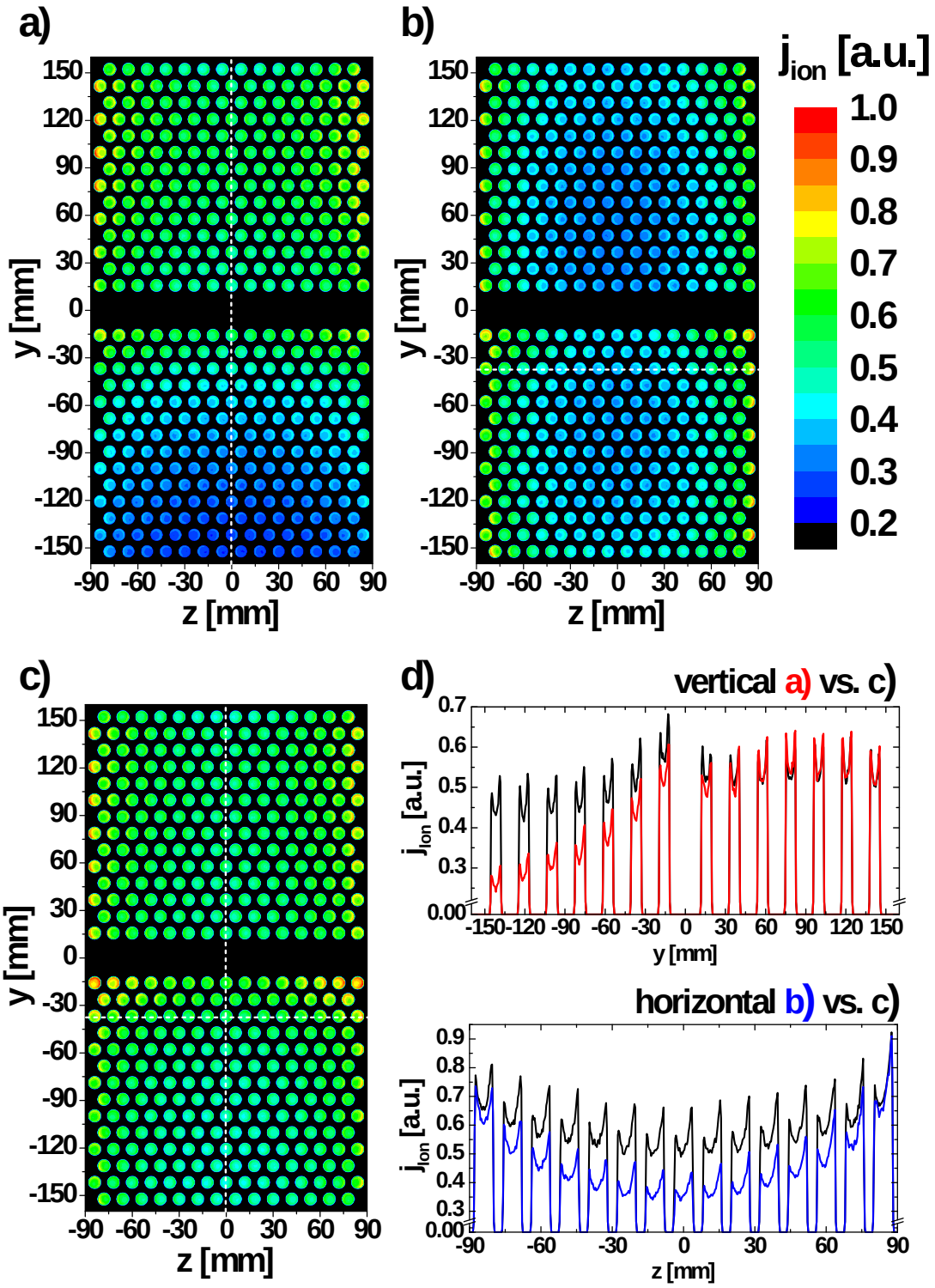


**Figure 6.27.:** a)-c) Contour plots of the simulated extracted negative-ion current density profiles over the plasma grid considering different cesium flux conditions: a) Short pulse profile for a previous vacuum phase with a sticking coefficient of $s = 0.7$. b) Long pulse profile considering the atomic cesium flux from the bias plate. c) Short pulse profile for homogeneous ion production considering an atomic cesium flux during a vacuum phase for $s = 0.01$. d) Horizontal and vertical line plots across the dashed lines in the contour plots.

release from the bias plate. The bias plate forms a frame around the plasma grid. Hence, a more intense cesium flux is created at the peripheral areas of the grid area, as it is shown in figure 6.18.
The coupled transport simulation, considering the spatial distribution of the cesium flux for short and long pulses, shows that an inhomogeneous production rate can not be compensated by the negative-ion transport process. Several physical effects regarding the transport of cesium and negative ions were identified and evaluated that contribute to the generation of inhomogeneities of the current-density distribution.
Nevertheless, there are additional factors that may cause inhomogeneities of the current-density profile. The magnetic filter field can create a plasma drift that influences the distribution of the particle densities and temperatures in the source volume. This influences the transport and destruction of the negative ions, but also the distribution of the ion generation. While the flux of atomic hydrogen is not affected by the drift, it causes an asymmetric distribution of positive ions, which has effect on the negative-ion production. As described in section 3.1.1, the positive ions are very important for the emission of negative ions from the plasma sheath in order to compensate the negative space charge close to the production area.
The combination of CsFlow3D and TrajAn can now be extended in order to evaluate the impact of these physical effects on the current-density distribution. This is the first step to allow a numerical optimization of the current-density distribution.
The inhomogeneities that were determined by the coupled simulation are disadvantageous for the use in the ITER neutral beam injection system. Nevertheless, the linear coupling with the cesium flux represents a worst case scenario. The saturation of the work function of the plasma grid surface after a long cesium exposition might result in a significant improvement of the homogeneity.
Furthermore, the design of future large-scale ion source, like ELISE, will be different from the IPP prototype source that was investigated. A better homogeneity is expected by the higher volume-to-surface ratio in these systems. Additionally, several design aspects were improved as a consequence of the experience with the prototype source. The use of multiple cesium ovens and a magnetic filter field configuration with an improved homogeneity were integrated in the new source design.

# 7. Consequences for Future Ion Sources

Results from numerical studies with CsFlow3D and from experimental investigations indicate several consequences for the improvement regarding the homogeneity and long-time stability of future ion sources.
The experimental studies of the de- and adsorption kinetics of cesium layers revealed a high surface affinity. The CsFlow3D simulations during the vacuum and discharge phase show that the cesium is transported onto the plasma grid by the activation of cesium reservoirs on the chamber walls and the bias plate.
This activation is, however, limited to areas that have intensive contact with the plasma and the backstreaming ions. Certain reservoirs, especially those close to the evaporation oven, are not exposed to the plasma or the backstreaming ions and stay passive during source operation. Large reservoirs of cesium are accumulated on these areas during both the vacuum and plasma phases of ion source operation. These cesium reservoirs are wasted and cannot contribute to the cesium transport onto the plasma grid. In MANITU, the wasted cesium is removed mechanically after the operation periods that can last up to several months.
This is disadvantageous for the remote handling requirements of the ITER negative-ion source, since the available cesium resources are limited in this case. The waste of cesium will reduce the time until a replacement of the cesium reservoir is necessary, which means a higher frequency of maintenance. There are several ways to reduce or avoid this problem.
A possible way to improve this situation is to align the nozzles of the evaporation oven directly onto the erosion zones, which includes also an optimization of the shape of the nozzles in order to generate a corresponding flow profile. Both, the erosion patterns and the flow profile for a specific geometry of the nozzle system can be simulated with the CsFlow3D code. This allows optimization studies in dependence of both factors.
The described method can be used in combination with a permanent activation

of the passive areas by an intensified heating of the specific areas close to the nozzles. According to the desorption measurement, a wall temperature above 90 °C will be required in order to balance the maximum accumulation rate for the current configuration of cesium injection.
An important reason for the buildup of large, inactive reservoirs is the limited contact with the plasma that effectively releases cesium during the discharge phases. The driver of the ion source is located in the middle of the rectangular chamber of the negative-ion source. This geometric configuration creates an intense plasma contact with the side walls, while the contact with surface areas at the top and bottom of the source is very limited. Hence, an expansion of the RF-coil to a racetrack geometry in order to increase the wall contact is a possible solution to resolve this issue.
Inhomogeneous flux profiles were predicted by the transport simulation as a consequence of the position of the cesium oven in the upper half of the source chamber. The use of two evaporation ovens was predicted to improve the flux homogeneity. Nevertheless, a more important consequence for the improvement of the homogeneity by the use of two ovens in parallel is that special care has to be taken in order to maintain a similar cesium injection from both systems. The long-term measurement of the oven performance indicates that this is only possible in combination with an appropriate monitoring of the performance of both ovens.
Using a configuration with two or more evaporation ovens will, however, not improve the control of the cesium flux onto the plasma grid. The simulation of the cesium transport during the plasma phase showed that the release of cesium from the chamber walls takes place in a very uncontrolled fashion. Available options for cesium control are very limited for the given configuration despite of thermal activation, as it is predicted in the transport simulation to take place on the bias plate in MANITU during long plasma pulses. This effect could be utilized in combination with a temperature control of the bias plate. A bias plate that is kept permanently at a low temperature, like 20 °C, could be used to collect cesium. This cesium can then be released on purpose by disabling the temperature control. An extension of this concept is the use of cold areas near the plasma grid. These cold-spots can be used for a controlled absorption and re-emission of cesium close to the plasma grid.

# 8. Summary and Future Steps

A high performance neutral beam injection system is required for the heating and current drive of the large-scale fusion experiment ITER. Due to the required neutral beam energy of 1 MeV, a system based on the acceleration and neutralization of negative hydrogen ions is necessary. The IPP contributes to the ITER heating system by the development of a RF-driven source for negative ions. RF sources are preferred due to their nearly maintenance-free operation that is beneficial for the remote handling requirements of ITER. Ambitious technical requirements have to be fulfilled by this source that must produce a current density of 200 (300) $A/m^2$ accelerated $D^-(H^-)$ ions at a source filling pressure of 0.3 Pa with an electron-to-ion ratio $< 1$ and a pulse length of up to 1 hour. The extracted beam current demands a large-scale ion source (1.9 x 0.9 $m^2$). An important requirement especially when the large size of the extraction area is taken into consideration is the homogeneity of the extracted ion beam, which has to be better than $\pm 10$ %.

Only a negative-source using the surface production of $H^-$ by the conversion of neutral and ionic hydrogen is capable of fulfilling these requirements. These positive and neutral hydrogen particles are created by RF-coupling in the driver of the ion source. The conversion efficiency for the surface production depends on the work function, making the reduction of the plasma grids work function a primary objective. This low work function plasma grid surface is obtained by the injection of cesium into the ion source. The state of the cesium on the plasma grid during plasma operation is the dominating factor for the negative-ion production.

Understanding the dynamics of cesium during the vacuum as well as during the discharge phases of the ion source is essential to produce cesium conditions that are homogeneous in space and stable in time. Monte Carlo based numerical transport models are important to understand the cesium dynamics within the ion source and can help to optimize the stability and homogeneity of the cesium flux onto the plasma grid. Input data regarding the ad- and desorption of cesium from the walls of the ion-source vessel are necessary to perform meaningful computations.

Available data regarding the ad- and desorption kinetics of cesium on metal samples exist, however, only for fractional monolayers of cesium under ultra-high vacuum conditions ($< 10^{-8}$ Pa) at high sample temperatures ($> 1000$ °C) and for the case of a cesium vapor pressure equilibrium. The conditions in negative-ion sources are significantly different, where a higher background pressure ($10^{-3}$ - $10^{-4}$ Pa) and lower wall temperatures ($T_{\mathrm{Walls}} = 20$ - $50$ °C, $T_{\mathrm{Plasma\ grid}} = 150$ °C) are used. The results of calculations for the dynamics of cesium that rely on the available data for elemental cesium would indicate a quick depletion of cesium through the plasma grid apertures during the night. This is in complete disagreement with experimental observations at all negative-ion sources that use cesium. An understanding of the cesium dynamics and associated numerical transport calculations require input data that are relevant for the conditions within the RF-driven ion source.

To acquire this data, dedicated investigations were performed in experiments at the University of Augsburg. The experimental setup was designed to allow measurements at plasma parameters and pressure conditions that are similar to those near the plasma grid surface of the RF-driven ion source. Besides the gathering of input data for numerical studies, the experimental setup was also used to test new cesium diagnostics and to optimize the cesium injection system.

Measurements of the ad- and desorption of cesium from a temperature-stabilized metal sample with a quartz microbalance were performed. A molybdenum sample, similar to the material of the plasma grid in the ion source, at relevant temperatures of 20 - 160 °C was investigated in the experiment. The dependence of the desorption rate and the sticking coefficient of cesium on the source walls was derived, both of which serve as input parameters for the transport simulations.

The desorption measurement showed a significantly higher surface affinity than expected for elemental cesium. Stable multilayer structures of cesium were deposited on the sample for temperatures below 55 °C, which should be not possible taking into account the vapor pressure of elemental cesium. This is an effect of the influence of chemical reactions with impurities that stabilize the adsorbed cesium. Significant cesium desorption from the sample was measured for temperatures above 65 °C, but at desorption rates at several order of magnitude below those expected from the vapor pressure of pure cesium.

The microbalance was used to determine data regarding the surface affinity of cesium for ion source relevant temperature and pressure conditions. The measured temperature dependence of the thermal desorption rate is in agreement with spec-

troscopic investigations of thermal evaporation of cesium from a plasma-heated surface within the long pulse negative-ion source test facility MANITU. This data set helps to understand the effects of thermally-released cesium within the negative-ion source and facilitates realistic transport simulations of the cesium dynamics.

The cesium coating of the plasma grid surface results in a significant reduction of the work function that is a dominant factor for the surface generation of negative ions. A photoelectric determination of the work function of a cesium-coated sample during plasma exposition is limited by the interference of the inevitable currents onto the sample during the discharge. It was possible to overcome this problem by pulsing the hydrogen plasma while limiting the work function measurement time to the plasma-off cycles in order to generate a quasi-continuous plasma exposition. This modification is a significant expansion of the measurement capabilities of the existing work function setup at the University of Augsburg. It is now possible to measure the work function under plasma conditions that are similar to those close to the plasma grid surface of the RF-driven ion source at IPP.

A minimum work function of a cesium-coated molybdenum sample of $2.69 \pm 0.08$ eV, significantly higher than the literature value of pure cesium (2.14 eV), was determined under ion-source relevant vacuum conditions. Equivalent measurements during plasma exposure showed a lower work function of $2.2 \pm 0.2$ eV, which indicates a cleaning effect by the bombardment with plasma particles during the discharge.

Disabling the cesium flux onto the sample resulted for both cases in a time-dependent increase of the work function. This degradation of the surface is an effect of cesium compounds with a significantly higher work function than pure cesium. Re-enabling the cesium exposure counteracts the degradation effects and revealed the necessity for a stable and permanent cesium flux onto the surface in order to maintain a low work function. These degradation and re-conditioning effects are also observed in negative-ion sources when the source is operated the first time at the morning without cesium exposure during the night.

The results of the measurements show that a low work function cesium layer can be re-established on a substrate of cesium compounds with a high work function. This explains the requirement of a permanent cesium injection into the ion source. The observed regeneration effect of the work function by adding fresh layers cesium is very advantageous to obtain a stable ion production. It is impossible to maintain a stable cesium coverage of 0.5 monolayers, as required for the optimum

work function, for the operation conditions within negative-ion sources, which are far away from UHV vacuum conditions.

Stable and reliable cesium injection systems are required to ensure that the plasma grid is supplied permanently with fresh cesium, which keeps the work function at a low level during source operation. A detector based on the surface ionization principle was designed to provide a new method to monitor atomic cesium flows in a vacuum environment. The detector design allows long-term flow measurements with periods of several weeks for ten hours per day. With this new diagnostic it is possible for the first time to test and optimize different designs of cesium injection systems in a controlled laboratory environment prior to their use at the IPP negative-ion sources.

The monitoring system was applied to evaluate a design optimization of the existing evaporation oven design. A significant improvement of the oven was achieved by a systematic improvement of the heating configuration for the body of the oven, which is the part that contains the liquid cesium. The use of the improved oven design at the IPP negative-ion source test facilities allows a more reproducible and stable cesium injection.

It was possible to determine a typical cesium injection rate of 10 mg/h for the operation conditions that are used at the IPP test facilities, which is an important input parameter for the cesium transport simulation. However, an additional long-term test revealed a deterioration of the cesium flow from the oven with advancing operation time (1 - 2 weeks) after breaking an ampoule containing 1000 mg of cesium. This test showed the requirement to increase the operation temperatures of the oven in order to maintain a constant cesium flow and demonstrated the benefit of a permanent flow monitoring by surface ionization detection.

In order to take advantage of the online-monitoring of the cesium flow at the IPP test facilities, a surface ionization detector that is integrated in the nozzle system of the existing evaporation oven was developed. This is the first step towards an online monitoring of the flow from the oven. This will allow a flow control by a feedback loop via the oven temperature in order to maintain a constant injection rate. Besides its use to obtain an advanced control the cesium injection rate, this system will provide a measurement of the cesium consumption of the IPP negative-ion sources, which allows a correlation of the injected amount of cesium and the source performance. First tests of this online-monitoring system are running at the moment.

The observed decrease of the oven performance with the operation time is related

to the large inner area of the oven that enhances the effects of re-distribution processes, and, thus, the vulnerability of cesium within the oven to chemical reactions. A consequence for future designs that use a liquid reservoir is to reduce the surface to volume ratio of the system.
Furthermore, the use of an oven configuration with a heated valve that can be closed during the inactive phases of the oven is a method to reduce the influence of cesium contamination. A valve-based cesium oven is successfully applied for the negative-ion sources at the NIFS[1] in Japan.
Another way to overcome the decrease of the oven performance with the operation time is to use a different design of the cesium source. The reservoir of liquid cesium has the inherent disadvantage that the cesium is vulnerable to chemical contamination. Commercial cesium dispensers, based on the decomposition of stable cesium compounds instead of the thermal evaporation of a reservoir of pure cesium, are a possible alternative that may resolve the encountered stability problems. A prototype system of an oven that contains a 10 mg cesium dispenser was designed and successfully tested with the surface ionization detector. This shows the feasibility of this concept and is the first step for its application at a negative-ion source. For the future, long-term stability tests with several 100 mg of cesium, however, are required to evaluate the advantages of the dispenser oven, since 1000 - 3000 mg of cesium are consumed by the negative-ion source during an experimental campaign that can last up to 3 months.
Data of the ad- and desorption kinetics of cesium and the total injection rate of the IPP evaporation oven at relevant conditions were determined. A computer model is, however, required to extrapolate these results from the laboratory experiments to the negative-ion source test facilities. No commercial nor scientific code has been available that allows an adequate numerical description of the cesium dynamics within negative-ion sources.
The 3D Monte Carlo based code CsFlow3D was developed and applied to simulate the transport of neutral and ionic cesium during the vacuum ($p = 10^{-3}$ - $10^{-4}$ Pa) and the plasma phases ($p = 0.3$ Pa) of the RF-driven negative-ion source, used at the MANITU test facility. This long pulse test facility MANITU was chosen for numerical investigations of the cesium dynamics, since the long-pulse stability at high source performance is an important requirement for the ITER neutral beam heating system. Furthermore, the access to the test facility allowed a validation of the code results by the comparison with experimental observations.
A free molecular flow regime for cesium is obtained during the vacuum phases.

[1] NIFS: **N**ational **I**nstitute for **F**usion **S**cience, Nagoya, Japan.

Collisions with particles of the hydrogen gas and plasma background have to be considered for the transport during the plasma phases. The required spatially resolved 3D maps of the particle densities and temperatures were approximated from experimental investigations at IPP, while the complete 3D magnetic field configuration of the source was taken from a computer model.
With the CsFlow3D code and the gathered input data, it was possible to perform a realistic simulation of the cesium dynamics during both, vacuum phases and long plasma pulses, of the ion source. A validation of the model was done by a comparison with a Rutherford backscattering measurement of the cesium deposition on a metal sample that was located in MANITU during an operational period of one month.
Several important aspects were investigated for the first time with CsFlow3D. A determination of the cesium loss during the vacuum phase through the apertures system is important in order to evaluate the possible reduction of the voltage holding capability of the beam formation and acceleration system. The model showed a low loss rate of 0.25 mg/h for a typical injection of 10 mg/h and source wall temperatures of 40 - 50 °C. The accumulation of up to several thousand cesium monolayers on the chamber source walls, especially close to the nozzle system of the cesium oven, is predicted by the model considering the evaporation of 1000 mg of cesium. This effect limits the total loss through the apertures, which is in agreement with experimental observations where large amounts of the injected cesium are found within the ion source. These predictions can also be helpful to evaluate the influence of design modifications of the cesium injection on the voltage holding capability of the ion source.
The cesium flux onto the plasma grid was found to be a superposition of the contributions from both the evaporation oven and re-distribution processes from the chamber walls. A simulation during the vacuum phase for wall temperatures of 26 °C and 47 °C predicts a cesium flux onto the plasma grid of the order of $10^{12}$ $cm^{-2}$ $s^{-1}$ with an inhomogeneous distribution. The flux onto the upper half of the plasma grid is more intense in both cases. This can be explained as an effect of the position of the cesium oven being located near the top of the source. An increase of the cesium flux onto the plasma grid by a factor of two is predicted by CsFlow3D for the increase of the wall temperature from 26 °C to 47 °C. This explains the corresponding reduction of the conditioning time of the ion source that was observed at the IPP negative-ion source test facilities.
Cesium reservoirs are formed during the vacuum phases before the plasma pulses. The activation of these reservoirs is an important mechanism for the cesium

transport during the discharge. Transport calculations were used to predict the distribution of the dominant erosion areas and to simulate the dynamics of the re-distribution process. The release of cesium at the beginning of the discharge takes place predominantly on the backplate and on the sidewalls of the ion source close to the driver. As a consequence of the high electron density and temperature near these surface areas, the released cesium is essentially instantly ionized as its mean free path length is below a centimeter. An ion-dominated cesium flux on the order of $10^{13}$ cm$^{-2}$ s$^{-1}$ onto the plasma grid is predicted by the simulation. The direct flux onto the plasma grid from the cesium injection from the oven is by a factor of ten lower than the re-distributed flux during the plasma phase. This indicates that the cesium re-distribution from the walls is the dominant process for the cesium flux onto the plasma grid. Depending on the available amount of cesium in the reservoirs, this flux, however, is depleted within the first seconds of the discharge. Hence, the simulation predicts no conditioning problems when the source is operated in a series of short discharges with long vacuum phases, like it is done at the short-pulse test facility BATMAN.

Furthermore, the simulation showed an inhomogeneous flux profile. A more intense cesium flux was computed onto the upper part of the plasma grid, which is a direct consequence of the inhomogeneous distribution of cesium reservoirs.

Additional dynamic effects were found for a long pulse duration. A significantly higher flux onto the plasma grid on the order $10^{14}$ cm$^{-2}$ s$^{-1}$ is generated as a consequence of the heating of the bias plate in MANITU by the thermal load from the plasma. The bias plate, located at a distance of 1 cm from the plasma grid, is used to enhance the effect of the bias voltage that is used to reduce the number of co-extracted electrons. Both the electron density and temperature are lower near the plasma grid compared to what is found near the driver. Hence, the cesium release from the bias plate creates a neutral-dominated cesium flux onto the plasma grid, which is more intense at the peripheral areas of the grid. This intensity increase at the edge is a result of the geometry of the bias plate that forms a frame around the plasma grid area. The time trace of the optical emission spectroscopy (OES) signal of neutral cesium shows that the predicted dynamics is in qualitative agreement with experimental observations. Furthermore, a reasonable agreement of the computed density of neutral cesium near the plasma grid with the density that was approximated with the OES was found. As a next step, the ratio of ionic and atomic cesium should be investigated and compared with the results of the simulations. Since it is not possible by the OES to measure the density of ionic cesium, a new diagnostic method needs to be

developed.
Numerical investigations of the dynamics and characteristics of the cesium flux onto the plasma grid for vacuum phases and plasma pulses of several 100 sec were done. It was possible to identify the fundamental processes that determine the profile and the dynamics of the cesium flux onto the plasma grid. The CsFlow3D simulation improved significantly the basic understanding of the spatial distribution and dynamics of the cesium flux for the current configuration of the ion source.
Now it is possible to perform a numerical optimization of the cesium transport with respect to the homogeneity and stability of the cesium flux onto the plasma grid. Nevertheless, approximations regarding the release of cesium during the discharge had to be used for the simulation of the cesium dynamics in MANITU. In particular, specific experimental data are required for the cesium release due to plasma exposition of the side walls, which is probably a plasma-chemical process. Future applications of the CsFlow3D code with an improved data set are predictions of the cesium dynamics and homogeneity for the ITER negative-ion source. This large-scale ion source will have an increased volume-to-surface ratio compared to the IPP prototype source. The extrapolated data can be used for advanced engineering of the system. Besides the large-scale ion sources, the code could be applied to simulate the cesium dynamics in small-scale negative-ion sources that are used in particle accelerators. These comparative studies will help to improve the understanding of the cesium dynamics and transport, in general.
The acquired knowledge of the cesium transport can, however, be applied to design new ways for an optimized cesium distribution and control within MANITU and to perform evaluations regarding the results for the existing configuration. One possible solution to improve the cesium homogeneity is the use of two ovens. This concept has not been tested at the IPP test facilities due to technical limitations, but is planned for the future ELISE test facility. A simulation of this configuration predicts that the use of two ovens improves the homogeneity. Nevertheless, no improvement of the cesium control is expected since this design modification helps only to obtain a more symmetric spatial distribution of the cesium reservoirs on the source walls.
Despite of controlling the temperature of the source walls, the options to influence the cesium flux onto the plasma grid are very limited for the given source configuration. The use of an array of cesium dispensers with a controllable cesium injection rate close to the plasma grid is a possible way to obtain active control

on the cesium dynamics at the IPP test facilities.
In order to prepare the use of this system at the IPP test facilities, a numerical optimization of the arrangement and the distance to the plasma grid of this dispenser array was done, which also allows an evaluation of the corresponding flux properties. A constant and homogeneous cesium flux onto the plasma grid on the order of $10^{13}$ $cm^{-2}$ $s^{-1}$ that is dominated by neutral cesium is predicted by the code during vacuum and plasma phases for an optimum distance of 8 cm to the grid and a total injection rate of 10 mg/h.
However, the CsFlow3D code predicts that the use of the dispenser array close to the plasma grid creates a high cesium leakage through the aperture system of 1.8 mg/h. This might limit the voltage holding capabilities of the extraction system. Furthermore, a sufficiently high temperature stability of the dispenser array is required in order to avoid unintended cesium release by the thermal load from the plasma.
The use of an integrated cesium injection system within the negative-ion source for ITER is very limited. The replacement of a depleted dispenser system within the negative-ion source is in conflict with the remote handling requirements of ITER. There are, however, no limitations for the use of dispensers as cesium sources in an external cesium oven where the exchange is similar to the ampoules. Nevertheless, source-integrated dispensers in combination with a basic cesium supply by an oven at the ion source backplate might be a solution to improve the understanding and control of the cesium dynamics within the IPP test facilities.
A major objective of the modelling efforts at IPP is to predict the response of the negative-ion current density on the dynamics and homogeneity of the cesium conditions on the plasma grid. Therefore, a coupled simulation environment of the cesium transport code CsFlow3D and the negative-ion transport code TrajAn was developed. The simulation was applied to investigate the influence of the dynamics and homogeneity of the cesium flux on the negative-ion current density distribution over the plasma grid for a short and long time discharge characteristics.
It was found that an unevenly distributed ion production, created for example by inhomogeneous cesium conditions, can not be compensated by the broadening due to magnetic fields and collisions during the transport process of the negative ions from the production surface to the extraction apertures. The simulation of the short pulse characteristics showed a top-down asymmetry of the current density profile over the plasma grid, while a current density distribution that is

peaked at the edge of the plasma grid was found during long pulses.
The coupled simulation environment can now be extended in order to evaluate the effect of inhomogeneous plasma parameters on the transport and production of negative ions. This is the first step towards a global model for the production and extraction of negative ions, which is highly desirable for a numerical optimization of the stability and homogeneity of the ion source.
An important issue that has to be resolved in future studies is the relation between the cesium deposition onto the plasma grid and the negative-ion production - a process that is also correlated to the co-extracted electron current, according to observations at the IPP test facilities. Dedicated laboratory experiments of the negative-ion and electron density for a given cesium flux and sample temperature are, therefore, desirable. A modification of the ICP experiment at the University of Augsburg by a Faraday cup to enable negative-ion extraction is a possible way to accomplish this objective.

# A. Appendix - Work Function

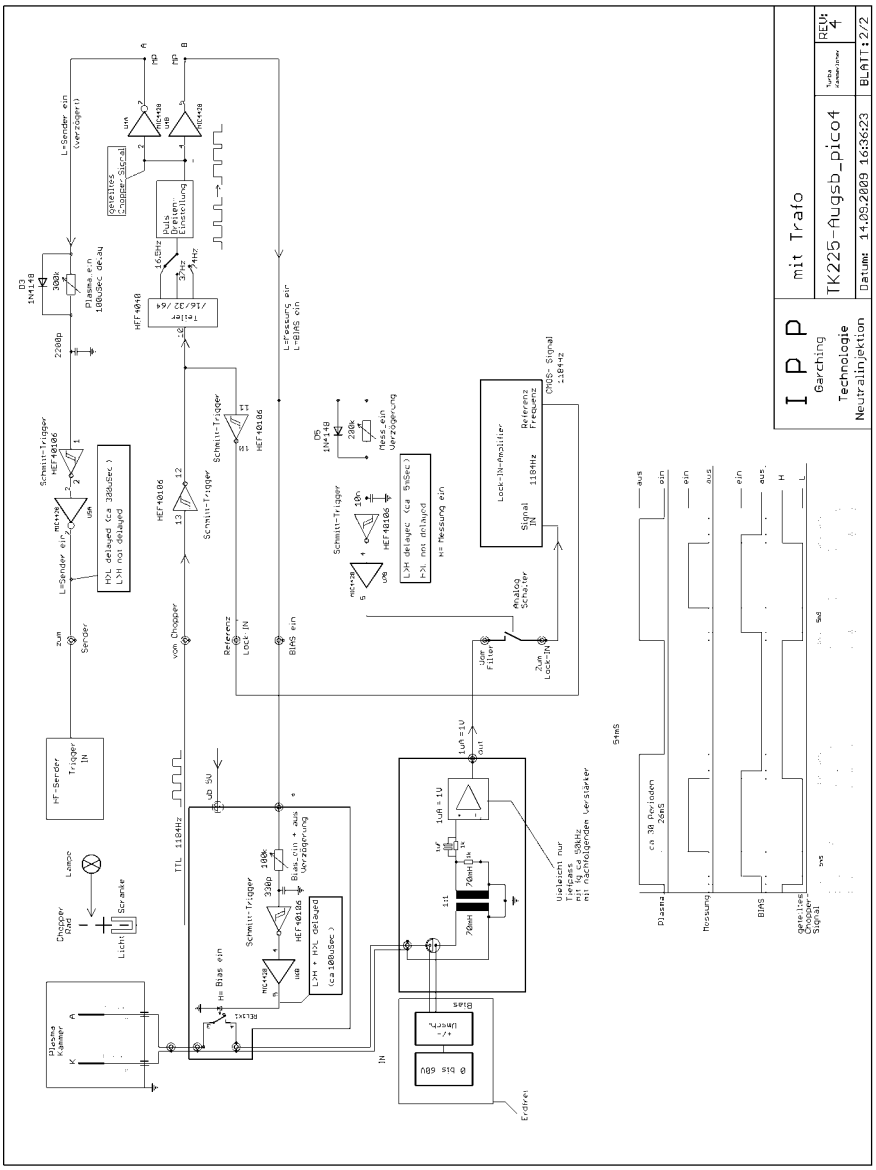


**Figure A.1.:** Measurement circuit for the pulsed work function measurement during plasma operation, which was developed by P. Turba (IPP).

# B. Appendix - Numerical Methods

## B.1. Bilinear Interpolation

The numerical algorithms used within the scope of this thesis need input data of (electric/magnetic) fields or particle data at arbitrary coordinates. Numerical codes to compute these fields or measurements of particle properties generate input data of these maps on a predefined computational grid. Numerical interpolation methods have to be used to compute field data, given on a computational grid, at arbitrary, 3D coordinates. In order to show the principle, an example of a two-dimensional linear interpolation method is presented, while 3D methods were implemented in the transport codes. Their application is, however, only a matter of more bookkeeping.
The data set for the interpolation routine is given by a matrix $f_{i,j}$ corresponding to a point $(x_i, y_j)$ of the computational grid. In order to access an arbitrary, non-tabulated data point at coordinates $(x, y)$, the four next-neighbour points on the computational grid are determined by the routine:

$$\begin{aligned} x_i &\leq x \leq x_{i+1}, \\ y_j &\leq y \leq y_{j+1}. \end{aligned} \tag{B.1}$$

This procedure is shown by figure B.1. For a bilinear interpolation, the weighting factors $t$ and $u$ are determined:

$$\begin{aligned} t &= \frac{x - x_i}{x_{i+1} - x_i}, \\ u &= \frac{y - y_i}{y_{j+1} - y_j}. \end{aligned} \tag{B.2}$$

These factors represent the distances of the interpolation point $(x, y)$ to the points on the computational grid. In case of a small distance to a specific grid point $(x_i, y_j)$, the corresponding value of $f_{i,j}$ is more pronounced in the calculation. In case of a 2D interpolation, the values are proportional to the area by the square to

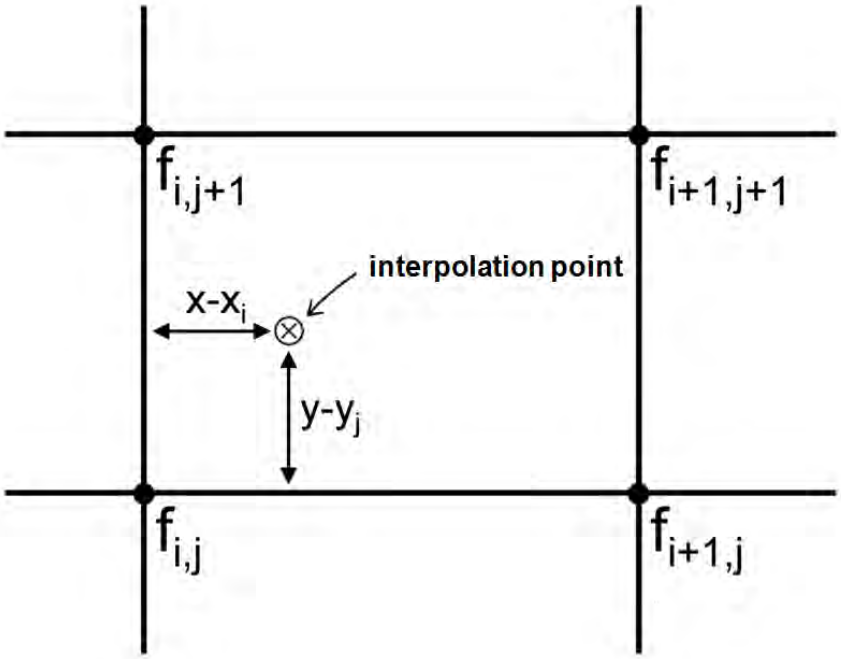


**Figure B.1.:** *Schematic drawing of the interpolation process for a given computational grid.*

the opposite points of the computational grid and the result of the interpolation $f_{\text{int}}(x, y)$ is then calculated by [WPF96]:

$$f_{\text{int}}(x,y) = (1-t)(1-u)\cdot f_{i,j} + t(1-u)\cdot f_{i+1,j} + \\ +(1-t)u\cdot f_{i,j+1} + tu\cdot f_{i+1,j+1}. \tag{B.3}$$

Inserting the grid point $(x_i, y_j)$ into B.3 results in $t = u = 0$ and the value $f_{i,j}$ is obtained. The method for 3D bilinear interpolation is very similar and instead of weighting the area relations, it is necessary to use the volume relations.

## B.2. Numerical Solution of Ordinary Differential Equations

All transport codes within the scope of this work require the solution of ODEs (**o**rdinary **d**ifferential **e**quation: ODE) in order to calculate the dynamics of charge species within electric and magnetic fields. The force on these particles is given by the non-relativistic Lorentz equation:

$$\frac{d^2\vec{r}}{dt^2} = \frac{q}{m}\left(\vec{E}(\vec{r}) + \frac{d\vec{r}}{dt}\times\vec{B}(\vec{r})\right). \tag{B.4}$$

The time-dependent vector of the particle coordinate $\vec{r}(t)$ is called trajectory, while $\vec{v}(t) = \frac{d\vec{r}}{dt}(t)$ is the current particle velocity at time $t$. Equation (B.4) requires, however, the specification of initial conditions of the position and starting velocity at time $t_0$:

$$\begin{aligned} \vec{r}(t_0) &= \vec{x}_0, \\ \frac{d\vec{r}}{dt}(t_0) &= \vec{v}_0, \end{aligned}$$

in order to ensure a unique solution.
The numerical solution of a second order ODE requires a transformation of the ode two a system of first order differential equations [WPF96]:

$$\frac{\mathrm{d}}{\mathrm{d}t}\begin{pmatrix}\vec{v}\\ \vec{r}\end{pmatrix} = \begin{pmatrix}\frac{q}{m}\left(\vec{E}(\vec{r}) + \vec{v}\times\vec{B}(\vec{r})\right)\\ \vec{v}\end{pmatrix} = \vec{F}(\vec{r},\vec{v}). \tag{B.5}$$

For the sake of simplicity, the vector $\vec{y}(t) = \begin{pmatrix}\vec{v}(t)\\ \vec{r}(t)\end{pmatrix}$ is introduced and it is possible to transform equation (B.5) by integration:

$$\vec{y}(t) = \vec{y}(t_0) + \int_{t_0}^{t} \vec{F}(\vec{y}(\tilde{t}))\mathrm{d}\tilde{t}. \tag{B.6}$$

The right hand of the integral equation (B.6) contains numerical data of electric and magnetic fields and depends also on $\vec{y}(t)$ itself. Thus an analytical approach is only possible for special cases. The solution has to be obtained by the application of numerical methods using discrete time intervals $\Delta t$ to compute a numerical approximation.
The explicit Euler method is a simple method to solve equation (B.6). In this case, the approximation of the integral in the time interval $[t_n, t_{n+1}]$ is done by:

$$\vec{y}_{n+1} = \vec{y}_n + \Delta t \cdot \vec{F}(\vec{y}_n) + O(\Delta t^2). \tag{B.7}$$

The variables with index $n$ correspond to $\vec{y}_n$=$\vec{y}\,(t_n)$. Equation (B.7) is repeated until a user-defined condition regarding the particle position or time is fulfilled. The determination of the field data $\vec{E}(\vec{r}_n)$ and $\vec{B}(\vec{r}_n)$ is done by numerical interpolation methods, as shown in section B.1.

# C. Appendix - Magnetic Field

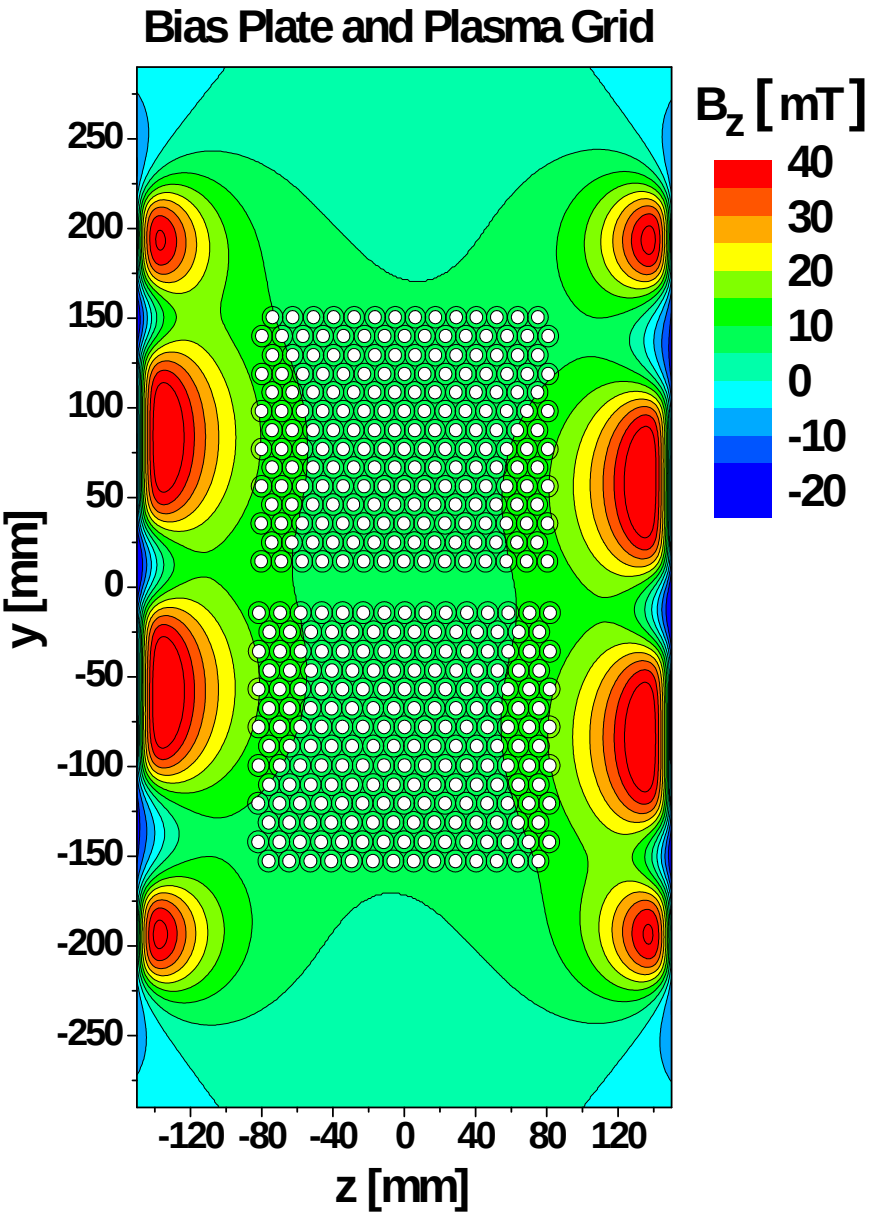


**Figure C.1.:** Contour plot of the magnetic flux density at the bias plate and plasma grid of the negative-ion source test facility MANITU computed with the Permag [Cir06] code.

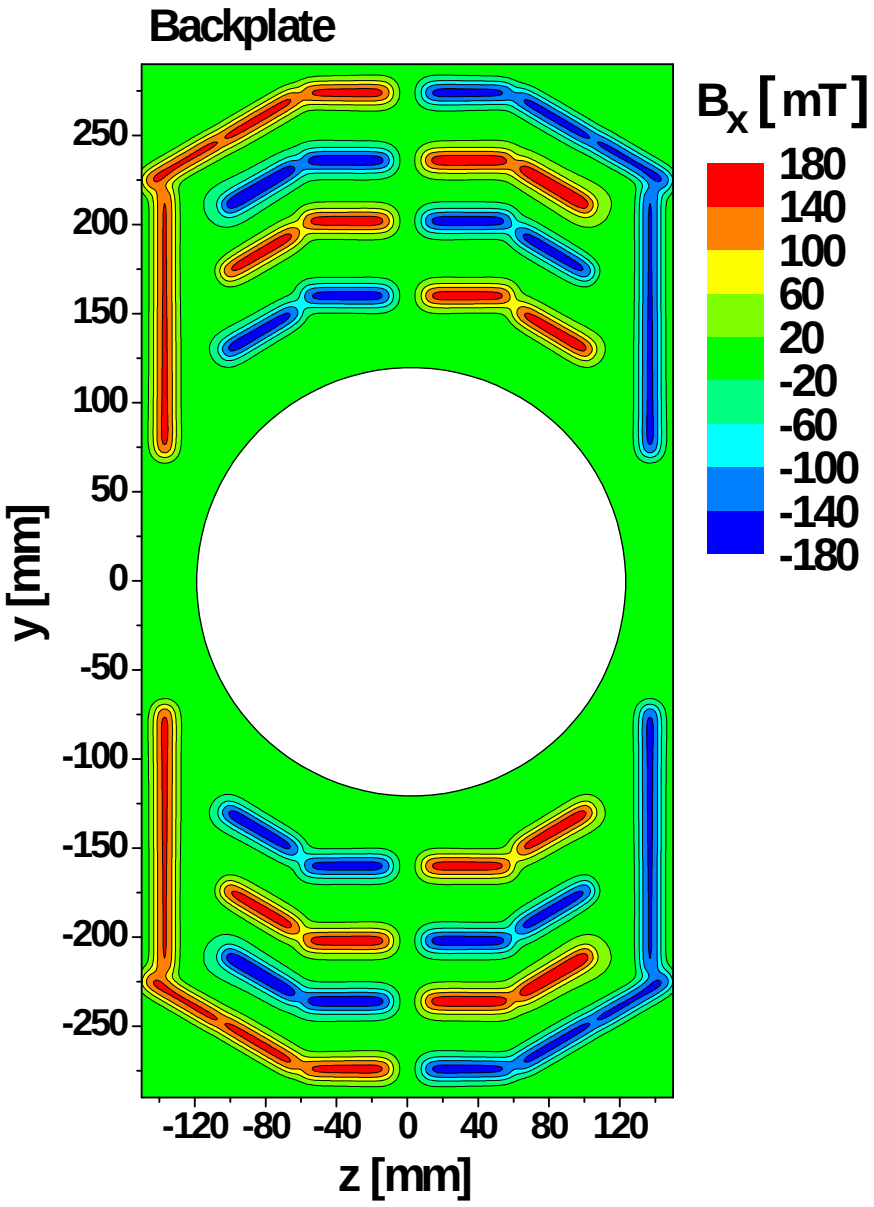


**Figure C.2.:** Contour plot of the magnetic flux density at the backplate of the negative-ion source test facility MANITU computed with the Permag [Cir06] code.

The Permag code [Cir06] was used to compute the complete 3D topology of the magnetic field configuration within the negative ion source. The position of the permanent magnets for the filter field is shown in figure 3.9. Figure C.1 and C.2 show contour plots of important magnetic field components close to the plasma grid and the backplate of the RF-driven negative-ion source.

# D. Appendix - Field Particle Data

## D.1. Plasma Density

A field map of the plasma density $n_{\mathrm{Plasma}}$ in the expansion region and the driver was determined according to probe measurements [MDCK$^+$09][TBM04]. A homogeneous, axi-symmetric profile was assumed to generated 3D field maps of the plasma density within the source. The data were modelled by the following formula:

$$n_{\mathrm{Plasma}}\left(\tilde{x}, r\right) = \frac{n_0(\tilde{x})}{1 + \exp\left(1.49\frac{r - r_{\mathrm{c}}(\tilde{x})}{\lambda(\tilde{x})}\right)}\ [\mathrm{m}^{-3}], \tag{D.1}$$

where $\tilde{x} = \frac{x[mm]}{240}$ is the distance from the center of the plasma grid and $r$ the corresponding radius. The variation of $n_{\mathrm{Plasma}}\left(\tilde{x}, r\right)$ in the expansion region ($\tilde{x} \leq 1$) is determined by:

$$n_0(\tilde{x}) = 1.5 \cdot 10^{18} \exp\left(2\ (\tilde{x} - 1)\right), \tag{D.2}$$

$$\lambda(\tilde{x}) = 0.05 - 0.02\,\tilde{x}, \tag{D.3}$$

$$r_{\mathrm{c}}(\tilde{x}) = 0.15 - 0.03\,\tilde{x}, \tag{D.4}$$

while in the driver ($\tilde{x} > 1$) a continous transition with constant values of $r_{\mathrm{c}}(\tilde{x}) = 0.12$, $\lambda(\tilde{x}) = 0.03$ and $n_0(\tilde{x}) = 1.5 \cdot 10^{18}$ [MDCK$^+$09] was used.

## D.2. Electron Temperature

The field map of the electron temperature $T_{\mathrm{e}}$ was determined according to JANUS probe measurements presented in [Die07]. A homogeneous, axi-symmetric profile was assumed to generated 3D field maps of the electron temperature within the source. The data was modelled by the following formula:

$$T_{\mathrm{e}}\left(\tilde{x}, r\right) = \frac{T_0(\tilde{x})}{1 + \exp\left(1.49\frac{r - r_{\mathrm{c}}(\tilde{x})}{\lambda(\tilde{x})}\right)}\ [\mathrm{eV}]. \tag{D.5}$$

Identical parameters for the radial dependence as in formula D.3 and D.4 were used for the electron temperature. The axial dependence of $T_0(\tilde{x})$

$$T_0(\tilde{x}) = 20 \exp\left(-\frac{(-\tilde{x}+1)}{0.26}\right). \tag{D.6}$$

In the driver ($\tilde{x} > 1$) a constant electron temperature of $T_\mathrm{e}$=20 eV was used. Axial profiles of the plasma density $n_\mathrm{Plasma}$ and the electron temperature $T_\mathrm{e}$ are shown in figure D.1.

## D.3. Hydrogen Gas Density and Temperature

A constant background density of $\mathrm{n_{H_2}}$=5x$10^{19}$ $\mathrm{m^{-3}}$ with a constant gas temperature of $\mathrm{T_{H_2}}$=1200 K was used for the transport simulations, according to data given in [FFF$^+$06][FW06].

## D.4. Plasma Potential

The plasma potential map $\Phi_\mathrm{Plasma}$ was derived from Langmuir-probe measurements [Die07][CKF08][MDCK$^+$09] at different points within the negative-ion source test facility BATMAN. The following parabolic dependence of the plasma potential on the radius $r$ was used in the expansion region:

$$\Phi_\mathrm{Plasma}(\tilde{x}, r) = \Phi_0(\tilde{x}) \cdot \left(1 - a(r)\ r^2\right)\ [\mathrm{V}], \tag{D.7}$$

$$a(r) = 0.2\,\frac{(1-\tilde{x})}{l_\mathrm{y}^2}, \tag{D.8}$$

where is defined as $l_\mathrm{y} = L_\mathrm{y}/2$. The axial depenence of the plasma potential is given by:

$$\Phi_0(\tilde{x}) = 40 \exp\left(-\ (\tilde{x}-1) \ln\left(\frac{1}{2}\right)\right). \tag{D.9}$$

A higher plasma potential is obtained within the driver and the following linear relation was used:

$$\Phi_\mathrm{Plasma}(\tilde{x}, r) = 40 + (\tilde{x}-1)\ 14.28\ [\mathrm{V}], \tag{D.10}$$

and a maximum plasma potential of $\Phi_\mathrm{Plasma} = 50$ V is reached within the driver.

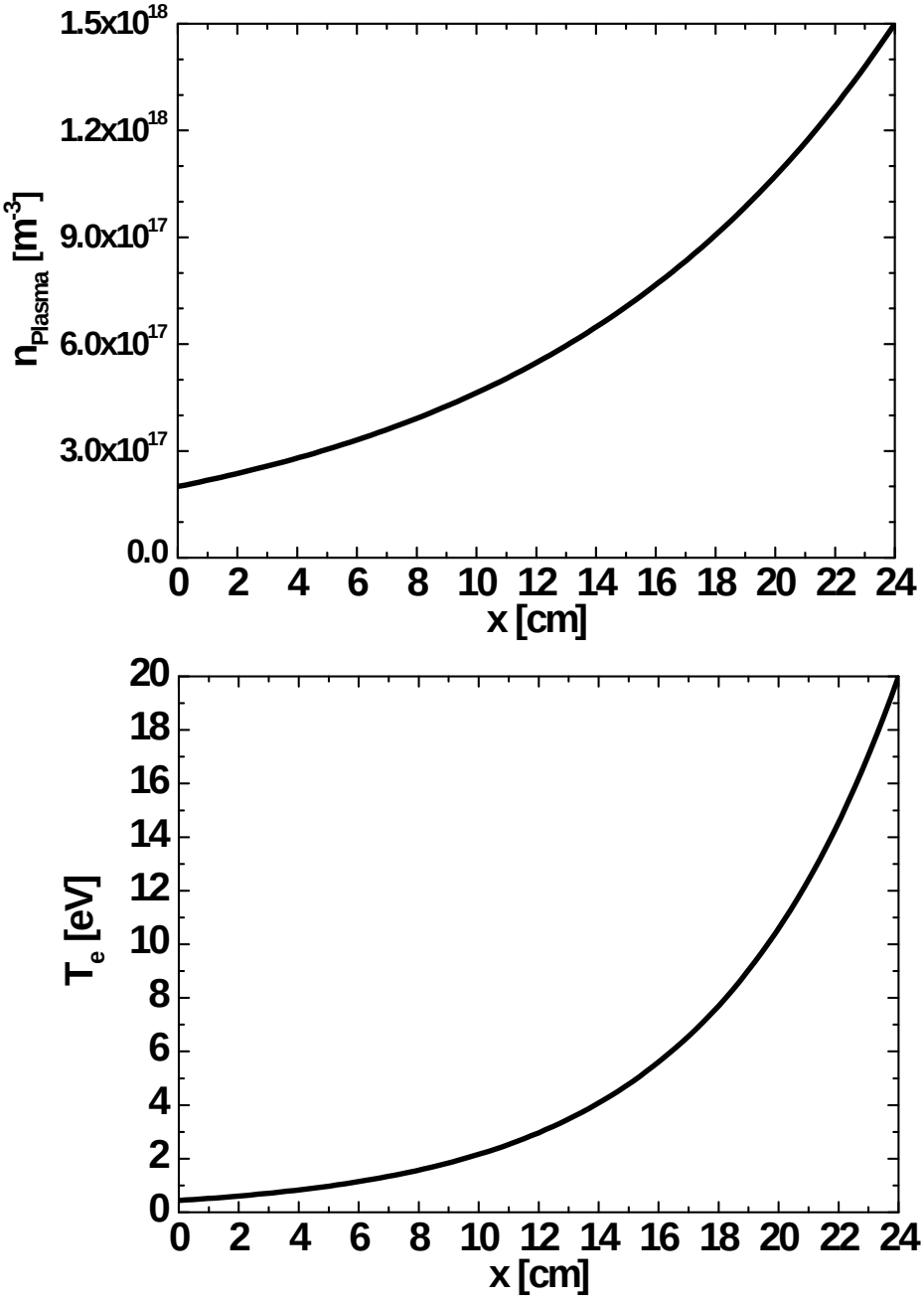


**Figure D.1.:** Axial profiles of the electron density and temperature used in CsFlow3D.

# E. Constants and Abbreviations

| Constant | Meaning | Value |
|---|---|---|
| $e$ | elementary charge | $1.602\text{x}10^{-19}$ C |
| $h$ | Planck constant | $6.63\text{x}10^{-34}$ Js |
| $k_\text{b}$ | Boltzman constant | $1.38\text{x}10^{-23}$ J/K |
| $m_\text{e}$ | electron mass | $9.10\text{x}10^{-31}$ kg |
| $m_\text{H}$ | proton mass | $1.67\text{x}10^{-27}$ kg |
| $m_\text{Cs}$ | mass of cesium | $= 133\, m_\text{H}$ |
| $\pi$ | | 3.141593 |

| Abbreviation | Meaning |
|---|---|
| CD | current drive |
| DSMC | direct simulation Monte Carlo |
| ECRH | electron cyclotron resonance heating |
| EG | extraction grid |
| GG | grounded grid |
| ICP | inductively coupled plasma |
| ICRH | ion cyclotron resonance heating |
| IPP | Max-Planck Institut für Plasmaphysik |
| ml | cesium monolayer |
| | $4.5\text{x}10^{14}$ cesium atoms per $\text{cm}^{-2}$ |
| NBI | neutral beam injection |
| N-NBI | negative neutral beam injection |
| OES | optical emission spectroscopy |
| PG | plasma grid |
| QMB | quartz microbalance |
| RF-driven | radio frequency driven |
| SID | surface ionization detector |

# Bibliography

[AGK+85] P. W. Van Amersfoort, J. J. C. Geerlings, L. F. Tz. Kwakman, et al., *Formation of negative hydrogen ions on a cesiated W(110) surface; the influence of hydrogen implantation*, J. Appl. Phys. **58** (1985), 3566.

[ATG85] P. W. Van Amersfoort, Y. Tong, and E. H. A. Granneman, *A model for the stationary cesium coverage on a converter surface in a cesium seeded hydrogen discharge*, J. Appl. Phys. **58** (1985), 2317.

[AW78] M. Allan and S. F. Wong, *Effect of vibrational and rotational excitation on dissociative attachment in hydrogen*, Phys. Rev. Lett. **41** (1978), 1791.

[Bac06] M. Bacal, *Physics aspects of negative ion sources*, Nucl. Fusion **46** (2006), 250.

[Bar90] C. F. Barnett, *ORNL-6086*, Tech. report, Oak Ridge National Laboratory, 1990.

[BD69] G.A. Boutry and H. Dormont, Philips Tech. Rev. **30** (1969), 225.

[BDD74] Y. Belchenko, G. Dimov, and V. Dudinikov, *Powerful injector of neutrals with a surface-plasma source of negative ions*, Nucl. Fusion **14** (1974), 113.

[Bir91] C.K. Birdsall, *Particle-In-Cell charged-particle simulations, plus Monte Carlo collisions with neutral atoms, PIC-MCC*, IEEE Trans. Plasma Science **19** (1991), no. 2, 65.

[Bir94] G. A. Bird, *Molecular gas dynamics and the direct simulation of gas flows*, Clarendon Press, Oxford, 1994.

[BL91] C. K. Birdsall and A. B. Langdon, *Plasma physics via computer simulation*, IOP Publishing, 1991.

[BND77] M. Bacal, E. Nicolopoulou, and H. Douset, Proc. Int. Symp. Production and Neutralization of Negative Ions and Beams, 26 (New York), BNL, 1977.

[Bor86] H. U. Borgstedt, *Analytical problems*, ch. Chemical reactions in alkali metals, p. 125, Springer, Berlin/Heidelberg, 1986.

[BPS75] K.H. Berkner, R.V. Pyle, and J. W. Stearns, *Intense, mixed-energy hydrogen beams for CTR injection*, Nucl. Fusion **15** (1975), 249.

[BS04] Bermann-Schaefer, *Lehrbuch der Experimentalphysik, Band 3, Optik*, de Gruyter, Berlin, 2004.

[CBC07] D. Ciric, D. Brown, and C. Challis, *Overview of the JET neutral beam enhancement project*, Fusion Eng. Des. **82** (2007), 610.

[CD09] B. Crowley and S. Dietrich, *A Langmuir probe system incorporating the Boyd-Twiddy method for EEDF measurement applied to an inductively coupled plasma source*, Plasma Sources Sci. Technol. **18** (2009), no. 1, 014010.

[Cir06] D. Ciric, *Private communication*, 2006, JET Joint Undertaking, Abingdon.

[CKF08] S. Christ-Koch and U. Fantz, *Profile der Plasmaparameter und Dichte negativer Wasserstoffionen mittels Laserdetachmentmessungen in HF-angeregten Ionenquellen*, Ph.D. thesis, Universität Augsburg, 2008.

[CMP04] L. Cattaneo, C. Maeda, and R. Petersen, *Alkamax application note*, Tech. Report 4, SAES Getters, 2004.

[Die07] S. Dietrich, *Messungen von Plasmaparameterprofilen mittels der Janus-Sonde*, Technology Meeting (Ringberg), IPP, Technology Division, 2007.

[DP80] J.-L. Desplat and C.A. Papageorgopoulos, *Interaction of cesium and oxygen on W(110): I. Cesium adsorption on oxygenated and oxidized W(110)*, Surf. Sci. **92** (1980), no. 1, 97.

[Eas70] D. E. Eastman, *Photoelectric work functions of transition, rare-earth, and noble metals*, Phys. Rev. B **2** (1970), no. 1, 1.

[EB85] W. Eckstein and J. P. Biersack, *Reflection of low-energy hydrogen from solids*, Appl. Phys. A **38** (1985), 123.

[EdSO+95] M.J.J. Eerden, M.C.M Van de Sanden, D.K. Otorbaev, et al., *Cross section for the mututal neutralization reaction $H_2^+ + H^-$, calculated in a multiple-crossing Landau-Zener approximation*, Phys. Rev. A **51** (1995), no. 4, 3362.

[F+08] P. Franzen et al., *Physical and experimental background of the design of the ELISE test facility*, AIP Conf. Proc. **1097** (2008), 451.

[FBS98] J. Fan, I. Boyd, and C. Shelton, *Monte Carlo modeling of YBCO vapor deposition*, Tech. report, Defense Technical Information Center OAI-PMH Repository, 1998.

[Fel86] L. Feldman, *Fundamentals of surface and thin film analysis*, Prentice Hall PTR, New York, 1986.

[FFF+06] U. Fantz, H. Falter, P. Franzen, et al., *Spectroscopy a powerful diagnostic tool in source development*, Nucl. Fusion **46** (2006), S297.

[FFH+07] P. Franzen, H. Falter, B. Heinemann, et al., *RADI - a RF source size-scaling experiment towards the ITER neutral beam negative ion source*, Fusion Eng. Des. **82** (2007), no. 4, 407.

[FFK+07] U. Fantz, P. Franzen, W. Kraus, et al., *Negative ion RF sources for ITER NBI: Status of the development and recent achievements*, Plasma Phys. Control. Fusion **49** (2007), B563.

[FFK+08] P. Franzen, U. Fantz, W. Kraus, et al., *The IPP RF Source: A high power, lower pressure negative ion source for the neutral beam injection system of ITER*, AIP Conference Proceedings **993** (2008), 51.

[Fow31] R. H. Fowler, *The analysis of photoelectric sensitivity curves for clean metals at various temperatures*, Phys. Rev. **38** (1931), 45.

[Fri12] R. Friedl, Ph.D. thesis, to be submitted, Universität Augsburg, 2012.

[FW06] U. Fantz and D. Wünderlich, *A novel diagnostic technique of $H^-(D^-)$ densities in negative hydrogen ion sources*, New J. Phys. **8** (2006), 301.

[Gam28] G. Gamov, *Zur Quantentheorie des Atomkernes*, Zeitschrift für Physik **51** (1928), 204.

[Gra80] W. G. Graham, *Properties of alkali metals adsorbed onto metal surfaces*, Proceedings of the Second International Symposium on the Production and Neutralisation of Negative Hydrogen Ions and Beams (Brookhaven National Laboratory, Upton, New York), AIP, 1980.

[Gre02] J. Greenwood, *The correct and incorrect generation of a cosine distribution of scattered particles for Monte Carlo modelling of vacuum systems*, Vacuum **67** (2002), 217.

[GWF09] R. Gutser, D. Wünderlich, and U. Fantz, *Negative hydrogen ion transport in RF-driven ion sources for ITER NBI*, Plasma Phys. Control. Fusion **51** (2009), 045005.

[H+09] R. Hemsworth et al., *Status of the ITER heating neutral beam system*, Nucl. Fusion **49** (2009), 045006.

[HE88] R. W. Hockney and J. W. Eastwood, *Computer simulation using particles*, Taylor and Francis, 1988.

[HFF+09] B. Heinemann, P. Franzen, U. Fantz, et al., *Design of the "half-size" ITER neutral beam source for the test facility ELISE*, Fusion Eng. Des. **84** (2009), 915, Proceeding of the 25th Symposium on Fusion Technology - (SOFT-25).

[HKM+06] C. Hill, D. Küchler, C. Mastrostefano, et al., *$H^-$ source developments at CERN*, Rev. Sci. Instrum. **77** (2006), 03A521.

[Hop09] C. Hopf, *Private communcation*, 2009.

[HR63] B. Hopkins and J. Riviere, *The work function of polycrystalline tungsten foil*, Proceedings of the Physical Society **81** (1963), no. 3, 590.

[HTA08] R. Hemsworth, A. Tanga, and V. Antoni, *Status of the ITER neutral beam injection system*, Rev. Sci. Instrum. **79** (2008), 02C109.

[Hub06] J.D. Huba, *NRL plasma formulary*, Naval Research Laboratory, 2006.

[Hut02] H. Hutchinson, *Principles of plasma diagnostics*, Cambridge University Press, Cambridge UK, 2002.

[IAE02] IAEA, *ITER technical basis 2002 ITER EDA documentation series no. 24 (plant description document, sec. 2.5.1.)*, Tech. report, International Atomic Energy Agency (IAEA), 2002.

[IKS92] J. D. Isenberg, H. J. Kwon, and M. Seidl, *Surface production of $H^-$ ions by backscattering of $H^+$ and $H_2^+$ ions in the 3-50 eV ion energy range*, AIP Conference Proceedings on the production and neutralization of negative ions and beams **287** (1992), 38.

[JL87] R.K. Janev and W.D. Langer, *Elementary processes in hydrogen-helium plasmas*, Springer Series on Atoms and Plasmas, Berlin, 1987.

[Jou06] K. Jousten, *Wutz Handbuch Vakuumtechnik: Theorie und Praxis; 9. aufl.*, Vieweg, Wiesbaden, 2006.

[JR78] R.K. Janev and Z.M. Radulovic, *Ion-ion recombination and ion-pair formation processes in alkali-hydrogen diatomic systems*, Phys. Rev. A **17** (1978), no. 3, 889.

[K+00] M. Kawai et al., *Study of plasma uniformity on JT-60U negative ion source*, Rev. Sci. Instrum. **71** (2000), 755.

[KBF+09] W. Kraus, M. Berger, U. Fantz, et al., *Long pulse $H^-$ beam extraction with a RF-driven ion source with low fraction of co-extracted electrons.*, AIP Conference Proceedings **1097** (2009), 275.

[KF07] S. König and U. Fantz, *Untersuchungen der Eigenschaften cäsierter Oberflächen in Wasserstoffplasmen*, Tech. report, Max-Planck Institut für Plasmaphysik, 2007.

[KFF+08] W. Kraus, H.-D. Falter, U. Fantz, et al., *Long pulse large area beam extraction with a RF-driven $H^-/D^-$ source*, vol. 79, AIP Conference Proceedings, 2008, p. 02C108.

[KFF+09] W. Kraus, P. Franzen, U. Fantz, et al., *Long pulse $H^-/D^-$ beam extraction with an RF-driven ion source on a high power level*, AIP Conference Proceedings **81** (2009).

[KH06] A. Krylov and R.S. Hemsworth, *Gas flow and related beam losses in the ITER neutral beam injector*, Fusion Eng. Des. **81** (2006), 2239.

[KPW+00] A. Kirschner, V. Philipps, J. Winter, et al., *Simulation of the plasma-wall interaction in a Tokamak with the Monte Carlo code ERO-TEXTOR*, Nucl. Fusion **40** (2000), 989.

[Kra09] W. Kraus, *Private communication*, 2009.

[Küg09] K. J. Kügler, *Physikalische Grundlagen der Vakuumtechnik*, VDI Wissensforum, 2009.

[Law67] J. D. Lawson, *Some criteria for a power producing thermonuclear reactor*, Proceedings of the Physical Society B **70** (1967), 6.

[LB08] Landolt-Börnstein, *Group IV Physical Chemistry*, Springer, Berlin, 2008.

[LDD+91] K. N. Leung, G. J. DeVries, W. F. DiVergilio, et al., *RF-driven multicusp $H^-$ ion source*, Rev. Sci. Instrum. **62** (1991), 100.

[Lid07] D. Lide, *CRC Handbook of Chemistry and Physics, 88th Edition (CRC Handbook of Chemistry and Physics)*, CRC, 2007.

[LL58] L.D. Landau and E.M. Lifshitz, *Quantum mechanics: Non-relativistic theory, course of theoretical physics*, vol. 3, Pergamon Press, London, Paris, 1958.

[LL05] M. Lieberman and A. Lichtenberg, *Principles of plasma discharges and materials processing; 2nd ed.*, Wiley, Newark, NJ, 2005.

[LS60] J. Van Laar and J.J. Schear, Philips Res. Rep. **15** (1960), 1.

[LS92] B. S. Lee and M. Seidl, *Surface production of $H^-$ ions by hyperthermal hydrogen atoms*, Appl. Phys. Letters **61** (1992), 2857.

[ŁSK+06] M. Łukomski, S. Sutton, W. Kedzierski, et al., *Electron-impact ionization cross sections out of the ground and excited states of cesium*, Phys. Rev. A **74** (2006), 032708.

[MCT+08] R. McKay, K. Clements, A. Thyagaraja, et al., *Test-particle simulations of collisional impurity transport in rotating spherical tokamak plasmas*, Plasma Phys. Control. Fusion **50** (2008), no. 6, 065017.

[MDCK+09] P. McNeely, S. Dudin, S. Christ-Koch, et al., *A Langmuir probe system for high power RF-driven negative ion sources on high potential*, Plasma Sources Sci. Technol. **18** (2009), 014011.

[Mit89] J. Mitterauer, *Contamination test of a cesium field ion thruster*, J. Propulsion **7** (1989), 364.

[MSD93] S. Ma, R.D. Sydora, and J.M. Dawson, *Binary collision model in gyrokinetic simulation plasmas*, Computer Physics Communications **77** (1993), 190.

[O+00] Y. Okumura et al., *Negative ion source for TOKAMAK neutral beam injection*, Rev. Sci. Instrum. **71** (2000), 1219.

[Oha98] Y. Ohara, *Development of high power ion sources for fusion*, Rev. Sci. Instrum. **69** (1998), 908.

[OHI89] Y. Okumura, M. Hanada, and T. Inone, *Proc. 5th int. symp. production and neutralization of negative ions and beams*, vol. 169, 1989.

[PAL07] A. Pailloux, T. Alpettaz, and E. Lizon, *Candlestick oven with a silica wick provides an intense collimated cesium atomic beam*, Rev. Sci. Instrum. **78** (2007), no. 2, 023102.

[Pam95] J. Pamela, *The physics of production, acceleration and neutralization of large negative ion beams*, Plasma Phys. Control. Fusion **37** (1995), A325.

[PBB07] D. Packan, J. Bonnet, and A. Bresson, *Neutral cesium velocity vector and absolute number density LIF optical measurement with application to a flight model MICROSCOPE cesium FEEP thruster*, IEPC-2007-219 30th International Electric Propulsion Conference (Florence, Italy, September 17-20), 2007.

[Pet09] J. Peters, *The new DESY RF-driven multicusp $H^-$ ion source*, AIP Conference Proceedings **1097** (2009), 171.

[RB59] E. Rothe and R. Bernstein, *Total collision cross sections for the interaction of atomic beams of alkali metals with gases*, J. Chem. Phys. **31** (1959), 1619.

[RGS+08] G. Rouleau, E. Geros, J. Stelzer, et al., *Tungsten filament material and cesium dynamic equilibrium effects on a surface converter ion source*, vol. 79, AIP Conference Proceedings, 2008, p. 02A514.

[Ruf10] B. Ruf, *Private communcation*, 2010.

[RWL82] B. Rasser, J.N.M. Van Wunnik, and J. Los, *Theoretical models of the negative ionization of hydrogen on clean tungsten, cesiated tungsten and cesium surfaces at low energies*, Surf. Sci. **118** (1982), 697.

[Sau59] G. Sauerbrey, *Verwendung von Schwingquarzen zur Wägung dünner Schichten und zur Mikrowägung*, Zeitschrift fur Physik **155** (1959), 206.

[SCF85] M. Succi, R. Canino, and B. Ferrario, *Atomic absorption evaporation flow rate measurements of alkali metal dispensers*, Vacuum **35** (1985), no. 12, 579.

[SCF+99] E. Speth, M. Ciric, J. Feist, et al., *RF ion sources for fusion applications: Design, development and performance*, Fus. Eng. Des. **46** (1999), 383.

[Sch09] L. Schiesco, *Sputtering yield in MANITU*, Tech. report, Max-Planck-Institut für Plasmaphysik, Technology Division, 2009.

[SCM+07] M. Shimada, D.J. Campbell, V. Mukhovatov, et al., *The progress in the ITER physics basis: Chapter 1: Overview and summary*, Nucl. Fusion **47** (2007), no. 6, S1.

[SFAP01] P. Scheubert, U. Fantz, P. Awakowicz, and H. Paulin, *Experimental and theoretical characterization of an inductively coupled plasma source*, J. Appl. Phys. **90** (2001), no. 2, 587.

[SFF+06] E. Speth, H.D. Falter, P. Franzen, et al., *Overview of the RF source development programme at IPP Garching*, Nucl. Fusion **46** (2006), 220.

[SFH+02] A. Staebler, P. Franzen, J. Hobirk, et al., *The role of neutral beam injection geometry in advanced discharge scenarios on ASDEX Upgrade*, 29th EPS Conference on Plasma Physics and Controlled Fusion (Montreaux), vol. 26B, ECA, 2002.

[SLL+03] B. Streibl, P. Lang, F. Leuterer, et al., *Chapter 2.: Machine design, fueling and heating in ASDEX UPGRADE*, Fusion Sci. Techn. **44** (2003), 578.

[Son94] W. Songster, *The Cs-H system*, Journal of Phase Equilibria **15** (1994), 1.

[SPA09] SAES Getters SPA., *Alkaline metal dispensers - product data sheet and application manual*, SAES Getters, Via Gallarate, 215 20151 Milano, Italy, 2009.

[Spe89] E. Speth, *Neutral beam heating of fusion plasmas*, Rep. Prog. Phys. **52** (1989), 57.

[SS68] L. W. Swanson and R. W. Strayer, *Field-electron-microscopy studies of cesium layers on various refractory metals: Work function change*, J. Chem. Phys. **48** (1968), 2421.

[Sta05] P. Starke, *Chemische Erosion verschiedener Kohlenstoff-Materialien durch Wasserstoff-Isotope in Niederdruckplasmen*, Ph.D. thesis, University of Augsburg, 2005.

[SW89] P. Spädtke and S. Wipf, *KOBRA3 - a code for the calculation of space charge influenced trajectories in 3 dimensions*, GSI Report **89-09** (1989).

[Swe73] D. R. Sweetman, *Ignition condition on tokamak experiments and role of neutral injection heating*, Nucl. Fusion **13** (1973), 157.

[SWF00] R. Schletti, P. Wurz, and T. Fröhlich, *Metallic work function measurement in the range 2 - 3.3 eV using a blue light-emitting diode source*, Rev. Sci. Instrum. **71** (2000), 499.

[T+98] R. Trainham et al., *Long pulse operation of the Kamaboko negative ion source on the MANTIS test bed*, Production and Neutralization of Negative Ions and Beams (C. Jacquot, ed.), AIP, 1998, p. 105.

[T+00] Y. Takeiri et al., *Negative hydrogen ion source development for large helical device neutral beam injector*, Rev. Sci. Instrum. **71** (2000), 1225.

[Tay29] J. B. Taylor, *Eine Methode zur direkten Messung der Intensitätsverteilung in Molekularstrahlen*, Zeitschrift fur Physik **57** (1929), 242.

[TBM04] A. Tanga, M. Bandyopadhyay, and P. McNeely, *Measurement of ion flow in a negative ion source using a mach probe*, Appl. Phys. Lett. **84** (2004), 182.

[TIK+06] M. Taniguchi, T. Inoue, M. Kashiwagi, K. Watanabe, M. Hanada, T. Seki, M. Dairaku, and K. Sakamoto, *Acceleration of MeV-class energy, high-current-density $H^-$-ion beams for ITER neutral beam system*, Rev. Sci. Instrum. **77** (2006), 03A514.

[TL33] J. B. Taylor and I. Langmuir, *The evaporation of atoms, ions, and electrons from cesium films on tungsten*, Phys. Rev **6** (1933), 423.

[TL37] J. Taylor and I. Langmuir, *Vapor pressure of caesium by the positive ion method*, Phys. Rev. **51** (1937), 753.

[vAGR+86] P. W. van Amersfoort, J. J. C. Geerlings, R. Rodink, E. H. A. Granneman, and J. Los, *Formation of negative hydrogen ions on a coadsorbed layer of cesium and hydrogen on W(110)*, J. Appl. Phys. **59** (1986), 241.

[VY88] N. B. Vargaftik and V. S. Yargin, *Alkali-metal liquid and vapor thermophysical properties*, J. Eng. Phys. **54** (1988), 109.

[Wes00] J. Wesson, *The science of JET*, Tech. report, JET Joint Undertaking, 2000.

[Wes04] Wesson, *Tokamaks*, Oxford University Press, Oxford, UK, 2004.

[WFHK83] E. Wimmer, A. J. Freeman, J. R. Hiskes, and A. M. Karo, *All-electron local-density theory of alkali-metal bonding on transition-metal surfaces: Cs on W(001)*, Phys. Rev. B **28** (1983), 3074.

[WGF09] D. Wünderlich, R. Gutser, and U. Fantz, *PIC code for the plasma sheath in large caesiated RF sources for negative hydrogen ions*, Plasma Sources Sci. Technol. **18** (2009), no. 4, 045031.

[Wil66a] R. Wilson, *Electron and ion emission from polycrystalline surfaces of Be, Ti, Cr, Ni, Cu, Pt, and type-304 stainless steel in cesium vapor*, J. Appl. Phys. **37** (1966), 3161.

[Wil66b] R. G. Wilson, *Electron and ion emission from polycrystalline surfaces of Nb, Mo, Ta, W, Re, Os, and Ir in cesium vapor*, J. Appl. Phys. **37** (1966), 4125.

[Wim10] C. Wimmer, *Diploma Thesis*, 2010.

[WPF96] S. Teukolksy W. Press and B. Flannery, *Numerical recipes in Fortran 90: The art of parallel scientific computing 2nd edition.*, Cambridge University Press, Cambridge, 1996.

[WSMK05] R. F. Welton, M. P. Stockli, S. N. Murray, and R. Keller, *Recent advances in the performance and understanding of the SNS ion source*, AIP Conference Proceedings **763** (2005), 296.

My PhD work would not have been possible without the help and encouragement from my colleagues and supervisors. I would like to thank everybody who have helped and encouraged me during my PhD work:

- I am heartily thankful to my supervisor, **Prof. Dr.-Ing. Ursel Fantz**, without her encouragement, guidance and support from the initial to the final stage this disseration would not have been possible.
- I would like to thank my examination committee, especially **Prof. Dr. Achim Wixforth**.
- I would like to thank the complete **NNBI-Team** for the pleasant working atmosphere and their support, **especially**
- **Dr. Dirk Wünderlich**, **Dr. Peter Franzen** and **Dr. Paul McNeely** for their advise and for their support.
- **Dipl.-Ing. Markus Fröschle** for his assistance in mechanical engineering and CATIA related question.
- **Mr. Peter Turba** and **Mr. Martin Kammerloher** for their assistance in electrical engineering.
- **Mr. Jürgen Steinberger** for assembling the tungsten filaments for the surface ionization detector.
- I would like the thank the **EPP-Team** for their support during the cesium experiments, **especially**
- **Dr. Stephan Dietrich**, **Mr. Christian Wimmer** and **Dipl.-Phys. Roland Friedl.**

Overall, I must acknowledge that my wife **Susanne** has sacrificed a lot in the last three years and helped me everyday to complete my PhD.

# Lebenslauf

| | |
|---|---|
| Name: | Raphael Gutser |
| Geboren: | 28.08.1980 in Schwabmünchen |
| Familienstand: | verheiratet |

| | |
|---|---|
| 09/1987 - 07/1991 | Grundschule Mindelheim |
| 09/1991 - 06/2000 | Gymnasium Maristenkolleg Mindelheim<br>Erwerb der allgemeinen Hochschulreife |
| 07/2000 - 04/2001 | Grundwehrdienst<br>Flugabwehrraketengruppe 22, Penzing |
| 05/2001 - 06/2001 | Inlingua-Sprachenschule Washington D.C. |
| 09/2001 - 11/2006 | Studiengang Diplom Physik an der Universität Augsburg<br>Erwerb des Diploms in Physik |
| 12/2006 - 03/2007 | Wissenschaftlicher Mitarbeiter Universität Augsburg |
| 04/2007 - 03/2010 | Doktorand am Max-Planck-Institut für Plasmaphysik, Garching<br>Bereich Technologie, Arbeitsgruppe Neutralteilcheninjektion |